



Provided by the author(s) and University of Galway in accordance with publisher policies. Please cite the published version when available.

Title	Topology preserving and robust variational image segmentation models with applications in medical imaging
Author(s)	Duggan, Noirin
Publication Date	2015-07-14
Item record	<a href="http://hdl.handle.net/10379/5309">http://hdl.handle.net/10379/5309</a>

Downloaded 2024-04-19T22:13:59Z

Some rights reserved. For more information, please see the item record link above.





TOPOLOGY PRESERVING AND ROBUST  
VARIATIONAL IMAGE SEGMENTATION MODELS  
WITH APPLICATIONS IN MEDICAL IMAGING

Nóirín Duggan B.E.

A thesis submitted for the degree of Doctor of  
Philosophy

September 2014

Professor in Discipline: Prof. G. Ó Laighin  
Supervisors: Dr. M. Glavin & Dr. E. Jones

# Declaration

I hereby declare that the work contained in this thesis is my own except where otherwise indicated, and it has not been submitted by me in pursuance of any other degree.



---

Nóiriín Duggan

September 2014

# Abstract

Computer vision refers to the process of enabling computers to mimic the human visual system. The central concern of this thesis is a sub-task of computer vision known as image segmentation, which refers to the decomposition of an image into its most relevant regions. Image segmentation by its nature is a poorly defined task, considering that what constitutes the ‘best’ decomposition of an image changes according to the task at hand. In this context, the specific focus of this thesis is to investigate the general topic of segmentation robustness; toward this goal, three aspects of this topic have been explored, with a new algorithm proposed in each case.

The first algorithm addresses the problem of boundary detection in low-contrast images. The proposed technique consists in solving the well-known Mumford-Shah functional using a highly efficient convex segmentation scheme, the output of which is a simplified binary representation of the original image. Using this binary representation, an edge detector is generated, the output of which is input into a geodesic active contour scheme to produce the final curve representing the boundary of the structure. Results indicate that the proposed scheme yields enhanced performance compared to existing methods.

The second algorithm addresses the issue of robustness with respect to topology preservation. In this context, a segmentation model is proposed that consists of a non-local topology preserving constraint and a data fidelity constraint that increases robustness in the presence of noise. Results indicate that the proposed method performs better than existing methods at imposing a topology prior in the presence of noise.

The third algorithm consists of a novel approach for lung nodule candidate detection in Computed Tomography which is based on the application of global segmentation methods combined with mean curvature minimisation and simple rule-based filtering. Nodules with vascular connection tend to be characterised by irregular geometrical features that make them difficult to detect using local image metrics. Experimental results indicate that the proposed method can accurately detect nodules exhibiting a diverse range geometrical features.

Taken together, the proposed techniques improve robustness in three important areas; namely, robustness with respect to image features, robustness with respect to topology preservation and finally, robustness with respect to diverse geometrical features of the target object.

# Contents

<b>1</b>	<b>Introduction</b>	<b>1</b>
1.1	Summary of Contributions . . . . .	7
<b>2</b>	<b>Mathematical Image Segmentation</b>	<b>10</b>
2.1	Introduction . . . . .	10
2.2	Variational Image Segmentation . . . . .	11
2.2.1	K-means . . . . .	12
2.2.2	Kass Snakes . . . . .	13
2.2.3	Geodesic Active Contours . . . . .	14
2.2.4	Active Contours without Edges . . . . .	14
2.3	Methods and Algorithms . . . . .	15
2.3.1	Level Set Segmentation . . . . .	15
2.3.2	Graph Cut Segmentation . . . . .	17
2.3.3	Convex Methods . . . . .	18
2.4	Conclusion . . . . .	19
<b>3</b>	<b>Boundary Reinforcement</b>	<b>21</b>
3.1	Introduction . . . . .	21
3.2	Boundary Reinforcement: using a Split Bregman Edge Detector and a Topology Preserving Level Set . . . . .	25
3.2.1	Methodology . . . . .	25

3.2.2	Experimental Results . . . . .	29
3.3	Boundary Reinforcement: using Continuous Maximum Flow and a Geodesic Active Contour method . . . . .	34
3.3.1	Methodology . . . . .	34
3.3.2	Experiments & Results . . . . .	37
3.3.3	Discussion . . . . .	48
3.3.4	Conclusion . . . . .	52
3.4	Summary & Conclusion . . . . .	53
<b>4</b>	<b>Topology Preserving Active Contours</b>	<b>54</b>
4.1	Introduction . . . . .	54
4.2	Topology Preserving Active Contours . . . . .	57
4.2.1	Topology Preserving Term . . . . .	57
4.2.2	Topology Preserving Active Contours model . . . . .	58
4.3	Numerical Method . . . . .	63
4.4	Experiments & Results . . . . .	65
4.4.1	Two dimensional examples . . . . .	65
4.4.2	Three dimensional examples . . . . .	72
4.4.3	Extensions . . . . .	72
4.5	Comparison with other models . . . . .	74
4.5.1	The CV model . . . . .	74
4.5.2	Topology Preserving Model . . . . .	75
4.5.3	Comparison with Global CV method . . . . .	77
4.6	Conclusion . . . . .	80
<b>5</b>	<b>Lung nodule candidate detection</b>	<b>81</b>
5.1	Introduction . . . . .	81
5.2	Methodology . . . . .	85
5.2.1	Computation of a Global 2-phase Segmentation output . . . . .	85
5.2.2	Chest wall removal . . . . .	86
5.2.3	Nodule Separation . . . . .	86

5.2.4	Rule Based Classifier . . . . .	87
5.2.5	Summary of the Complete Algorithm . . . . .	88
5.3	Experiments . . . . .	89
5.4	Conclusion . . . . .	97
<b>6</b>	<b>Summary &amp; Conclusion</b>	<b>98</b>
6.1	Thesis Summary . . . . .	98
6.2	Summary of Contributions . . . . .	100
6.3	Conclusion . . . . .	101
6.4	Future Work . . . . .	103
<b>A</b>	<b>Appendices</b>	<b>106</b>
<b>B</b>	<b>Manuscripts currently under review</b>	<b>137</b>
<b>C</b>	<b>Theorem 4.2.3 Expanded</b>	<b>153</b>
<b>D</b>	<b>Software Implementation</b>	<b>158</b>

# List of Figures

1.1	A simple binary image consisting of geometric shapes showing (a) the original image (b) an edge representation of the shapes . . . . .	3
1.2	Segmentation result of model that uses only edge information . . . . .	4
1.3	This figure shows the same as above but with noise added (a) noise added (gaussian noise with variance of 15%) (b) corresponding edge representation . . . . .	4
1.4	This image shows the segmentation result of a model that relies solely on edge information . . . . .	4
1.5	Segmentation result of model that uses regional homogeneity information . . . . .	5
1.6	Photo by R.C. James . . . . .	5
2.1	Level set function represented by a cone and the location where the plane intersects the curve (shown in black) gives the location of the curve points. . . . .	16
2.2	The level set function on the left, with the curve on the right. The image shows the level set function at two instances in time as a split occurs. Image source:[1]; included here with permission. . . . .	16

- 3.1 Two examples of echocardiograms. Part (a) shows a four chamber view where LV refers to left ventricle, RV right ventricle, RA and LA, refer to right and left atrium respectively. Part (b) shows a two chamber view. The upper chamber is the left ventricle. Both the endocardial boundary and the location of the mitral valves are shown. 24
- 3.2 The figure shows the outward normal vectors corresponding to two neighbouring points,  $x$  and  $y$ . . . . . 27
- 3.3 (a) shows a view of the left ventricle of the heart generated by an ultrasound scanner (b) is the output of the GSB method, (c) is the edge set extracted from the binary output of the GSB method. This edge-set is supplied to the topology preserving step. . . . . 30
- 3.4 (a) the left ventricle view of the heart (b) shows the result of manually delineating the interior boundary of the chamber (c) is the segmentation result of the GSB+TPLS method, (d) is the GAC result and (e) shows both results superimposed, while (f) shows the CV result. 32
- 3.5 Example output of CMF method for 2 datasets; (a) and (d) are the original frames; (b), (e) and (g) show the corresponding output of CMF method, using values of  $\nu = 0.5$ ,  $\nu = 1e - 02$  and  $\nu = 0.5$  respectively; (c), (f) and (h) effect of edge map generated from binary segmentation. Figures (e) and (g) show the effect of varying  $\nu$ . Part (g) shows a cleaner result however (e) more accurately represents the underlying (closed) structure. . . . . 38
- 3.6 Results achieved by each method on four sample frames (Rows R1–R4). Each frame shows an example of boundaries characterised by weak edges. Note that the columns (C3–C6) represent outputs from each of the different algorithms . . . . . 40
- 3.7 Results showing the similarity between the results of each algorithm and the expert manual delineations. Note that the columns (C3–C6) represent outputs from each of the different algorithms superimposed with the manual delineations. . . . . 41

3.8	Step-by-step results of the proposed method for each of the frames (C1) which appearing in Figures 3.6 and 3.7. C1: Original frame, C2: The output of the CMF method, C3: The corresponding edge detector output. C4: Final result of proposed Method. C5: Final result superimposed on expert manual delineation. . . . .	44
3.9	Sombrero galaxy image [2]. The blue glow corresponds to the combined light of billions of old stars and the orange ring marks the sites of young stars. Courtesy NASA/JPL-Caltech . . . . .	45
3.10	An image of a flock of birds where it can be observed that the boundary of the flock is fragmented. The test results achieved by the GAC, CV and CMF + GAC are presented in figures (c), (d) and (e). Photograph by Lucas Felzmann. Used with permission. . . . .	46
4.1	The proposed algorithm applied to the two discs example with 70% noise. The model parameters are set to $\gamma = 0.195$ and $\mu = 0.4$ . . . .	66
4.2	Proposed algorithm applied to the Hand image with 15% noise. The model parameters are set to $\gamma = 2.2$ and $\mu = 0.5$ . Image source: obtained from authors of [3] . . . . .	67
4.3	Proposed algorithm applied to the highly textured Bear photograph. The model parameters are set to $\gamma = 3$ and $\mu = 0.8$ . Image source: Berkeley Image Database . . . . .	68
4.4	Proposed algorithm applied to an MRI scan of a brain. The model parameters are set to $\gamma = 1.45$ and $\mu = 0.5$ . Image source: Laboratory of Neuro Imaging, University of Southern California . . . . .	69
4.5	Proposed algorithm applied to an MRI scan of a brain. The model parameters are set to $\gamma = 2$ and $\mu = 1.2$ . . . . .	70
4.6	Proposed algorithm applied to an MRI scan of a brain. The model parameters are set to $\gamma = 2$ and $\mu = 2$ . . . . .	71
4.7	Proposed algorithm applied to a 3-D MRI scan of a brain. The model parameters are set to $\gamma = 1e - 06$ and $\mu = 0.2$ . . . . .	72

- 4.8 Proposed algorithm applied to an image of a squirrel. The model parameters are set to  $\gamma = 2.8e - 05$  and  $\mu = 0.3$ . Image source: Image was obtained from internet. . . . . 73
- 4.9 Comparison between proposed model and CV model [4]. Parameters for CV model:  $\gamma = 2.2$ , iterations = 1500. Parameters for Proposed model:  $\gamma = 2.2$  and  $\mu = 0.5$ . . . . . 74
- 4.10 Comparison between proposed model and CV model [4]  $\gamma = 2.2$ , iterations = 1500. Parameters for Proposed model:  $\gamma = 1.45$  and  $\mu = 0.5$  . . . . . 75
- 4.11 Comparison between proposed model and CV model [4]  $\gamma = 20$ , iterations = 300. Parameters for Proposed model:  $\gamma = 10$ ,  $\mu = -1$ , iterations = 700. Image source: Lung Image Consortium (LIDC) Database [5, 6] . 76
- 4.12 Comparison between proposed model and Le Guyader/Vese model [7]. Parameters for Le Guyader/Vese model:  $\mu = 0.64$ , iterations = 1500. Parameters for Proposed model:  $\gamma = 1.45$  and  $\mu = 0.5$  . . . . . 76
- 4.13 Comparison between proposed model and Le Guyader/Vese model [7]. Parameters for Le Guyader/Vese model:  $\mu = -0.5$ , iterations = 1000. Parameters for Proposed model:  $\gamma = 2.2$  and  $\mu = 0.5$  . . . . . 77
- 4.14 Comparison between proposed model and Le Guyader/Vese model [7]. Parameters for Le Guyader/Vese model:  $\mu = -0.5$ , iterations = 1000. Parameters for Proposed model:  $\gamma = 10$ ,  $\mu = -1$ , iterations = 700 . . 77
- 4.15 Comparison between proposed model and Global CV method [8, 9]. Parameters for Global CV method:  $\gamma = 0.18$ , *iter*300 . Parameters for Proposed model:  $\gamma = 2.2$  and  $\mu = 0.5$  . . . . . 78
- 4.16 Comparison between proposed model and Global CV method [8, 9]. Parameters for Global CV method:  $\gamma = 0.25$ , iterations1000 . Parameters for Proposed model:  $\gamma = 2.2$  and  $\mu = 0.5$  . . . . . 78
- 4.17 Comparison between proposed model and Global CV method [8, 9]. Parameters for Global CV method:  $\gamma = 0.1$ , iterations = 300 . Parameters for Proposed model:  $\gamma = 10$ ,  $\mu = -1$ , iterations = 700 . . . 79

- 5.1 Examples of nodules included in the test set. The majority of the nodules in the test set exhibit some degree of attachment to surrounding vascular tissue; isolated nodules were also included (as can be observed in the rightmost column). The arrowheads point to the location of the nodule in each case. . . . . 89
- 5.2 Example of normal operation of rule-based classifier: (a) Annotated Data indicating nodule (b) Initial Segmentation Results + Chest wall removal (c) Corresponding Detection Results (d) Corresponding Detection Results with annotation . . . . . 91
- 5.3 Results achieved by the method on 6 sample frames (Rows R1 R6). Each row shows an example of a nodule with vascular attachment. C1: The original data with expert annotation. C2: 2 phase global segmentation result C3: Results of the rule-based detection method C4: Detection results post MBO processing C5: Detection results with superimposed expert annotation. . . . . 92
- 5.4 Example of a nodule processed using only the rule-based classifier (i.e. using only steps 1-3 of the algorithm)(a) Original annotated dataset (b) slice 71 of dataset: nodule looks well delineated from surrounding structures but is actually part of a large connected component (c) the connected component which contains the nodule (d) an adjacent slice (e) Step 4: Detection with MBO (f) Annotation overlayed on result. 93
- 5.5 Second example of a nodule processed using only the rule-based classifier (a) Original annotated dataset (b) nodule looks well isolated from surrounding structures but is actually part of a large connected component (c) connected component which includes the nodule (d) an adjacent slice (e) Step 4: Detection with MBO (f) Annotation overlayed on result. . . . . 94
- 5.6 Example of a case where MBO-detection scheme fails (a) Original Annotated dataset (b) 2-phase segmentation (c) Connected component (d) Detection with MBO - failure. . . . . 95

# Acknowledgements

I would like to acknowledge my supervisors Martin Glavin and Edward Jones. Thank you for your support and for giving me the opportunity and freedom to work on interesting projects and for your helpful guidance, I am extremely grateful.

I am indebted to Luminita Vese for her support and for giving me an opportunity to work as part of her group in UCLA. Thank you for all of your guidance. It is impossible to overestimate the value of the support you provided.

I am very grateful to my collaborators, especially Egil Bae and Hayden Schaeffer. Working with you was an extremely fruitful experience and one that I will continue to value.

Many thanks go to all of the people both in Galway and Los Angeles who supported me with their friendship during this chapter of my life. It's not possible to mention you each by name but be assured, I am extremely grateful for your support.

I would like to thank my family, most importantly, my parents - the best in the world - Patrick and Eibhlís. Thank you for your unconditional love and support.

I would like to acknowledge that this work was supported in part by Irish Research Council, the UC Lab Fees Research Grant 12-LR-236660 and NSF DMS Award 1217239.

# 1

## Introduction

The ability to see and extract information from visual scenes is one of the most important human capabilities. Replicating this task with computers is known as computer vision and is an extensively studied problem. Face recognition is perhaps one of the most ubiquitous uses of computer vision, however the true range of applications is vast. Automated visual inspection systems for assembly line manufacturing are prevalent in virtually all industries while other applications include automotive driver assistance systems, real-time traffic management as well as intelligent video surveillance systems. Emerging technologies include image overlay projection in medical surgery where a 3-D visualisation of the underlying anatomical structures is superimposed onto a patient's body, providing improved visualisation for surgeons.

Within an image or a natural scene, the task of separating objects from the

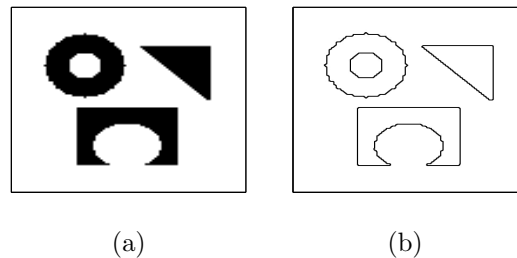
background is called segmentation; it is this topic which is the primary focus of this thesis. An alternative description of segmentation is the abstraction of a visual scene into a collection of regions corresponding to distinct objects. Given that what constitutes an ‘object’ is subjective and application dependent, segmentation as an image processing task, is not well defined.

Segmentation is generally the first and one of the most important tasks in computational image analysis. Very often the success or failure of the image analysis tool is directly related to the success or failure of the segmentation method. To understand its significance within computer vision, consider for example accurate 3-D reconstruction from 2-D photographs, which relies on accurately isolating the structure from the surrounding image environment, which is precisely the task of segmentation. The use of augmented reality is becoming more prevalent in applications related to navigation, gaming, industrial design. The success of these applications depends on accurate/convincing interaction between overlaid objects (imagine characters in a video game) with the objects that are actually present in the scene, this again relies on accurate segmentation of the objects.

Computer vision algorithms for segmentation typically proceed by seeking a partition of an image into homogeneous regions, bounded by smooth, continuous edges [10]. However these assumptions are often not sufficient for ensuring accurate segmentation. The challenge is related to the variability in object representation as well as the effects of image degradation. Consider for example the effects of object orientation, shape variability, occlusions, the presence of extraneous detail, degradations due to poor illumination, noise and sampling artefacts; a human being has little trouble in identifying objects under a variety of imaging conditions, however the effectiveness of a computer algorithm incorporating only basic assumptions about continuous edges or homogeneous regions of the object, is often very limited under challenging imaging conditions. In some applications, the challenge of the task can be reduced by using simplifying assumptions based on prior knowledge of the image domain. If global features of the object of interest are known they can be incorporated into the segmentation model. One application for which prior knowledge is

typically known, and also the application for which the algorithms proposed in this thesis are demonstrated on, is medical imaging. For this application, the modality of the image acquisition tool, the area of the body being imaged, expected pathologies *etc.* are usually all known in advance. From this information, prior knowledge can be derived about the approximate geometry of the object of interest, its orientation, topology, dynamical characteristics *etc.* This information can then be incorporated into the segmentation model to create more robust system [11]. The algorithms proposed in this thesis exploit this kind of information in their design.

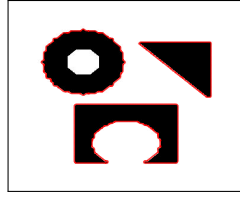
Many existing segmentation methods exploit either the discontinuities in the image ('jumps' in brightness) or homogeneity i.e. coherency with respect to some property. Methods that depend on discontinuities are often called edge-based methods, while methods that consider homogeneity are referred to as region-based methods. To illustrate the idea of these methods, consider Figure 1.1. Figure 1.1(a) shows an



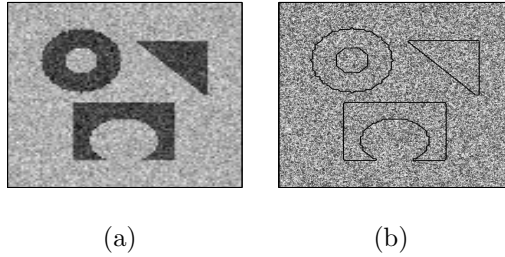
**Figure 1.1:** A simple binary image consisting of geometric shapes showing (a) the original image (b) an edge representation of the shapes

image consisting of geometric shapes, Figure 1.1(b) provides another representation of the shapes, this time where the objects are represented only by their respective edges.

Figure 1.2 shows the result of a segmentation model that uses just edge/discontinuity information, where the edges are identified by the red curves. It can be observed that the segmentation result is quite accurate (missing only the inner circle of the ring-shaped object). If some noise is introduced into Figure 1.1(a) then the segmentation task becomes more complicated. This is demonstrated in Figure 1.3. Figure 1.3(a)



**Figure 1.2:** Segmentation result of model that uses only edge information



**Figure 1.3:** This figure shows the same as above but with noise added (a) noise added (gaussian noise with variance of 15%) (b) corresponding edge representation

shows the same image as Figure 1.1(a), but this time with noise added (gaussian noise with variance of 15%). Figure 1.3(b) shows the edge representation of Figure 1.3(a). Figure 1.3(b) highlights the difference between boundaries and edges. In simple noise free binary images both concepts mean the same thing, however in more complex images such as Figure 1.3(a), each transition in brightness represents an edge, as demonstrated in Figure 1.3(b). Therefore a segmentation model that makes use of edge information alone will produce inaccurate results as can be observed in Figure 1.4. Region based models address this issue by incorporating assumptions

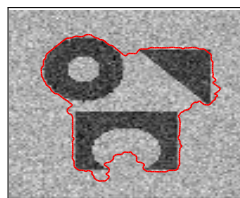


**Figure 1.4:** This image shows the segmentation result of a model that relies solely on edge information

about about regional homogeneity. In Figure 1.3(a) it can be observed that the

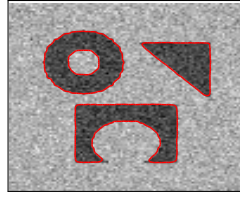


**Figure 1.5:** Segmentation result of model that uses regional homogeneity information

mean intensity/brightness of both the foreground shapes and the background does not vary significantly. Using this observation, a region based segmentation model can produce a segmentation result as shown in Figure 1.5:

The past 3 decades have witnessed extraordinary advances with respect to the capabilities of automated segmentation. Figures 1.1(a) and 1.5 represent trivial tasks for modern segmentation models. Despite these advances however, segmentation is still considered an open problem. Numerous studies have shown that for humans, the task of segmentation is closely coupled with concept of object recognition *i.e.* human beings see not simply just what an image contains, but a combination of the input to the retina and what prior knowledge indicates should be there [12, 13, 14, 15, 16, 17]. As an illustration of this idea, consider the following image:



**Figure 1.6:** Photo by R.C. James

Extracting the relevant information from the image is not straightforward even for human beings. However, once it is known that the figure contains an image of a dalmatian, accurately segmenting the image becomes much easier. The combination of prior knowledge as well as the features of the image make the segmentation task less complex. Replicating the task with a computer, however, is not yet possible using currently available techniques. It can be observed in Figure 1.6 that salient

features such as regional homogeneity or discontinuity in brightness do not help in defining the object.

Existing approaches for image segmentation include mathematical morphology, wavelet theory [18, 19, 20], Fourier analysis [21, 22], stochastic approaches [23, 24] and energy minimisation methods/optimisation theory [25, 26, 4, 27, 28]. In this thesis, the paradigm used for image segmentation is energy minimisation. Image segmentation in an energy minimisation framework involves designing a cost functional that encodes the characteristics of the desired segmentation result. The optimal solution of this cost functional is taken as the segmentation result. In the case of more low-level approaches such as morphological or filter based techniques, quantitatively comparing the quality of segmentation results achieved with different parameter configurations is not straightforward. In the case of variational approaches, the quality of the segmentation is encoded in the ‘cost’ of a particular configuration. In this way, different results can be easily compared by measuring the respective cost of each solution, which simplifies comparison between different solutions [29].

Another advantage of variational techniques, is that they offer the possibility of combining both local and global image features. In the case of a filtering operation, the output gives an estimation of prominent features present. In many cases this output needs further processing so that the objects existing in the image may be revealed. In a variational framework, the easy integration of global information means that the underlying coherent structures may be more easily identified in a single step [30]. These two advantages in particular, give variational methods an enhanced generality compared to low-level functions. This thesis deals with the general problem of **how to increase segmentation robustness using purely data driven approaches**. A summary of contributions is provided in the following section.

## 1.1 Summary of Contributions

### Boundary Refinement for Low Contrast Images

The **first contribution** of this thesis is a new technique for boundary detection in images with low-contrast boundaries. The technique consists of solving the well-known Mumford-Shah (MS) functional using a highly efficient convex segmentation scheme, the output of which is a simplified binary representation of the original image. Using this binary representation, an edge detector is generated which is then used as input to a Geodesic Active Contour (GAC) scheme to produce the final curve representing the boundary of the structure. The technique exploits the natural properties of the Mumford-Shah functional to effectively reinforce weak boundaries of low contrast images. The method was validated using a combination of medical and non-medical data. In the case of medical data, the method was compared to segmentation results from classical data driven approaches and validated against manual delineations performed by two trained experts. Results indicate that the proposed scheme gave enhanced performance boundary detection compared to existing methods.

### Topology Preserving Active Contours

The **second contribution** of this thesis is a topology preserving segmentation model consisting of a non-local topology preserving constraint that forces the curve to avoid breaking or self-intersection via a variational self-repelling term, and a data fidelity constraint to increase robustness in the presence of noise. In many segmentation tasks, especially in medical imaging, the target shape has a known topology; when this is the case it would be advantageous to initialise the segmentation contour with the same topology as the desired object and have this topology preserved throughout the course of the contour evolution. The objective of this research was to produce a robust topology-preserving scheme for these applications. The proposed method was tested on standard synthetic examples, real photographic data,

and real medical images. The algorithm was tested on images with varying degrees of noise as well as edge structure types.

## Lung nodule candidate detection in Computed Tomography

The **third contribution** consists of a novel approach for lung nodule candidate detection in Computed Tomography (CT). The proposed algorithm is based on the application of global segmentation methods combined with mean curvature minimisation and simple rule-based filtering. Nodules with vascular connection tend to be characterised by irregular geometrical features that make them hard to detect using local image metrics. Experimental results indicate that the proposed method can accurately detect nodules exhibiting a diverse range of geometrical features.

## List of Publications

### Publications resulting from work done in this thesis

- A **Nóirín Duggan**, Hayden Schaeffer, Carole Le Guyader, Edward Jones, Martin Glavin, Luminita Vese, Boundary Detection in Echocardiography Using a Split Bregman Edge, IEEE International Symposium on Biomedical Imaging: From Macro to Nano 2013. San Francisco. DOI:10.1109/ISBI.2013.6556415
- B **Nóirín Duggan**, Egil Bae, Edward Jones, Martin Glavin, Luminita Vese, A Simple Boundary Reinforcement Technique for Segmentation without Prior, Pattern Recognition Letters, Volume 46, 1 September 2014, pp 27-35. DOI: 10.1016/j.patrec.2014.04.014.
- C Hayden Schaeffer, **Nóirín Duggan**, Carole Le Guyader, Luminita Vese, Topology Preserving Active Contours, Communications in Mathematical Sciences. Volume 12, Issue 7. Pages: 1329–1342. DOI: 10.4310/CMS.2014.v12.n7.a8.

The full text of these publications is included in appendix A.

The remainder of the thesis is laid out as follows: Chapter 2 presents a review of the most influential models and algorithms which have been proposed on the subject of mathematical image segmentation. Chapter 3 describes the proposed boundary refinement contribution in detail. The proposed topology preserving model is described in chapter 4, while chapter 5 presents the proposed nodule detection scheme. Chapter 6 provides a summary of the contributions of this thesis and suggests some directions for future work.

# 2

## Mathematical Image Segmentation

### 2.1 Introduction

In the previous section, the basic objective of segmentation was described conceptually as well as the primary concepts of discontinuity and regional homogeneity. In this chapter an overview is presented of the major contributions to the field of mathematical segmentation. The chapter is divided into three sections: first an overview of segmentation in an optimisation framework is presented, followed by a review of the most important segmentation models proposed in the literature. The chapter concludes with an overview of some of the algorithms that are used to solve these models.

## 2.2 Variational Image Segmentation

In image analysis and computer vision, the segmentation problem, as formulated by Mumford and Shah [31], consists in computing a decomposition:

$$\Omega = \Omega_1 \cup \Omega_2 \cup \dots \cup \Omega_n \cup K \quad (2.1)$$

of the domain of the image  $I$  such that (a) The image  $I$  varies smoothly and/or slowly within each  $\Omega_i$  and (b) The image  $I$  varies discontinuously and/or rapidly across most of the boundary  $K$  between different  $\Omega_i$ . In the above formulation,  $\Omega \subset \mathbb{R}^N$  and  $I : \Omega \rightarrow \mathbb{R}$ , where (as in standard notation)  $\mathbb{R}^N$  denotes an  $n$ -dimensional vector space over the field of the real numbers, denoted  $\mathbb{R}$ .

Variational modelling describes a mathematical framework for modelling dynamical systems that are characterised by dissipation, and specifically to systems with the mathematical structure of gradient flows [32]. The idea is based on the Principle of Least Action *i.e.* the assumption that the movement of an entity in nature is governed by the principle of energy conservation. An example of this is Fermat's Principle, which states that "light travels between two given points along the path of shortest time". Using this assumption of energy conservation, models that describe the motion of objects can be designed. Applying variational modelling to problems outside of classical mechanics, such as image segmentation, requires designing an objective function such that the minimiser, or the solution which requires the 'least energy', is the optimum solution.

To illustrate the idea, we consider an objective function formulated as:

$$\min_u J(u) \quad (2.2)$$

where  $J$  represents the energy to be minimised, which depends on some quantity  $u$ . If  $u$  is a function, then  $J$  is a functional (it maps a set of functions to a real number  $\mathbb{R}$ ). If  $\frac{\partial J}{\partial u}$  represents the first variation of  $J$ , then the necessary condition for a given function,  $u^*$ , to be an optimiser of  $J$  is if:

$$\left. \frac{\partial J}{\partial u} \right|_{u^*} = 0 \quad (2.3)$$

Equation 2.3 is called the Euler-Lagrange equation. An optimiser of  $J$  can be computed by using gradient descent/ascent which involves introducing an artificial time parameter,  $t$ , such that:

$$\frac{\partial u}{\partial t} = \pm \frac{\partial J}{\partial u} \quad (2.4)$$

The steady state solution of the above will be an optimiser of  $J$ . In [33, 1] the previous ideas are illustrated with the example of image denoising; by finding the Euler Lagrange equation of the following variational model:

$$F(I) = \int |\nabla I|^2 dx \quad (2.5)$$

known as the Dirichlet integral, we arrive at the famous linear heat flow equation:

$$\frac{\partial I}{\partial t} = \Delta I \quad (2.6)$$

which in image processing, is used as a smoothing filter.

The above energy minimisation paradigm will be applied throughout this thesis for solving the segmentation problem. The subsequent sections of this chapter will look in more detail at different energy formulations from the literature which have proven to be very influential.

### 2.2.1 K-means

K-means [34, 35] is an iterative algorithm for clustering a set of objects into  $K$  groups. The assignment of an object to a particular group is achieved using a cost function, where the ‘cost’ of an assignment is measured as the distance between that object and the current group mean. When all objects are clustered, the means are recalculated and the process is repeated until convergence.

More formally, given a set of observations  $[s_1, s_2, \dots, s_n]$ , the goal of K-means clustering is to partition the points into clusters  $\{C_1, C_2, \dots, C_k\}$ , where  $k \leq n$ , such that the intra-cluster mean is a minimum. With respect to image segmentation, the observations  $[s_1, s_2, \dots, s_n]$  could represent, for example, intensities of each pixel

in the image. The clusters  $\{C_1, C_2, \dots, C_k\}$  would then correspond to regions with a common mean intensity.

Originally developed as a method for pulse-code modulation in the field of signal processing, the method has also been a fundamental building block in the field of image segmentation because it represents one of the simplest examples of encoding a partitioning task as a cost minimisation problem. The idea that assignments should be made in order to maximise the intra-group similarity, is an essential idea among all region-based image segmentation models that later followed, including [4] which will be discussed in section 2.2.4.

### 2.2.2 Kass Snakes

One of the first proposals to cast image segmentation as an energy minimisation problem was the approach of Kass *et al.*[25] in which the segmentation of a given image is computed by evolving curves in the direction of the negative energy gradient using appropriate partial differential equations. Due to the way the curve moves, the model has become known as the Snakes model. In this approach, boundaries are detected using the strength of the gradient at each pixel. The curve in [25] is represented by a parametric contour  $C(s) : [0, 1] \rightarrow \Omega$  which is evolved by minimising the functional:

$$J_1(C) = - \int |\nabla I(C)|^2 ds + \nu_1 \int |C_s|^2 ds + \nu_2 \int |C_{ss}|^2 ds \quad (2.7)$$

where the first term attracts the curve toward the object in the image and the second and third terms control the smoothness of the contour and  $\nu_1$  and  $\nu_2$  are nonnegative weighting parameters. By minimising the energy (2.7), the objective is to locate the curve at the points of maximal  $|\nabla I(C)|$ , which acts as an edge-detector, while maintaining smoothness in the curve. The model is initialised by placing a curve near to the target object.

### 2.2.3 Geodesic Active Contours

An assumption in [25] is that objects can be recovered using simple (*i.e.* non self-intersecting) curves, while the curve itself, is represented parametrically using splines. To avoid self-intersection and overlap of contour points, reparameterisation is required (*i.e.* a new curve is generated that is geometrically identical to the previous one but with a new parameterisation).

Similarly, sophisticated reparameterisation schemes are needed to handle topological changes, which are necessary for segmenting multiple objects or objects with an unknown topology.

To overcome the need for reparameterisation, techniques based on curve evolution theory [36, 26] allow for motion based on geometric measures such as unit normal and curvature. To obtain a new length constraint independent of parameterisation, Caselles *et al.* [26] and Kichenassamy *et al.* [37] simultaneously proposed the implicit Geodesic Active Contour (GAC), the energy functional of which is given by:

$$E(C) = \int_0^1 g(|\nabla I(C(q))|) |C'(q)| dq \quad (2.8)$$

$$\text{where } g = \frac{1}{1 + \beta |\nabla I|^p} \text{ with } p = 1 \text{ or } 2 \quad (2.9)$$

In the above equation  $q \in [0, 1]$  and  $g(|\nabla I(C(q))|) |C'(q)| dq$  is a new length obtained by scaling the Euclidean element of length  $ds$  by the function  $g$  which contains information about the gradient of the image  $I$  [26]. In the above equation  $\beta$  controls the sharpness of the detected edges. The curve is attracted to pixels for which  $g(|\nabla I(C(q))|)$  (and hence the associated energy potential) is close to zero.

### 2.2.4 Active Contours without Edges

The assumption in both the Snakes and GAC models, is that objects are distinguished by sharp gradients at their boundaries. Another energy minimisation approach is the Mumford-Shah (MS) model [31], which in its most general form seeks both an edge set and an approximation of the image that is smooth everywhere

except across the edge set (as explained in section 2.2). There has been a considerable amount of research done on computing minimisers by numerical algorithms. In many cases, the image is well-approximated by a piecewise constant function.

In [4, 38] the authors presented a level-set formulation of the piecewise constant variant of the MS model. Considering an image with two regions, the object to be segmented is denoted  $S$  and the background denoted  $\Omega \setminus S$ , the authors proposed the following model:

$$\min_{S, c_1, c_2} \int_{\Omega \setminus S} |I(x) - c_1|^2 dx + \int_S |I(x) - c_2|^2 dx + \nu |\partial S| \quad (2.10)$$

The last term of the energy functional is the length of the boundary of  $S$  weighted by the parameter  $\nu$ , while the first terms represent the data-fidelity constraint, where  $c_1$  and  $c_2$  are two scalars that attempt to approximate the image in the interior and exterior region. In order to find a minimiser by a numerical algorithm, it was proposed in [4, 38] to represent the partition with a level set function, resulting in the following problem:

$$\min_{\phi, c_1, c_2} \left( \int_{\Omega} |I(x, y) - c_1|^2 H(\phi) dx + \int_{\Omega} |I(x, y) - c_2|^2 (1 - H(\phi)) dx + \nu \int_{\Omega} |\nabla H(\phi)| dx \right) \quad (2.11)$$

where  $H$  is the Heaviside function, defined such that  $H(z) = 1$  if  $z \geq 1$  and  $H(z) = 0$  if  $z < 0$  and is used to select either the interior or exterior of the curve. This work is known as Active Contours Without Edges (ACWE) or Chan-Vese (CV) method.

The MS and CV model has many extensions, for example to 4 or more regions [39], to multilayer images in [40], texture [41] and to curves with free endpoints [42, 43].

## 2.3 Methods and Algorithms

In this section, an overview is presented of the existing optimisation schemes for solving the variational models introduced in section 2.2.

### 2.3.1 Level Set Segmentation

The level set method is a general method to describe moving curves or shapes that may undergo topological change *e.g.* merging, pinching apart. The core idea of the method, is that the curve is embedded into a higher dimensional function, as exemplified in Figure 2.1, called the level set function. If  $\phi$  denotes the level set function then the zero-crossing of the function, i.e. the set of points where  $\phi = 0$ , then gives the location of the curve.

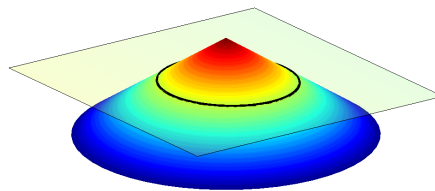


**Figure 2.1:** Level set function represented by a cone and the location where the plane intersects the curve (shown in black) gives the location of the curve points.

Figure 2.2 illustrates how topological changes are handled using the level set function.

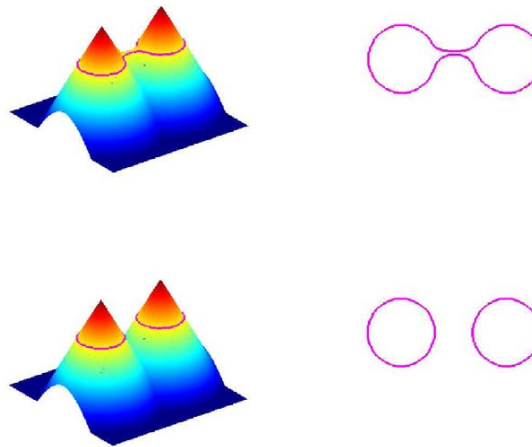


**Figure 2.2:** The level set function on the left, with the curve on the right. The image shows the level set function at two instances in time as a split occurs. Image source:[1]; included here with permission.

The level set equation is given by:

$$\phi_t + F_n |\nabla \phi| = 0 \quad (2.12)$$

where  $F_n$  is the normal velocity at the interface. The level set function has the following properties  $\phi(x) \leq 0$  in the interior of the curve and  $\phi(x) > 0$  in the exterior. The method evolves a curve by updating the level set function at fixed coordinates through time, rather than tracking a curve through time, as in a parametric setting.

The usual choice of  $\phi$  is the signed distance function defined as:

$$\begin{aligned} d(x) &= \min_{y \in C} |x - y| \text{ if } x \text{ is interior to } C \\ &\quad - \min_{y \in C} |x - y| \text{ if } x \text{ is exterior to } C \end{aligned} \quad (2.13)$$

Therefore for the level set function,  $\phi(x) = d(x)$ . Another point to note, is that if 2.12 is discretised, then from one timestep to the next, computation only needs to take place on a narrow band around  $\phi = 0$  (since computing  $\phi_t$  and  $\nabla \phi$  only requires knowing the values of  $\phi$  on a narrow band around  $\phi = 0$ ).

In an implicit formulation, both topological changes and also extension to higher dimensions are handled naturally.

The level set method is limited by two important factors: firstly, as with many other variational models in image processing, the solutions are not global, which means in practice the curve may get trapped in local minima unless the initialisation (*i.e.* the placement of the initial curve with respect to the object boundary) is very good. Secondly to preserve numerical stability, the time step is limited by the Courant Friedrichs Lewy (CFL) condition for explicitly solving convection partial differential equations which results in slow convergence.

### 2.3.2 Graph Cut Segmentation

The most important drawback of the level set method is that globally optimal solutions are not guaranteed. An alternative way to handle the image segmentation problem is via graph cuts, which are guaranteed to find global solutions. Graph

cuts was first used as a computer vision tool by Greig *et al.* [44] in connection with markov random fields [24]. In this framework, the image is interpreted as a grid-graph where pixels (or voxels) are represented by vertices and the similarity between two pixels, as the weight of the edges connecting these two vertices. The objective in this approach is to cut the graph with minimum cost, forming segmented regions of similar pixels.

Methods based on graph theory have been applied extensively in the image processing literature, applications include stereo and motion [45], [46], [27], [47], [48], [49], medical imaging [50], [51], [52], [53], image segmentation [54], multicamera scene reconstruction [55], and image restoration [46], [27], [44], [56].

Describing the framework more formally, we let  $G$  denote a graph, defined as  $G = (\mathcal{V}, \mathcal{E})$ . The graph has a set of vertices,  $\mathcal{V}$ , and a set of directed edges,  $\mathcal{E}$ , that connect them. Each edge is assigned some weight (or cost). The graph usually contains two special vertices called terminals, the source,  $s$ , and the sink,  $t$ . A cut on the graph corresponds to a partition of the vertices into two disjoint sets  $V_s$  and  $V_t$  such that  $s \in V_s$  and  $t \in V_t$ . The cost of the cut is the sum of costs of all edges that go from  $V_s$  to  $V_t$ :

$$C(V_s, V_t) = \sum_{u \in V_s, v \in V_t, (u,v) \in E} c(u, v). \quad (2.14)$$

The goal is to find a cut of minimum cost on  $G$ . It was proven by Ford and Fulkerson in [57] that the minimum cut problem is equivalent to finding the maximum flow from the source to sink where the edge weights represent the maximum capacity of flow that can be transmitted through the edges. The consequence of this equivalence is that cuts of minimum cost can be very efficiently computed by max-flow algorithms such as proposed in [57].

Compared to variational approaches, graph cut methods are guaranteed to find global solutions; however, they are unable to compute isotropic energy minimisers and incur a large memory overhead when segmenting fine features.

### 2.3.3 Convex Methods

Another approach to overcome the local-minima issue has been through the use of convex-relaxation techniques. Discrete optimisation methods such as graph cuts [27] tend to exhibit a grid bias in representing continuous perimeters [58], leading to visible artifacts in the segmentation results. It is possible to overcome this issue by considering more neighbouring nodes [54, 59] or high-order interaction potentials [60, 61], however doing so leads to higher computational costs. Unlike level sets, the solutions of convex relaxation methods are guaranteed to be globally optimal. One of the first works proposing convex relaxation methods for classical segmentation models was presented by Chan *et al.* [62] in which it was shown that (2.10) can be exactly minimised via the convex problem:

$$\min_{\phi(x) \in [0,1]} \int_{\Omega} |I(x) - c_1|^2 \phi(x) + |I(x) - c_2|^2 (1 - \phi(x)) dx + \nu \int_{\Omega} |\nabla \phi(x)| dx. \quad (2.15)$$

It was shown that if  $\phi^*$  is a minimiser of (2.15) and  $t \in (0, 1]$  is any threshold level, the partition  $S = \{x \in \Omega : \phi(x) \geq t\}$ ,  $\Omega \setminus S = \{x \in \Omega : \phi(x) < t\}$  is a global minimiser to the model (2.10). The binary function:

$$\phi^t(x) := \begin{cases} 1, & \phi(x) \geq t \\ 0, & \phi(x) < t \end{cases}, \quad (2.16)$$

is the characteristic function of the region  $S$ .

Very fast solvers have been proposed to solve (2.15). These methods are based on finding a spatially continuous version of the Min Cut / Max Flow equivalence. In chapters 3 and 5 these fast solvers are used to solve the MS segmentation model.

## 2.4 Conclusion

In this chapter some of the major contributions to mathematical segmentation were described. Section 2.2 dealt with the various models that have been proposed which differ with respect to the image property that is used to define distinct regions, either

the image gradient or regional homogeneity. Section 2.3 dealt with the methods that have been proposed to solve these models. These methods differ according to the types of solutions that they provide *i.e.* local or global, and also according to whether the framework in which the problem is solved is discrete (in the case of graph cuts) or continuous, in the case of the level set method and convex relaxation techniques. The following chapters describe the contributions of this thesis which are based on the core models and algorithms described in the previous sections. In particular, chapter 3 proposes an algorithm for the segmentation of objects with low-contrast boundaries, in chapter 4 a model incorporating topology preserving constraints as well as regional constraints is proposed for the segmentation of objects with a known topology. Finally in chapter 5, a method is proposed for lung nodule detection. The algorithm is based on a 3-D global segmentation model combined with mean curvature smoothing to detect nodules which have a complex geometry.

# 3

## Boundary Reinforcement

### 3.1 Introduction

Robust segmentation depends, among other things, upon the accuracy with which object boundaries can be localised. Many real world phenomena are characterised by visually faint boundaries, *e.g.* clouds, smoke, satellite images of distant galaxies, shoals of fish or a flock of birds swarming. To tackle such problems in the context of image segmentation, it is necessary to incorporate as many visual cues as possible. In the context of image segmentation this amounts to making use of both local and global information. An example of local information is the intensity at a particular pixel relative to adjacent pixels (the intensity gradient). Global information on the other hand, refers to the characteristics of prominent regions or neighbourhoods of pixels within an image. Segmentation models based on global information are often

referred to as region based models. As discussed in chapters 1 and 2, the assumption of region based models is that a solution is defined by regions that are uniform/homogeneous according to some characteristic, for example intensity [4]. Intensity gradient based methods on the other hand (*e.g.* [26]), assume that the boundary of an object is defined by a sharp intensity gradient. In real-world examples, however; these assumptions do not always hold. To tackle the segmentation problem presented by any of the examples above, some way of ‘reinforcing’ the boundaries of these phenomena is required. In this context, this chapter proposes two segmentation algorithms that integrate local and global information to accomplish the task of boundary reinforcement.

A number of schemes for combining edge and region information have been suggested in the literature. In [63], an energy minimisation approach for tracking objects was proposed, where region and edge information were integrated in separate terms of an energy functional. The boundary term moves the curve towards edges and maintains regularity. The region term moves the curve inward or outward depending on whether it is located outside or inside the object (respectively), and the model also includes a motion-based term that evolves the curve based on flow between frames. In order to solve the resulting minimisation problem, the level set method was applied. In this method the quality of segmentation often depends on the quality of the detected edges. Bresson *et al.* [64] proposed a method combining the data fidelity term of the CV model and the edge attraction term of the Geodesic Active Contour (GAC) model in a global minimisation framework.

In [65], the authors represented the edges by a binary function, leading to a non-convex minimisation problem closely related to the phase field representation. A convex relaxation of the piecewise smooth MS model was proposed in [66], by lifting the problem to a higher dimensional space. Although computationally intensive, this approach has the advantage of converging to a close approximation of a global minimum, without getting stuck in a local minimum. In [67] a generalisation of the MS model was proposed with an extra term that enforces closeness between the gradient of the reconstructed image and the original image. Compared to the piece-wise

MS model, the motivation behind this model is to provide a better reconstruction of edges with low contrast changes, specifically intensity discontinuities known as *roof edges*. A numerical algorithm based on the level set method was proposed in [67] to solve the resulting evolution equation. Closely related is the diffusion equation of Perona and Malik [68], which converges to a local minimiser of the MS model if an appropriate data fitting term is added.

In Rajpoot *et al.* [69] an intensity invariant, real-time method was proposed to extract boundary information by analysing the monogenic signal [70]. The proposed method uses a local phase based filter to extract edge information. The method produces a finer edge extraction than gradient detectors; however, due to its intensity invariance, tends to over-segment the image. Another approach for generating feature detectors proposed for application to echocardiography, is the 2D + T method of Mulet-Parada *et al.* [71]. They demonstrated in their experiments that a local phase-based approach produces more accurate edge results than conventional gradient magnitude methods.

In the following sections two segmentation approaches are investigated for the segmentation of images characterised by low intensity gradients. The general approach of both methods consists of computing a global minimiser to a classical segmentation model; then in order to obtain a single curve that estimates the boundary of the object, a level set curve evolution approach is used. In the first approach, the Geometric Split Bregman (GSB) method is used to approximate the edge map by solving an energy model proposed in [64] consisting of a hybridisation of the edge based model [26] with the CV model [4], while in the second approach an alternate formulation using the Continuous Maximum Flow (CMF) method [8, 9] is employed, this time solving just the CV model (2.10) [4]. To approximate the final boundary, the Topology Preserving Level Set (TPLS) method [7] is used in the first approach, while in the second approach, the GAC method [26] is used.

The integration of the regional information through the edge detector provides a different combination model than in previous methods. Similar to [65, 67], a variation of the MS model is applied to improve the edge detection step. While in

[65] the goal was to improve the ‘standard’ Canny edge model, what is proposed in this thesis is to delineate structures with low contrast boundaries by reinforcing the weak edges. The proposed methods were validated using ultrasound cardiac data. Ultrasound remains one of the most popular medical imaging modalities, however degradations due to speckle, signal drop out, intensity inhomogeneity as well as relatively low spatial resolution [72, 73, 74] make accurate visualisation of structures difficult.

Figure 3.1 shows two examples of echocardiograms. Of particular interest to clinicians is the left ventricle which is responsible for pushing oxygen rich blood to aorta, the main artery that carries blood to the rest of the body. The focus of the experiments in this section is to localise the boundaries of the left ventricle (as indicated in Figure 3.1(b)).

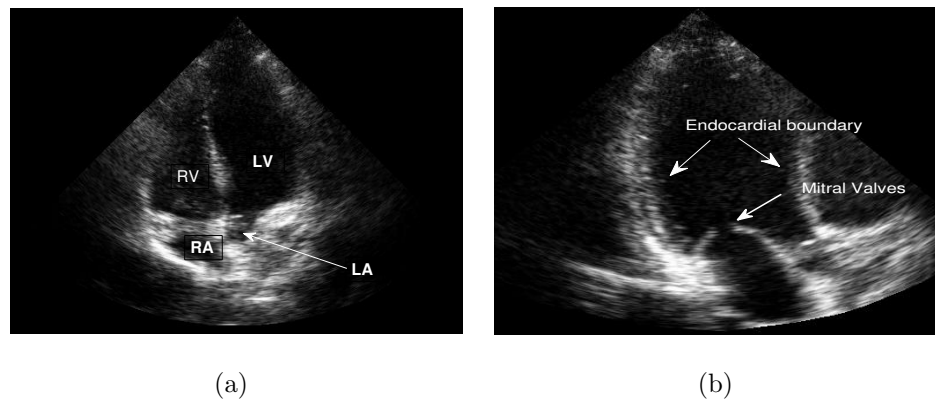


**Figure 3.1:** Two examples of echocardiograms. Part (a) shows a four chamber view where LV refers to left ventricle, RV right ventricle, RA and LA, refer to right and left atrium respectively. Part (b) shows a two chamber view. The upper chamber is the left ventricle. Both the endocardial boundary and the location of the mitral valves are shown.

## 3.2 Boundary Reinforcement: using a Split Bregman Edge Detector and a Topology Preserving Level Set

### 3.2.1 Methodology

The proposed algorithm consists of a number of steps; firstly to increase contrast between significant structures, the geometric segmentation method proposed in [64] was applied to the dataset. The method combines the GAC model [26] and the ACWE model [4] in a convex formulation (originally proposed in [62]). To solve the model the split Bregman method [75] was used. To obtain a single curve that estimates the boundary of the target object, the TPLS method [7] is applied to the dataset. Finally, a diffusion based post processing method is applied to smooth the final curve (removing any local variations due to the data).

#### 3.2.1.1 Geometric Split Bregman Method

The first step in the proposed method is to produce an edge-detector to estimate the major edge-set in the image, for this the GSB method is used. In [64] the authors solve the model:

$$\min_{0 \leq u \leq 1} |\nabla u|_g + \mu \langle u, r \rangle \quad (3.1)$$

where  $r = (c_1 - I)^2 - (c_2 - I)^2$

where  $u$  is an approximation of the true image,  $|\nabla u|_g = \int_{\Omega} g |\nabla u| \, dx \, dy$  is the weighted Total Variation,  $g$  is an edge-function (2.9), while  $\langle u, r \rangle$  is the data fidelity term, defined as:

$$\langle u, r \rangle = \int_{\Omega} ur \, dx \, dy \quad (3.2)$$

for which  $\mu$  acts as a scaling parameter. To apply the split Bregman approach [76] to (3.1) an auxiliary variable  $\vec{d} \leftarrow \nabla u$  is introduced. A quadratic penalty function is then added to weakly enforce the resulting equality constraint [77]. Bregman iteration is applied to strictly enforce the constraint  $\vec{d} = \nabla u$ . The resulting optimisation problem is:

$$(u^{k+1}, \vec{d}^{k+1}) = \arg \min_{0 \leq u \leq 1, \vec{d}} |d|_g + \mu \langle u, r \rangle + \frac{\lambda}{2} \|\vec{d} - \nabla u - \vec{b}^k\|^2 \quad (3.3)$$

$$\vec{b}^{k+1} = \vec{b}^k + \nabla u^k - \vec{d}^k. \quad (3.4)$$

The reader is referred to [76] for specific details of the solution.

The constants  $c_1$  and  $c_2$ , represent the averages of  $I$  inside and outside of the set  $\{(x, y) \in \Omega : u(x, y) > \mu\}$  respectively, are updated at each iteration  $k$ ; thus the output  $\tilde{I}$  is a binary image taking the final values  $c_1$  and  $c_2$  over the two regions. In the problem currently being investigated, a gradient based edge detector oversegments the image by locating false edges outside the chamber region (*i.e.* edges that do not correspond to the ‘true’ boundary, but do exist, and therefore can be located). The GSB method acts as a regularised edge detector, locating major regions of interest, while avoiding these false edges. Using the Split Bregman implementation makes the computational cost of implementing this method equivalent to that of simple edge detectors (*e.g.* Canny). However, it also locates the inner and outer chamber regions, since these regions generally present a sharp contrast.

### 3.2.1.2 Topology Preserving Level Set Method

Once the edge detector is obtained, the second step in the proposed solution is to produce a curve representing the outline of the left ventricle boundary.

To achieve this, the topology constraining model developed in [7] is applied. To initialise the method for frame 1 of the dataset, an initial guess contour was placed inside the left ventricle chamber. Each subsequent frame was initialised using the final segmentation of the previous frame. Since the edge detector described in the previous section corresponds to a global minimiser of (3.1), the placement of the initial contour does not make a significant difference to the final segmentation result (it does, however, need to be placed inside the chamber region). As a length constraint, the authors in [7] use the GAC model (2.8), which in a level-set formulation

is given by:

$$F(\phi) := \int_{\Omega} g(|\nabla I(x)|) \delta(\phi(x)) |\nabla \phi(x)| \, dx \quad (3.5)$$

The evolution equation of (3.5) is given by:

$$\frac{\partial(\phi)}{\partial t} := |\nabla \phi(x)| \operatorname{div} \left( g(|\nabla I|) \frac{\nabla \phi}{|\nabla \phi|} \right) \quad (3.6)$$

The segmentation model proposed in [7] minimises a functional formed of (3.5) [26] and the following functional:

$$E(\phi) = - \int_{\Omega} \int_{\Omega} \exp\left(-\frac{\|x-y\|^2}{\sigma^2}\right) \langle \nabla \phi(x), \nabla \phi(y) \rangle \cdot H(\phi(x) + l) H(l - \phi(x)) H(\phi(y) + l) H(l - \phi(y)) \, dx \, dy \quad (3.7)$$

Here  $x$  and  $y$  are two neighbouring points as determined by the windowing function  $\exp(-\frac{\|x-y\|^2}{\sigma^2})$ ; where  $\sigma$  controls the width of windowing function,  $l$  controls the width of narrow band around the zero level line of the level set function (as discussed in section 2.3.1), and the unknown  $\phi$  is a level set function whose zero-level curve will define the evolving contour, while  $H$  is the Heaviside function.

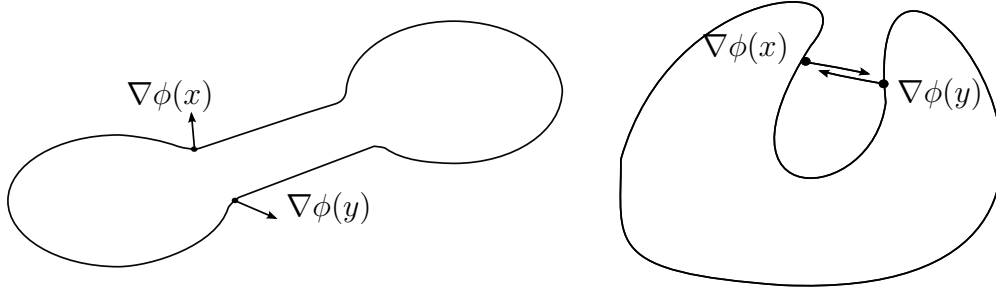


**Figure 3.2:** The figure shows the outward normal vectors corresponding to two neighbouring points,  $x$  and  $y$ .

If the outward normal vectors (see *e.g.* Figure 3.2) to the level lines passing through  $x$  and  $y$  have opposite directions, the inner product term  $-\langle \nabla \phi(x), \nabla \phi(y) \rangle$  causes the energy functional to increase sharply thereby avoiding breaking or merging of the curve. In the level set framework, it is common to add a balloon term

$\eta|\nabla\phi|$ , for constant  $\eta$ , which helps to accelerate the pace of the evolution. The associated Euler-Lagrange equation for the complete TPLS model is given by:

$$\begin{aligned} \frac{\partial\phi}{\partial t} = & |\nabla\Phi| \left[ \operatorname{div} \left( g \frac{\nabla\phi}{\|\nabla\phi\|} \right) + \eta g(|\nabla I|) \right] \\ & + 4 \frac{\chi}{\sigma^2} H_\epsilon(\phi(x) + l) H_\epsilon(l - \phi(x)) \\ & \cdot \int_{\Omega} \left[ \left( (x_1 - y_1) \frac{\partial\phi}{\partial y_1}(y) + (x_2 - y_2) \frac{\partial\phi}{\partial y_2}(y) \right) \right. \\ & \left. \cdot \exp\left(\frac{-\|x-y\|^2}{\sigma^2}\right) H_\epsilon(\phi(y) + l) H_\epsilon(l - \phi(y)) \right] dy \end{aligned} \quad (3.8)$$

where the component  $kg(|\nabla I|)|\nabla\phi|$  is added to increase the speed of convergence. In (3.8)  $\chi$  is a weighting parameter for the topology constraint (which regulates the influence of the topology constraint against the other constraints in the model). In (3.8)  $g$  is a function of  $\|\nabla I\|$ , however this is limiting since in practice it leads to a noisy edge set. By using the binary output image,  $\tilde{I}$  from Section 3.2.1.1 an alternative definition of  $g$  is used:

$$g(\tilde{I}, \|\nabla\tilde{I}\|) := \gamma\tilde{I} + \frac{1}{1 + \beta\|\nabla\tilde{I}\|^2} \quad (3.9)$$

thus attracting the curve to the regions of major interest while avoiding false edges.

### 3.2.1.3 Edge Smoothing

To overcome the effects of the low spatial resolution of 2D echocardiography which together with imaging acquisition effects (as discussed in section 3.1) combine to produce boundaries often defined by jagged and oscillatory edges, the output contour from the TPLS method is evolved according to a mean curvature smoothing model defined by:

$$\frac{\partial\phi}{\partial t} = b\kappa|\nabla\phi| \quad (3.10)$$

where  $b$  is a positive constant while  $\kappa$  represents the mean curvature [36].

The output of this model is a smooth curve that accurately estimates the boundary of the chamber. The final segmentation result corresponds to this final curve.

### 3.2.1.4 Complete Segmentation Model

The complete segmentation model, and main contribution of this section, is the combination of variations of both the GSB and the TPLS methods, which are both adapted to boundary detection in 2D echocardiography (henceforth the model will be referred to as the GSB + TPLS method). To summarise, the first step is the use of GSB method to generate a binary form of the original image in order to extract its major edge set. This information is used to better initialise the TPLS, which locates the endocardial boundary. At the final stage, the curve is refined slightly using mean curvature flow in order to smooth the final edge set.

The following section presents the results of applying the GSB + TPLS method to real-world echocardiographic images. The results are analysed by comparing them to manually delineated curves.

## 3.2.2 Experimental Results

To validate the GSB + TPLS method it was tested on 20 frames from 2 echocardiographic datasets obtained from the cardiology unit of a local hospital. The method was also compared to results obtained from the GAC method [26] and the CV model [4]. Manually delineated frames (performed by an expert observer) were used as a performance benchmark.

The initial step was to apply the GSB method to the datasets, where  $\mu$ , the weighting parameter for the fidelity term, was set to 0.002 (the parameters for each model were empirically derived). Figure 3.3 shows a sample output of the GSB method, together with its corresponding edge map.

In the topology preserving model, the topology constant,  $\chi$  was set to  $-0.5$  and the balloon term,  $\eta$  was set to 0.3. The initialisation for the segmentation was done by manually placing a contour in the first frame of each dataset. As a stopping criterion, the  $l_2$  norm between the current and previous  $\phi$  was used:

$$\|\phi_n - \phi_{n-1}\|_2 \tag{3.11}$$

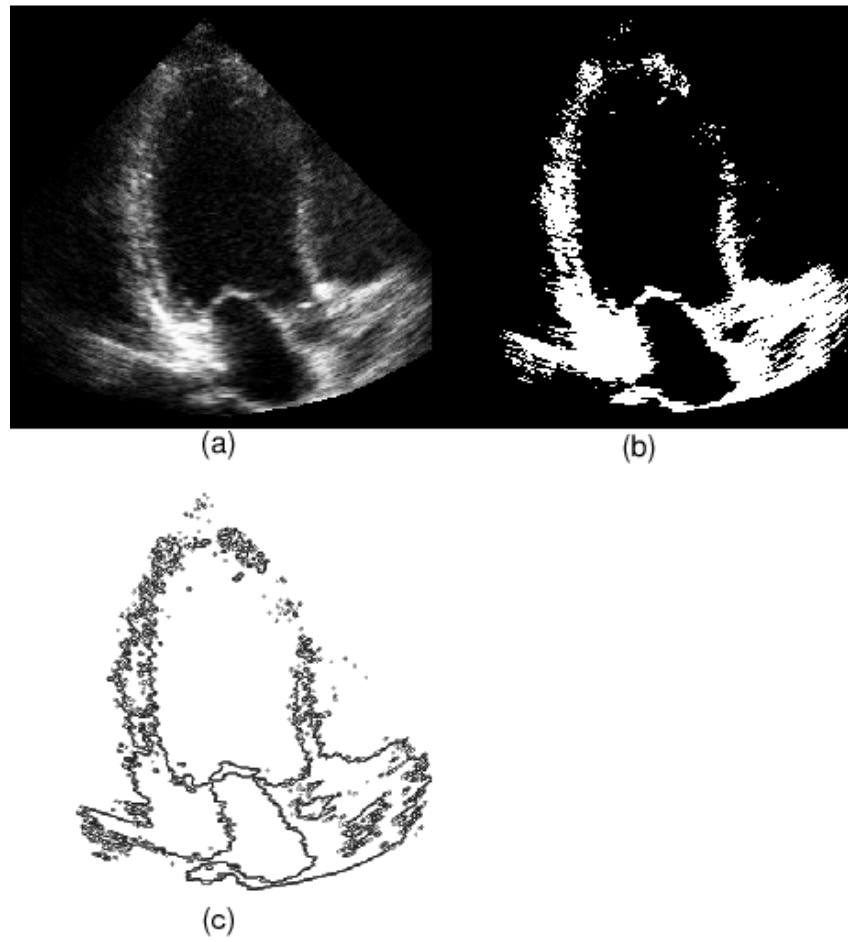


**Figure 3.3:** (a) shows a view of the left ventricle of the heart generated by an ultrasound scanner (b) is the output of the GSB method, (c) is the edge set extracted from the binary output of the GSB method. This edge-set is supplied to the topology preserving step.

When the difference between the current and previous  $\phi$  begins to converge then the segmentation is deemed to be complete. A sample of the results obtained with the proposed model, together with those obtained with the GAC and CV methods is shown in Figure 3.4. In Figure 3.4(d), the GAC method ‘leaks’ through the open valves (located at the bottom of the image), while the CV method (Figure 3.4(f)) is disrupted due to the lack of intensity homogeneity of the echocardiographic data (apparent in the upper part of 3.4(a)). The common result observed by the CV method applied to the dataset is that the curve partitions the image into two parts: one region corresponding to the cleanest part of the interior chamber (dark region inside of the heart) and another region containing everything else in the image. It can be seen that the result produced by the GSB+TPLS method achieves the best similarity to the manually delineated result.

### 3.2.2.1 Quantitative Evaluation

The images used in the experiments are from scans done on living patients therefore the exact dimensions of the cardiac chamber are not available as a gold standard. In light of this, the most common standard is the use of delineations done by an expert observer. This is the method employed for these experiments. The metrics used for comparison were the Dice coefficient [78], the Hausdorff Distance (HD) and the Mean Absolute Distance (MAD) [79]. The Dice coefficient measures the percentage overlap between 2 areas. It is defined as:

$$\text{Dice}(A, B) = \frac{2\|area(A) \cap area(B)\|}{\|area(A)\| + \|area(B)\|} \quad (3.12)$$

The HD metric is the maximum of the set of distances between corresponding points calculated for two curves. It is defined as:

$$\text{HD}(A, B) = \max\{\max_i\{d(\mathbf{a}_i, B)\}, \max_j\{d(\mathbf{b}_j, A)\}\} \quad (3.13)$$

where  $A$  and  $B$  represent two curves, consisting of pointsets  $A = \{\mathbf{a}_1, \mathbf{a}_2, \dots, \mathbf{a}_m\}$  and  $B = \{\mathbf{b}_1, \mathbf{b}_2, \dots, \mathbf{b}_m\}$ , and  $d(\mathbf{a}_i, B) = \min_j\|\mathbf{b}_j - \mathbf{a}_i\|$ , computes the distance between corresponding points in  $A$  and  $B$ . The MAD measures the average absolute distance

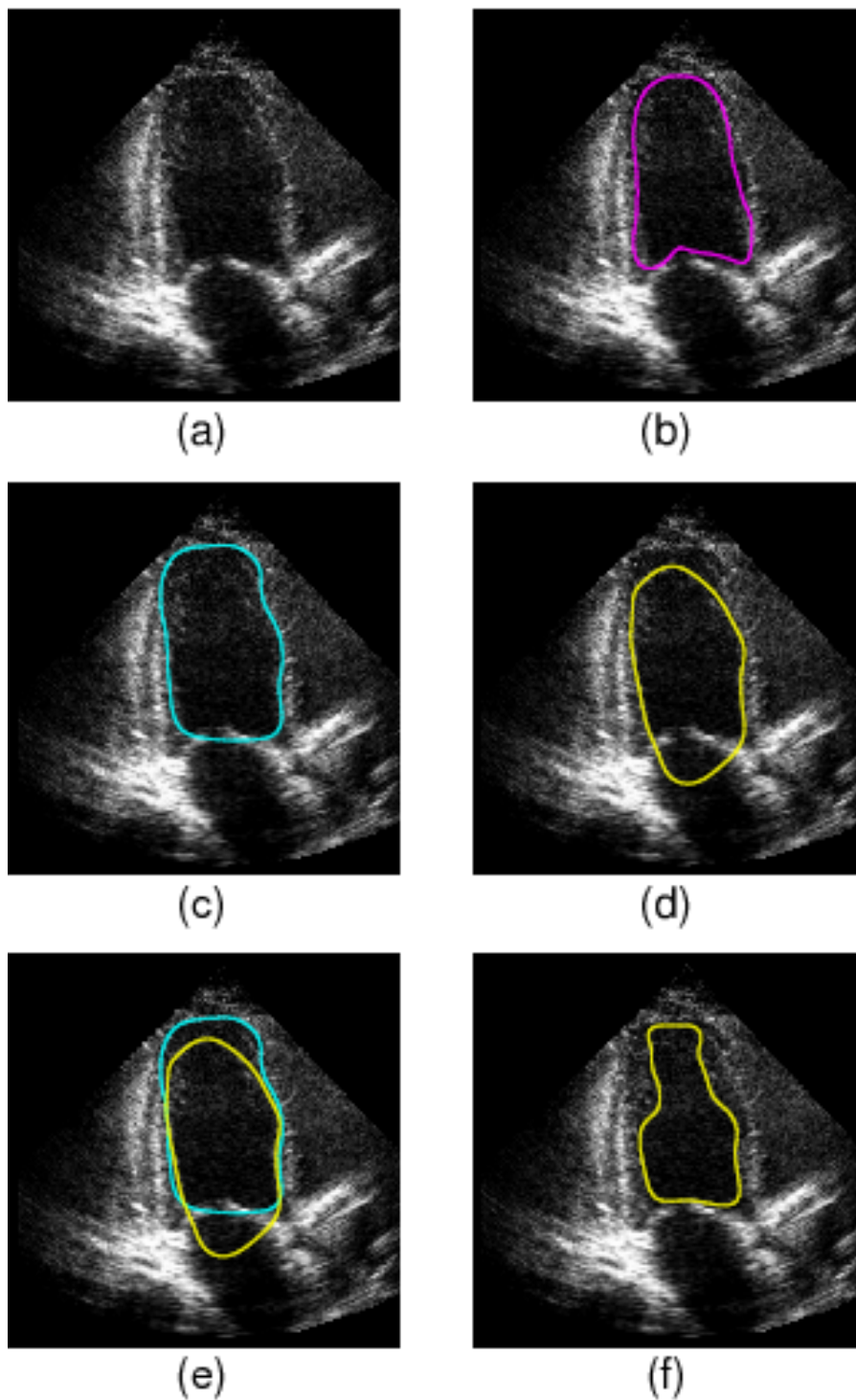


**Figure 3.4:** (a) the left ventricle view of the heart (b) shows the result of manually delineating the interior boundary of the chamber (c) is the segmentation result of the GSB+TPLS method, (d) is the GAC result and (e) shows both results superimposed, while (f) shows the CV result.

between the set of corresponding points calculated for two curves. It is defined as:

$$\text{MAD}(A, B) = \frac{1}{2} \left\{ \frac{1}{n} \sum_{i=1}^n d(\mathbf{a}_i, B) + \frac{1}{m} \sum_{j=1}^m d(\mathbf{b}_j, A) \right\} \quad (3.14)$$

All of the contour points from the corresponding curves were used to compute each metric. A summary of the results of this validation for each method is given in Table 3.1. With respect to the Hausdorff measurement in Table 3.1, the GSB + TPLS method obtained an average HD of 4.01mm from the reference contour, which was a significant improvement on the either of the CV or GAC methods, which obtained averages of 7.12mm and 5.14mm respectively. The proposed method obtained an average of 1.06mm distance with respect to the MAD, which again was an improvement on the either of the CV or GAC methods, which obtained averages of 2.43mm and 2.07mm respectively. With respect to the Dice coefficient, the GSB + TPLS method obtained an average overlap of 0.89, compared to 0.82 and 0.87 achieved by the CV and GAC methods respectively.

**Table 3.1:** Mean and standard deviation (SD) results of comparison with reference manual delineations over 20 frames. HD = Hausdorff distance; MAD = mean absolute distance; Measurement unit = millimeters.

	HD		MAD		Dice	
	Mean	SD	Mean	SD	Mean	SD
GSB+TPLS	<b>4.01</b>	1.06	<b>1.62</b>	0.3	<b>0.89</b>	0.04
CV	7.12	6.43	2.43	2.12	0.82	0.17
GAC	5.14	1.77	2.07	0.64	0.87	0.06

### 3.3 Boundary Reinforcement: using Continuous Maximum Flow and a Geodesic Active Contour method

This section describes an alternate approach for boundary reinforcement: using a global segmentation scheme, however in this work an alternate formulation consisting of the continuous max-flow algorithm is employed while the GAC method is used to estimate the final boundary. The purpose of exploring this alternate approach is to investigate whether a faster and more accurate solution can be obtained with the use of the CMF algorithm in combination with the GAC method. The model solved by the Geometric Split-Bregman algorithm in the previous section uses a geodesic length term, whereas in this section the standard length term is used. Instead of using edge information in both steps of the segmentation algorithm as in the previous section, the algorithm proposed in the current section separates the region segmentation step from the edge segmentation.

#### 3.3.1 Methodology

##### 3.3.1.1 Compute Global Segmentation

The first step of the proposed CMF + GAC method is to compute a segmentation using the CV model with two regions:

$$\min_{S, c_1, c_2} \lambda \left( \int_{\Omega \setminus S} |I(x) - c_1|^2 dx + \int_S |I(x) - c_2|^2 dx \right) + \nu |\partial S|. \quad (3.15)$$

As per section 2.3.3, in [62] it was shown that (3.15) can be exactly minimised via the convex problem:

$$\min_{\phi(x) \in [0,1]} \int_{\Omega} |I(x) - c_1|^2 \phi(x) + |I(x) - c_2|^2 (1 - \phi(x)) dx + \nu \int_{\Omega} |\nabla \phi(x)| dx. \quad (3.16)$$

A very efficient algorithm was proposed for solving the problem (3.16) in [8, 9]. The basic approach is to derive an augmented Lagrangian algorithm based on the following dual problem of (3.16):

$$\sup_{p_s, p_t, p} \int_{\Omega} p_s(x) \, dx \quad (3.17)$$

subject to:

$$|p(x)|_2 \leq \nu, \quad \forall x \in \Omega; \quad (3.18)$$

$$p_s(x) \leq |I(x) - c_1|^2, \quad \forall x \in \Omega; \quad (3.19)$$

$$p_t(x) \leq |I(x) - c_2|^2, \quad \forall x \in \Omega; \quad (3.20)$$

$$p \cdot n = 0, \quad \text{on } \partial\Omega. \quad (3.21)$$

$$\operatorname{div} p(x) - p_s(x) + p_t(x) = 0, \quad \text{a.e. } x \in \Omega. \quad (3.22)$$

where the dual variables are scalar and vector functions:  $p_s, p_t : \Omega \mapsto \mathbb{R}$  and  $p : \Omega \mapsto \mathbb{R}^N$ , where  $N$  is the dimension of the image domain  $\Omega$ . The dual problem can be interpreted as a maximum flow problem over a continuous domain, therefore the following algorithm was referred to as a Continuous Max-Flow algorithm (CMF).

In order to solve the maximisation problem, a Lagrange multiplier  $\phi$  was introduced for the constraint (3.22), and the augmented Lagrangian functional (which maps a set of functions to a real number  $\mathbb{R}$ ) was formulated as follows:

$$L_c(p_s, p_t, p, \phi) := \int_{\Omega} p_s \, dx + \int_{\Omega} \phi (\operatorname{div} p - p_s + p_t) \, dx - \frac{c}{2} \|\operatorname{div} p - p_s + p_t\|^2 \quad (3.23)$$

where for a function  $a$ ,  $\|a\|^2 = \int_{\Omega} |a(x)|^2 \, dx$ . Assuming the problem has been discretised such that  $p_s, p_t$  and  $\phi$  are defined for each pixel in the discrete image domain  $\Omega$  and  $\int, \nabla$  and  $\operatorname{div} = -\nabla^*$  are discrete integration and differential operators. In all experiments in this section, a mimetic discretisation of the differential operators [80] is used. An augmented lagrangian method is applied by alternatively maximising  $L_c$  for the dual variables  $p_s, p_t, p$  with constraints (3.18)-(3.21) and update the Lagrange multiplier  $\phi$  as follows:

Initialise  $p_s^1, p_t^1, p^1$  and  $\phi^1$ .

For  $k = 1, \dots$  until convergence:

$$- p_s^{k+1} := \arg \max_{p_s(x) \leq |I(x) - c_1|^2 \forall x \in \Omega} \left( \int_{\Omega} p_s \, dx - \frac{c}{2} \|p_s - p_t^k - \operatorname{div} p^k + \phi^k / c\|^2 \right)$$

which can easily be computed pointwise in closed form.

$$- p^{k+1} := \arg \max_{\|p\|_{\infty} \leq \nu} -\frac{c}{2} \|\operatorname{div} p - p_s^{k+1} + p_t^k - \phi^k / c\|^2,$$

where  $\|p\|_{\infty} = \sup_{x \in \Omega} |p(x)|_2$ . This problem can either be solved iteratively or approximately in one step using a linearisation such as described in [9]. In the current implementation the linearisation was used.

$$- p_t^{k+1} := \arg \max_{p_t(x) \leq |I(x) - c_2|^2 \forall x \in \Omega} -\frac{c}{2} \|p_t - p_s^{k+1} + \operatorname{div} p^{k+1} - \phi^k / c\|^2$$

This problem can also easily be computed in closed form pointwise.

$$- \phi^{k+1} = \phi^k - c(\operatorname{div} p^{k+1} - p_s^{k+1} + p_t^{k+1});$$

- Set  $k = k + 1$  and repeat.

The output  $\phi$  at convergence will be a solution to (3.16) and one can obtain a partition that solves (2.10) by the thresholding procedure described above. More details on implementation of the algorithm can be found in [9].

### 3.3.1.2 Boundary Localisation through local curve evolution

The initial segmentation produced by the CMF method corresponds to a simplified binary representation of the image, in which 2 prominent regions are identified and represented by binary functions with an intensity of either 1 or 0. However, the segmentation result obtained in this first step is not expected to be a good representation of the target object. Globally optimal solutions of the region based model 3.15, often have a complicated topology, that do not represent a simple connected

object with a closed boundary. In the second step of the proposed algorithm, the edge of the binary image from section 2.1 is used to create a more prominent edge attraction force in the GAC model defined in equation (2.8). The evolution equation of the GAC model is given by:

$$\frac{\partial \phi}{\partial t} = \left( \eta g + \xi \operatorname{div} \left( g \frac{\nabla \phi}{\|\nabla \phi\|} \right) \right) |\nabla \phi| \quad (3.24)$$

where  $\eta$  and  $\xi$  are two non-negative constants that act as weighting parameters.

In the proposed method, the edge map  $g$ , is generated using the binary output of step 1 using:

$$g(\nabla I_{CMF}) = \frac{1}{1 + |G * \nabla I_{CMF}|} \quad (3.25)$$

where  $G$  represents a Gaussian Kernel.

Compared to the globally optimal output of Section 2.1, the final output of the combined approach is expected to have a much simpler topology, consisting in most cases of one connected component.

The GAC method was implemented using the Additive Operator Splitting (AOS) scheme for solving PDE equations in the form of  $u_t = \operatorname{div}(g * u)$ . The details of the implementation can be found in [81, 82].

To summarise the approach, first a binary approximation of the original image is created and the major edge set extracted using the CMF method. This information is used to yield a better edge attraction force in the GAC method, which locates the object boundary. Figure 3.5 shows the result the CMF method for 2 sample frames, as well as the edge map generated using (3.25).

In the following section, the experimental results of the proposed method are presented.

### 3.3.2 Experiments & Results

To test the proposed CMF + method, a sample combination of medical and non-medical data was selected that naturally exhibits low contrast boundaries. In the

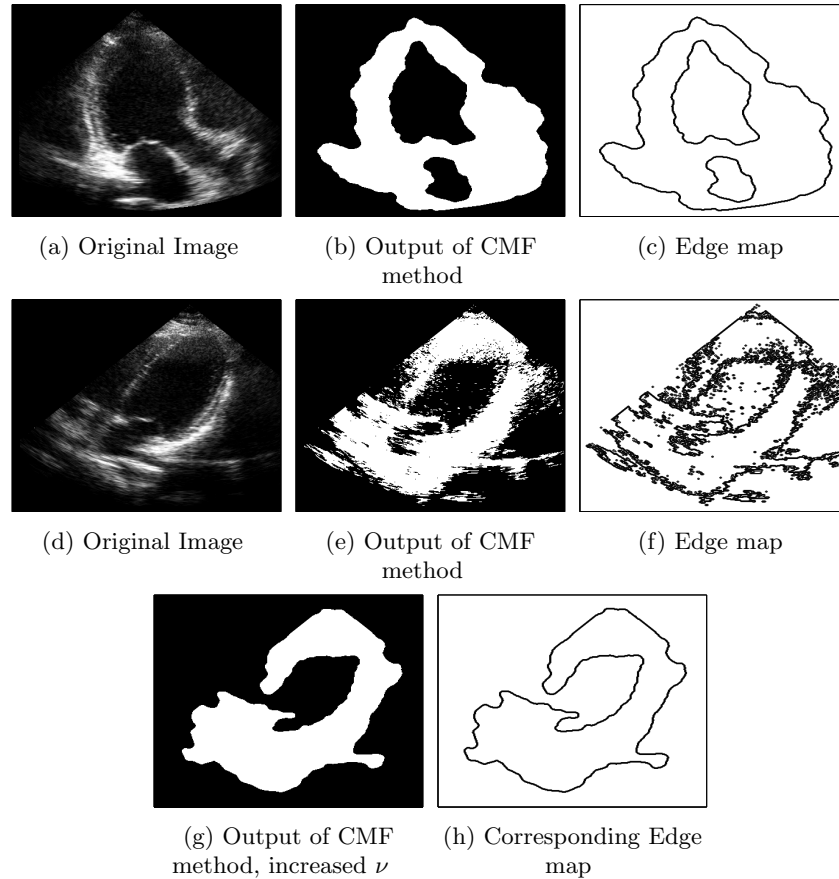


**Figure 3.5:** Example output of CMF method for 2 datasets; (a) and (d) are the original frames; (b), (e) and (g) show the corresponding output of CMF method, using values of  $\nu = 0.5$ ,  $\nu = 1e-02$  and  $\nu = 0.5$  respectively; (c), (f) and (h) effect of edge map generated from binary segmentation. Figures (e) and (g) show the effect of varying  $\nu$ . Part (g) shows a cleaner result however (e) more accurately represents the underlying (closed) structure.

case of the medical data, five low quality echocardiography datasets were obtained from the cardiology unit of a local hospital. The other test images consist of an image of a galaxy and also an image of a swarm of birds, these images were obtained from the internet (and included here with appropriate permissions). For both medical and non-medical data, the criteria for inclusion in the test was based on qualitative analysis; in the case of the medical data, the quality of the datasets were described as ‘challenging/low’ by two expert medical observers. In the case of the non-medical data, it can be observed in both cases that the boundary of the foreground entity

is defined by either a low contrast or a fragmented boundary.

The method was validated by comparing it to two classical data driven segmentation models: CV approach and the standard GAC model. In the medical image test, the method was also compared to the local-phase based feature detection approach of [69, 83] (this method having been designed specifically for echocardiography). The result of each method was also quantitatively compared to manual delineations performed by two expert observers. Three of the five datasets were delineated by one observer, while the other observer delineated the remaining two datasets.

A sample of the final results obtained on the echocardiography data, together with those obtained with the GAC and CV and local-phase based methods is shown in Figures 3.6 and 3.7 (the contour used to initialise each method is also included in Figure 3.6). Figure 3.6 shows the final result obtained with each method, while Figure 3.7 shows the similarity of each method to the reference delineation.

Starting with Row 1 in Figures 3.6 and 3.7, with respect to the GAC method, it can be seen (for example in Figure 3.6 (R1,C2)), that the absence of a sharp contrast in the upper right corner causes the method to over segment the chamber in this region. The local-phase based method performs comparatively well, however over segments the chamber in the upper left region. The CV method produces a better result, however slightly under segments the chamber in this same region. The proposed CMF + GAC method achieves a result visually quite similar to the manual delineation.

In Row 2 of Figures (3.6, 3.7), the CV obtains the most accurate result (see Figure 3.7 (R2,C2)). The absence of a sharp boundary disrupts the GAC method while the local-phase method over segments the chamber. The proposed CMF + GAC method obtains a mostly accurate result, however under segments the chamber in the lower left region.

Row 3 presents an example of an abnormally shaped chamber as well as limited window width in the upper right region. As in the previous examples, the GAC and local-phase based methods tend to over-segment (see Figures 3.7 (R3, C2-C3)) while the CV method, together with the CMF + GAC approach capture the true shape

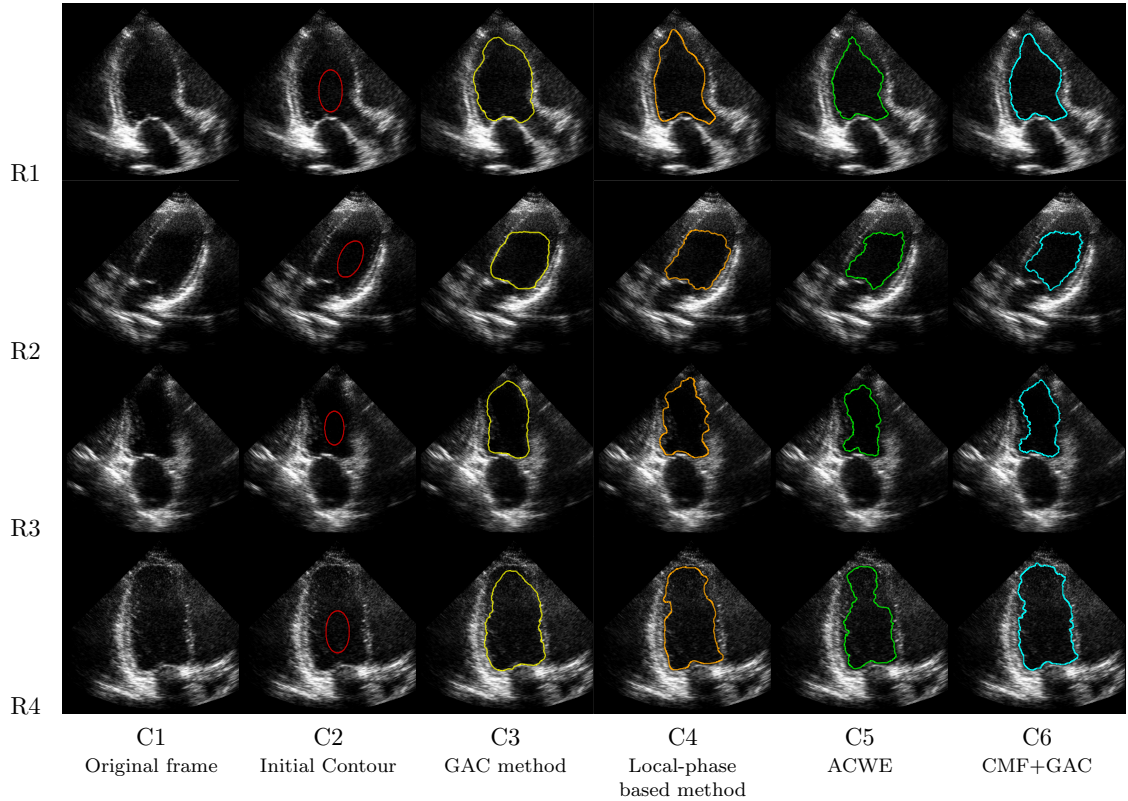


**Figure 3.6:** Results achieved by each method on four sample frames (Rows R1–R4). Each frame shows an example of boundaries characterised by weak edges. Note that the columns (C3–C6) represent outputs from each of the different algorithms

more accurately. The CMF + GAC method obtains a greater degree of similarity in the upper region of the chamber.

Table 3.2 shows the quantitative results for each of the frames in Figures 3.6 and 3.7. It can be observed that for each frame, with one exception (R2), the proposed method gives a better overall performance compared to each of the other methods.

For the medical test-set, the quantitative results showing the similarity between manual delineations carried out by two expert observers and each of the methods is presented in Table 3.3. With respect to the Hausdorff measurement, the CMF + GAC obtained an average HD of 4.48 mm from the reference contour, which was an improvement on each of the other methods, with the CV, GAC and local-phase method obtaining averages of 6.29 mm, 4.7 mm and 6.77 mm respec-

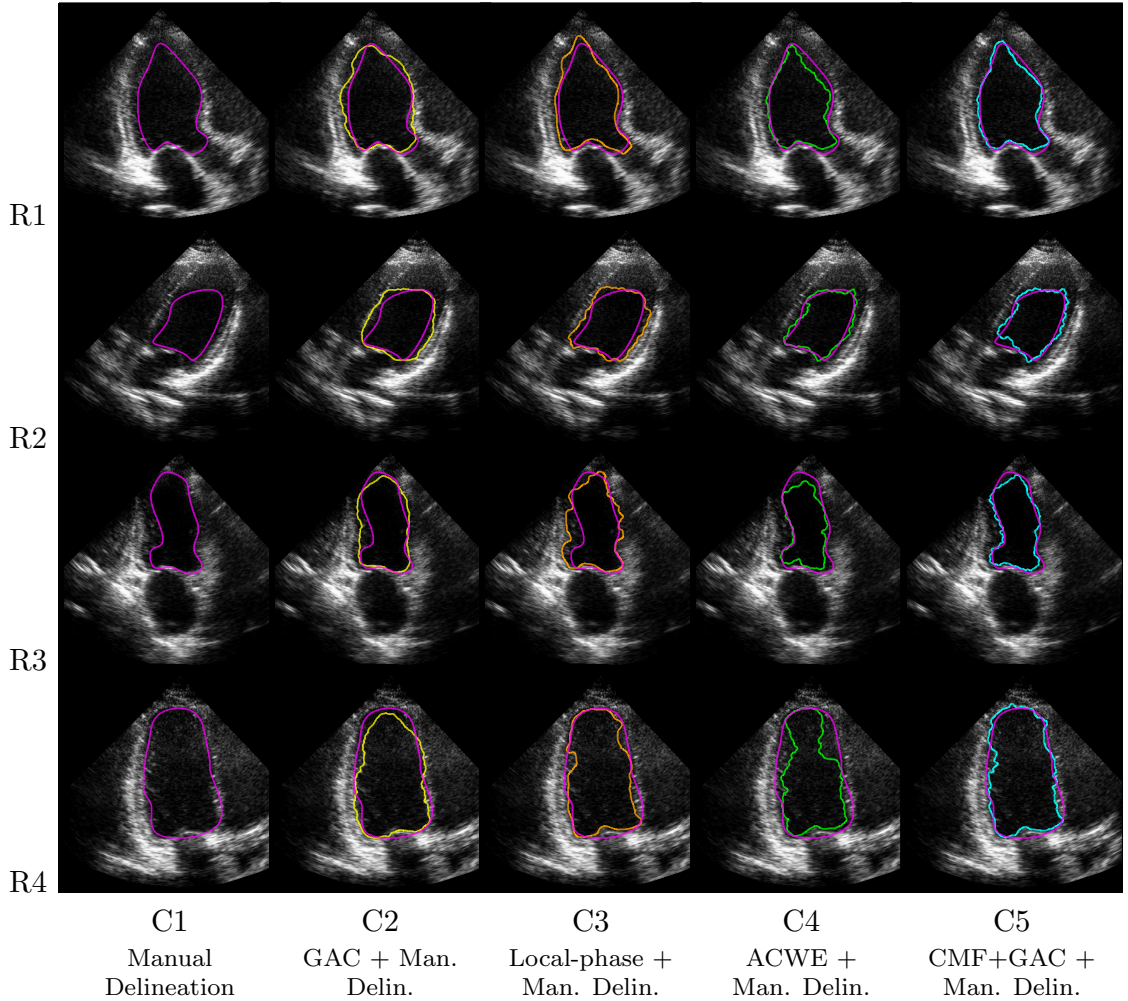


**Figure 3.7:** Results showing the similarity between the results of each algorithm and the expert manual delineations. Note that the columns (C3–C6) represent outputs from each of the different algorithms superimposed with the manual delineations.

tively. The second table presents the MAD results. In this case, the CMF + GAC achieved an average distance of 1.31 mm compared to 1.9 mm, 1.84 mm and 1.9 mm respectively for the CV, GAC and local-phase methods. The third table presents the result of the dice overlap metric. When comparing the overlap percentage between the CMF + GAC method and the manually delineated results it achieved a result of 91% compared to 86% achieved by the CV method, 88% achieved by the GAC method and 87% achieved by the local-phase method.

Figure 3.8 shows the CMF result for each frame in Figure 3.6. The results

**Table 3.2:** Quantitative Results for Figure 3.6

Frame 1 (R1)	CMF + GAC	Local Phase	CV	GAC
HD	<b>2.65</b>	4.62	4.13	5.58
MAD	<b>1.03</b>	1.68	1.39	2.59
Dice	<b>0.94</b>	0.89	0.9	0.87
Frame 2 (R2)	CMF + GAC	Local Phase	CV	GAC
HD	3.79	4.03	<b>2.66</b>	4.97
MAD	1.24	1.81	<b>0.96</b>	1.89
Dice	0.9	0.87	<b>0.92</b>	0.87
Frame 3 (R3)	CMF + GAC	Local Phase	CV	GAC
HD	<b>3.74</b>	6.88	5.45	6.19
MAD	<b>1.19</b>	1.96	1.6	1.68
Dice	<b>0.9</b>	0.85	0.85	0.88
Frame 4 (R4)	CMF + GAC	Local Phase	CV	GAC
HD	4.77	5.29	9.18	<b>4.49</b>
MAD	<b>1.52</b>	1.67	3.08	1.93
Dice	<b>0.92</b>	0.91	0.8	0.9

obtained from non-medical data are shown in Figures 3.9 and 3.10.

Figure 3.9 presents the results of testing the CMF + GAC method, together with the CV and GAC method on an image of a galaxy [2]. The results show that the GAC method finds the strongest boundary therefore missing the lower gradient regions, while the CV method captures the bright star-like points dotted around the image, which are not part of the galaxy. It can be observed that the CMF + GAC results achieves the best approximation of the boundary (as confirmed by a trained astronomer).

Figure 3.10 gives an example of birds swarming. In this example, the final results of both the GAC and the CMF + GAC methods, are quite similar, both giving the approximate boundary of the swarm; while the CV method partitions the image into visually the most intensity homogeneous regions, consequently missing, in many areas, the actual boundary. Both the GAC and CMF + GAC methods achieve comparable results, with a smoother boundary than the CV model.

The parameters used for each method are listed in Table 3.4. Parameter selection

**Table 3.3:** Quantitative results computed using Hausdorff, MAD and Dice metrics for medical data. Experiments were conducted on a sample of 55 frames across 5 echocardiographic datasets. Represented here is the average distance for each metric computed over a sample set of frames from each dataset.

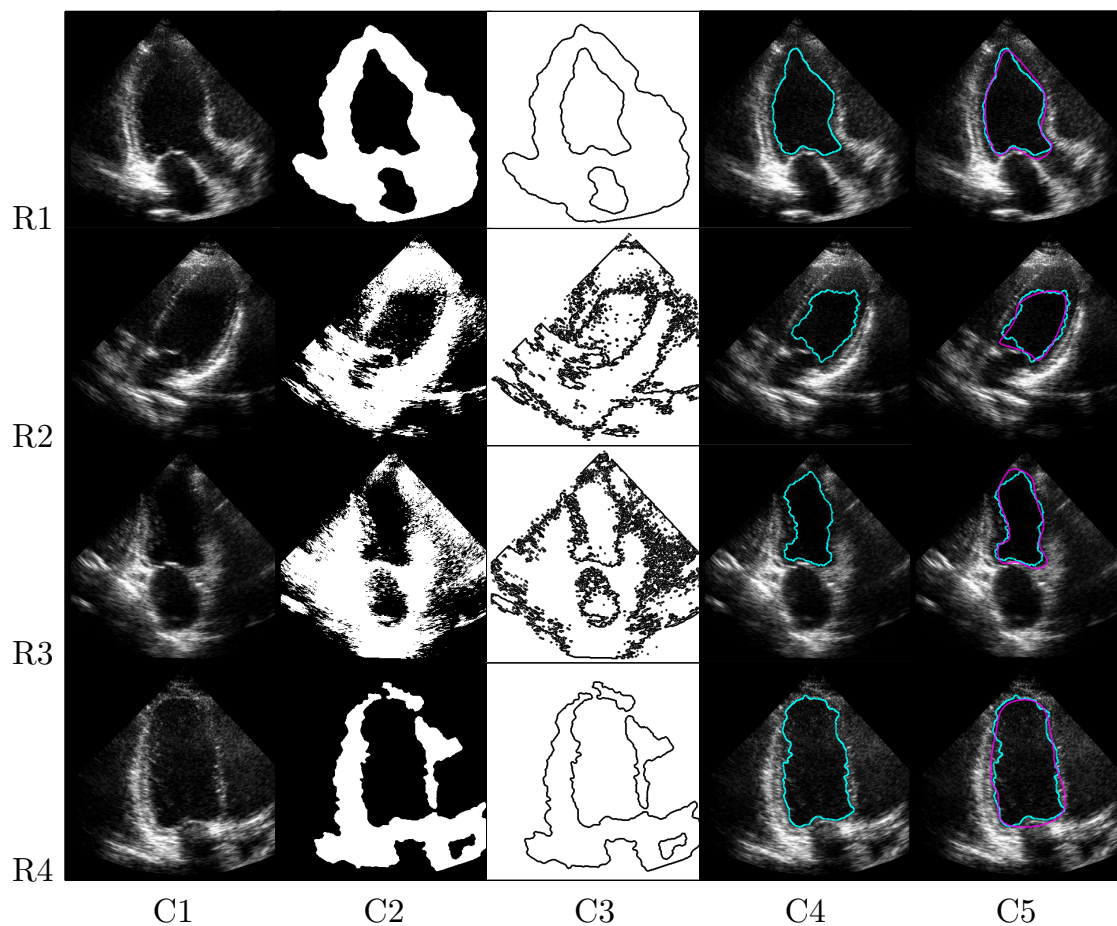
<b>HD</b>							
	Dataset 1	Dataset 2	Dataset 3	Dataset 4	Dataset 5	Average	% diff
CMF + GAC	<b>4.6</b>	5.28	<b>3.34</b>	<b>4.69</b>	<b>4.49</b>	<b>4.48</b>	
CV	6.78	9.91	3.37	5.91	5.47	6.29	40.4
Standard geodesic	5.31	<b>3.8</b>	4.08	5.64	4.66	4.7	4.9
Using Phase derived edge maps	6.62	5.48	5.02	8.22	8.52	6.77	51.1

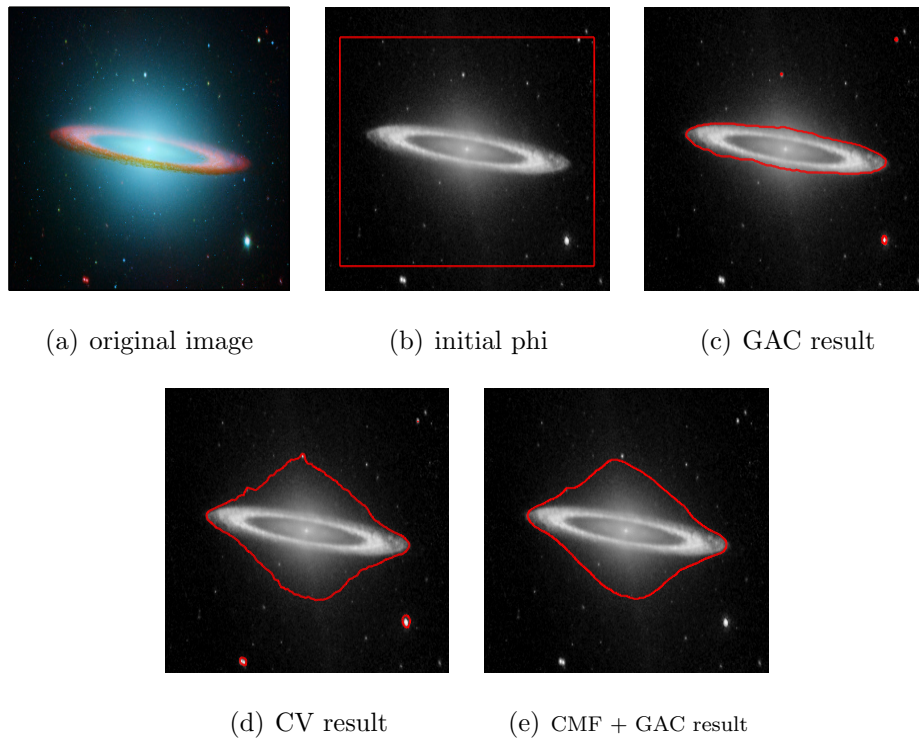
<b>MAD</b>							
	Dataset 1	Dataset 2	Dataset 3	Dataset 4	Dataset 5	Average	% diff
CMF + GAC	<b>1.17</b>	1.51	0.94	<b>1.54</b>	<b>1.41</b>	<b>1.31</b>	
CV	1.82	3.46	<b>0.89</b>	1.9	1.45	1.9	45
Standard geodesic	2.06	<b>1.39</b>	1.81	1.85	2.11	1.84	40.5
Using Phase derived edge maps	1.72	1.6	1.98	2.26	1.95	1.9	45

<b>Dice</b>							
	Dataset 1	Dataset 2	Dataset 3	Dataset 4	Dataset 5	Average	% diff
CMF + GAC	<b>0.93</b>	0.92	0.93	<b>0.88</b>	0.9	<b>0.91</b>	
CV	0.87	0.75	0.93	0.84	0.9	0.86	5
Standard geodesic	0.89	<b>0.93</b>	0.87	0.87	0.86	0.88	3
Using Phase derived edge maps	0.9	0.9	0.85	0.83	0.87	0.87	4



**Figure 3.8:** Step-by-step results of the proposed method for each of the frames (C1) which appearing in Figures 3.6 and 3.7. C1: Original frame, C2: The output of the CMF method, C3: The corresponding edge detector output. C4: Final result of proposed Method. C5: Final result superimposed on expert manual delineation.



**Figure 3.9:** Sombrero galaxy image [2]. The blue glow corresponds to the combined light of billions of old stars and the orange ring marks the sites of young stars. Courtesy NASA/JPL-Caltech

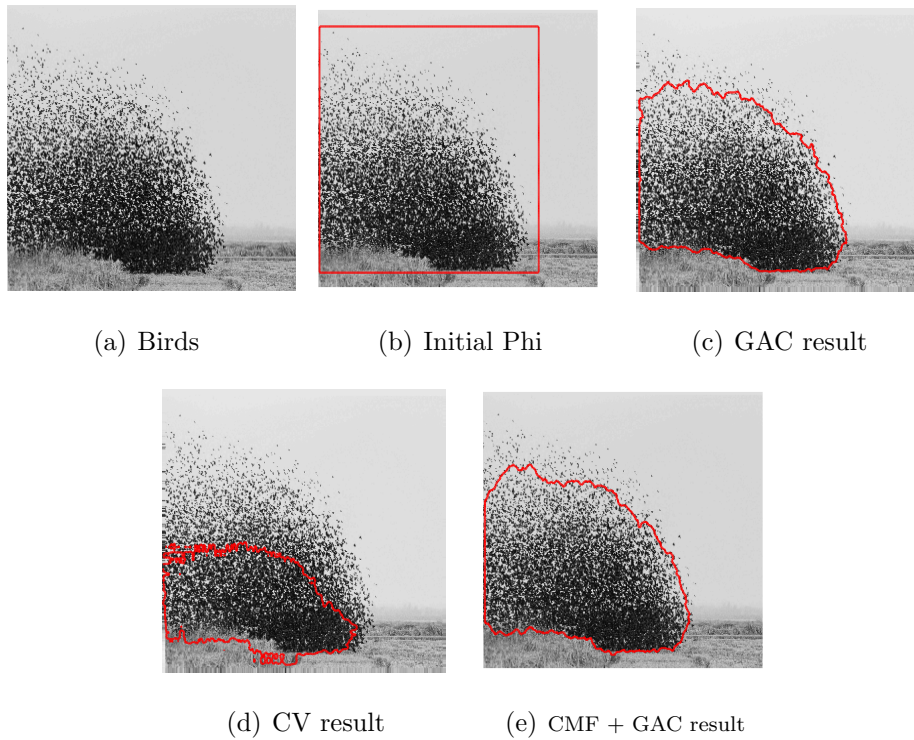


**Figure 3.10:** An image of a flock of birds where it can be observed that the boundary of the flock is fragmented. The test results achieved by the GAC, CV and CMF + GAC are presented in figures (c), (d) and (e). Photograph by Lucas Felzmann. Used with permission.

was done in the following way: an initial set of parameters (for example, in the case of the proposed method, those controlling length as well as the initial estimate of regional intensity) were chosen empirically for each test case and dataset. For each method, these initial parameters were varied by factors of  $\pm 5\%$ ,  $\pm 10\%$  and  $\pm 20\%$ , if a better correspondence with the manual delineations was achieved then these updated parameters were used in the experiments. For the experiments on medical data, the intensity estimates,  $c_1$  and  $c_2$  from equation (2.10) were kept constant over the course of the energy minimisation. Each method was manually initialised by placing a contour in each frame.

**Table 3.4:** Test Parameters

	Dataset 1	Dataset 2	Dataset 3	Dataset 4	Dataset 5	Galaxy Image	Birds Image
Number of frames	15	10	10	10	10	-	-
<b><i>CMF + GAC parameters</i></b>							
Initial mean intensity estimates	[0.03,0.18]	[0.05,0.28]	[0.016,0.15]	[0.017,0.12]	[0.033, 0.16]	[0.26,0.003]	[0.02,0.7]
Length parameter $\nu$ (CMF)	0.5	0.35	0.01	0.001	0.001	0.5	0.01
penalty parameter $c$	0.5	0.5	0.5	0.5	0.5	0.5	0.5
expansion parameter ( $\xi$ ) (GAC)	1	1	1	1.3	1	1	0.6
smoothness parameter ( $\eta$ )(GAC)	10	10	10	10	10	10	10
<b><i>CV parameters</i></b>							
smoothness parameters ( $\nu$ )	16.5	18	2.025	1.23	2.97	4	600
contrast ( $\lambda$ )	950	1200	318.75	78.75	128	500	1500
<b><i>GAC parameters</i></b>							
smoothness	10	10	10	10	10	4	5
expansion weight	0.67	0.9	0.6	0.57	0.6	0.6	1
<b><i>Local Phase parameters</i></b>							
Wavelength parameter	42	28	7	16	38.85	-	-
expansion weight ( $\alpha$ )	1	1	0.6	0.6	0.6	-	-

Sensitivity to variance in parameter choice is presented in Table 3.5. The table shows the average percentage error (for all datasets) due to change in the parameters used for each method. The CMF + GAC method shows robust performance with respect to the length parameter, however changing the initial estimates for inner and outer region intensity produces a significant fluctuation in performance, this is mirrored, though to a lesser degree, in the percentage error due to the image or

contrast parameter in the CV methods. Among the details which are highlighted in this table is the lack of stability of the GAC method with this data; shifting the length parameter by 5% for example, produces an error of almost 44% in the final result.

### Computational Time

The average CPU time required to compute the global segmentation (step 1) was found to be approximately 0.6 seconds, while the full curve evolution method took on average 9.7 seconds. In total, the proposed method took an average of 10.5 seconds. In comparison to the reference methods, the Local Phase Method took on average 10.1 seconds, the Geodesic method 14.7 seconds and the CV method took 5 seconds. The experiments were carried out in Matlab and C (the core processing functions were implemented in C, while the analysis was done using Matlab). The elements of the code which were compiled in C was done using using “MATLAB executable” (MEX) files. The experiments were run on a 64-bit, Intel Core 2 Duo CPU 3.00GHz processor with 4 GB of installed memory. The average image size was 376x376 pixels. The parallel processing capability of the processor was not used.

### 3.3.3 Discussion

The results of the experiments on non-medical data demonstrate that the CMF + GAC approach achieves either similar performance to both the CV and GAC methods or enhanced performance in certain cases. This is illustrated, for example, in Figure 3.9 where the lack of sharp contrast a causes the GAC approach to fail and also in Figure 3.10, in which the predominant intensity densities do not represent the actual boundary which disrupts the CV method. The CMF + GAC approach achieves better results compared to either method in these tests. The qualitative results for the medical data in Figures 3.6 to 3.7 largely mirror this observation.

With respect to the quantitative results in Table 3.3, the proposed approach achieved the best overall result compared to each reference method; obtaining an average HD of 4.48mm, an average MAD of 1.31mm and an average Dice coefficient

**Table 3.5:** Percentage error due to each parameter. Average taken over all frames

<b>Proposed Method</b>	<b>HD</b>		<b>MAD</b>		<b>Dice</b>	
	Average	Std	Average	Std	Average	Std
vary length parameter by +/- 5%	0.92	1.12	0.16	0.15	0.01	0.01
vary length parameter by +/- 10%	1.74	1.94	0.38	0.37	0.03	0.03
vary length parameter by +/- 20%	6.33	11.57	2.68	5.83	0.26	0.61
vary c1 or c2 by +/- 5%	5.59	9.47	3.36	4.48	0.93	1.35
vary c1 or c2 by +/- 10%	12.12	22.97	6.41	8.99	1.34	1.75
vary c1 or c2 by +/- 20%	28.71	44.09	13.64	16.51	2.37	2.48
Expansion Parameter (tuned for 1 dataset)						
vary expansion parameter by +/-5%	6.39	6.39	2.99	1.51	0.41	0
vary expansion parameter by +/-10%	14.5	1.72	12.13	10.65	1.32	0.91
vary expansion parameter by +/-20%	74.69	60.21	28.28	25.74	5.99	5.5
<b>CV</b>	<b>HD</b>		<b>MAD</b>		<b>Dice</b>	
	Average	Std	Average	Std	Average	Std
vary length parameter by +/-5%	4.19	9.38	3.12	6.02	1.12	2.96
vary length parameter by +/-10%	11.71	19.02	5.55	6.47	1.52	2.3
vary length parameter by +/-20%	11.03	8.48	6.12	4.76	1.59	2.23
vary image parameter by +/-5%	15.96	20.53	7.09	8.64	1.95	3.18
vary image parameter by +/-10%	20.15	28.63	7.62	8.55	2.06	2.86
vary image parameter by +/-20%	31.57	33.87	16.6	15.49	3.86	4.08
<b>GAC</b>	<b>HD</b>		<b>MAD</b>		<b>Dice</b>	
	Average	Std	Average	Std	Average	Std
vary expansion parameter by +/-5%	25.64	36.9	21.09	30.5	4.68	7.69
vary expansion parameter by +/-10%	48.92	35.57	47.1	28.44	10.37	7.86
vary expansion parameter by +/-20%	102.89	56.99	87.07	50.38	13.98	10.32
vary contour parameter by +/-5%	43.78	61.76	34.42	44.15	6.49	7.21
vary contour parameter by +/-10%	44.48	61.26	35.53	43.12	5.54	7.07
vary contour parameter by +/-20%	47.74	60.45	38.8	40.23	6.39	6.58
<b>Phase</b>	<b>HD</b>		<b>MAD</b>		<b>Dice</b>	
	Average	Std	Average	Std	Average	Std
vary wavelength parameter by +/-5%	6.63	5.06	2.55	1.75	0.41	0.37
vary wavelength parameter by +/-10%	7.5	5.25	3.9	2.51	0.68	0.55
vary wavelength parameter by +/-20%	10.31	5.28	5.95	3.03	0.91	0.59
Expansion Parameter (tuned for 3 datasets)						
vary expansion parameter by +/-5%	0	0	0.01	0.01	0	0
vary expansion parameter by +/-10%	2.18	2.36	1.24	1.12	0.23	0.2
vary expansion parameter by +/-20%	11.74	10.81	6.85	4.42	1.27	0.87

**Table 3.6:** Comparison of Execution Time. Measured in seconds.

	Binary Segmentation	Edge Map Generation	Contour Evolution	Total
Proposed Approach	0.65	0.03	9.74	10.42
Geodesic	-	0.03	14.7	14.73
CV	-	-	5.07	5.07
Local Phase method	-	0.23	9.9	10.13

of 0.91. Comparing these results to the next most accurate method, which was the GAC method, using the Hausdorff metric, a 5% improvement was achieved over the GAC method, a 40% improvement as measured by MAD, while for the Dice coefficient, an improvement of 3% was obtained. With respect to individual datasets, in 4 out of 5 cases, the proposed approach achieved the lowest Hausdorff Distance. For the MAD, this was the case in 3 out of 5 cases, while again in 4 out of 5 cases the proposed method achieved the best, or joint best result when compared using Dice coefficient.

The results also highlight some limitations of the model, such as in Figure 3.7 (R2,C5). In this example, due to the extremely low contrast boundary in the left region of the chamber, the length parameter of the CMF method was strongly relaxed, which has the positive effect of reinforcing the boundary but also preserving noise (as exhibited in Figures 3.5(e),(f)). This effect disrupted the CMF + GAC approach in this instance, and is also connected to the fluctuation in performance highlighted in sensitivity results in Table 3.5. Due to the lack of clear distinction between the intensity characteristics of the regions (i.e. the inner chamber and the inner wall of the myocardium), choosing robust data fidelity parameters is challenging. The sensitivity results in Table 3.5 for each of the CMF + GAC, CV and GAC approaches reflect this finding. These results highlight some of the limitations of data driven approaches in general, in handling particularly low quality data, in which the intensity profile between key regions is very similar. Notwithstanding this observed fluctuation, however; and considering the results as a whole, it can be ob-

served that the CMF + GAC approach gives the most accurate segmentation. The overall sensitivity results indicate that the local-phase approach is the most robust to parameter variance, while this approach yielded the least accuracy in terms of proximity to manual delineation.

When considering the quantitative results in Table 3.3, it can be seen that the level-set CV method, while less accurate than the CMF + GAC approach, achieves reasonable results on low quality data. This could raise the question as to what advantage does solving the MS functional using the CMF approach have over a traditional level set formulation? In the traditional CV approach, tuning all algorithmic parameters can be a challenging and rather unintuitive process; for example how the level set function should be initialised, how frequently and accurately it should be re-initialised, the time step sizes need to be chosen. Choosing the correct parameters for the CMF approach essentially means selecting the regularisation parameter  $\nu$  and the penalty parameter  $c$  in the Augmented Lagrangian method. The algorithm converges reliably for a wide range of  $c$ , (it was unnecessary to change the value of this parameter for any of the experiments). In addition, the CMF approach shows stronger robustness with respect to parameter  $\nu$  (compare rows 2-3 under CMF + GAC approach, to rows 2-3 of CV method, in Table 3.5). The CMF approach is guaranteed to converge to a global minimiser, in contrast to the level set approach which may get stuck in an inferior local minimum.

The combination of the CMF approach with the GAC method also has some interesting topological properties. Although the method contains no explicit topology preserving constraint, by relaxing the length constraint for the CMF approach, it becomes possible to favour the generation of closed regions, shown for example in Figure 3.5(e). Figure 3.6 (R1,C3), however, shows an example where this is impossible; in this example, the top left portion of the chamber is outside of the viewing window, as a result, there is not enough information for the CMF method to ‘reinforce’ the boundary. However; by increasing the stiffness properties ( $\alpha$ ) of the GAC contour, it is still possible to maintain a closed topology. The reason for this is that the GAC method converges to a local minimiser with simple topology,

which in this application is a better solution than the global minimiser, since the target structure also has a simple topology. In this way the combination of local and global segmentation methods works to preserve topology.

While it has been shown that the proposed method is capable of accurately segmenting low contrast images; it should be noted that the method used to generate edge sets (step 1) is not proposed as a general edge detection approach; for example, the detection of extremely fine structures would prove problematic for the model. Instead the method has been designed for the partition of structures with weak boundaries, as exemplified in a variety of real-world applications, a sample of which have been highlighted in the preceding sections.

Finally, it is evident from the results that global features play a more significant role in the CMF + GAC method than local edge features, this is a key feature of the method. While the overall objective of the scheme is accurate boundary estimation, this goal is achieved by integrating regional information into the edge detector process using the CMF method. It is this regional information that makes boundary reinforcement possible.

### 3.3.4 Conclusion

In this section a method to generate edge detectors has been presented that allows for the effective segmentation of regions bounded by weak edges. As demonstrated using a sample of real-world medical and non-medical data, compared to classical image driven approaches, the proposed method is capable of more accurately detecting boundaries from low contrast images.

The proposed method increases robustness in two ways: first by incorporating regional information into the process of edge map generation, weak boundaries are effectively reinforced. Secondly, the edge map output, which corresponds to a 2 region global segmentation result, yields a more robust solution compared to schemes that rely purely on local optimisation techniques.

Overall, it can be observed that the qualitative and quantitative results clearly demonstrate the improved performance of the CMF + GAC approach over purely

regional or intensity based methods as exemplified in the GAC and CV methods.

### 3.4 Summary & Conclusion

In this chapter, two sequential models for boundary refinement were proposed. The first using a combination of the GSB and TPLS methods and the second using the CMF approach with the GAC method. The split Bregman method together with the CMF approach represent two examples of globally convex methods. In general, the max-flow algorithm converges to a lower precision and usually faster. A difference between the CMF algorithm and the split Bregman and other algorithms for solving the convex segmentation problem, is that no projection onto the set  $[0,1]$  is needed at each iteration of the algorithm. These constraints are satisfied automatically at convergence. Therefore the algorithm progresses in the steepest descent direction. All other algorithms use what is called a “forward backward scheme” to handle the  $[0,1]$  constraints which is slower and less accurate. The choice of the GAC method over the TPLS was also found to be beneficial. The main drawback of the TPLS model is the computational cost due to the non-local term appearing in the evolution equation [7]. The choice of the GAC method permitted a faster convergence without significant penalty in terms of topology preservation. The empirical results also underline this observation. Over 20 frames, the GSB + TPLS method achieved an average MAD of 1.62 and an average Dice coefficient of 0.89, while over 50 frames the CMF + GAC an average MAD of 1.17 mm and finally an average Dice coefficient of 0.93.

The preceding chapter dealt with an aspect of segmentation robustness described as boundary reinforcement. In the next chapter, regional constraints are incorporated into an existing topology preserving segmentation model to increase robustness in the presence of noise.

# 4

## Topology Preserving Active Contours

### 4.1 Introduction

In chapter 3, a method was proposed for the segmentation of images with low-contrast boundaries, a second aspect of segmentation robustness will be investigated in this chapter, namely the performance of the Topology Preserving Level Set (TPLS) models in the presence of noise. As described in chapter 2, active contour models are variational methods for segmenting complex scenes using edge or regional information. Many of these models employ the level set method to numerically minimise a given energy, which provides a simple representation for the resulting curve evolution problem. During the evolution, the curve can merge or break, thus these methods tend to have steady state solutions that are not homeomorphic to the initial condition. In many applications, the topology of the edge set

is known, and thus can be enforced. In this work, a topology preserving variational term is combined with the region based active contours models in order to segment images with known structure. The advantage of this method over current topology preserving methods is that the proposed model locates boundaries of objects and not only edges. This is particularly useful for highly textured or noisy data.

Active contours methods segment images by evolving a curve until it captures either boundaries and/or edges. The curve dynamics are typically defined to descend a specified energy potential towards the minimum. In general, the energy functional specifies constraints on the structure of the curve as well as quantitative measures of edges and boundaries. In many applications, the topological structure of the edge set is known *a priori* and thus can be embedded in the initial curve. Therefore, it would be desired that the final solution be homeomorphic to the initial data, although in the popular level set based methods this cannot be guaranteed. Some works in the literature (for example, [7, 3]) have incorporated forcing terms to prevent the change in topology that occurs during the curve evolution process, but mainly focus on locating edges. In this way, these methods are interpolating edge detector information under the condition that some known structure must be preserved. In this work, it is shown that by using regional information it is possible to segment the image while constraining the topology. The main contribution is the combination of region based active contour models with topological forces.

Recalling from section 2.2.4, in [4, 38] the authors proposed the model in (2.10) as a piecewise constant variant of the MS model.

In practice, it is possible to get solutions of Equation (2.10) to be homeomorphic to the initial condition; for example see the Gestalt theoretical solutions in [4]. However, these solutions are typically local minimisers of the functional in Equation (2.10) (due to the non-convex structure of the energy). In order to guarantee preservation of the curve topology during its evolution, an additional variational term must be included.

In [3], the authors proposed to use a TPLS method in order to prevent the topological changes common to the level set framework. Their method relies on the

discrete representation of the curve at the pixel level. They proposed examining the sign changes of the level set function over each of the pixels near the zero level curve to control the structural changes. By using the notation of simple points (those that can be removed without effecting the topology of the set), they build an algorithm that enforces fixed topology. Thus as the curve evolves, the algorithm monitors the sign changes and prevents structural changes.

For level set based shape optimisation, [84] proposed using the following logarithmic barrier functional to enforce constant topology:

$$\mathcal{H}(\phi) = - \int_{\mathcal{C}} \log [\phi(x + d\nabla\phi(x))] ds - \int_{\mathcal{C}} \log [-\phi(x - l\nabla\phi(x))] ds \quad (4.1)$$

where  $d$  and  $l$  are small positive constants and  $\phi$  is a signed distance function whose zero level set is the curve  $\mathcal{C}$ . Equation (4.1) prevents sign changes from occurring near a band around the zero level curve defined by the normal directions and by the parameters  $d$  and  $l$ .

In [7] the Geodesic Active Contour (GAC) model was augmented by the following energy functional:

$$T(\phi) := - \iint_{\Omega \times \Omega} \nabla\phi(x) \cdot \nabla\phi(y) e^{-\frac{\|x-y\|^2}{d^2}} W_l(\phi(x))W_l(\phi(y)) dx dy \quad (4.2)$$

where  $W_l(\phi(x)) := H(\phi(x) + l)H(l - \phi(x)) = \{x \in \Omega \mid |\phi(x)| \leq l\}$ .

to preserve structure during edge detection. The model is able to segment the image while remaining homeomorphic to the initial data, but relies on the edge detector in order to locate the proper edges. If the image contains noise, corruption, or texture, edge detection can become unreliable. In particular, since edge detectors rely on gradients to locate jumps, both noise and texture can make this task difficult. Also, when boundaries are not represented by sharp intensity contrast, edge detectors are ineffective. To handle these more general cases, in the current work region based methods are used for robustness with respect to noise, while the topology preserving method in Equation (4.2) is used to enforce structure.

## 4.2 Topology Preserving Active Contours

The proposed model is expressed within the level set framework proposed in [85]. A curve  $\mathcal{C}$  is represented as the zero level set of a continuous Lipschitz function  $\phi : \Omega \rightarrow \mathbb{R}$ , *i.e.*  $\mathcal{C} = \{\phi = 0\}$ . This implicit curve representation greatly simplifies the theoretical and practical implementation of the curve's evolution process (as it descends towards the minimiser). For example, the length functional [86] can be written as:

$$\text{Length}(\mathcal{C}) = \int_{\Omega} |\nabla H(\phi)| = \int_{\Omega} \delta(\phi) |\nabla \phi| \quad (4.3)$$

where  $H$  is the Heaviside function defined to be 1 for positive arguments and 0 otherwise and  $\delta = H'$  is the Dirac delta measure. In order to differentiate Equation (4.3) with respect to  $\phi$  a continuous approximation of  $\delta$  must be used. For example, parameterising the approximation by  $\epsilon > 0$ , a standard approximation is  $\delta_{\epsilon}(x) = \frac{1}{\pi} \frac{\epsilon}{\epsilon^2 + x^2}$ . Since  $\epsilon$  must be taken at the grid resolution, for imaging problems it is commonly set to  $\epsilon = 1$ . For the rest of this work, it will be assumed that the following properties hold for the approximated Dirac delta function (dropping the subscript): 1.  $\delta \in C^{\infty}$ , 2.  $\int \delta(x) dx = 1$ , and 3.  $\delta(x) \geq \beta > 0$  for all  $x$ .

### 4.2.1 Topology Preserving Term

Recall the topological term from Section 4.1 which will be used in the proposed model. The variational term was proposed in [7] and is defined as:

$$T(\phi) := - \iint_{\Omega \times \Omega} \nabla \phi(x) \cdot \nabla \phi(y) e^{-\frac{\|x-y\|^2}{a^2}} W_l(\phi(x)) W_l(\phi(y)) dx dy \quad (4.4)$$

Since the gradient of the function  $\phi$  is perpendicular to its level sets, the first term provides a measure of how close the level sets are to intersecting. If the gradients are pointing in almost opposite directions (nearly anti-parallel), this indicates that the points  $x$  and  $y$  are from different neighbourhoods of the curve and are likely to undergo a topological change. The anti-parallel condition is also the reason for the negative sign in Equation (4.4). On the other hand, if the gradients are

perpendicular to each other and the points are close to each other in space, then the points  $x$  and  $y$  are from the same segment of the curve. The exponential provides a reasonable definition of closeness of the points  $x$  and  $y$ . And lastly, the functions  $W_l$  extend the computational domain from the zero level set of  $\phi$  to a neighbourhood around the zero level set. In practice, this provides a buffer region around the curve and defines a minimal distance between different segments of the curve.

### 4.2.2 Topology Preserving Active Contours model

The proposed topological preserving active contours model is:

$$\min_{\phi, c_1, c_2} E(\phi, c_1, c_2) = \int_{\Omega} \delta(\phi) |\nabla \phi| + \mu T(\phi) + \gamma \int_{\Omega} (I - c_1)^2 H(\phi) + (I - c_2)^2 H(-\phi) \, dx \quad (4.5)$$

In order to minimise Equation (4.5), the first variation with respect to each variable is computed. The second two variables  $c_j$  for  $j = 1, 2$  are the regional means and are calculated as follows:

$$c_1 = \frac{\int_{\Omega} I H(\phi) \, dx}{\int_{\Omega} H(\phi) \, dx} \quad (4.6)$$

$$c_2 = \frac{\int_{\Omega} I H(-\phi) \, dx}{\int_{\Omega} H(-\phi) \, dx} \quad (4.7)$$

These expressions are the exact relationship given by the first variations. For the level set function, the standard technique is to embed the first variation of Equation (4.5), with respect to  $\phi$ , in an evolution equation. This yields the following:

$$\begin{aligned} \partial_t \phi = & \delta(\phi) \operatorname{div} \left( \frac{\nabla \phi}{|\nabla \phi|} \right) + 4 \frac{\mu}{d^2} W_l(\phi) \int_{\Omega} (x - y) \cdot \nabla \phi(y) e^{-\frac{\|x-y\|^2}{d^2}} W_l(\phi(y)) \, dy \\ & + \gamma \delta(\phi) ((I - c_2)^2 - (I - c_1)^2) \end{aligned} \quad (4.8)$$

with homogeneous Neumann boundary conditions. The time dependent equation is further rescaled to (since  $\delta$  is strictly positive):

$$\begin{aligned} \partial_t \phi = & |\nabla \phi| \operatorname{div} \left( \frac{\nabla \phi}{|\nabla \phi|} \right) + 4 \frac{\mu}{d^2} W_l(\phi) \int_{\Omega} (x - y) \cdot \nabla \phi(y) e^{-\frac{\|x-y\|^2}{d^2}} W_l(\phi(y)) \, dy \\ & + \gamma \left( (I - c_2)^2 - (I - c_1)^2 \right) \end{aligned} \quad (4.9)$$

The first term is the mean curvature of the zero level line, the second term is the topological force, and the last two terms are the regional forces. Notice that at steady state and under the assumption that  $|\nabla \phi| = 1$ , (4.9) corresponds to the first variation of (4.5) along the zero level curve (*i.e.* the steady state of (4.8)). The motivation for this rescaling is to correctly balance the topological force with the other terms in the evolution equation. The topological force plays two roles; it encourages a particular structure on the curve as well as influences movement to different regions. Therefore, the topological term interacts with both the mean curvature (structure term) and the regional forces. From [7], the rescaling of the curvature term is well-behaved with the topology term. However, the influence of the regional forces should be spread in order to balance with the topological force. This is done by simply removing  $\delta$ .

All together, this model has several (strictly-positive) parameters:  $\gamma$ ,  $\mu$ ,  $d$  and  $l$ . The parameters  $d$  and  $l$  control the regions of influence in space. For the experiments, the parameters were set to  $d = 4$  and  $l = 1$ . The energy balancing parameters  $\gamma$  and  $\mu$  determine the curve structure. If  $\mu$  is small relative to  $\gamma$ , then the resulting evolution will undergo topological changes. In practice, keeping  $\mu$  close to 1 produces appropriate results. The genus number of a particular structure is equal to the number of handles (or holes) the structure contains. The parameter  $\mu$  can be weakened in order to encourage a particular genus with some flexibility (allowing small amounts of deviation from the initial curve).

**Remark 4.2.1.** *In the level set framework, it is common to add a balloon term  $\eta|\nabla \phi|$ , for constant  $\eta$ , which helps to shrink or grow the curve (depending on the sign of  $\eta$ ). With respect to dynamics of the proposed model, the additional term would force Equation (4.9) out of the true steady state, for non-zero  $\eta$ . In order to*

avoid this effect, the parameter can be made time-dependent  $\eta(t)$ , with the condition that  $\eta(t) = 0$  for all  $t > T$ . This is done in some numerical experiments to accelerate the curve towards the edge set.

**Remark 4.2.2.** If  $\mu$  is large relative to the other parameters (as well as larger than 1), then it is clear that the resulting evolution will not produce satisfactory results. However, the growth that occurs resembles that of the fingering effect seen in Hele-Shaw equations [87, 88]. This may be due to the self-repelling and competing dynamics of the topological force.

The rescaled model will descend a new energy potential, although the minimum should be identical. The following theorem explains the rescaled equations descent behavior.

**Theorem 4.2.3.** Let  $\phi(t, x) \in C^1([0, T]; W^{1, \infty}(\Omega))$  be the solution to Equation (4.9) with Neumann boundary conditions and  $|\nabla\phi| = 1$  a.e. in  $\Omega$ . Then for all  $t > 0$ , the evolution equation decreases an energy, i.e.  $\partial_t \bar{E}(\phi, c_1, c_2) \leq 0$ , where the energy is defined below:

$$\bar{E}(\phi, c_1, c_2) = \int_{\Omega} |\nabla\phi| + \mu T(\phi) + \gamma \int_{\Omega} ((I - c_1)^2 - (I - c_2)^2)\phi \, dx \quad (4.10)$$

*Proof.* It is possible to formally differentiate under the integral to find the energy's time derivative as follows (for simplicity, the subscript on the integrals is dropped).

$$\begin{aligned} \partial_t \bar{E}(\phi(t, -), c_1(t), c_2(t)) &= \int \frac{\nabla\phi}{|\nabla\phi|} \cdot \nabla\phi_t \, dx \\ &- \mu \iint [\nabla\phi_t(x) \cdot \nabla\phi(y) + \nabla\phi(x) \cdot \nabla\phi_t(y)] e^{-\frac{\|x-y\|^2}{a^2}} W_l(\phi(x))W_l(\phi(y)) \\ &+ \nabla\phi(x) \cdot \nabla\phi(y) e^{-\frac{\|x-y\|^2}{a^2}} [W'_l(\phi(x))W_l(\phi(y))\phi_t(x) + W_l(\phi(x))W'_l(\phi(y))\phi_t(y)] \, dx \, dy \\ &+ \gamma \int 2(I - c_1)c_{1t}\phi + (I - c_1)^2\phi_t + 2(I - c_1)c_{2t}\phi - (I - c_2)^2\phi_t \, dx \quad (4.11) \\ &= \text{Term}_1 + \text{Term}_2 + \text{Term}_3 \end{aligned}$$

Investigating this expression term by term; using integration by parts the first term yields:

$$\text{Term}_1 = \int \frac{\nabla\phi}{|\nabla\phi|} \cdot \nabla\phi_t \, dx = - \int \text{div} \left( \frac{\nabla\phi}{|\nabla\phi|} \right) \phi_t \, dx \quad (4.12)$$

where boundary terms vanish because of the boundary conditions. For the third term in the expression, it is noted that since  $c_1$  and  $c_2$  satisfies the first variation exactly (for a given  $t$ ) the expression simplifies to:

$$\text{Term}_3 = \gamma \int ((I - c_1)^2 - (I - c_2)^2) \phi_t \, dx \quad (4.13)$$

And lastly, the second term is made up of two subterms which will be handled separately:

$$\begin{aligned} \text{Term}_2 &= -\mu \iint [\nabla\phi_t(x) \cdot \nabla\phi(y) + \nabla\phi(x) \cdot \nabla\phi_t(y)] e^{-\frac{\|x-y\|^2}{d^2}} W_l(\phi(x))W_l(\phi(y)) \\ &\quad + \nabla\phi(x) \cdot \nabla\phi(y) e^{-\frac{\|x-y\|^2}{d^2}} [W_l'(\phi(x))W_l(\phi(y))\phi_t(x) + W_l(\phi(x))W_l'(\phi(y))\phi_t(y)] \, dx \, dy \\ &= -\mu(\text{Term}_{2a} + \text{Term}_{2b}) \end{aligned} \quad (4.14)$$

The main task is to separate the variables  $x$  and  $y$  as is done in [7]. This can be done via Fubini's theorem [89], by switching integration order and recombining terms to get:

$$\begin{aligned}
\text{Term}_{2a} &= \iint [\nabla\phi_t(x) \cdot \nabla\phi(y) + \nabla\phi(x) \cdot \nabla\phi_t(y)] e^{-\frac{\|x-y\|^2}{d^2}} W_l(\phi(x))W_l(\phi(y)) \, dx \, dy \\
&= \iint \nabla\phi_t(x) \cdot \nabla\phi(y) e^{-\frac{\|x-y\|^2}{d^2}} W_l(\phi(x))W_l(\phi(y)) \, dx \, dy \\
&\quad + \iint \nabla\phi(x) \cdot \nabla\phi_t(y) e^{-\frac{\|x-y\|^2}{d^2}} W_l(\phi(x))W_l(\phi(y)) \, dx \, dy \\
&= - \int \left( \int \operatorname{div}_x \left( \nabla\phi(y) e^{-\frac{\|x-y\|^2}{d^2}} W_l(\phi(x))W_l(\phi(y)) \right) \, dy \right) \phi_t(x) \, dx \\
&\quad - \int \left( \int \operatorname{div}_x \left( \nabla\phi(x) e^{-\frac{\|x-y\|^2}{d^2}} W_l(\phi(x))W_l(\phi(y)) \right) \, dx \right) \phi_t(y) \, dy \\
&= -2 \int \left( \int \operatorname{div}_x \left( \nabla\phi(y) e^{-\frac{\|x-y\|^2}{d^2}} W_l(\phi(x))W_l(\phi(y)) \right) \, dy \right) \phi_t(x) \, dx \\
&= -2 \int \left( \int \left( \frac{2(x-y)}{d^2} \cdot \nabla\phi(y) e^{-\frac{\|x-y\|^2}{d^2}} W_l(\phi(x))W_l(\phi(y)) \right) \, dy \right) \phi_t(x) \, dx \\
&\quad - 2 \int \left( \int \left( \nabla\phi(y) \cdot \nabla\phi(x) e^{-\frac{\|x-y\|^2}{d^2}} W_l'(\phi(x))W_l(\phi(y)) \right) \, dy \right) \phi_t(x) \, dx
\end{aligned} \tag{4.15}$$

where the second equality is simply integration by parts and the last equality is true by a change of variables. For the second subterm, a similar approach yields:

$$\begin{aligned}
\text{Term}_{2b} &= \\
&\iint \nabla\phi(x) \cdot \nabla\phi(y) e^{-\frac{\|x-y\|^2}{d^2}} [W_l'(\phi(x))W_l(\phi(y))\phi_t(x) + W_l(\phi(x))W_l'(\phi(y))\phi_t(y)] \, dx \, dy \\
&= \iint \nabla\phi(x) \cdot \nabla\phi(y) e^{-\frac{\|x-y\|^2}{d^2}} W_l'(\phi(x))W_l(\phi(y))\phi_t(x) \, dx \, dy \\
&\quad + \iint \nabla\phi(x) \cdot \nabla\phi(y) e^{-\frac{\|x-y\|^2}{d^2}} W_l(\phi(x))W_l'(\phi(y))\phi_t(y) \, dx \, dy \\
&= 2 \int \left( \int \nabla\phi(x) \cdot \nabla\phi(y) e^{-\frac{\|x-y\|^2}{d^2}} W_l'(\phi(x))W_l(\phi(y)) \, dy \right) \phi_t(x) \, dx
\end{aligned} \tag{4.16}$$

In this form both of the subterms can be combined together to get (with some cancellation):

$$\text{Term}_2 = \frac{4\mu}{d^2} \int \left( \int \left( (x-y) \cdot \nabla\phi(y) e^{-\frac{\|x-y\|^2}{d^2}} W_l(\phi(x))W_l(\phi(y)) \right) \, dy \right) \phi_t(x) \, dx \tag{4.17}$$

Each of the terms above separate the time derivative of  $\phi$  from the main part of the integrand. Factoring out  $\phi_t$  and combining all the computed terms yields:

$$\begin{aligned}
& \partial_t \bar{E}(\phi(t, -), c_1(t), c_2(t)) \\
&= - \int \left[ \operatorname{div} \left( \frac{\nabla \phi}{|\nabla \phi|} \right) + \gamma ((I - c_1)^2 - (I - c_2)^2) \right. \\
&\quad \left. + \frac{4\mu}{d^2} W_l(\phi) \int (x - y) \cdot \nabla \phi(y) e^{-\frac{\|x-y\|^2}{d^2}} W_l(\phi(y)) \, dy \right] \phi_t(x) \, dx \\
&= - \int \phi_t^2 \, dx \\
&\leq 0
\end{aligned} \tag{4.18}$$

since  $\phi$  satisfies Equation (4.9) and  $|\nabla \phi| = 1$  a.e. □

### 4.3 Numerical Method

The time step is set to  $dt = 0.5$  and the space step  $dx = 1$  (in the equations below,  $dx$  is dropped). To solve Equation (4.9) to steady state, an additive operator splitting scheme is used. In the following equations the function  $\phi$  is represented using vector notation for simplicity, where  $\phi^n$  is an approximation of  $\phi(x_i, t_n) = \phi(x_i, ndt)$ . The discretised equation is:

$$\begin{aligned}
\phi^{n+1} &= \frac{1}{2} \sum_p (I - 2dt A_p(\phi^n))^{-1} \left( \phi^n + dt \, \gamma ((I - c_2)^2 - (I - c_1)^2) \right. \\
&\quad \left. + 4 \frac{dt}{d^2} \mu W_l(\phi^n) \int_{\Omega} (x - y) \cdot \nabla \phi^n(y) e^{-\frac{\|x-y\|^2}{d^2}} W_l(\phi^n(y)) \, dy \right)
\end{aligned} \tag{4.19}$$

where  $p$  is the direction ( $x$  and  $y$ ) and the operator  $A_p := (a_{ij})$  is defined pixel-wise as follows:

$$a_{ij}(\phi) = \begin{cases} |\nabla \phi_i| \left( \frac{2}{|\nabla \phi_i| + |\nabla \phi_j|} \right) & \text{if } j \in \mathcal{N}(i) \\ -|\nabla \phi_i| \sum_{k \in \mathcal{N}(i)} \left( \frac{2}{|\nabla \phi_i| + |\nabla \phi_n|} \right) & \text{if } j = i \\ 0 & \text{otherwise} \end{cases} \tag{4.20}$$

where  $\mathcal{N}(i)$  is the neighbourhood around  $i$  (adjacent pixels). For each  $p$ , the inversion of the operator  $I - 2dtA_p$  can be done via Thomas algorithm [90], since the operator is a strictly diagonally dominant tridiagonal linear system. The resulting method has linear complexity at each time step. If one considers the method without the topological force, then it can be shown that the discretisation is unconditionally stable.

The dimensional generalisations are direct, for example, the 3-D discretised equation is below:

$$\begin{aligned} \phi^{n+1} = & \frac{1}{3} \sum_p (I - 3dtA_p(\phi^n))^{-1} (\phi^n + dt \gamma ((I - c_2)^2 - (I - c_1)^2) \\ & + 4 \frac{dt \mu}{d^2} W_l(\phi^n) \int_{\Omega} (x - y) \cdot \nabla \phi^n(y) e^{-\frac{\|x-y\|^2}{d^2}} W_l(\phi^n(y)) dy \end{aligned} \quad (4.21)$$

Extension essentially involves a double integral becoming a triple integral in the 3-D case (represented in both the 2-D and 3-D cases by ‘ $\int_{\Omega}$ ’ notation, where  $\Omega \subset \mathbb{R}^2$  or  $\mathbb{R}^3$ ). One example of segmentation using the proposed algorithm in 3 dimensions is provided.

Since the topological term must have the level set function close to a signed distance function, re-initialisation is required. Following the method in [91], the following systems are iterated to convergence:

$$\phi_{ij}^{n+1} = \begin{cases} \phi_{ij}^n - dt (\text{sign}(\phi_{ij}^0) |\phi_{ij}^n| - D_{ij}) & \text{if } (i, j) \in \Lambda \\ \phi_{ij}^n - dt \text{sign}(\phi_{ij}^0) G(\phi)_{ij} & \text{otherwise} \end{cases} \quad (4.22)$$

where the set  $\Lambda$  contains all  $(i, j)$  such that

$$\phi_{ij}^0 \phi_{i+1,j}^0 < 0, \phi_{ij}^0 \phi_{i,j+1}^0 < 0, \phi_{ij}^0 \phi_{i-1,j}^0 < 0, \text{ or } \phi_{ij}^0 \phi_{i,j-1}^0 < 0$$

In Equation (4.22),  $D_{ij}$  is the numerical distance to  $\mathcal{C}$  and can be calculated by:

$$D_{ij} = \frac{\phi_{ij}^0}{\sqrt{(D_x^0 \phi_{ij}^0)^2 + (D_y^0 \phi_{ij}^0)^2}} \quad (4.23)$$

The upwind discretised [92] re-initialisation equation is given by:

$$G(\phi)_{ij} = \begin{cases} \sqrt{\max((D_x^- \phi_{ij})_+^2, (D_x^+ \phi_{ij})_-^2) + \max((D_y^- \phi_{ij})_+^2, (D_y^+ \phi_{ij})_-^2)} - 1 & \text{if } \phi_{ij} > 0 \\ \sqrt{\max((D_x^- \phi_{ij})_-^2, (D_x^+ \phi_{ij})_+^2) + \max((D_y^- \phi_{ij})_-^2, (D_y^+ \phi_{ij})_+^2)} - 1 & \text{if } \phi_{ij} < 0 \end{cases} \quad (4.24)$$

where  $D^0$ ,  $D^+$ , and  $D^-$  are the central, forward, and backward differences. It should be noted that from [91], it is known that this method's error is independent of the number of iterations, therefore the re-initialisation process does not affect the location of the curve. This is particularly important for the topology preservation, since the drifting caused by some re-initialisation algorithms could affect the results.

## 4.4 Experiments & Results

The method is tested on several synthetic and real images containing various features. A 3 dimensional result is provided using the current algorithm as well as a possible extension for textured images. For the noisy images presented here, the noise variance is reported as the percentage of the maximum intensity value of the given image. In each example, the choice of the initial location of phi was chosen to be close to boundary of the object such as to achieve a faster segmentation.

### 4.4.1 Two dimensional examples

In Figure 4.1 the algorithm is tested on a synthetic image containing two black discs on a white background. Noise with 70% variance is added to test the algorithm's ability to preserve topology with highly corrupt images. As the curve evolves, it first captures part of the boundary of the discs then shrinks inward along the edges. The steady state solution resembles a bent dumbbell and is homeomorphic to the initial curve.

For comparison with existing methods, the algorithm is tested on the Hand image in Figure 4.2. As the curve grows outward along each digit, each segment evolves separately. The steady state solution contains one continuous curve. Similar

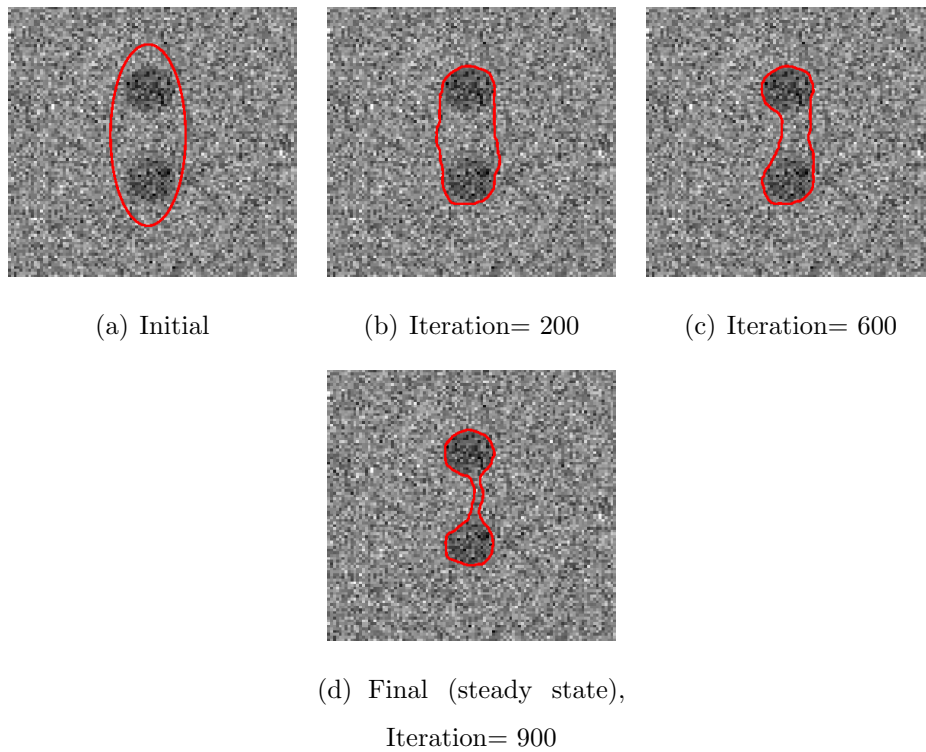


**Figure 4.1:** The proposed algorithm applied to the two discs example with 70% noise. The model parameters are set to  $\gamma = 0.195$  and  $\mu = 0.4$ .

results can be found in [7] and in [3] for the noise-free case only. The addition of the large amount of noise (15% variance) further connects the digits, making the segmentation more complicated than in the noise-free case.

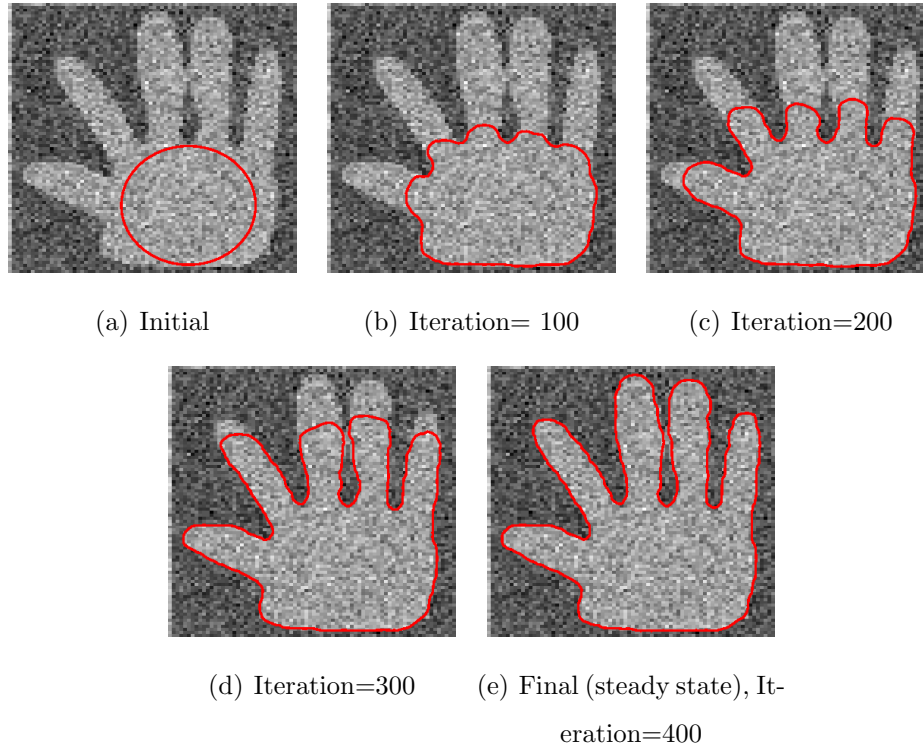


**Figure 4.2:** Proposed algorithm applied to the Hand image with 15% noise. The model parameters are set to  $\gamma = 2.2$  and  $\mu = 0.5$ . Image source: obtained from authors of [3]

In Figure 4.3, the algorithm is tested on a photograph of a bear. The image is highly textured, which can cause issues with gradient-based edge detectors. The curve locates the boundary of the bear without capturing the nose or grass (whose mean is closer to the background).

For the next three examples, the algorithm is tested on MRI scans of a human brain (in the presence of Gaussian noise). In the first image (Figure 4.4), the curve quickly locates the boundary of the brain (within 90 iterations), and continues to grow inward to refine the detection. In the other two images (Figures 4.5 and 4.6), with the choice of initialisation, the curve grows along the boundary of the object as well as shrink within the small regions. The steady state solutions are all home-

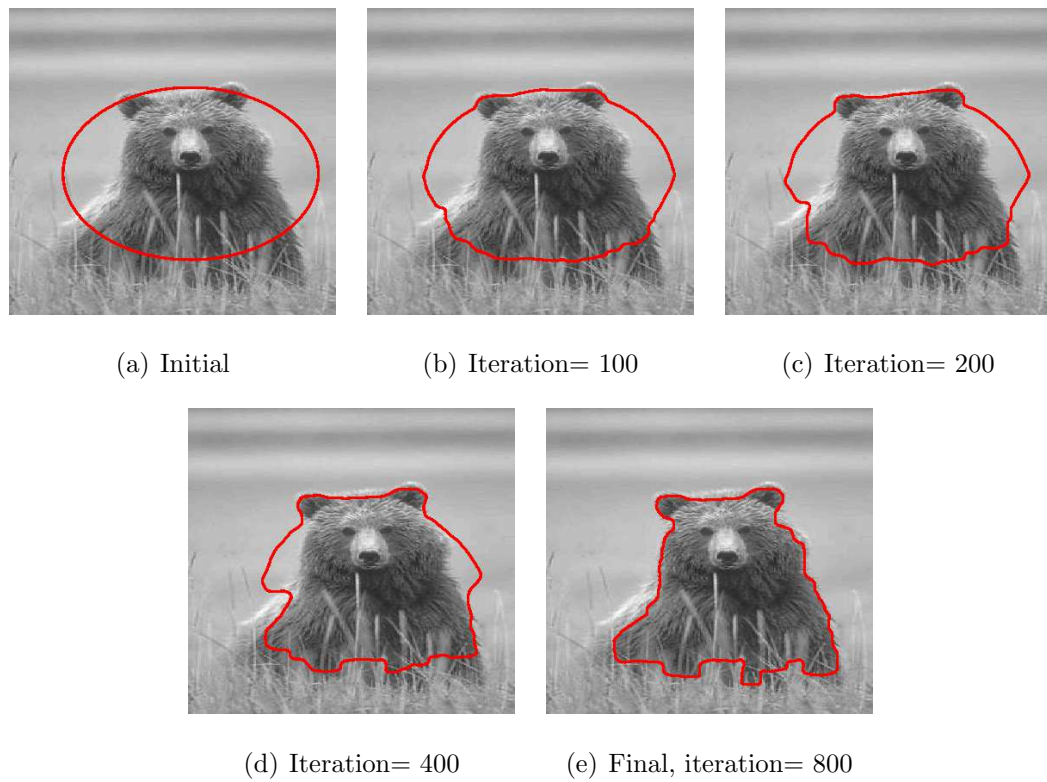


**Figure 4.3:** Proposed algorithm applied to the highly textured Bear photograph. The model parameters are set to  $\gamma = 3$  and  $\mu = 0.8$ . Image source: Berkeley Image Database

omorphous to the initial condition as well as contain the fine details of the detected object.

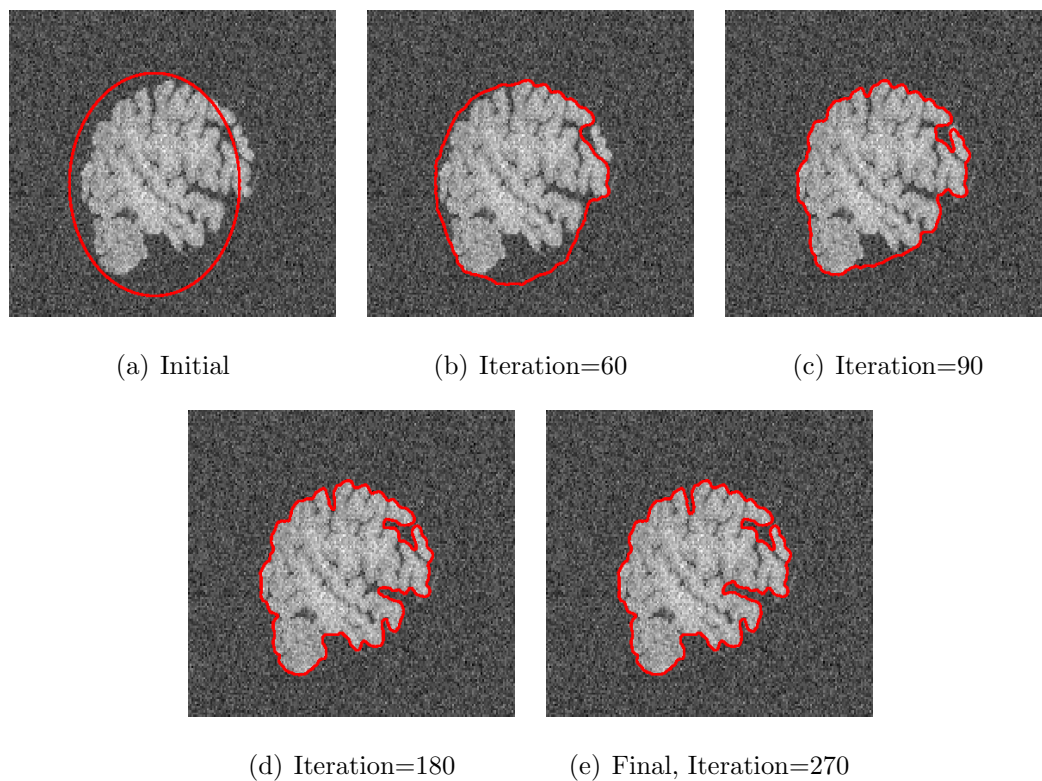


**Figure 4.4:** Proposed algorithm applied to an MRI scan of a brain. The model parameters are set to  $\gamma = 1.45$  and  $\mu = 0.5$ . Image source: Laboratory of Neuro Imaging, University of Southern California

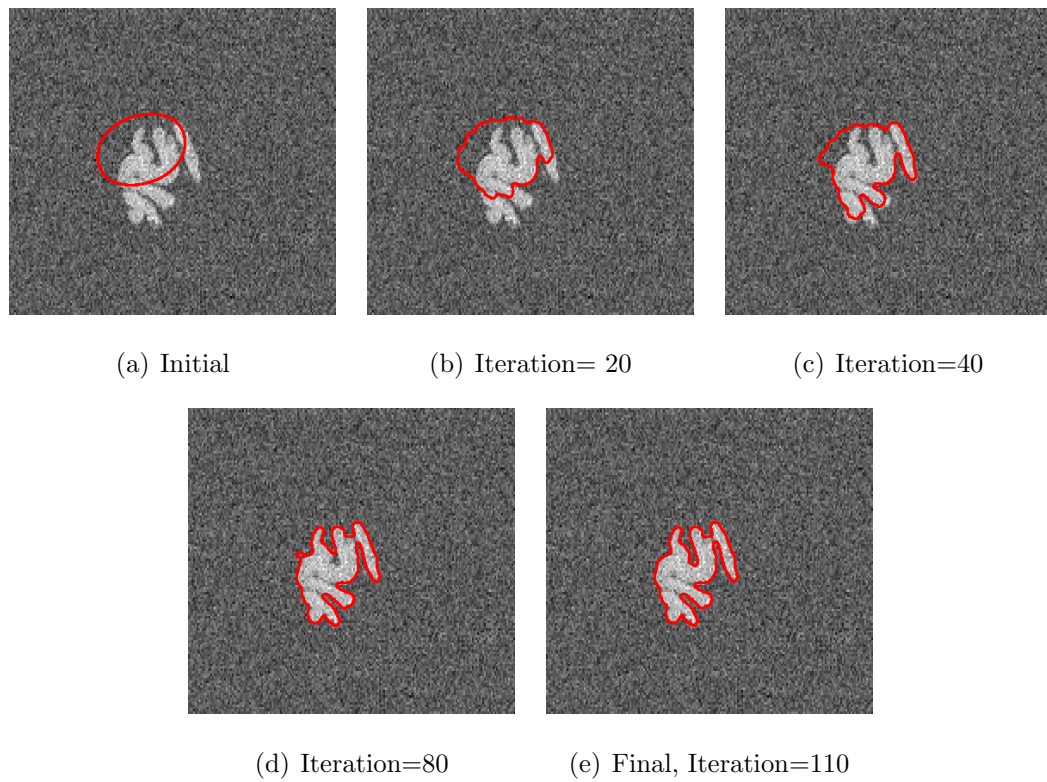


**Figure 4.5:** Proposed algorithm applied to an MRI scan of a brain. The model parameters are set to  $\gamma = 2$  and  $\mu = 1.2$ .

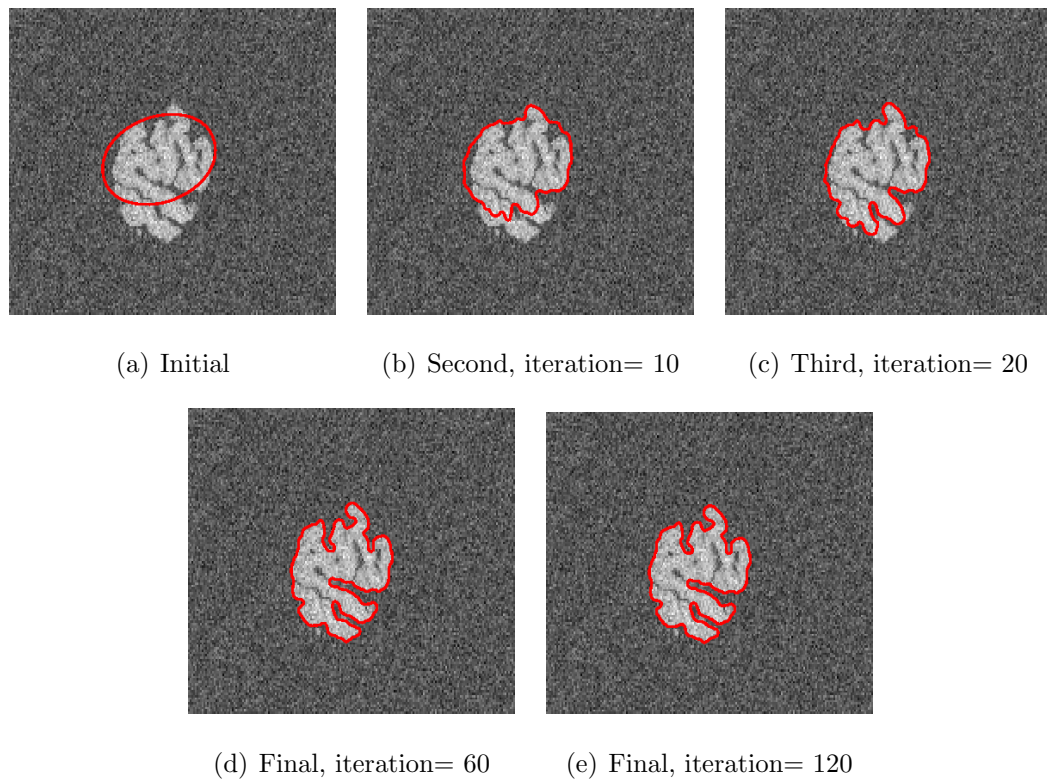


**Figure 4.6:** Proposed algorithm applied to an MRI scan of a brain. The model parameters are set to  $\gamma = 2$  and  $\mu = 2$ .

### 4.4.2 Three dimensional examples

As a proof of concept, a 3-D example using an MRI brain scan is provided in Figure 4.7. By monitoring the Euler characteristic of the zero level set function, it was numerically verified that the structure is preserved. From the two different perspectives of the steady state solution displayed in Figure 4.7, the finer boundary structures can be seen as well as the crevasses. In the 3D case, to accelerate the convergence to steady state, the term  $\eta(t)|\nabla\phi|$  is added to the evolution equation and set  $\eta(t) = 0.05$  for  $t < 400$  and  $\eta(t) = 0$  otherwise.

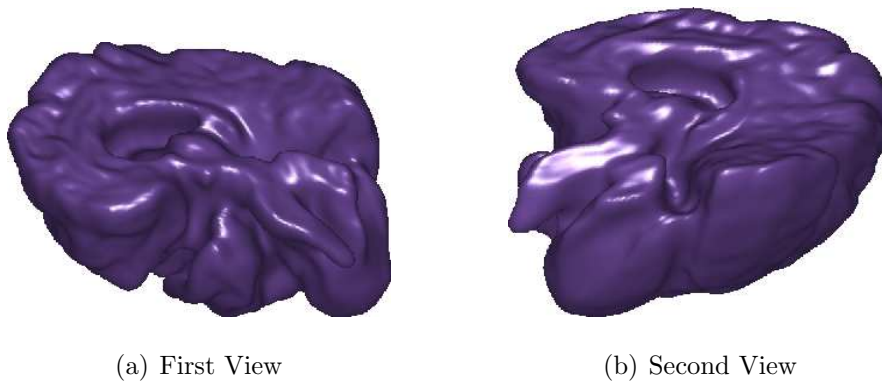


**Figure 4.7:** Proposed algorithm applied to a 3-D MRI scan of a brain. The model parameters are set to  $\gamma = 1e - 06$  and  $\mu = 0.2$ .

### 4.4.3 Extensions

The regional terms used in Equation (4.5) fit the data to the means in each region; however, it is possible to fit the data to any probabilistic model. For textured images, the authors of [93] proposed modeling the regional intensity values as sampled from a Gaussian distribution. Using the regional term from [93], the proposed model can be extended to the following:

$$\begin{aligned} \min_{\phi, c_1, c_2, \sigma_1, \sigma_2} E_G(\phi, c_1, c_2, \sigma_1, \sigma_2) &= \int_{\Omega} \delta(\phi) |\nabla \phi| + \mu T(\phi) \\ &+ \gamma \int_{\Omega} \left( \log(\sigma_1) + \frac{(I - c_1)^2}{\sigma_1} \right) H(\phi) + \left( \log(\sigma_2) + \frac{(I - c_2)^2}{\sigma_2} \right) H(-\phi) dx \end{aligned} \quad (4.25)$$

As a proof of concept, this extension is tested on an image of a squirrel in Figure 4.8. In order to avoid local minima, a balloon forcing term with coefficient equal to 0.12 is included. Since the foreground and background texture are seemingly random, modeling their intensity values as Gaussian with different parameters seems to capture the correct boundary.

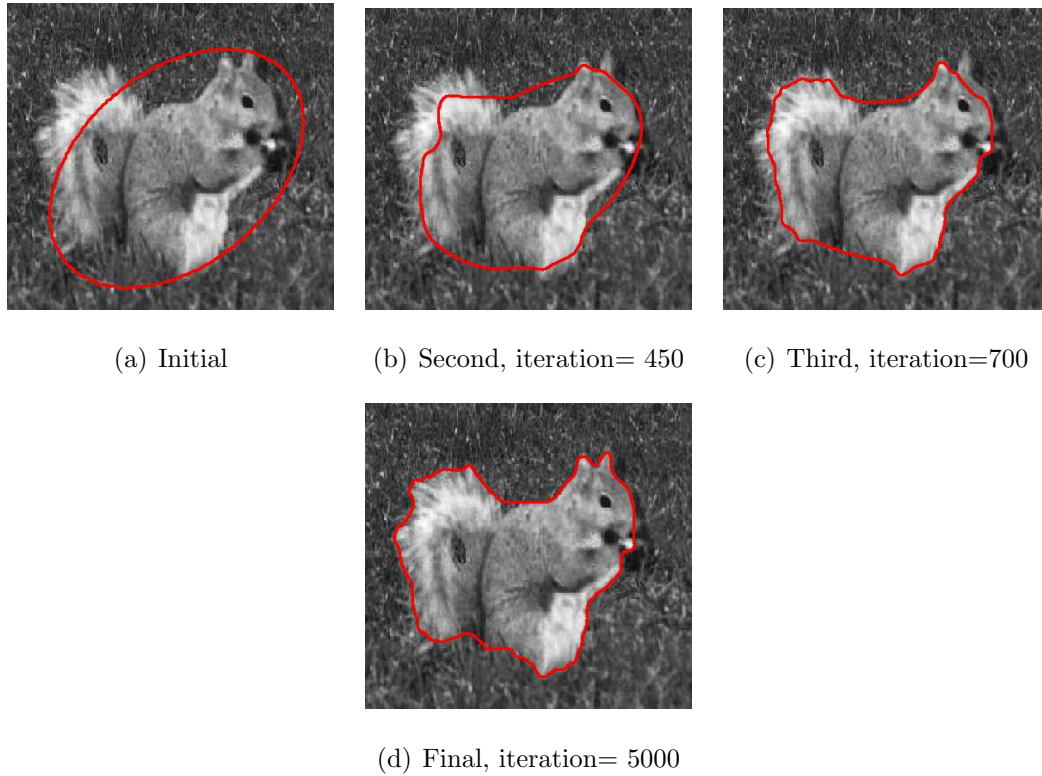


**Figure 4.8:** Proposed algorithm applied to an image of a squirrel. The model parameters are set to  $\gamma = 2.8e - 05$  and  $\mu = 0.3$ . Image source: Image was obtained from internet.

## 4.5 Comparison with other models

To examine the performance of the proposed method against previously published models some examples are presented below. The comparison models are the CV model [4], the Topology preserving model proposed in [7] and a global segmentation model as proposed in [8, 9].

### 4.5.1 The CV model

The first comparison model is the CV model [4]. In Figure 4.9(b), it can be seen that the solution of the CV model contains a hole and therefore fails to achieve an accurate segmentation.

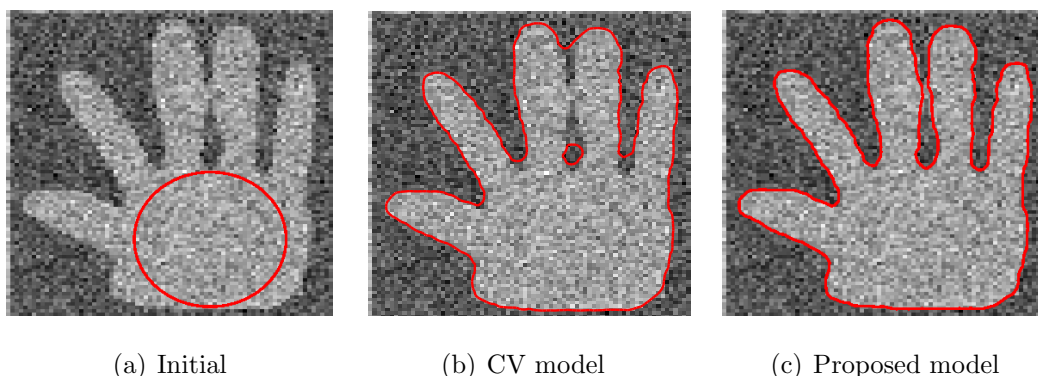


**Figure 4.9:** Comparison between proposed model and CV model [4]. Parameters for CV model:  $\gamma = 2.2$ , iterations = 1500. Parameters for Proposed model:  $\gamma = 2.2$  and  $\mu = 0.5$ .

In Figure 4.10, it can be observed that the final steady state solution of the CV model achieves a segmentation very similar to that achieved by the proposed model, however as can be observed in 4.10(b), at an intermediate result, the topology of the curve is not preserved.

Figure 4.11 shows an example of a pulmonary nodule as imaged by a Computed Tomography scan. Next to the nodule (which contains the manually inserted initialisation contour) are structures corresponding to blood vessels. The goal of this segmentation operation is to delineate only the structure corresponding to the

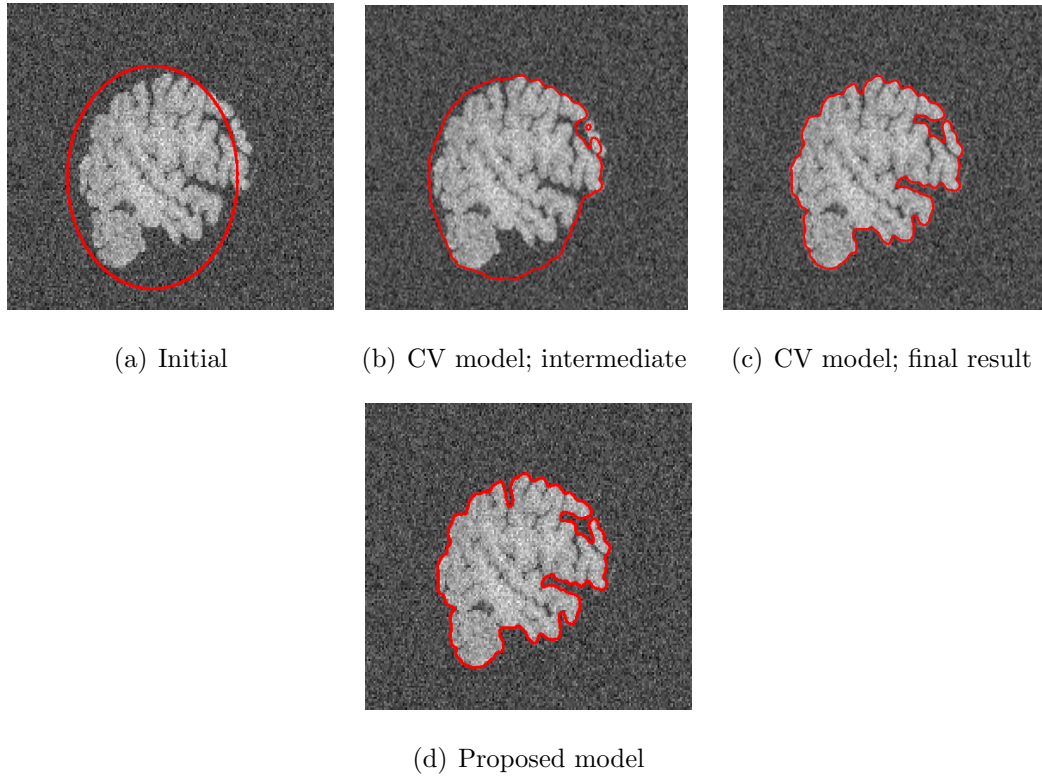


**Figure 4.10:** Comparison between proposed model and CV model [4]  $\gamma = 2.2$ , iterations = 1500. Parameters for Proposed model:  $\gamma = 1.45$  and  $\mu = 0.5$

nodule. In Figure 4.11(b) the CV model finds the structures corresponding to the brightest intensity, while the proposed model captures the boundary of the nodule as shown in 4.11(c) .

## 4.5.2 Topology Preserving Model

In this section the proposed method is compared to the method of [7]. In Figure 4.12(a) it can be observed that the contour used for initialisation is different to that of 4.9(b), this is the case because the method [7] relies on the presence of edges to locate the object boundaries, using the same initialisation as in 4.9(a) would result in insufficient attraction force to move the contour. It can be observed from the result in 4.12(b) that the method preserves topology but fails to accurately capture the outline of the hand. The proposed method accurately captures the boundary of

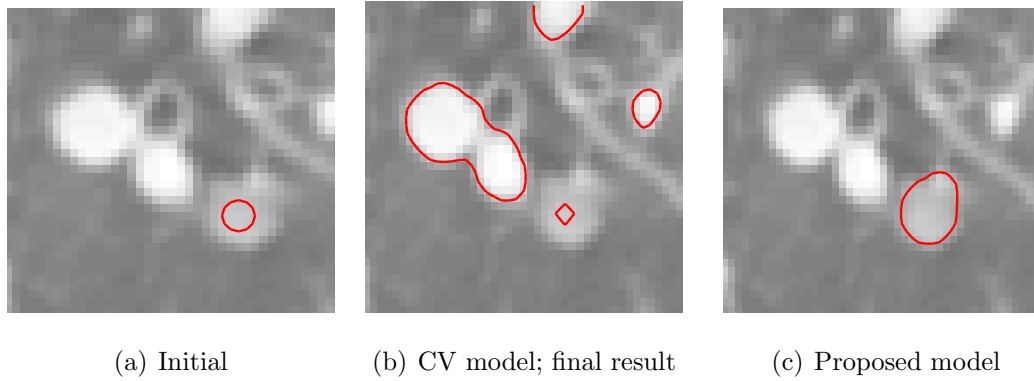


**Figure 4.11:** Comparison between proposed model and CV model [4]  $\gamma = 20$ , iterations = 300. Parameters for Proposed model:  $\gamma = 10$ ,  $\mu = -1$ , iterations = 700. Image source: Lung Image Consortium (LIDC) Database [5, 6]

the hand as shown in 4.12(c).

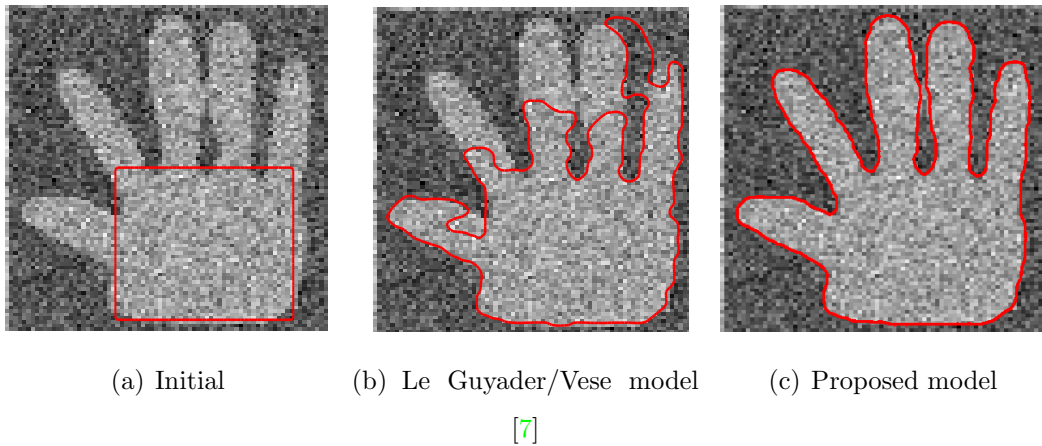


**Figure 4.12:** Comparison between proposed model and Le Guyader/Vese model [7]. Parameters for Le Guyader/Vese model:  $\mu = 0.64$ , iterations = 1500. Parameters for Proposed model:  $\gamma = 1.45$  and  $\mu = 0.5$

This result is mirrored in Figures 4.13(b) where it can be observed that the method of [7] again fails to accurately capture the boundary of the brain. Also in 4.14(b), where the absence of a sharp edge results in the method of [7], failing to accurately capture the boundary of the nodule. In each case, the lack of a clear edge

representing the boundary disrupts the method.

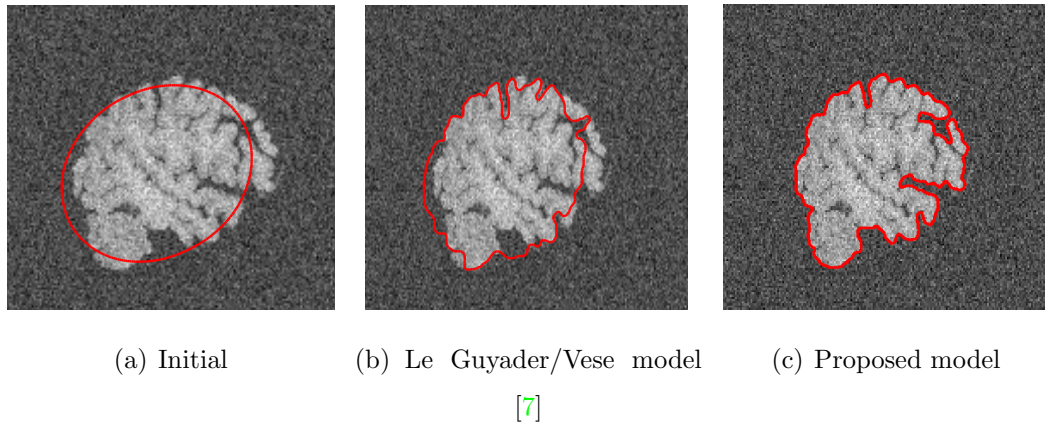


**Figure 4.13:** Comparison between proposed model and Le Guyader/Vese model [7]. Parameters for Le Guyader/Vese model:  $\mu = -0.5$ , iterations = 1000. Parameters for Proposed model:  $\gamma = 2.2$  and  $\mu = 0.5$

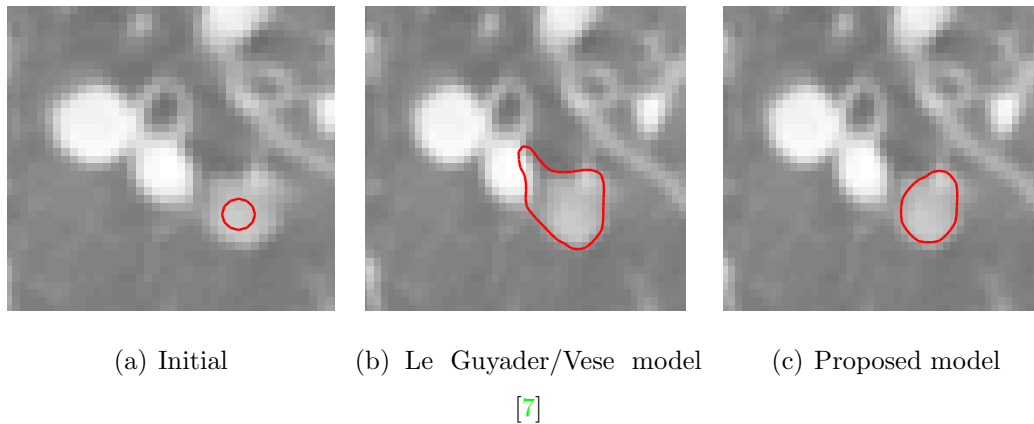


**Figure 4.14:** Comparison between proposed model and Le Guyader/Vese model [7]. Parameters for Le Guyader/Vese model:  $\mu = -0.5$ , iterations = 1000. Parameters for Proposed model:  $\gamma = 10$ ,  $\mu = -1$ , iterations = 700

### 4.5.3 Comparison with Global CV method

In the following experiments, the proposed method was compared to a global segmentation method proposed in [8, 9]. In Figure 4.15(a) it can be observed that

the global method fails to preserve topology in the region between the two middle fingers.

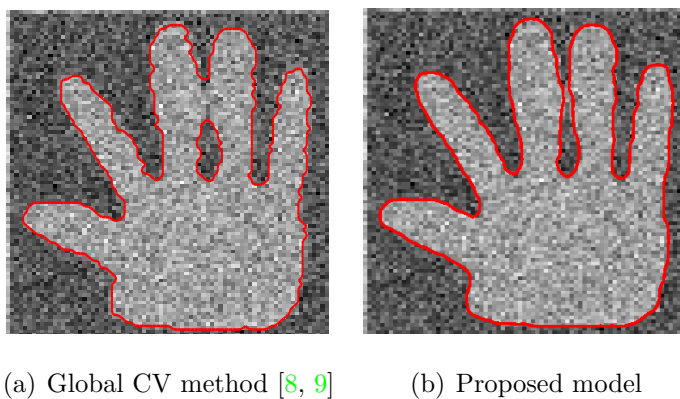


**Figure 4.15:** Comparison between proposed model and Global CV method [8, 9]. Parameters for Global CV method:  $\gamma = 0.18, iter300$ . Parameters for Proposed model:  $\gamma = 2.2$  and  $\mu = 0.5$

In Figure 4.16 it can be observed that again the global method again fails to preserve topology (with a hole appearing in 4.16(a)).

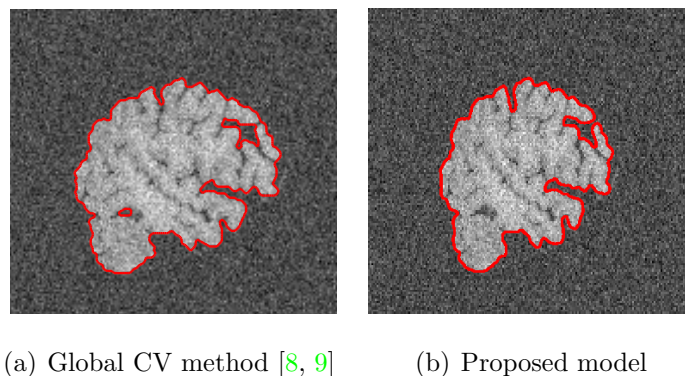
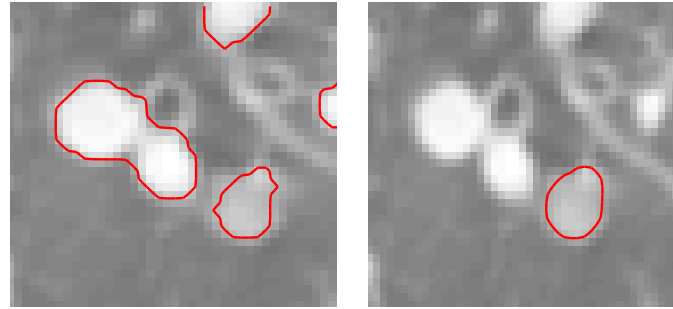


**Figure 4.16:** Comparison between proposed model and Global CV method [8, 9]. Parameters for Global CV method:  $\gamma = 0.25, iterations1000$ . Parameters for Proposed model:  $\gamma = 2.2$  and  $\mu = 0.5$

In Figure 4.17 the global method can be seen to partition the image into 2 homogeneous regions, which includes the nodule region and the blood vessels, failing

to achieve the objective of delineating only the nodule region.



(a) Global CV method [8, 9]

(b) Proposed model

**Figure 4.17:** Comparison between proposed model and Global CV method [8, 9]. Parameters for Global CV method:  $\gamma = 0.1$ , iterations = 300 . Parameters for Proposed model:  $\gamma = 10$ ,  $\mu = -1$ , iterations = 700

To investigate sensitivity to parameter change, 4 images were selected and  $\mu$  and  $\gamma$  were varied by  $\pm 5\%$  (*i.e.* each time one parameter was held constant while the other was varied). The images included the discs, the image of hand with noise, the brain image 4.5 and the image of the bear. Varying  $\mu$  and  $\gamma$  did not effect topology preservation or segmentation quality in the discs image, the brain image or the bear image. Topology preservation was affected however, in the case of the hand image, with the contour merging in the region of the third and fourth fingers. It should be noted that this image presents particular challenges from the perspective of topology preservation since the region between the third and fourth fingers is largely undifferentiated with respect mean intensity, which means that the data-fidelity force will therefore encourage the contour to include this entire region in the foreground segmentation. This experiment shows that the model lacks robustness to perturbations in parameter selection. However, as shown from the experiments on the whole, a suitable parameter configuration can be found to segment these difficult cases. In particular, for each application, a suitable parameter configuration needs to be selected to deal with the particular characteristics of the object to be segmented.

## 4.6 Conclusion

In the current section a region based topology preserving active contours model is proposed. Unlike previous work on topology preserving segmentation, the method is not dependent on an edge detector for pre-segmenting the image. Also, as demonstrated in the results, the method handles noisy and textured images well. For further applications, the model can easily be extended by either including a geodesic length term in place of the standard length or by changing the regional forces.

In the next chapter, a third aspect of segmentation robustness is investigated, in this case, robustness with respect to diverse object geometry. The following chapter proposes an approach for lung nodule detection based on a 3-D global segmentation method and mean curvature smoothing.

# 5

## Lung nodule candidate detection

### 5.1 Introduction

In the preceding chapters, two algorithms, each addressing different aspects of segmentation robustness were proposed. In this chapter, segmentation robustness with respect to diverse geometrical features of the target object will be investigated. The specific focus is the detection and segmentation task of pulmonary nodules. The first stage in computer aided pulmonary nodule detection schemes is a candidate detection step designed to provide a simplified representation of the lung anatomy, such that features like the chest wall, and large airways are removed, leaving only data which has greater potential to be a nodule. Nodules that are connected to blood vessels tend to be characterised by irregular geometrical features which can result in their remaining undetected by rule-based classifiers relying only local image

metrics. In this chapter, a novel approach for lung nodule candidate detection is proposed based on the application of global segmentation methods combined with mean curvature minimisation and simple rule-based filtering.

Every year, deaths due to lung cancer outnumber those related to other types of cancers around the world [94]. The most important indicator of the disease is the presence of pulmonary lung nodules [95, 96], the early detection of which is essential to increase the chances of successful treatment [97].

The most popular modality for imaging the thorax is Computed Tomography (CT) [95]. Currently the most common method for quantifying lesion development using CT is through manual detection and measurement of the nodule diameter. In addition to being error-prone and subjective [98], this technique is limiting because a 1-D measure is used to describe a 3-D non-symmetric, non-spherical object. At the same time, manually characterising the tumor using all of the 3-D data available would be extremely time-consuming [99].

Numerous studies have shown that Computer Aided Detection (CAD) systems can effectively assist radiologists in detecting lung nodules [100, 101, 102, 103, 104, 105]. In studies by Martin et al. [106] and Lee et al. [107] it was shown that the sensitivity of CAD systems for detecting small, isolated nodules was greater than achieved by a radiologist but that this sensitivity was lower than that of a radiologist for nodules with vascular attachment.

In [108] a nodule detection scheme is presented in which the first step is lung segmentation. This is achieved by thresholding the lung volume on a frame-by-frame basis. Noting that the volume histogram displays 2 prominent peaks, corresponding respectively to pixels inside the lungs and to pixels representing soft tissue and bone, for each frame, the authors in [108] select as a threshold the broad minimum which exists between these peaks. The next step is a corrective stage which has the purpose of excluding structures such as airways and including juxta-pleura nodules (*i.e.* lung wall-connected) excluded by the thresholding step. To re-include juxta-pleura nodules they apply morphological opening and to exclude the airways, they apply a 2-D region growing technique. This is followed by a region-labeling technique

designed to group contiguous structures in three dimensions. Finally, to obtain the candidacy mask the authors apply a volume threshold to these contiguous structures.

In Tan *et al.* [109], the first step is lung segmentation performed using a similar technique as proposed in [108]. In the next step, the authors compute the Divergence of Normalised Gradient (DNG) of the volume to estimate the center of nodules, they then use this in combination with nodule and vessel enhancement filters proposed in [110, 111] to detect nodule candidates. To obtain the nodule candidacy mask, the authors apply a different thresholding/filtering combination to each nodule type; *i.e.* isolated, juxtavascular (or vessel-connected), and juxtapleural nodules. For example for isolated nodules they apply a threshold of -600 Hounsfield Units (a quantitative scale for describing radiodensity) to the output of the lung segmentation, they then apply the nodule enhancement filter to this result. Subsequently another (gray level) threshold of 6 is applied to this nodule enhanced image. The output of this system is then combined with the result of the DNG method. Finally to this result, another volume threshold of 9 voxels is applied. The outputs of this last step are taken to be the isolated nodule candidates. The steps to extract both juxtavascular and juxtapleural nodules are similar to those outlined above and similarly involve a specific set of threshold parameters. The result of the procedure described above is multiple thresholded volumes consisting of nodule clusters corresponding to isolated, juxtavascular, and juxtapleural nodules. A logical OR-ing operation is then carried out to consolidate the results in one volume.

In [112], the detection scheme starts with the generation of a lung mask in a scheme similar to that proposed in [108]. The authors then apply multi-level thresholding [108] to the remainder of the volume to produce multiple 3-D lung nodule candidate masks. To remove vessels, they apply a morphological opening operation with specific radius to each mask, which is followed by another rule based filter (with sphericity and area criteria) to remove false positives. The final nodule mask is generated by logically OR-ing these intermediate masks. The thresholds as well as the radii of the structuring elements are determined empirically.

In [113] the authors apply a 2-D filter to each axial slice image to highlight

structures similar to discs or half-discs. To reduce the false positives, six 3-D features based on size, compactness, sphericity and gradient-intensity, are calculated for each candidate. The authors use an Support Vector Machine (SVM) to classify the data.

In consecutive CT slices, blood vessels often appear as circular objects closely resembling nodules. Using this fact, the authors in [114] proposed a scheme to generate multiple 2-D images based on different spherical viewpoints of each 3-D nodule candidate. The authors show that these different viewpoints allow the noncircular linear structure of components corresponding to vessels to be more easily identified. The authors then combined features generated from these image features with 3-D features such as diameter and compactness [115]. In the final step, they employ a linear classifier [115, 116] to classify the results.

Murphy *et al.* [117] proposed a detection scheme that uses shape index and curvedness to detect nodule candidates. Using these features the authors filtered the datasets to produce seed points in areas of high filter response and expanded these points using hysteresis thresholding to produce region clusters. To reduce false positives, they applied two consecutive classification steps using k-Nearest-Neighbour. In analysing the results according to nodule size, the authors reported that for nodules with a diameter greater than 8.6mm, the sensitivity rate was under 45%. These findings highlight the difficulty in detecting nodules characterised by irregular shapes by means of local image features alone, a fact the authors themselves acknowledged.

The purpose of this chapter is to present an algorithm for the detection of the lung lobe interior with particular emphasis on detecting nodules with vascular attachment. The output of the algorithm is a set of regions that can be analysed further, either manually or using an advanced classifier to determine whether they represent a true nodule. As can be observed in the previous review, several of the proposed schemes make use of a combination of multi-thresholding methods as well as spherical shape filters to isolate nodules [108, 112, 114, 109], however as noted in [118], when nodules are connected to other high density structures, separating them with intensity thresholds alone is in most cases, impossible. In the same way,

incorporating spherical constraints early into a detection scheme can be limiting, especially in the case of nodules exhibiting a high degree of vascular attachment and which therefore represent quite a complex geometry. In this chapter, a novel approach for lung nodule candidate detection is proposed based on the application of global segmentation methods combined with mean curvature minimisation and simple rule-based filtering. Unlike the previously reviewed approaches which rely on successive filtering steps, the proposed approach makes use of sophisticated variational models [4] and a continuous maximum flow algorithm to obtain the solutions numerically. The entire algorithm consists of several successive steps that are described in detail below.

## 5.2 Methodology

A challenge for obtaining a good segmentation is that many objects inside the lung have very similar intensity distributions to the nodule, in particular blood vessels and the chest wall. This makes it difficult to separate the intensity profile of the nodule from other tissue classes using a multiregion segmentation framework. In this context, an algorithm is developed in which a two region segmentation model is first used to capture the nodules, chest wall and other objects of similar intensity in a foreground region, and the air and remaining objects in a background region. The algorithm then attempts to separate the potential nodules from the rest of the tissue that were captured in the foreground region. This concerns mainly the chest wall and surrounding blood vessels, which is handled in two separate steps.

### 5.2.1 Computation of a Global 2-phase Segmentation output

The first step of the proposed method aims to extract the chest wall, nodules, blood vessels and other tissue of similar intensity values into one region using the active contour model with two regions [4]. The methodology applied here involves

computing a global minimum to this model using the Continuous Maximum Flow (CMF) scheme. The details of the CMF algorithm have been described previously in section 3.3.1.1.

In simple cases, the two region segmentation algorithm may separate out the nodule as a single connected component. In more difficult scenarios, the nodule region may be connected to either the chest wall or surrounding blood vessels.

## 5.2.2 Chest wall removal

The 3-D global segmentation described in the previous section essentially segments the volume into 2 classes: tissue and air. The next step is to separate the chest wall from the structures that are interior to the lung. This is done using a combination of connected component labeling as well as morphological opening.

First a connected component labeling operation is used to identify the largest component in the volume. This step identifies the chest wall together with additional structures connected via vessels to the chest wall. A correction step consisting of a morphological opening operation [119] is used to remove these additional structures. The result of the morphological opening operation, which corresponds to the chest wall is then subtracted from the 3-D segmentation result leaving just structures in the interior lung lobe.

## 5.2.3 Nodule Separation

The issue of separating the nodules from surrounding tissue is addressed by applying mean curvature minimisation using the method of Merriman-Bence-Osher (MBO) [120] to the output of the segmentation. The effect of this method is to ‘simplify’ the underlying structures of the nodule candidates (or vessels); essentially, through the diffusion process, a spiculated mass will become smoother/more spherical, while structures connected to each other by (relatively) thin connections will be separated.

Let  $\phi^0$  denote the binary function indicating the segmentation result after removal of the chest wall. The MBO algorithm applied to  $\phi^0$  is a discrete time ap-

proximation of mean curvature motion and can be described as follows:

For  $k = 1, 2, \dots, K$

$$\psi = G_\sigma * \phi^k \quad (5.1)$$

$$\phi^{k+1}(x) = \begin{cases} 1, & \text{if } \psi(x) \geq 0.5 \\ 0, & \text{if } \psi(x) < 0.5 \end{cases} . \quad (5.2)$$

Equation (5.1) above is time step of the heat equation, which is equivalent to convolution with the Gaussian kernel  $G_\sigma$ , and can be solved efficiently by the Fast Fourier Transform (FFT). After each MBO iteration, a rule based classifier is applied to each connected component of the result, to check if the component is a nodule candidate. The rule based classifier is described in the next section. The number of iterations  $K$  is set in advance to prevent too much smoothing.

#### 5.2.4 Rule Based Classifier

The effect of the MBO step is to make a spiculated mass smoother and more spherical in shape, which allows structures to be identified as potential nodules using simple geometric features. The final step in determining nodule candidacy is the application of a simple rule-based classifier, in which candidacy is determined by the following features: area, volume, circularity, elongation.

The following definitions are used for each feature: assuming that the nodules are spherical, the area and volume of the nodule candidates can be computed using the standard formulae: Area =  $\pi r^2$ ; Volume =  $3/4\pi r^3$ .

Elongation is defined simply as the ratio of the largest dimension in the x,y or z direction over the minimum dimension in any direction i.e.

$$\text{Elongation} = \frac{\max([x\text{Length}, y\text{Length}, z\text{Length}])}{\min([x\text{Length}, y\text{Length}, z\text{Length}])}$$

Circularity is defined as:

$$\text{Circularity} = \frac{4\pi \text{Area}}{\text{Perimeter}^2}$$

In the above equation, ‘Area’ and ‘Perimeter’ are calculated using the median slice of the connected component. The respective maximum and minimum thresholds for each feature are listed in section 5.3. This step closely follows the method proposed by Choi et al. in [121] and further details can be found therein.

### 5.2.5 Summary of the Complete Algorithm

In summary, the proposed nodule candidacy detection algorithm comprises the following steps; first a global 2 phase segmentation is performed, which segments the volume into 2 classes: tissue and air. The next step is to further segment the tissue into chest wall and interior lobe data; done using morphological techniques. The main part of the proposed scheme is the use of mean curvature smoothing to isolate vascular connected nodules. The detection step is carried out by applying the rule-based classifier once before the MBO smoothing and subsequently on each connected component after each MBO iteration. The final lung nodule candidacy mask is obtained by logically OR-ing all of the intermediate detection results. The entire algorithm is outlined below.

Input: 3-D CT lung image

1. Obtain two region segmentation by global minimisation of (3.16).
2. Remove chest wall from the segmentation result as described in section 5.2.2 and let  $\phi^0$  denote indicator function of the remaining region.
3. Apply rule based classifier to each remaining connected component as in section 5.2.4
  - Store positive connected components as potential nodule candidates
4. For iterations  $k=1, \dots, K$ :
  - Apply one step of MBO scheme (5.1), (5.2) to obtain  $\phi^k$ .
  - Apply rule based classifier on each component of  $\phi^k$ . If positive: store connected component as potential nodule candidate and for all points  $x$

inside connected component and set indicator function  $\phi^k(x) = 0$ .

Output: Set of nodule candidates, represented by a binary function.

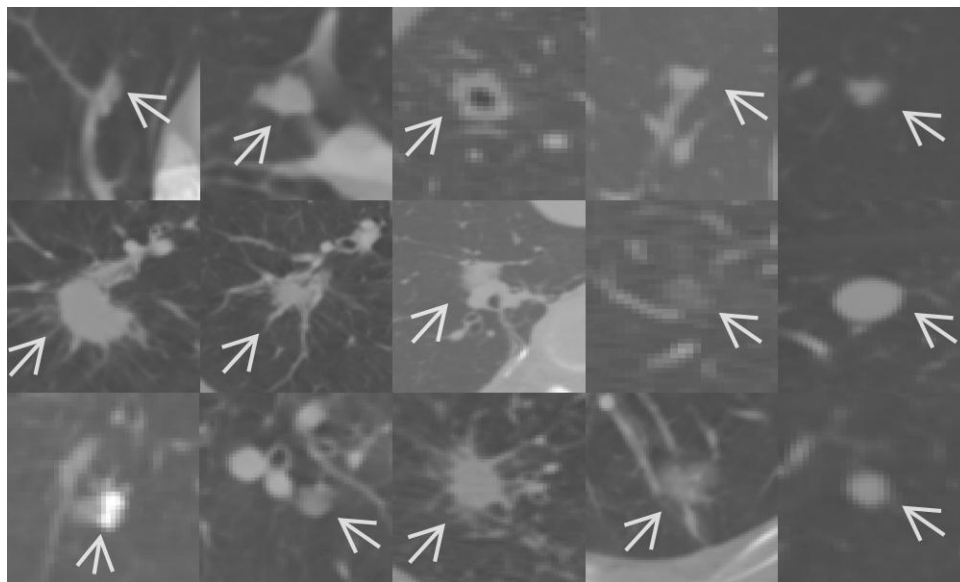


**Figure 5.1:** Examples of nodules included in the test set. The majority of the nodules in the test set exhibit some degree of attachment to surrounding vascular tissue; isolated nodules were also included (as can be observed in the rightmost column). The arrowheads point to the location of the nodule in each case.

### 5.3 Experiments

The test data used in the experiments was selected from the Lung Image Consortium (LIDC) Database [5, 6] which is a publicly and freely available resource available for download<sup>1</sup>. The data in LIDC database was collected from five institutions from across the United States using a range of scanner manufacturers and models. During the data collection process it was attempted to collect no more than one scan per patient so that data would not correlated, also none of the scans were performed

---

<sup>1</sup><http://ncia.nci.nih.gov/>

specifically for inclusion in the database in order to have a varied set of technical parameters represented.

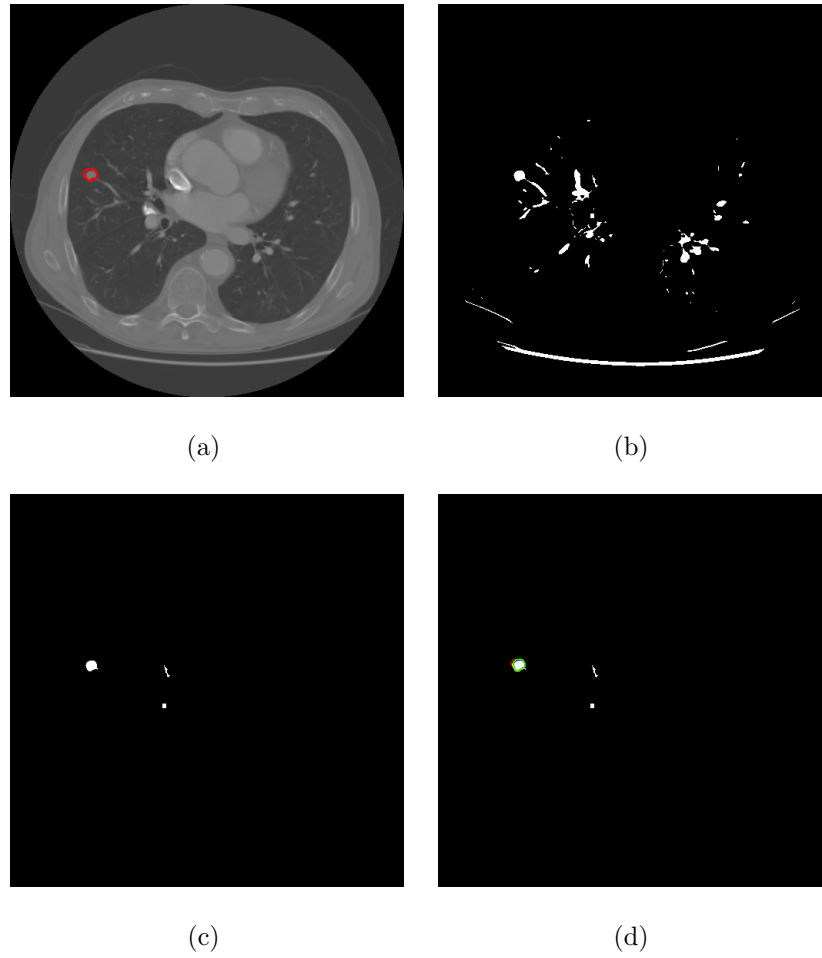
For the experiments a test set consisting of 16 dataset volumes was used which included a total of 27 nodules. The test set included nodules exhibiting vascular attachment as well as those isolated from surround structures. The standard of reference were the expert annotations provided with this database.

Figure 5.1 shows examples of nodules in the test set. Figure 5.2 highlights the normal operation of the rule based classifier. It can be observed in Figure 5.2(b) that the nodule in question is isolated from other structures in the lung after application of the first segmentation step and the rule-based classifier easily selects the nodule, as shown in 5.2(c). A set of results from the algorithm are demonstrated in Figure 5.3, which displays 6 sample slices from the test set. In contrast to Figure 5.2(a), each nodule in Figure 5.3 exhibits connectivity with surrounding tissue. The first segmentation step is unable to sufficiently separate the nodules from surrounding tissue in these cases due to their similar intensity profiles. Application of the MBO scheme has the effect of either removing fine structures attached to the nodule, such as fine blood vessels, or splitting the regions into two or more geometrically simpler components, one of which encompasses the nodule region.

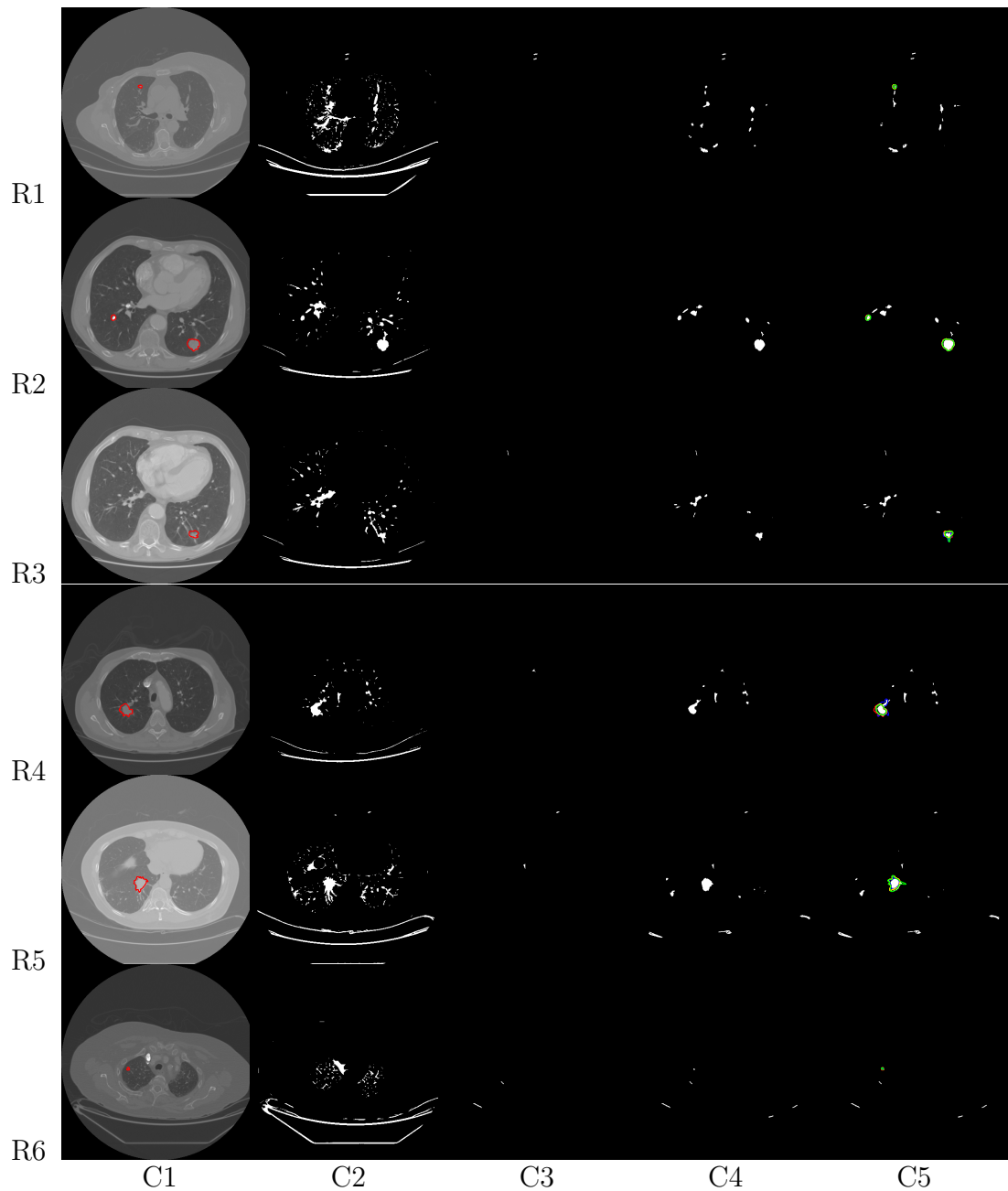
In Figures 5.4 and 5.5, two examples of nodules are shown which in 5.4(a) and 5.5(a) appear to be isolated. Using only steps 1-3 of the algorithm results in the nodules remaining undetected because, as adjacent slices reveal, there is some degree of vascular attachment. The nodules are detected (Figures 5.4(e) and 5.5(e)) when the MBO method (step 4) is used as part of the detection algorithm.

Figure 5.6 shows a case where the detection algorithm fails to detect a nodule. In this case, the degree of connectivity between the nodule and surrounding structures was too extensive for the proposed method to work. Figure 5.6(c) shows the connected structure of which the nodule forms a part.

The following empirically derived parameters were used in the experiments: the length parameter,  $\nu$  was set to  $1e - 12$ , for the 3-D global segmentation. The initial estimates for the mean value of both regions,  $c1$  and  $c2$ , were set to 0.3 and



**Figure 5.2:** Example of normal operation of rule-based classifier: (a) Annotated Data indicating nodule (b) Initial Segmentation Results + Chest wall removal (c) Corresponding Detection Results (d) Corresponding Detection Results with annotation



**Figure 5.3:** Results achieved by the method on 6 sample frames (Rows R1 R6). Each row shows an example of a nodule with vasular attachment. C1: The original data with expert annotation. C2: 2 phase global segmentation result C3: Results of the rule-based detection method C4: Detection results post MBO processing C5: Detection results with superimposed expert annotation.

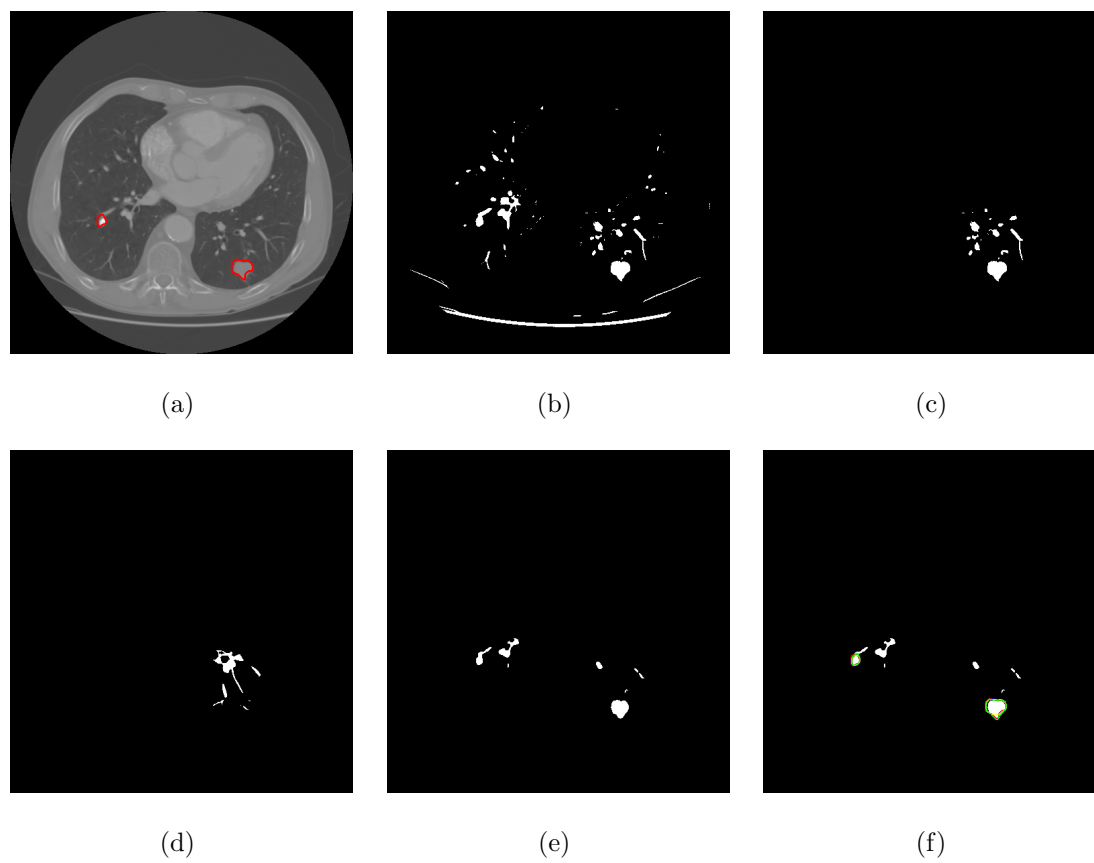


**Figure 5.4:** Example of a nodule processed using only the rule-based classifier (i.e. using only steps 1-3 of the algorithm)(a) Original annotated dataset (b) slice 71 of dataset: nodule looks well delineated from surrounding structures but is actually part of a large connected component (c) the connected component which contains the nodule (d) an adjacent slice (e) Step 4: Detection with MBO (f) Annotation overlaid on result.

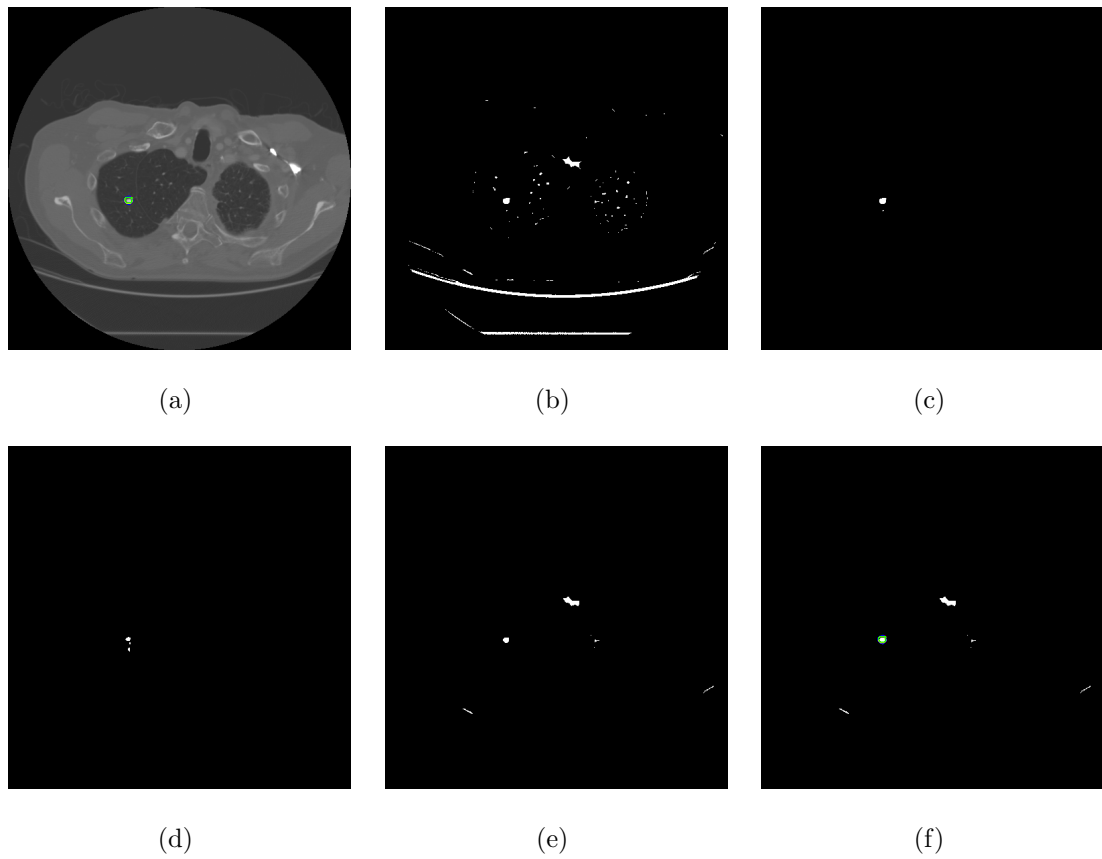


**Figure 5.5:** Second example of a nodule processed using only the rule-based classifier (a) Original annotated dataset (b) nodule looks well isolated from surrounding structures but is actually part of a large connected component (c) connected component which includes the nodule (d) an adjacent slice (e) Step 4: Detection with MBO (f) Annotation overlaid on result.

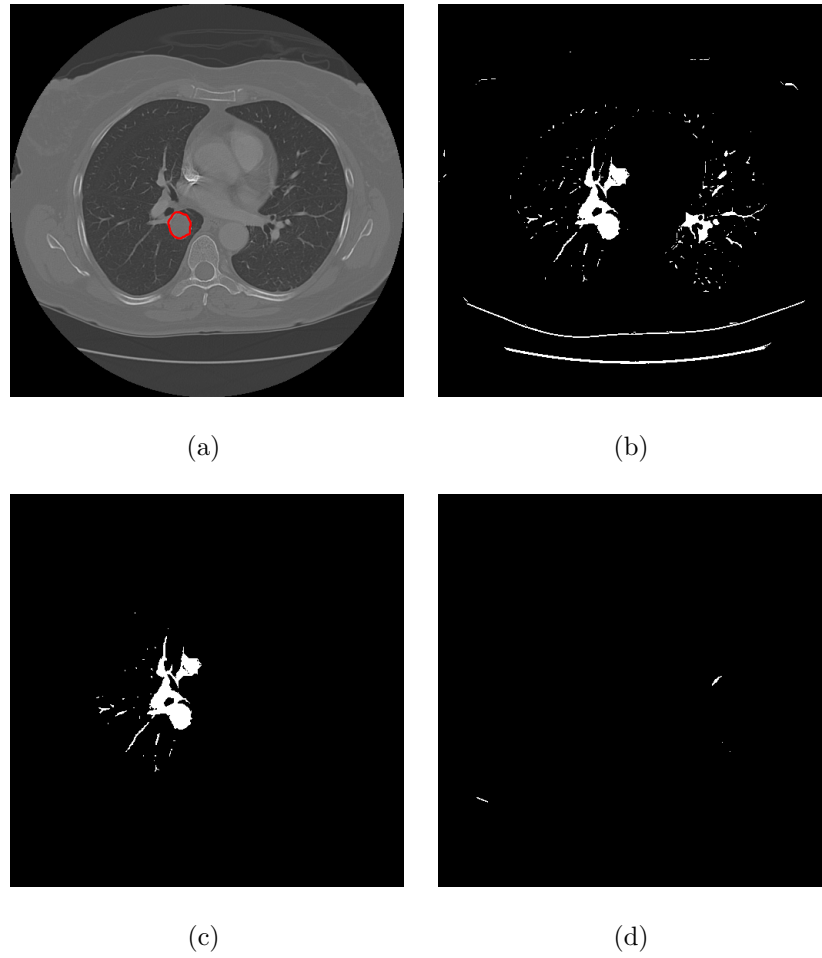


**Figure 5.6:** Example of a case where MBO-detection scheme fails (a) Original Annotated dataset (b) 2-phase segmentation (c) Connected component (d) Detection with MBO - failure.

0.6 respectively. The morphological opening operation used to remove the chest wall was carried out using a spherical kernel of radius 13. For the MBO scheme, with the exception of one dataset,  $\sigma$  for the Gaussian kernel was set to 1, while the maximum number of iterations used was 20. For one dataset,  $\sigma$  was reduced to 0.7, with the number iterations remaining at 20. The thresholds used for the rule based classifier were chosen in the same way as in [121] in which estimates were chosen based on the data in the LIDC dataset. The maximum diameter,  $T_{max}^d$ , was set to 30, minimum diameter  $T_{min}^d$  was set to 3, correspondingly the maximum area threshold was  $(T_{max}^d/2)^2\pi$ , minimum area threshold was  $(T_{min}^d/2)^2\pi$ , maximum volume threshold was set to  $3(T_{max}^d/2)^3\pi/4$ , minimum threshold was set to  $3(T_{min}^d/2)^3\pi/4$ , maximum elongation was set to 4, while minimum circularity was set to  $\frac{1}{6}$ .

Minimum and maximum diameter thresholds for the rule-based classifier were chosen based on data in the LIDC dataset, where 97% of the nodules recorded have a diameter in the 3-30mm range (with 86% in the 3-12mm range and a further 11% in the 12-30mm range). With respect to the test set used in these experiments, 80% of the nodules were in the 3-12mm diameter range, with the remaining 20% in the 12-30mm range. The greater representation of larger nodules in the test set was in response to the previously discussed findings in [117], in which it was reported that larger nodules tended to be characterised by irregular shapes and thus were harder to detect.

As described, the MBO parameters were changed for one dataset. This dataset presented a nodule with a diameter of 6mm that also exhibited a connection with neighbouring blood vessels. For this nodule, a  $\sigma$  value of 1 represented an over-smoothing and consequent detection failure, while a  $\sigma$  value of 0.7 resulted in accurate detection. The effect of increasing/decreasing  $\sigma$  is to increase or decrease the width of the Gaussian kernel, and as such, increase or decrease the level of shape smoothing that occurs. It was found that a  $\sigma$  value of 1 produced good results for all but one dataset. To make the system more robust to parameter choice, a smaller sigma value can be used and the number of iterations increased. The effect

of increasing length parameter  $\nu$ , of the global segmentation scheme would be penalise length of the segmented objects *i.e.* enforce smoothness in object boundaries, which would also mean losing smaller anatomical structures. Keeping this value low ensured that global segmentation scheme produced a tissue/air segmentation and that no anatomical details were lost in the first step of the detection process.

The results show that the algorithm successfully detected all but one of the nodules present (see Figure 5.6). This resulted in an average detection rate of 96%, while an average of 16 false positives were detected per scan. Without the MBO smoothing step the detection rate was 44%.

## 5.4 Conclusion

In this chapter, an algorithm was proposed for the detection and segmentation of pulmonary lung nodules. Several studies [117, 107, 106] have highlighted the difficulty in detecting larger nodules, which tend to be characterised by greater shape diversity, hence the goal of this research was to increase segmentation robustness for these types of nodules. The proposed algorithm was tested on 16 datasets containing 27 nodules with various degrees of attachment to surrounding tissue. A 96% detection rate was obtained. These initial results show that the proposed method has the potential to be an effective module in an automated detection pipeline.

# 6

## Summary & Conclusion

### 6.1 Thesis Summary

Image segmentation has long been considered a critical step in computational image analysis. In this context, the goal of this thesis was to investigate the general topic of segmentation robustness with particular emphasis on three specific areas: first robustness to image features, specifically robust boundary detection in images with weak intensity gradients; secondly, robustness with respect to topology preservation, specifically topology preservation in the presence of noise; and finally, robustness to diverse geometrical features, this work focussing on the detection of lung nodules with vascular connection.

The first task addressed was the problem of boundary detection in environments where objects are defined by weak intensity gradients. The details of the proposed

boundary refinement scheme for low contrast images are presented in chapter 3. The proposed scheme consists of solving the well-known MS functional using a highly efficient convex segmentation scheme. Using the solution of this convex scheme, an edge detector is generated which is then input into a GAC scheme to produce the final curve representing the boundary of the structure. The proposed method has some interesting characteristics; the output of the first step corresponds to a 2 region global minimiser of the MS segmentation model. It is known that convex segmentation schemes require fewer parameters and are more robust to parameter choice than traditional implementations of variational segmentation methods. Secondly, a highly efficient CMF scheme [9] is used to solve the convex model, for which the binary segmentation output can be generated in approximately 0.2 seconds. The method was validated using a combination of medical and non-medical data. In the case of medical data, the method was compared to segmentation results from classical data driven approaches and validated against manual delineations performed by two trained experts. The results clearly demonstrate an improved performance when the proposed method is applied.

Chapter 4 addresses the topic of topology preservation. Segmentation models using the level set method to numerically minimise a given energy can have solutions that are not homeomorphic to the initial condition. In many cases this property is beneficial but in some applications it is preferable to maintain the topology of the initialisation curve, such that it is matched to the target shape. In this chapter a description of a region based topology preserving active contours model is presented to handle such cases. The proposed model consists of a non-local topology preserving constraint which forces the curve to avoid breaking or self-intersection via a variational self-repelling term. The topology preserving term is combined with a data fidelity constraint to increase robustness in the presence of noise. The proposed method was tested using standard synthetic examples, real photographic data, and real medical images with varying degrees of noise and edge structure types.

In chapter 5, details of the proposed segmentation algorithm for lung nodule detection is presented. The goal here was to isolate anatomical data with a strong

likelihood of corresponding to lung nodules. The proposed detection scheme comprises the following steps: first a global 2 phase segmentation is performed, which segments the volume into 2 classes consisting of tissue and air. The next step is to further segment the tissue into lung wall and interior lobe data using morphological techniques. The main part of the proposed scheme is the use of mean curvature smoothing to isolate vascular connected nodules. The detection step is carried out by applying the rule-based classifier once before the Merriman-Bence-Osher (MBO) smoothing and subsequently on each connected component after each MBO iteration. The algorithm was tested on 16 datasets containing nodules with vascular attachment, and achieved a detection rate of 96%.

## 6.2 Summary of Contributions

The main contributions of the thesis can be summarised as follows:

### Boundary Refinement for Low Contrast Images

- A new technique for generating an edge detector function was developed that exploits the natural properties of the MS functional to effectively reinforce weak boundaries of low contrast images.
- A sequential scheme for boundary detection was proposed using the edge detector function together with the GAC method. The proposed scheme increases robustness in two ways: the globally convex segmentation scheme is invariant to initial conditions and is easily adapted to the data. Secondly, the addition of a segmentation scheme based on local curve evolution produces a solution that helps preserve topology between the initial and target shape, a property lacking in globally convex segmentation schemes.
- The boundary detection scheme was implemented and compared against other data-driven approaches. The results clearly demonstrate improved perfor-

mance on real-world low contrast images.

## Topology Preserving Active Contours

- The primary contribution of the topology preserving work was the proposal of a new segmentation model consisting of a combination of region based active contour models with topological forces. The proposed model was implemented and its performance was demonstrated on a combination of synthetic, natural and medical images, including 3-D data.
- The improved performance of proposed topology preserving model was demonstrated over related previous work. The proposed model is capable of preserving the topology more satisfactorily than the Chan-Vese model, previous topology preserving schemes, as well as global segmentation segmentation methods in noisy environments.

## Lung nodule candidate detection in Computed Tomography

- The final contribution is the proposal of a novel algorithm for robust lung nodule candidate detection in CT. The main component of the proposed scheme is the use of mean curvature smoothing to isolate vascular connected nodules. Nodules which remained undetected when filtered using simple geometric features were detected when the mean curvature smoothing step was included.

## 6.3 Conclusion

In this thesis, three variational approaches have been described for the task of image segmentation. The models proposed in chapters 3 and 4 are proposed as generic schemes that could be used in a diverse range of imaging applications, while the model described in chapter 5 is proposed specifically for lung nodule detection. Taken together, the proposed techniques contribute and improve existing knowledge

in the area of segmentation robustness with respect to image features, topology preservation and with respect to diverse geometrical features.

Experimental results indicate that the edge detector proposed in chapter 3 clearly out performs existing data driven approaches. The method is not proposed as a general edge detector however. Without a strong regional gradient, extracting the edge set would not be possible, *e.g.* the detection of extremely thin structures would present a problem for the method. Nonetheless, the technique has the potential to be a useful tool for applications in which the object or objects are defined by low-contrast boundaries *e.g.* the segmentation of gaseous phenomena such as clouds or smoke or in echocardiography, as demonstrated in this thesis.

Experimental results demonstrate that the proposed topology preserving model described in chapter 4, is more effective than existing data driven approaches at imposing a topology prior in noisy imaging conditions. The method is not anticipated, however, to be as robust with respect to topology preservation as imposing a statistical shape prior. To rigorously enforce the topology prior in the proposed method, suitable bounds for weighting term of the topology constraint would need to be found for each specific application, whereas for a shape prior model the topology constraint could be imposed irrespective of weighting parameters. Nonetheless, the advantages of the proposed scheme over a shape prior model include faster runtime, due to the absence of a training step, as well as increased generality, owing to the fact that the proposed scheme does not impose constraints about the geometric structure of the target object.

Finally, experimental results demonstrate that the proposed lung nodule detection method performs well with nodules presenting a complex geometry, achieving a 96% detection rate on the nodules tested. The method fails however, when the degree of connectivity between the nodule and surrounding structures is too extensive (*i.e.* greater than the diameter of the nodule itself). There is also a risk that in the present scheme particularly challenging nodules, while being separated from surrounding structures, could become over-smoothed and as a result, be in incorrectly labeled in a subsequent classification step.

The proposed algorithms are each examples of data driven approaches. Factors that can limit the success of such approaches, include when there are occlusions in the image and also when domain knowledge is unavailable *i.e.* nothing is known about what the image contains and therefore assumptions based on the types of edge structures present, or topology, cannot be made. While the methods proposed in this thesis, are most relevant to applications where some domain knowledge is known (which is typical for example in medical imaging), to deal with the latter scenario, a recent trend in the image analysis literature involves coupling the tasks of segmentation and recognition. This approach, termed ‘semantic segmentation’, refers to the task of assigning a semantic label to each region in an image *e.g.* “cow”, “grass”, “ocean”. To achieve this, characteristic features of different objects are defined in object classes. Semantic segmentation schemes proceed iteratively, where at each step, the features of the emerging regions are compared/matched to those of the defined object classes. By combining high level recognition with low level feature information in this way, computer based image processing is beginning to mimic more closely how human visual perception operates and therefore promises to be a fruitful avenue of research. The success of semantic segmentation will nonetheless continue to be reliant on the ability of data-driven schemes to provide an initial partitioning of a given image into the most relevant regions, hence the development of data-driven schemes, such as those proposed in this thesis, will continue to be very relevant into the future.

## 6.4 Future Work

The research presented in this thesis is comprised of a number of related topics, many of which could be extended further. Some possible avenues for future work are listed here:

- In the case of the edge detection and topology preserving algorithms, the most natural direction of future work, would be an extension to the multiphase case. The edge reinforcement algorithm could be extended using the convex

formulation of a continuous multiphase segmentation model proposed in [122]. While the topology preserving model could be extended to the multiphase case using the model defined in [38] (finding a convex formulation of this model is still an open problem).

- As discussed in section 6.3, semantic segmentation models are becoming more prevalent in the literature. The approach is particularly useful in applications where the image content is unknown. After extension to the multiphase case, both the edge reinforcement algorithm and the topology preserving model could be incorporated into a semantic segmentation framework.
- In chapter 3 regional information in the form of mean intensity of the prominent regions was used to generate an edge detector. Since the publication of the CMF method, other globally convex formulations have been proposed incorporating more complex regional descriptors such as in [123]. It would be interesting to investigate the effectiveness of these descriptors in the context of generating edge attraction forces.
- Statistical shape priors are commonly applied in medical image segmentation. A study in which the proposed boundary detection scheme was compared to a shape prior method such as proposed in [124] would be very interesting.
- An interesting application of the algorithm proposed in chapter 3, would be in the area of detection of gaseous phenomena such as clouds or smoke. One example would be storm detection. As imaged by aerial or satellite equipment, both the leading and trailing edges of the storms are displayed with low intensity. In this context, the boundary reinforcement properties of the proposed 2-phase global segmentation could be used as part of a detection algorithm to more accurately predict, for example, when storms are going to hit.
- The topology preserving scheme could be adapted to an engineering applica-

tion by establishing suitable operating bounds for the topology parameter.

- The most natural extension of the lung nodule candidate detection algorithm, would be to analyse further the generated regions either manually or using an advanced classifier to determine whether they represent a true nodule.
- To improve the detection algorithm in cases where nodules present extensive connectivity to surrounding structures, prior geometrical knowledge about the shape could be taken into account, such that potential nodules attached, for example, to the chest wall get disconnected.
- Similarly to overcome the risk of oversmoothing in the detection algorithm, each new connected component which is generated by the mean curvature step, could be used as input information to a final supervised segmentation algorithm. By using these new connected components as background and foreground points in a supervised scheme, the full detail of potential nodules could be recovered, while also remaining separated from surrounding tissue belonging to different regions.

# A

## Appendices

The research in this thesis has resulted in the following publications:



# A simple boundary reinforcement technique for segmentation without prior <sup>☆</sup>



Nóirín Duggan <sup>a,b,\*</sup>, Egil Bae <sup>b</sup>, Edward Jones <sup>a</sup>, Martin Glavin <sup>a</sup>, Luminita Vese <sup>b</sup>

<sup>a</sup>Electrical & Electronic Engineering, National University of Ireland, Galway, Galway, Ireland

<sup>b</sup>Department of Mathematics, University of California Los Angeles, 405 Hilgard Avenue, Los Angeles, CA 90095-1555, United States

## ARTICLE INFO

### Article history:

Received 12 August 2013

Available online 30 April 2014

### Keywords:

Image segmentation  
Convex optimization  
Variational methods  
Edge detection  
Echocardiography images

## ABSTRACT

Accurate boundary detection is a critical step of the image segmentation process. While most edge detectors rely on the presence of strong intensity gradients, this criteria can limit robustness in many real world cases. In this work we propose a scheme which makes use of a combination of both global and local segmentation methods to capture the boundary of target objects in low contrast images. This approach has several advantages: the globally convex segmentation scheme is immune from initial conditions and is easily adapted to the data. The addition of a segmentation scheme based on local curve evolution produces a solution which is shown to help preserve topology between the initial and target shape, a property lacking in globally convex segmentation schemes. Experimental results show that the proposed method achieves enhanced performance compared to classical data-driven segmentation schemes proposed in the literature.

© 2014 Elsevier B.V. All rights reserved.

## 1. Introduction

Image segmentation is arguably one of the most important tasks in computer vision and has been an active area of research over the last three decades. Efforts directed at this task have included variational approaches, statistical and more recently combinatorial methods. Many of the most successful segmentation methods have been formulated as energy minimization problems in which the key object detection criteria are incorporated into the energy functional.

One of the first proposals to cast image segmentation as an energy minimization problem was the approach of [11] who computed the segmentation of a given image by evolving curves in the direction of the negative energy gradient using appropriate partial differential equations. In this approach, boundaries are detected using the strength of the gradient at each pixel. In [11] the curve is represented explicitly, which can lead to some drawbacks, in particular in order to avoid self-intersection and overlap of contour points, reparameterization is required. Similarly, sophisticated reparameterization schemes are needed to handle topological

changes, which are necessary for segmenting multiple objects or objects with an unknown topology.

To overcome the need for reparameterization, techniques based on implicit curve evolution theory [15,3] allow for motion based on geometric measures such as unit normal and curvature. To obtain a new length constraint which is independent of parameterization, Caselles et al. [3] and Kichenassamy et al. [12] simultaneously proposed the implicit geodesic active contour, the energy functional of which is given by:

$$E(C) = \int_0^1 g(|\nabla I(C(q))|) |C'(q)| dq \quad (1)$$

where  $g = \frac{1}{1 + \beta |\nabla I|^p}$  with  $p = 1$  or  $2$

If we let  $\Omega$  denote the image domain, where  $\Omega \subset \mathbb{R}^N$  then in the above equation, the image is represented by,  $I: \Omega \rightarrow \mathbb{R}$ .  $C(q): [0, 1] \rightarrow \Omega$  represents the curve, while  $\beta$  controls the sharpness of the detected edges. In the level set method of Osher and Sethian [15], the curve is represented implicitly as the zero level line of some embedding function  $\phi: \Omega \rightarrow \mathbb{R}$ :  $C = \{x \in \Omega \mid \phi(x) = 0\}$  where  $\phi(x) \leq 0$  in the interior of the curve and  $\phi(x) > 0$  in the exterior. The level set method evolves a curve by updating the level set function at fixed coordinates through time, rather than tracking a curve through time, as in a parametric setting. In an implicit formulation, both topological changes and also extension to higher dimensions are handled naturally.

<sup>☆</sup> This paper has been recommended for acceptance by D. Coeurjolly.

\* Corresponding author at: Electrical & Electronic Engineering, National University of Ireland, Galway, Galway, Ireland.

E-mail address: [nduggan@math.ucla.edu](mailto:nduggan@math.ucla.edu) (N. Duggan).

Another energy minimization approach for detecting edges in an image is the Mumford–Shah model [14], which in its most general form seeks both an edge set and an approximation of the image which is smooth everywhere except across the edge set. There has been a considerable amount of research on computing minimizers by numerical algorithms. In [5,23] the authors presented a level-set formulation of the piecewise constant variant of the Mumford–Shah model. Considering an image with two regions, the object to be segmented is denoted  $S$  and the background denoted  $\Omega \setminus S$ , the authors proposed the following model:

$$\min_{S, c_1, c_2} \int_{\Omega \setminus S} |I(x) - c_1|^2 dx + \int_S |I(x) - c_2|^2 dx + \nu |\partial S|. \quad (2)$$

The last term of the energy functional is the length of the boundary of  $S$  weighted by the parameter  $\nu$ , while the first terms represent the data-fidelity where  $c_1$  and  $c_2$  are two scalars that attempt to approximate the image in the interior and exterior region. In order to find a minimizer by a numerical algorithm, it was proposed in [5,23] to represent the partition with a level set function, resulting in the following problem:

$$\min_{\phi, c_1, c_2} \left( \int_{\Omega} |I(x, y) - c_1|^2 H(\phi) dx + \int_{\Omega} |I(x, y) - c_2|^2 (1 - H(\phi)) dx + \nu \int_{\Omega} |\nabla H(\phi)| dx \right) \quad (3)$$

where  $H$  is the Heaviside function, defined such that  $H(z) = 1$  if  $z \geq 0$  and  $H(z) = 0$  if  $z < 0$  and is used to select either the interior or exterior of the curve. This work is known as Active Contours without Edges (ACWE) or Chan–Vese (CV) method. More recently, efficient convex optimization algorithms have been developed which result in global minimizers, e.g. the Split Bregman algorithm [9] and continuous max-flow [26,27].

To increase robustness, schemes have been proposed which combine region and edge terms [16,1]. In [16], an energy minimization approach for tracking objects was proposed, where regional and edge information were integrated in separate terms of an energy functional, in addition to a motion based term. In order to solve the resulting minimization problem, the level set method was applied. The quality of segmentation often depends on the quality of the detected edges. Bresson et al. [1] proposed a method which combines the data fidelity term of the ACWE model and the edge attraction term of the geodesic active contour (GAC) model in a global minimization framework.

Another line of research attempts to minimize the full Mumford–Shah model with curves that contain endpoints in order to detect edges. The Mumford–Shah model and the GAC model were extended to include more general edge sets in [22,21]. In [24], the authors represented the edges by a binary function, leading to a non-convex minimization problem closely in spirit to the phase field representation. A convex relaxation of the piecewise smooth Mumford–Shah model was proposed in [18], by lifting the the problem to a higher dimensional space. Although computationally expensive, this approach has the advantage of converging to a close approximation of a global minimizer, without getting stuck in a local minimizer. In [2] a generalization of the Mumford–Shah model was proposed with an extra term which enforced closeness between the gradient of the reconstructed image and the original image. The motivation behind this model is to better reconstruct edges with low contrast changes. A numerical algorithm based on the level set method was proposed. Closely related is also the diffusion equation of Perona and Malik [17], which converges to a local minimizer of the Mumford–Shah model if an appropriate data fitting term is added.

In Rajpoot et al. [19] an intensity invariant, real-time method was proposed to extract boundary information by analyzing the monogenic signal [7]. The proposed filter uses a local phase based method to extract edge information. The method produces a finer

edge extraction than gradient detectors; however, due to its intensity invariance, tends to over-segment the image. Another approach for generating feature detectors proposed for application to echocardiography, is the method of Mulet-Parada et al. [13], a 2D + T method, in which it was demonstrated that a local phase-based approach produces more accurate edge results than conventional gradient magnitude methods.

The problem we addressed in the current work was how to increase segmentation robustness using a purely data driven approach. Incorporating prior information into a segmentation scheme is of course an advantage if such information exists, however this is not always the case; with this in mind, in the current work we sought to develop a method for images with weak boundaries by looking at new ways to incorporate pre-existing information. In the preliminary conference paper [6], a combination technique was presented using Geometric Split Bregman method with a topology preserving level set technique for application to echocardiography with the similar objective of detecting low-contrast boundaries. The method described here similarly proposes a sequential model using a global segmentation scheme, however in this work we make use of the alternate formulation using continuous maximum flow method while using the Geodesic Active Contour method to capture the final boundary. Similarly to [24,2], we also apply a variation of the Mumford–Shah model to improve the edge detection step. While in [24] the goal was to improve the ‘standard’ canny edge model, our proposal is to delineate structures with low contrast boundaries by reinforcing the weak edges.

To summarize our contributions, in this paper we propose:

1. A new technique for generating an edge detector function which exploits the natural properties of the Mumford–Shah functional to effectively reinforce weak boundaries.
2. A combination of the proposed edge detector with the GAC method and demonstrate its applicability to images with weak edges, such as echocardiography medical images.

The remainder of the paper is organized as follows: In Section 2, we describe the proposed segmentation model. Section 3 contains experimental results on both medical and non-medical real images. Section 4 presents the discussion of the results and Section 5 concludes the paper.

## 2. Methodology

In this paper we propose a sequential model which addresses some of the weaknesses of these previous methods. The type of images focused on in this work often have weak edges and boundaries. Therefore, an edge detection method based directly on the image gradients is not expected to work well. In order to obtain a clearer edge map, we first approximate the image by a piecewise constant function, by efficiently computing a global minimizer to the model (2) with the Continuous Maximum Flow (CMF) algorithm [26,27] Then in order to obtain a single curve which captures the boundary of the object, we apply the geodesic active contour (GAC) method where the edge attraction term is constructed from the edge map in the first step.

### 2.1. Computation of edge detector from global segmentation output

The first step of our method is to extract a rough edge map by using the ACWE model with two regions. In recent work, efficient algorithms have been proposed for computing global minima to this model. In [4] it was shown that (2) can be exactly minimized via the convex problem

$$\begin{aligned} \min_{\phi(x) \in [0,1]} & \int_{\Omega} |I(x) - c_1|^2 \phi(x) + |I(x) - c_2|^2 (1 - \phi(x)) dx \\ & + \nu \int_{\Omega} |\nabla \phi(x)| dx. \end{aligned} \quad (4)$$

It was shown that if  $\phi^*$  is a minimizer of (4) and  $t \in (0, 1]$  is any threshold level, the partition  $S = \{x \in \Omega : \phi(x) \geq t\}$ ,  $\Omega \setminus S = \{x \in \Omega : \phi(x) < t\}$  is a global minimizer to the model (2). The binary function

$$\phi^t(x) := \begin{cases} 1, & \phi(x) \geq t \\ 0, & \phi(x) < t \end{cases} \quad (5)$$

is the characteristic function of the region  $S$ .

A very efficient algorithm was proposed for solving the problem (4) in [26,27]. The basic idea is to derive an augmented Lagrangian algorithm based on the following dual problem of (4):

$$\sup_{p_s, p_t, p} \int_{\Omega} p_s(x) dx \quad (6)$$

subject to

$$|p(x)|_2 \leq \nu, \quad \forall x \in \Omega; \quad (7)$$

$$p_s(x) \leq |I(x) - c_1|^2, \quad \forall x \in \Omega; \quad (8)$$

$$p_t(x) \leq |I(x) - c_2|^2, \quad \forall x \in \Omega; \quad (9)$$

$$p \cdot n = 0, \quad \text{on } \partial\Omega. \quad (10)$$

$$\text{div } p(x) - p_s(x) + p_t(x) = 0, \quad \text{a.e. } x \in \Omega. \quad (11)$$

where the dual variables are scalar and vector functions:  $p_s, p_t : \Omega \rightarrow \mathbb{R}$  and  $p : \Omega \rightarrow \mathbb{R}^N$ , where  $N$  is the dimension of the image domain  $\Omega$ . The dual problem can be interpreted as a maximum flow problem over a continuous domain, therefore the following algorithm was referred to as a continuous max-flow algorithm (CMF).

In order to solve the maximization problem, a Lagrange multiplier  $\phi$  was introduced for the constraint (11), and the augmented Lagrangian functional was formulated as follows:

$$\begin{aligned} L_c(p_s, p_t, p, \phi) : \\ = \int_{\Omega} p_s dx + \int_{\Omega} \phi (\text{div } p - p_s + p_t) dx - \frac{c}{2} \|\text{div } p \\ - p_s + p_t\|^2 \end{aligned} \quad (12)$$

where for a function  $a$ ,  $\|a\|^2 = \int_{\Omega} |a(x)|^2 dx$ . Assume the problem has been discretized such that  $p_s, p_t$  and  $\phi$  are defined for each pixel in the discrete image domain  $\Omega$  and  $\int, \nabla$  and  $\text{div} = -\nabla^*$  are some discrete integration and differential operators. In all experiments in this paper, we have used a mimetic discretization of the differential operators [10]. An augmented lagrangian method could be applied by alternatively maximizing  $L_c$  for the dual variables  $p_s, p_t, p$  with constraints (7)–(10) and update the lagrange multiplier  $\phi$  as follows:

Initialize  $p_s^1, p_t^1, p^1$  and  $\phi^1$ . For  $k = 1, \dots$  until convergence:

- 
- $$p_s^{k+1} := \arg \max_{p_s(x) \leq |I(x) - c_1|^2 \forall x \in \Omega} \left( \int_{\Omega} p_s dx - \frac{c}{2} \|p_s - p_t^k - \text{div } p^k + \phi^k/c\|^2 \right)$$

which can easily be computed pointwise in closed form.

- 
- $$p^{k+1} := \arg \max_{\|p\|_{\infty} \leq \nu} -\frac{c}{2} \|\text{div } p - p_s^{k+1} + p_t^k - \phi^k/c\|^2,$$

where  $\|p\|_{\infty} = \sup_{x \in \Omega} |p(x)|_2$ . This problem can either be solved iteratively or approximately in one step via a simple linearization [27]. In our implementation we used the linearization.

- 
- $$p_t^{k+1} := \arg \max_{p_t(x) \leq |I(x) - c_2|^2 \forall x \in \Omega} -\frac{c}{2} \|p_t - p_s^{k+1} + \text{div } p^{k+1} - \phi^k/c\|^2$$

This problem can also easily be computed in closed form pointwise.

- 
- $$\phi^{k+1} = \phi^k - c (\text{div } p^{k+1} - p_s^{k+1} + p_t^{k+1});$$
- Set  $k = k + 1$  and repeat.

The output  $\phi$  at convergence will be a solution to (4) and one can obtain a partition which solves (2) by the thresholding procedure described above. More details on implementation of the algorithm can be found in the paper [27].

## 2.2. Boundary localization through local curve evolution

This initial segmentation corresponds to a simplified binary representation of the image, in which 2 prominent regions are identified and represented by binary functions with an intensity of either 1 or 0. However, the segmentation result obtained in this first step is not expected to be a good representation of the object we wish to detect. Globally optimal solutions of the region based model (2) often have a complicated topology, which do not represent a simple connected object with a closed boundary. In the second step, we make use of the edge of the binary image from Section 2.1 to create a more prominent edge attraction force in the geodesic active contour model defined in Eq. (1). The evolution equation of the GAC model is given by

$$\frac{\partial C}{\partial t} = (\kappa g - \langle \nabla g, N \rangle) N \quad (13)$$

where  $\kappa$  is the Euclidean curvature, and  $N$  is the unit inward normal.

In our proposed method, the edge map  $g$ , is generated using the clean binary output of step 1 using:

$$g(\nabla I_{CMF}) = \frac{1}{1 + |G * \nabla I_{CMF}|} \quad (14)$$

where  $G$  represents a Gaussian Kernel.

Compared to the globally optimal output of Section 2.1, the final output of the combined approach is expected to have a much simpler topology, consisting in most cases of one connected component.

The GAC method was implemented using the AOS (Additive Operator Splitting) scheme for solving PDE equations in the form of  $u_t = \text{div}(g * u)$ .

The details of the implementation can be found in [25].

To summarize our approach, we first create a binary approximation of the original image and extract the major edge set using CMF method. This information is used to yield a better edge attraction force in the GAC method, which locates the object boundary.

In the following section, the experimental results of the proposed method are presented.

## 3. Experiments

To test the method a sample combination of medical and non-medical real world data was selected which naturally exhibit low contrast boundaries. In the case of the medical data, a small test sample of 5 frames each were chosen from 5 low quality echocardiography datasets. The other test images consist of an image of a galaxy and also an image of a swarm of birds. The method was validated by comparing it to two classical data driven segmentation models: ACWE approach and the standard GAC model. In the

medical image test, we also compared the method to the local-phase based feature detection approach of [19,20], this method having been designed specifically for echocardiography. For each test case and dataset, parameters controlling length as well as the initial estimate of regional intensity were chosen based on the data, parameters were similarly optimized for each of the comparison methods. For the experiments on medical data, we kept the intensity estimates,  $c_1$  and  $c_2$  from Eq. (2), constant over the

course of the energy minimization (minimizing with respect to length). For the experiments,  $c_1$  was chosen to be in the range  $16e-3$  to  $5e-2$ , with  $c_2$  in the range between 0.12 to 0.28, while best results were obtained with the length parameter  $v$ , between  $1e-3$  and 0.5.

For the ACWE method the following smooth weight values were used [15, 2.03, 1.23, 18], while the contrast parameters were set to [950, 318.75, 78.75, 1200]. For the standard GAC method the length

**Table 1**

Quantitative results computed using Hausdorff, Mean Absolute Distance and Dice metrics for medical data. Experiments were conducted on a sample of 55 frames across 5 datasets. Represented here is the average distance for each metric computed over a test set of frames from each dataset.

	LAX1	LAX2	LAX3	LAX4	LAX6	Average	% Diff
<i>HD</i>							
Our proposed Method	<b>4.6</b>	5.28	<b>3.34</b>	<b>4.69</b>	<b>4.49</b>	<b>4.48</b>	
ACWE	6.78	9.91	3.37	5.91	5.47	6.29	40.4
Standard geodesic	5.31	<b>3.8</b>	4.08	5.64	4.66	4.7	4.9
Using Phase derived edge maps	6.62	5.48	5.02	8.22	8.52	6.77	51.1
<i>MAD</i>							
Our proposed Method	<b>1.17</b>	1.51	0.94	<b>1.54</b>	<b>1.41</b>	<b>1.31</b>	
ACWE	1.82	3.46	<b>0.89</b>	1.9	1.45	1.9	45
Standard geodesic	2.06	<b>1.39</b>	1.81	1.85	2.11	1.84	40.5
Using Phase derived edge maps	1.72	1.6	1.98	2.26	1.95	1.9	45
<i>Dice</i>							
Our proposed Method	<b>0.93</b>	0.92	0.93	<b>0.88</b>	0.9	<b>0.91</b>	
ACWE	0.87	0.75	0.93	0.84	0.9	0.86	5
Standard geodesic	0.89	<b>0.93</b>	0.87	0.87	0.86	0.88	3
Using Phase derived edge maps	0.9	0.9	0.85	0.83	0.87	0.87	4

Bold values indicate the method which gave the best performance (if two methods gave same performance than no value is embolded).

**Table 2**

Percentage error due to each parameter. Average taken over all frames.

Proposed method	HD Average	Std	MAD Average	Std	Dice Average	Std
Vary length parameter by +/-5%	0.92	1.12	0.16	0.15	0.01	0.01
Vary length parameter by +/-10%	1.74	1.94	0.38	0.37	0.03	0.03
Vary length parameter by +/-20%	6.33	11.57	2.68	5.83	0.26	0.61
Vary $c_1$ or $c_2$ by +/-5%	5.59	9.47	3.36	4.48	0.93	1.35
Vary $c_1$ or $c_2$ by +/-10%	12.12	22.97	6.41	8.99	1.34	1.75
Vary $c_1$ or $c_2$ by +/-20%	28.71	44.09	13.64	16.51	2.37	2.48
Expansion Parameter (tuned for 1 dataset)						
Vary expansion parameter by +/-5%	6.39	6.39	2.99	1.51	0.41	0
Vary expansion parameter by +/-10%	14.5	1.72	12.13	10.65	1.32	0.91
Vary expansion parameter by +/-20%	74.69	60.21	28.28	25.74	5.99	5.5
ACWE						
Vary length parameter by +/-5%	4.19	9.38	3.12	6.02	1.12	2.96
Vary length parameter by +/-10%	11.71	19.02	5.55	6.47	1.52	2.3
Vary length parameter by +/-20%	11.03	8.48	6.12	4.76	1.59	2.23
Vary image parameter by +/-5%	15.96	20.53	7.09	8.64	1.95	3.18
Vary image parameter by +/-10%	20.15	28.63	7.62	8.55	2.06	2.86
Vary image parameter by +/-20%	31.57	33.87	16.6	15.49	3.86	4.08
GAC						
Vary expansion parameter by +/-5%	25.64	36.9	21.09	30.5	4.68	7.69
Vary expansion parameter by +/-10%	48.92	35.57	47.1	28.44	10.37	7.86
Vary expansion parameter by +/-20%	102.89	56.99	87.07	50.38	13.98	10.32
Vary contour parameter by +/-5%	43.78	61.76	34.42	44.15	6.49	7.21
Vary contour parameter by +/-10%	44.48	61.26	35.53	43.12	5.54	7.07
Vary contour parameter by +/-20%	47.74	60.45	38.8	40.23	6.39	6.58
Phase						
Vary wavelength parameter by +/-5%	6.63	5.06	2.55	1.75	0.41	0.37
Vary wavelength parameter by +/-10%	7.5	5.25	3.9	2.51	0.68	0.55
Vary wavelength parameter by +/-20%	10.31	5.28	5.95	3.03	0.91	0.59
Expansion Parameter (tuned for 3 datasets)						
Vary expansion parameter by +/-5%	0	0	0.01	0.01	0	0
Vary expansion parameter by +/-10%	2.18	2.36	1.24	1.12	0.23	0.2
Vary expansion parameter by +/-20%	11.74	10.81	6.85	4.42	1.27	0.87

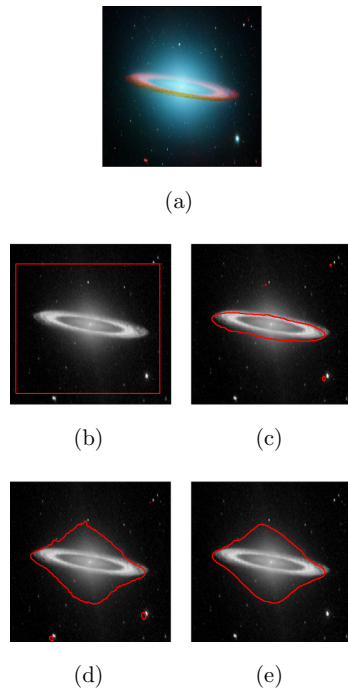


**Fig. 1.** Sombrero galaxy image [8]. The blue glow corresponds to the combined light of billions of old stars and the orange ring marks the sites of young stars: (a) original image, (b) initial phi, (c) Geodesic Result, (d) ACWE result, (e) CMF + GAC result. The results show that the GAC method finds the strongest boundary therefore missing the lower gradient regions (which also form part of the galaxy), while both the ACWE and CMF + GAC methods achieve accurate results. Parameters used for the CMF + GAC method:  $c_1 = 0.18$ ;  $c_2 = 0.09$ ;  $\nu = 5e - 1$ , expansion term = 1, length parameter = 10. Courtesy NASA/JPL-Caltech. (For interpretation of the references to color in this figure legend, the reader is referred to the web version of this article.)

parameter was set to 10 throughout, while the expansion term was chosen to be between 0.6 and 0.9. For the local-phase method, the following values were chosen for the wavelength parameter: [42, 7, 16, 28]. Each method was manually initialized by placing a contour in each frame. Sensitivity to variance in parameter choice is presented in Table 2.

For the medical data, quantitative results showing the similarity between manual delineations carried out by 2 expert observers and each of the methods is presented in Table 1. A sample of the final results obtained on the echocardiography data, together with those obtained with the GAC and ACWE and local-phase based methods is shown in Figs. 4 and 5 while results obtained from non-medical data are shown in Figs. 1 and 2. Fig. 3 shows an example of the CMF output and its corresponding edge map.

The average CPU time required to compute the global segmentation (step 1) was found to be in the order of 0.6 s, while the full curve evolution method took on average 9.7 s. In total, the proposed method took an average of 10.5 s. If we compare this with the reference methods, the Local Phase Method took on average 10.1 s, the Geodesic method 14.7 s and the ACWE method took 5 s. The experiments were carried out both in C and in Matlab, on a 64-bit, Intel Core 2 Dual CPU 3.00 GHz processor with 4 GB of installed memory. The average image size was  $376 \times 376$ . The parallel processing capability of the processor was not used.

Table 1 presents the average accuracy results for each dataset. With respect to the Hausdorff measurement, the CMF + GAC obtained an average Hausdorff distance of 4.48 mm from the

reference contour, which was an improvement on each of the other methods, with the ACWE, GAC and local-phase method obtaining averages of 6.29 mm, 4.7 mm and 6.77 mm respectively. The second table presents Mean Absolute Distance results. In this case, the CMF + GAC achieved an average distance of 1.31 mm compared to 1.9 mm, 1.84 mm and 1.9 mm respectively for the ACWE, GAC and local-phase methods. The third table presents the result of the dice overlap metric. When comparing the overlap percentage between the CMF + GAC method and the manually delineated results it achieved a result of 91% compared to 86% achieved by the ACWE method, 88% achieved by the GAC method and 87% achieved by the local-phase method.

Qualitative results on the medical data are presented in Figs. 4 and 5. Fig. 4 shows the final result obtained with each method, while Fig. 5 shows the similarity of each method to the reference delineation.

Starting with Row 1 in Figs. 4 and 5, with respect to the GAC method, it can be seen (for example in Fig. 4 (R1,C2)), that the absence of a sharp contrast in the upper right corner causes the method to over segment the chamber in this region. The local-phase based method performs comparatively well, however over segments the chamber in the upper left region. The ACWE method produces a better result, however slightly under segments the chamber in this same region. The proposed CMF + GAC method achieves a result visually quite similar to the manual delineation.

In Row 2 of Figs. (4, 5), the ACWE obtains the most accurate result (see Fig. 5 (R2,C2)). The absence of a sharp boundary disrupts the GAC method while the local-phase method over segments the

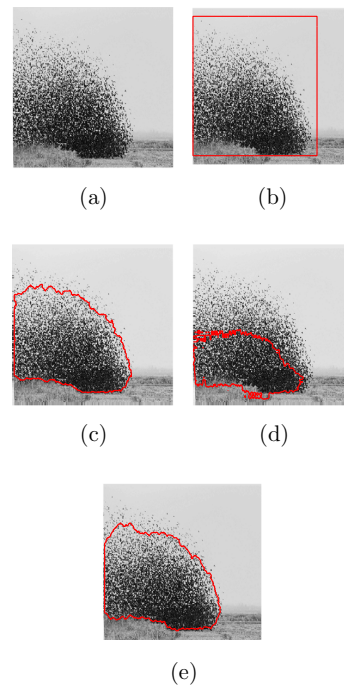


**Fig. 2.** Birds: (a) original, (b) initial phi, (c) Geodesic Result, (d) ACWE result, (e) CMF + GAC result. In this example, both the GAC and the CMF + GAC methods achieve good results while the ACWE method partitions the image into visually the most intensity homogeneous regions missing, in many areas, the actual boundary. Parameters – CMF + GAC method: initial  $c_1 = 0.02$ ;  $c_2 = 0.7$ ,  $\nu = 0.01$ ; expansion term = 0.6, length parameter = 10; Photograph by Lucas Felzmann. Used with permission.

chamber. The proposed CMF + GAC method obtains a mostly accurate result, however under segments the chamber in the lower left region.

Row 3 presents an example of an abnormally shaped chamber as well as limited window width in the upper right region. As in the previous examples, the GAC and local-phase based methods tend to over-segment (see Figs. 5 (R3,C2-C3)) while the ACWE method, together with the CMF + GAC approach capture the true shape more accurately. The CMF + GAC method obtains a greater degree of similarity in the upper region of the chamber.

The frame in Row 4 presents an example of the lack of intensity homogeneity often found in echocardiographic data. The ACWE method (Fig. 4 (R4,C4) and Fig. 5 (R4,C4)) finds the cleanest part of the chamber, however, as highlighted by the manual delineation, this does not represent the true boundary. The results obtained by both the local-phase as well as the CMF + GAC methods are visually quite similar, the phase based method achieves a smoother boundary. The GAC method slightly under-segments the upper chamber region.

Fig. 1 presents the results of testing the CMF + GAC method, together with the ACWE and GAC method on an image of a galaxy. The results show that the GAC method finds the strongest boundary therefore missing the lower gradient regions, while the ACWE method captures the bright star-like points dotted around the image, which are not part of the galaxy, it can be observed that the CMF + GAC results achieves the best approximation of the boundary.

Fig. 2 gives an example of birds swarming. In this example, the final results of both the GAC and the CMF + GAC methods, are quite similar, both giving the approximate boundary of the swarm; while the ACWE method partitions the image into visually the most intensity homogeneous regions, consequently missing, in many areas, the actual boundary. Both the GAC and CMF + GAC methods achieve comparable results, with a smoother boundary than ACWE.

Table 2 gives the average for all datasets of the percentage error due to change in the parameters used for each method. The CMF + GAC method shows robust performance with respect to the length parameter, however changing the initial estimates for inner and outer region intensity produces a significant fluctuation in performance, this is mirrored, though to a lesser degree, in the percentage error due to the image or contrast parameter in the ACWE methods. Among the details which are highlighted in this table is the lack of stability of the GAC method with this data; shifting the length parameter by 5% for example, produces an error of almost 44% in the final result.

#### 4. Discussion

It can be observed from the results of the experiments on non-medical data, that the CMF + GAC approach achieves either similar performance to both the ACWE and GAC methods or enhanced performance in certain cases; for example due to the lack of sharp contrast as illustrated in Fig. 1, causing the GAC approach to fail, or when the predominant intensity densities do not represent the actual boundary as in Fig. 2, which disrupts the ACWE method. The CMF + GAC approach achieves enhanced results compared to either method in these instances. The qualitative results for the medical data in Figs. 4,5 largely mirror this observation.

With respect to the quantitative results in Table 1, for each metric the proposed approach achieved the best overall result compared to each reference method; achieving an average Hausdorff metric of 4.48 mm, an average Mean Absolute Distance of 1.31 mm and an average Dice coefficient of 0.91. Comparing these results to the next most accurate method, which was the GAC

method, we see that for the Hausdorff metric, this represented a 5% improvement on the GAC method, a 40% improvement as measured by Mean Absolute Distance, while for the Dice coefficient, an improvement of 3% was gained. With respect to individual datasets, we can observe that in 4 out of 5 cases the proposed approach achieved the lowest Hausdorff Distance, for the Mean Absolute Distance this was the case in 3 out of 5 cases, while again in 4 out of 5 cases the proposed method achieved the best, or joint best result with respect to the Dice coefficient.

The results also highlight some limitations of the model, such as in Fig. 5 (R2,C5). In this example, due to the extremely low contrast boundary in the left region of the chamber, the length parameter of the CMF method was strongly relaxed, which has the positive effect of reinforcing the boundary but also preserving noise (as exhibited in Figs. 3(e), (f)). This effect disrupted the CMF + GAC approach in this instance. This result is also connected to the fluctuation in performance highlighted in sensitivity results in Table 2. Due to the lack of clear distinction between the intensity characteristics of the regions (i.e. the inner chamber and the inner wall of the myocardium), choosing data fidelity parameters which are robust with respect to variation is a challenging task.



(a) Original Image (b) Output of (c) Edge map  
CMF method



(d) Original Image (e) Output of (f) Edge map  
CMF method



(g) Output of (h) Corresponding  
CMF method, Edge map  
increased  $\nu$

Fig. 3. Example output of CMF method for 2 datasets; (a) and (d) original frames; (b), (e) and (g) corresponding output of CMF method, using values of  $\nu = 0.5$ ,  $\nu = 1e-02$  and  $\nu = 0.5$  respectively; (c), (f) and (h) edge map generated from binary segmentation. Figures (e) and (g) show the difference produced by varying  $\nu$ , (g) shows a cleaner result however (e) more accurately represents the underlying (closed) structure. The output of the CMF method is only shown to illustrate each step of the proposed method and is not part of the final output. To save space, the CMF result is only shown for a subset of the experiments.

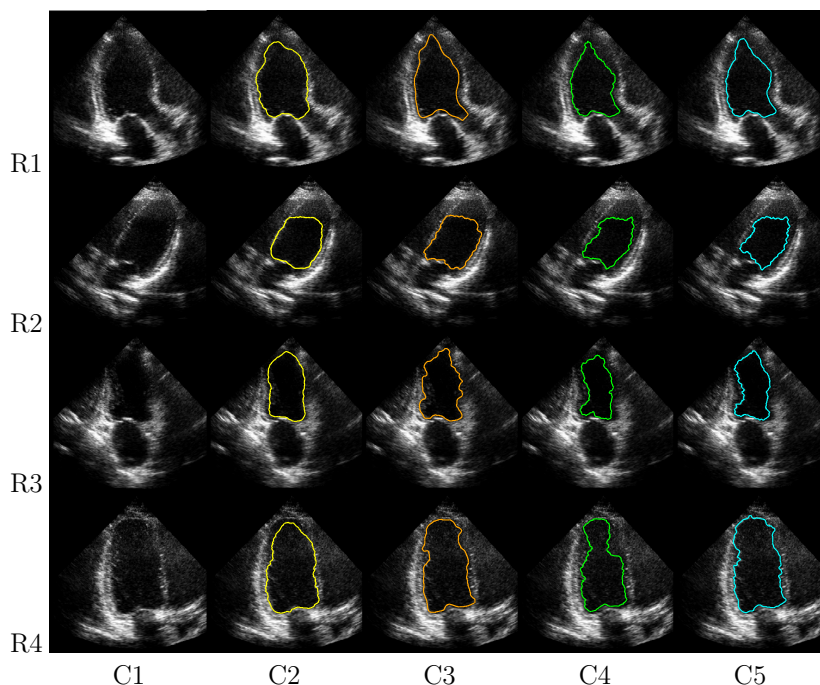


Fig. 4. Results achieved by each method on four sample frames (Rows R1–R4). Each frame shows an example of boundaries characterized by weak edges. C1: the original frame. C2: standard GAC method. C3: local-phase based method. C4: ACWE method. C5: results obtained using the proposed method.

The sensitivity results in Table 2 for each of the CMF + GAC, ACWE and GAC approaches reflect this finding. These results highlight the limitations of data driven approaches in general, in handling particularly low quality data. Notwithstanding this observed fluctuation, however; and considering the results as a whole, it can be observed that the CMF + GAC approach gives the most robust response with respect to accuracy. Overall the sensitivity results indicate that the local-phase approach is the most robust with respect to parameter variance, while this approach achieved the least accuracy in terms of similarity to manual delineation.

When considering the quantitative results in Table 1, it can be seen that using the level-set ACWE method on the whole, while less accurate than the CMF + GAC approach, is capable of achieving reasonable results on low quality data. With this in mind, it could be asked what advantage does solving the Mumford–Shah functional using the CMF approach have over a traditional level set formulation?

In the traditional ACWE approach, tuning all algorithmic parameters can be a challenging and rather unintuitive process, for example it needs to be decided how often and accurately the level set function should be initialized, how the time step sizes should be chosen etc. Choosing the correct parameters for the CMF approach essentially means selecting the regularization parameter  $\nu$  and the penalty parameter  $c$  in the Augmented Lagrangian method. The algorithm converges reliably for a wide range of  $c$ , (in all of our experiments, this value remained unchanged). In addition, the CMF approach shows good robustness with respect to parameter  $\nu$  (compare rows 2 to 3) under CMF + GAC approach, to rows 2–3 of ACWE method, in Table 2. The CMF approach is guaranteed to converge to a global minimizer, in contrast to the level set approach which may get stuck in an inferior local minimum.

The combination of the CMF approach with the GAC method also has some interesting properties with respect to topology. Although the method contains no explicit topology preserving constraint, by relaxing the length constraint for the CMF approach, it becomes possible to favor the generation of closed regions, this is shown for example in Fig. 3(e). Fig. 4 (R1, C3), however, shows an example where this is impossible. In this example, the top left portion of the chamber is outside of the viewing window, as such there is not enough information for the CMF method to ‘reinforce’ the boundary, however, by increasing the stiffness properties of the GAC contour, it is still possible to maintain a closed topology. The reason for this is that the GAC method converges to a local minimizer with simple topology, which in this application is a better solution than the global minimizer. In this way the combination of local and global segmentation methods works to preserve topology.

While it has been shown that the proposed method is capable of accurately segmenting low contrast images; it should be noted that the described method to generate edge sets (step 1) is not proposed as a general edge detector approach, the detection of extremely fine structures, for example, would prove problematic for the model. Instead the method has been designed for the partition of structures with weak boundaries, as exemplified in a variety of real-world applications, a sample of which we have highlighted in the current paper.

Finally, when observing the results it can be seen that global features play a more significant role in the results achieved by the CMF + GAC method, than local edge features, this is a key aspect of the method. While the overall objective of the scheme is accurate boundary estimation, this goal is achieved by integrating regional information into the edge detector process using the CMF method, it is this regional information which makes boundary reinforcement possible.

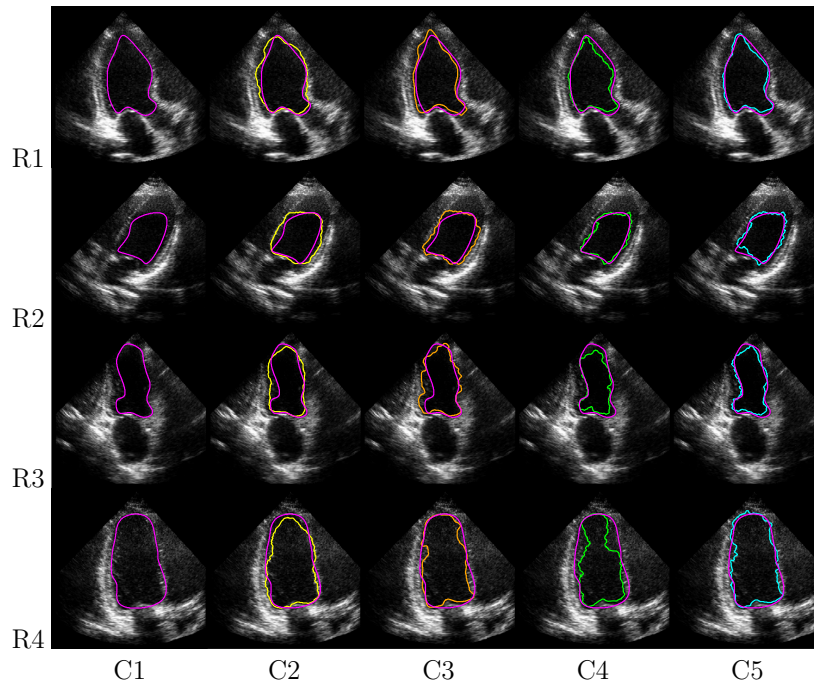


**Fig. 5.** Results showing the similarity between the proposed method and the expert manual delineations. C1–C5: from left to right, the GAC, local-phase method, ACWE and the CMF + GAC method combined with the manual delineation. It can be observed that the standard GAC method, as well as the local-phase based method tend to over-segment the chamber. C4: shows the results of the ACWE method, which on average gives a good result, however it can be seen in R1, R3 and R4; that the proposed method achieves the greater degree of similarity to the reference contour.

## 5. Conclusion

In this work we have presented a method to generate edge detectors which allow for the effective segmentation of regions bounded by weak edges and have demonstrated its performance on a sample of real-world medical and non-medical data. It was shown that compared to classical image driven approaches, the proposed method is capable of more accurately detecting boundaries from low contrast images.

The method we have proposed increases robustness in two ways - first by incorporating regional information into the process of edge map generation, weak boundaries are effectively reinforced, secondly the edge map output which corresponds to a 2 region global segmentation result, gives a more robust solution compared to traditional purely variational based schemes.

Overall, we believe that both the qualitative and quantitative results clearly demonstrate the improved performance of the CMF + GAC approach over purely regional or intensity based methods as exemplified in the GAC and ACWE methods.

## Acknowledgements

The authors would especially like to thank the authors of [19] for providing us with the implementation of the Local Phase method as well as the anonymous reviewers for their valuable comments and suggestions. This work was supported by the National Science Foundation Grant NSF DMS-1217239, UC Lab Fees Research Grant 12-LR-23660, Norwegian Research Council eVita project 214889 and the Irish Research Council.

## References

- [1] X. Bresson, S. Esedoglu, P. Vanderghenst, J.P. Thiran, S. Osher, Fast global minimization of the active contour/snake model, *J. Math. Imaging Vision* 28 (2007) 151–167.
- [2] T.D. Bui, S. Gao, Q. Zhang, A generalized Mumford-Shah model for roof-edge detection, in: *ICIP*, vol. 2, 2005, pp. 1214–1217.
- [3] V. Caselles, R. Kimmel, G. Sapiro, Geodesic active contours, *Int. J. Comput. Vision* 22 (1997) 61–79.
- [4] T. Chan, S. Esedoglu, M. Nikolova, Algorithms for finding global minimizers of image segmentation and denoising models, *SIAM J. Appl. Math.* (2006) 17.
- [5] T. Chan, L. Vese, Active contours without edges, *IEEE Trans. Image Process.* 10 (2001) 266–277.
- [6] N. Duggan, H. Schaeffer, C.L. Guyader, E. Jones, M. Glavin, L. Vese, Boundary detection in echocardiography using a split bregman edge detector and a topology-preserving level set approach, in: *International Symposium on Biomedical Imaging (ISBI)*, IEEE, 2013.
- [7] M. Felsberg, G. Sommer, The monogenic signal, *IEEE Trans. Signal Process.* 49 (2001) 3136–3144.
- [8] H.C. Ford, X. Hui, R. Ciardullo, G.H. Jacoby, K.C. Freeman, The stellar halo of M104. I. A survey for planetary nebulae and the planetary nebula luminosity function distance, *Astrophys. J.* 458 (1996) 455–466, <http://dx.doi.org/10.1086/176828>.
- [9] T. Goldstein, X. Bresson, S. Osher, Geometric applications of the split bregman method: segmentation and surface reconstruction, *J. Sci. Comput.* 45 (2010) 272–293.
- [10] J.M. Hyman, M.J. Shashkov, Natural discretizations for the divergence, gradient, and curl on logically rectangular grids, *Comput. Math. Appl.* 33 (1997) 81–104.
- [11] M. Kass, A. Witkin, D. Terzopoulos, Snakes: active contour models, *Int. J. Comput. Vision* (1987) 321–331.
- [12] S. Kichenassamy, A. Kumar, P. Olver, A. Tannenbaum, A. Yezzi, Conformal curvature flows: from phase transitions to active vision, *Arch. Ration. Mech. Anal.* 134 (1996) 275–301.
- [13] M. Mulet-Parada, J. Noble, 2d+t acoustic boundary detection in echocardiography, *Med. Image Anal.* 4 (2000) 21–30.
- [14] D. Mumford, J. Shah, Optimal approximations by piecewise smooth functions and associated variational problems, *Commun. Pure Appl. Math.* 42 (1989) 577–685, <http://dx.doi.org/10.1002/cpa.3160420503>.

- [15] S. Osher, J.A. Sethian, Fronts propagating with curvature-dependent speed: algorithms based on Hamilton–Jacobi formulations, *J. Comput. Phys* 79 (1988) 12–49.
- [16] N. Paragios, R. Deriche, Unifying boundary and region-based information for geodesic active tracking, in: *IEEE Conference on Computer Vision and Pattern Recognition*, 1999.
- [17] P. Perona, J. Malik, Scale-space and edge detection using anisotropic diffusion, *IEEE Trans. Pattern Anal. Mach. Intell.* 12 (1990) 629–639.
- [18] T. Pock, D. Cremers, H. Bischof, A. Chambolle, An algorithm for minimizing the Mumford–Shah functional, *ICCV (2009)* 1133–1140.
- [19] K. Rajpoot, V. Grau, J. Noble, Local-phase based 3d boundary detection using monogenic signal and its application to real-time 3-d echocardiography images, in: *IEEE International Symposium on Biomedical Imaging*, 2009, pp. 783–786.
- [20] K. Rajpoot, J.A. Noble, V. Grau, C. Szmigielski, H. Becher, Image-driven cardiac left ventricle segmentation for the evaluation of multiview fused real-time 3-dimensional echocardiography images, in: *MICCAI*, 2009, pp. 893–900.
- [21] H. Schaeffer, Active arcs and contours, UCLA CAM Report 12-54, 2012. URL: <<ftp://ftp.math.ucla.edu/pub/camreport/cam12-54.pdf>>.
- [22] H. Schaeffer, L. Vese, Active contours with free endpoints, *J. Math. Imaging Vision* (2013) 1–17.
- [23] L. Vese, T. Chan, A multiphase level set framework for image segmentation using the Mumford and Shah model, *Int. J. Comput. Vision* 50 (2002) 271–293.
- [24] L.L. Wang, Y. Shi, X.C. Tai, Robust edge detection using Mumford–Shah model and binary level set method, in: A. Bruckstein, B. Haar Romeny, A. Bronstein, M. Bronstein (Eds.), *Scale Space and Variational Methods in Computer Vision*, LNCS, vol. 6667, 2012, pp. 291–301.
- [25] J. Weickert, B.M.T.H. Romeny, M.A. Viergever, Efficient and reliable schemes for nonlinear diffusion filtering, *IEEE Trans. Image Process.* 7 (1998) 398–410.
- [26] J. Yuan, E. Bae, X.C. Tai, A study on continuous max-flow and min-cut approaches, in: *2010 IEEE Conference on Computer Vision and Pattern Recognition (CVPR)*, 2010, pp. 2217–2224.
- [27] J. Yuan, E. Bae, X.C. Tai, Y. Boykov, A spatially continuous max-flow and min-cut framework for binary labeling problems, *Numer. Math.* 126 (2014) 559–587.

**Nóirín Duggan**, Egil Bae, Edward Jones, Martin Glavin, Luminita Vese, A Simple Boundary Reinforcement Technique for Segmentation without Prior, Pattern Recognition Letters, Volume 46, 1 September 2014, pp 27-35. DOI: 10.1016/j.patrec.2014.04.014.  
Published

FAST COMMUNICATION

TOPOLOGY PRESERVING ACTIVE CONTOURS\*

HAYDEN SCHAEFFER<sup>†</sup>, NÓIRÍN DUGGAN<sup>‡</sup>, CAROLE LE GUYADER<sup>§</sup>, AND  
LUMINITA VESE<sup>¶</sup>

**Abstract.** Active contours models are variational methods for segmenting complex scenes using edge or regional information. Many of these models employ the level set method to numerically minimize a given energy, which provides a simple representation for the resulting curve evolution problem. During the evolution, the curve can merge or break, thus these methods tend to have steady state solutions which are not homeomorphic to the initial condition. In many applications, the topology of the edge set is known, and thus can be enforced. In this work, we combine a topology preserving variational term with the region based active contour models in order to segment images with known structure. The advantage of this method over current topology preserving methods is its ability to locate boundaries of objects and not only edges. This is particularly useful for highly textured or noisy data.

**Key words.** Active contour, topology preserving, region based models, non-local PDE.

**AMS subject classifications.** 68U10, 65K10.

1. Introduction

Active contour methods segment images by evolving a curve until it captures either boundaries and/or edges. The curve dynamics are typically defined to descend a specified energy towards the minimizer. In general, the energy contains information on the desired structure of the curve as well as quantitative measures of edges and boundaries. In many applications, the topological structure of the edge set is known *a priori* and thus can be embedded in the initial curve. Therefore, we would want the final solution to be homeomorphic to the initial data, although in the popular level set based methods this cannot be guaranteed. Some works in the literature (for example, [7, 10]) have incorporated forcing terms to prevent the change in topology that occurs during the curve evolution process, but mainly focus on locating edges. In this way, those methods are (in some sense) interpolating edge detector information under the condition that some known structure must be preserved. In this work, we show that by using regional information one is able to segment the image while constraining the topology. Our main contribution is the combination of region based active contour models with topological forces.

The first active contour model (Snakes) [8] used a variational method to find the edges in an image  $f$ . Defining the domain as  $\Omega \subset \mathbb{R}^2$  and the edge set as a curve

---

\*Received: August 15, 2013; accepted (in revised form): December 10, 2013. Communicated by Richard Tsai.

<sup>†</sup>520 Portola Plaza, Math Sciences Building 6363, Los Angeles, CA 90095, USA (hschaeffer@ucla.edu).

<sup>‡</sup>Electrical and Electronic Engineering Building, National University of Ireland, Galway, Ireland (nduggan@math.ucla.edu).

<sup>§</sup>INSA Rouen, Laboratory of Mathematics, 685 Avenue de l'Université, 76801 Saint-Etienne-du-Rouvray Cedex, France (carole.le-guyader@insa-rouen.fr).

<sup>¶</sup>520 Portola Plaza, Math Sciences Building 6363, Los Angeles, CA 90095, USA (lvese@math.ucla.edu).

$\mathcal{C}: [0,1] \rightarrow \mathbb{R}^2$ , then the Snakes model is defined below:

$$E_S(\mathcal{C}(s)) = \int_0^1 (\gamma_1 |\mathcal{C}'|^2 + \gamma_2 |\mathcal{C}''|^2) ds - \int_0^1 |\nabla f(\mathcal{C})|^2 ds, \quad (1.1)$$

where  $\gamma_1, \gamma_2 > 0$  are smoothing parameters. The first two terms determine the smoothness of the curve  $\mathcal{C}$ , while the last term keeps the curve close to the edges. Essentially, the last term in equation (1.1) is a variational edge detector that encourages the curve to remain along pixels with sharp gradients. A general edge detector is defined as a function  $g(|\nabla f|)$  which decays to 0 as  $|\nabla f|$  goes to infinity. Typically,  $g$  is small for large arguments and nearly 1 for small arguments, thereby acting as a smoothed edge indicator function.

The geodesic active contours (GAC) model [2, 9] determines the edge set by finding the geodesics of the function  $g$  defined above. Using the function  $g$ , the geodesic energy is defined as

$$E_{GAC}(\mathcal{C}) = \int_0^1 g(|\nabla f(\mathcal{C}(s))|) |\mathcal{C}'(s)| ds \quad (1.2)$$

and represents the length functional with respect to the new edge metric. The curve is drawn to pixels in which  $g(|\nabla f(\mathcal{C}(s))|)$  is close to zero.

While both the Snakes and GAC models measure the edge set via sharp gradients, the Mumford and Shah (MS) model [11] segments the image based on regional information as well as reconstructs a piecewise smooth approximation to the given data. By minimizing

$$E_{MS}(u, \mathcal{C}) = \mu \int_{\Omega \setminus \mathcal{C}} |\nabla u|^2 dx + \gamma \int_{\Omega} |u - f|^2 dx + \mathcal{H}^1(\mathcal{C}), \quad (1.3)$$

the MS model approximates  $f$  by  $u$  as well as finds the edge set  $\mathcal{C}$  which leaves  $u$  smooth. From the MS model perspective, the edge set is the set of boundaries between the smooth regions in the image.

In many cases, the image is well-approximated by a piecewise constant function. With this in mind, the Chan-Vese (CV) model [4] approximates  $f$  by a binary function, which is equal to  $c_1$  in the interior of the region defined by curve  $\mathcal{C}$  and  $c_2$  in the exterior of the region defined by curve  $\mathcal{C}$ . The associated energy is

$$E_{CV}(c_1, c_2, \mathcal{C}) = \gamma \int_{int(\mathcal{C})} |f - c_1|^2 dx + \gamma \int_{int(\mathcal{C})^c} |f - c_2|^2 dx + \nu \text{Length}(\mathcal{C}), \quad (1.4)$$

and minimizers of this energy are binary functions whose discontinuity set is small. The MS and CV models have many extensions, for example to vector valued images in [3], to 4 or more regions [17], to multilayer images in [5], and to curves with free endpoints [15, 16].

In practice, it is possible to get solutions of equation (1.4) to be homeomorphic to the initial condition; for example see the Gestalt theoretical solutions in [4]. However, these solutions are typically local minimizers of the functional above (due to the non-convex structure of the energy). In order to guarantee preservation of the curve topology during its evolution, an additional variational term must be included.

In [7], the authors proposed to use a topology-preserving level set method in order to prevent the topological changes common to the framework. Their method relies on the discrete representation of the curve on the pixel level. They proposed

examining the sign changes of the level set function over each of the pixels near the zero level curve to control the structural changes. By using the notation of simple points (those that can be removed without affecting the topology of the set), they build an algorithm which enforces fixed topology. Thus as the curve evolves, the algorithm monitors sign changes and prevents structural changes.

For level set based shape optimization, [1] proposed using the following logarithmic barrier functional to enforce constant topology:

$$\mathcal{H}(\phi) = - \int_{\mathcal{C}} \log[\phi(x + d\nabla\phi(x))] ds - \int_{\mathcal{C}} \log[-\phi(x - l\nabla\phi(x))] ds, \tag{1.5}$$

where  $d$  and  $l$  are small positive constants and  $\phi$  is a signed distance function whose zero level set is the curve  $\mathcal{C}$ . Equation (1.5) prevents sign changes from occurring near a band around the zero level curve defined by the normal directions and by the parameters  $d$  and  $l$ .

In [10], an alternative variational formulation is given for preserving the topology of level set based methods. The following energy was proposed:

$$T(\phi) := - \iint_{\Omega \times \Omega} \nabla\phi(x) \cdot \nabla\phi(y) G(\|x - y\|) W_l(\phi(x)) W_l(\phi(y)) dx dy, \tag{1.6}$$

where  $W_l(\phi(x)) = \chi_{\{x \in \Omega \mid |\phi(x)| \leq l\}}$ . In this formulation, the topological term is extended over a region via the  $W_l$  functions, rather than a contour integral as in previous methods. Topological changes are measured via gradients and the assumption is that opposite parallel gradients lead to structural changes (see Section 2.1 for more detail).

For edge detection, in [10] the GAC model was augmented by equation (1.6) to preserve structure during edge detection. The model is able to segment the image while remaining homeomorphic to the initial data, but relies on the edge detector in order to locate the proper edges. If the image contains noise, corruption, or texture, edge detection can become unreliable. In particular, because edge detectors rely on gradients to locate jumps, both noise and texture can make this task difficult. Also, when boundaries are not represented by sharp jumps, edge detectors are ineffective. To handle these more general cases, we use region based methods for robustness with the addition of equation (1.6) to enforce structure.

**2. Description of proposed model**

Our model is expressed within the level set framework proposed in [12]. A curve  $\mathcal{C}$  is represented as the zero level set of a Lipschitz continuous function  $\phi: \Omega \rightarrow \mathbb{R}$ , *i.e.*  $\mathcal{C} = \{x \in \Omega, \phi(x) = 0\}$ . This implicit curve representation greatly simplifies the theoretical and practical implementation of the curve evolution process (as it descends towards the minimizer). For example, the length functional [6] can be written as

$$\text{Length}(\mathcal{C}) = \int_{\Omega} |\nabla H(\phi)| = \int_{\Omega} \delta(\phi) |\nabla\phi|, \tag{2.1}$$

where  $H$  is the Heaviside function defined to be 1 for positive arguments and 0 otherwise and  $\delta = H'$  is the Dirac delta measure. In order to differentiate equation (2.1) with respect to  $\phi$  we must take a continuous approximation of  $\delta$ . For example, parameterizing the approximation by  $\epsilon > 0$ , a standard approximation is  $\delta_{\epsilon}(x) = \frac{1}{\pi} \frac{\epsilon}{\epsilon^2 + x^2}$ . Because  $\epsilon$  must be taken at the grid resolution, for imaging problems it is commonly set to  $\epsilon = 1$ . For the rest of this work, we will assume that the following properties hold for the approximated Dirac delta function (dropping the subscript): 1.  $\delta \in C^{\infty}$ , 2.  $\int \delta(x) dx = 1$ , and 3.  $\delta(x) \geq \beta > 0$  for all  $x$ .

**2.1. Topology preserving term.** Let us recall the topological term from Section 1 which we use in our model. The variational term was proposed in [10] and is defined as

$$T(\phi) := - \iint_{\Omega \times \Omega} \nabla \phi(x) \cdot \nabla \phi(y) e^{-\frac{\|x-y\|^2}{d^2}} W_l(\phi(x)) W_l(\phi(y)) \, dx \, dy, \quad (2.2)$$

where  $W_l(\phi(x)) := H(\phi(x)+l)H(l-\phi(x)) = \{x \in \Omega \mid |\phi(x)| \leq l\}$  and  $\phi$  is a signed distance function. Because the gradient of the function  $\phi$  is normal to its level sets, the first term provides a measure of how close level sets are to intersecting each other. If the gradients are nearly anti-parallel, this indicates that the points  $x$  and  $y$  are from different neighborhoods of the curve and are likely to undergo a topological change. The anti-parallel condition is also the reason for the negative sign in equation (2.2). On the other hand, if the gradients are perpendicular to each other and the points are close to each other in space, then the points  $x$  and  $y$  are from the same segment of the curve. The exponential provides a reasonable definition of closeness of the points  $x$  and  $y$ . And lastly, the functions  $W_l$  extend the computational domain from the zero level set of  $\phi$  to a neighborhood around the zero level set. In practice, this provides a buffer region around the curve and defines a minimal distance between different segments of the curve.

**2.2. Our model.** The proposed topology preserving active contours model is

$$\min_{\phi, c_1, c_2} E(\phi, c_1, c_2) = \int_{\Omega} \delta(\phi) |\nabla \phi| + \mu T(\phi) + \gamma \int_{\Omega} [(f - c_1)^2 H(\phi) + (f - c_2)^2 H(-\phi)] \, dx. \quad (2.3)$$

In order to minimize equation (2.3), we take the first variation with respect to each variable. The second two variables  $c_j$  for  $j=1,2$  are the regional means and are calculated as follows:

$$c_1 = \frac{\int_{\Omega} f H(\phi) \, dx}{\int_{\Omega} H(\phi) \, dx}, \quad (2.4)$$

$$c_2 = \frac{\int_{\Omega} f H(-\phi) \, dx}{\int_{\Omega} H(-\phi) \, dx}. \quad (2.5)$$

These expressions are the exact relationship given by the first variations. For the level set function, the standard technique is to embed the first variation of equation (2.3), with respect to  $\phi$ , in an evolution equation. This yields the following:

$$\begin{aligned} \partial_t \phi = & \delta(\phi) \operatorname{div} \left( \frac{\nabla \phi}{|\nabla \phi|} \right) + 4 \frac{\mu}{d^2} W_l(\phi) \int_{\Omega} (x-y) \cdot \nabla \phi(y) e^{-\frac{\|x-y\|^2}{d^2}} W_l(\phi(y)) \, dy \\ & + \gamma \delta(\phi) ((f - c_2)^2 - (f - c_1)^2), \end{aligned} \quad (2.6)$$

with Neumann boundary conditions. In equation (2.6), the first and third terms are concentrated along the curve, while the second term is acting nonlocally throughout the domain. To extend the support of the terms to the entire domain, we further rescale the PDE to

$$\partial_t \phi = |\nabla \phi| \operatorname{div} \left( \frac{\nabla \phi}{|\nabla \phi|} \right) + 4 \frac{\mu}{d^2} W_l(\phi) \int_{\Omega} (x-y) \cdot \nabla \phi(y) e^{-\frac{\|x-y\|^2}{d^2}} W_l(\phi(y)) \, dy$$

$$+ \gamma ((f - c_2)^2 - (f - c_1)^2). \tag{2.7}$$

The first term is the mean curvature of the zero level line (a common rescaling in the level set method), the second term is the topological force, and the last two terms are the regional forces. Notice that at steady state and under the assumption that  $|\nabla\phi|=1$ , equation (2.7) corresponds to the first variation of equation (2.3) along the zero level curve (*i.e.* the steady state of equation (2.6)). The motivation for this rescaling is to correctly balance the nonlocality of the topological force with the other terms in the evolution equation. The topological force plays two roles: it encourages a particular structure on the curve (*i.e.* the topology) as well as influences movement to different regions (*i.e.* a nonlinear force). Therefore, the topological term interacts with both the mean curvature (structure term) and the regional forces. From [10], the rescaling of the curvature term is well-behaved with the topology term. However, we must spread the influence of the regional forces in order to balance with the topological force. This is done by simply removing  $\delta$ . Theorem 2.2 provides further justification for the rescaled equation.

REMARK 2.1. If  $\mu$  is large relative to the other parameters (as well as larger than 1), then it is clear that the resulting evolution will not produce satisfactory results. However, the growth that occurs resembles the fingering effect seen in Hele-Shaw equations. This may be due to the self-repelling and competing dynamics of the topological force.

The rescaled model will descend a new energy, although the minimizer should be identical. The following theorem explains the rescaled equations descend behavior.

THEOREM 2.2. *Let  $\phi(t, x) \in C^1([0, T]; W^{1, \infty}(\Omega))$  be the solution to equation (2.7) with Neumann boundary conditions and  $|\nabla\phi|=1$  a.e. in  $\Omega$ . Then for all  $t > 0$ , the evolution equation decreases an energy, *i.e.*  $\partial_t \bar{E}(\phi) \leq 0$ , where the energy is defined below:*

$$\bar{E}(\phi) = \int_{\Omega} |\nabla\phi| + \mu T(\phi) + \gamma \int_{\Omega} ((f - c_1)^2 - (f - c_2)^2)\phi \, dx, \tag{2.8}$$

for fixed  $c_1$  and  $c_2$ .

*Proof.* We can formally differentiate under the integral to find the energy’s time derivative as follows (for simplicity, we drop the subscript on the integrals):

$$\begin{aligned} & \partial_t \bar{E}(\phi(t, -)) \\ &= \int \frac{\nabla\phi}{|\nabla\phi|} \cdot \nabla\phi_t \, dx - \mu \iint \left\{ [\nabla\phi_t(x) \cdot \nabla\phi(y) + \nabla\phi(x) \cdot \nabla\phi_t(y)] e^{-\frac{\|x-y\|^2}{d^2}} W_l(\phi(x))W_l(\phi(y)) \right. \\ & \quad \left. + \nabla\phi(x) \cdot \nabla\phi(y) e^{-\frac{\|x-y\|^2}{d^2}} [W'_l(\phi(x))W_l(\phi(y))\phi_t(x) + W_l(\phi(x))W'_l(\phi(y))\phi_t(y)] \right\} dx \, dy \\ & \quad + \gamma \int ((f - c_1)^2 - (f - c_2)^2)\phi_t \, dx \\ &= \text{Term}_1 + \text{Term}_2 + \text{Term}_3. \end{aligned}$$

We will investigate this expression term by term. For the first term, integration by parts yields

$$\text{Term}_1 = \int \frac{\nabla\phi}{|\nabla\phi|} \cdot \nabla\phi_t \, dx = - \int \text{div} \left( \frac{\nabla\phi}{|\nabla\phi|} \right) \phi_t \, dx,$$

where boundary terms vanish because of the boundary conditions.

Lastly, the second term is made up of two subterms which we will handle separately:

$$\begin{aligned} \text{Term}_2 &= -\mu \iint [\nabla\phi_t(x) \cdot \nabla\phi(y) + \nabla\phi(x) \cdot \nabla\phi_t(y)] e^{-\frac{\|x-y\|^2}{d^2}} W_l(\phi(x))W_l(\phi(y)) \\ &\quad + \nabla\phi(x) \cdot \nabla\phi(y) e^{-\frac{\|x-y\|^2}{d^2}} \left[ W_l'(\phi(x))W_l(\phi(y))\phi_t(x) \right. \\ &\quad \left. + W_l(\phi(x))W_l'(\phi(y))\phi_t(y) \right] dx dy \\ &= -\mu(\text{Term}_{2a} + \text{Term}_{2b}). \end{aligned}$$

The main task is to separate the variables  $x$  and  $y$  as done in [10]. This can be done via Fubini's theorem, by switching the order of integration and recombining terms to get

$$\begin{aligned} \text{Term}_{2a} &= \iint [\nabla\phi_t(x) \cdot \nabla\phi(y) + \nabla\phi(x) \cdot \nabla\phi_t(y)] e^{-\frac{\|x-y\|^2}{d^2}} W_l(\phi(x))W_l(\phi(y)) dx dy \\ &= \iint \nabla\phi_t(x) \cdot \nabla\phi(y) e^{-\frac{\|x-y\|^2}{d^2}} W_l(\phi(x))W_l(\phi(y)) dx dy \\ &\quad + \iint \nabla\phi(x) \cdot \nabla\phi_t(y) e^{-\frac{\|x-y\|^2}{d^2}} W_l(\phi(x))W_l(\phi(y)) dx dy \\ &= -\int \left( \int \text{div}_x \left( \nabla\phi(y) e^{-\frac{\|x-y\|^2}{d^2}} W_l(\phi(x))W_l(\phi(y)) \right) dy \right) \phi_t(x) dx \\ &\quad - \int \left( \int \text{div}_y \left( \nabla\phi(x) e^{-\frac{\|x-y\|^2}{d^2}} W_l(\phi(x))W_l(\phi(y)) \right) dx \right) \phi_t(y) dy \\ &= -2 \int \left( \int \text{div}_x \left( \nabla\phi(y) e^{-\frac{\|x-y\|^2}{d^2}} W_l(\phi(x))W_l(\phi(y)) \right) dy \right) \phi_t(x) dx \\ &= 2 \int \left( \int \left( \frac{2(x-y)}{d^2} \cdot \nabla\phi(y) e^{-\frac{\|x-y\|^2}{d^2}} W_l(\phi(x))W_l(\phi(y)) \right) dy \right) \phi_t(x) dx \\ &\quad - 2 \int \left( \int \left( \nabla\phi(y) \cdot \nabla\phi(x) e^{-\frac{\|x-y\|^2}{d^2}} W_l'(\phi(x))W_l(\phi(y)) \right) dy \right) \phi_t(x) dx. \end{aligned}$$

The second equality is simply integration by parts and the last equality is true by a change of variables. For the second subterm, a similar trick yields

$$\begin{aligned} \text{Term}_{2b} &= \iint \nabla\phi(x) \cdot \nabla\phi(y) e^{-\frac{\|x-y\|^2}{d^2}} \\ &\quad [W_l'(\phi(x))W_l(\phi(y))\phi_t(x) + W_l(\phi(x))W_l'(\phi(y))\phi_t(y)] dx dy \\ &= \iint \nabla\phi(x) \cdot \nabla\phi(y) e^{-\frac{\|x-y\|^2}{d^2}} W_l'(\phi(x))W_l(\phi(y))\phi_t(x) dx dy \\ &\quad + \iint \nabla\phi(x) \cdot \nabla\phi(y) e^{-\frac{\|x-y\|^2}{d^2}} W_l(\phi(x))W_l'(\phi(y))\phi_t(y) dx dy \\ &= 2 \int \left( \int \nabla\phi(x) \cdot \nabla\phi(y) e^{-\frac{\|x-y\|^2}{d^2}} W_l'(\phi(x))W_l(\phi(y)) dy \right) \phi_t(x) dx. \end{aligned}$$

In this form we can combine both of the subterms together to get (with some cancellation)

$$\text{Term}_2 = -\frac{4\mu}{d^2} \int \left( \int \left( (x-y) \cdot \nabla\phi(y) e^{-\frac{\|x-y\|^2}{d^2}} W_l(\phi(x))W_l(\phi(y)) \right) dy \right) \phi_t(x) dx.$$

Each of the terms above separate the time derivative of  $\phi$  from the main part of the integrand. Factoring out  $\phi_t$  and combining all the computed terms yields

$$\begin{aligned} & \partial_t \bar{E}(\phi(t, -)) \\ &= - \int \left[ \operatorname{div} \left( \frac{\nabla \phi}{|\nabla \phi|} \right) + \gamma ((f - c_2)^2 - (f - c_1)^2) \right. \\ & \quad \left. + \frac{4\mu}{d^2} W_l(\phi) \int (x - y) \cdot \nabla \phi(y) e^{-\frac{\|x - y\|^2}{d^2}} W_l(\phi(y)) \, dy \right] \phi_t(x) \, dx \\ &= - \int \phi_t^2 \, dx \\ &\leq 0, \end{aligned}$$

because  $\phi$  satisfies equation (2.7) and  $|\nabla \phi| = 1$  a.e. □

The argument above holds (with some additional work) for the original evolution equation (equation (2.6)) and the model (equation (2.3)). For clarity, we state it below.

**THEOREM 2.3.** *Let  $\phi(t, x) \in C^1([0, T]; W^{1, \infty}(\Omega))$  be the solution to equation (2.6) with Neumann boundary conditions. Then, for all  $t > 0$ , we have  $\partial_t E(\phi, c_1, c_2) \leq 0$ .*

In the case of the original PDE, the energy is minimized by the evolution of  $\phi$  and the variables  $c_1$  and  $c_2$ .

**2.3. Parameters.** Altogether this model has several (positive) parameters,  $\gamma$ ,  $\mu$ ,  $d$ , and  $l$ . Parameter  $d$  determines the region of nonlocality for the topology preserving term, specifically, the neighborhood defined in the topological term grows with  $d$ . Because the function  $\phi$  remains close to a signed distance function, parameter  $l$  determines the characteristic distance (in terms of pixel size) between any two points on the curve. For our experiments, the parameters were set to  $d = 4$  and  $l = 1$ . The energy balancing parameters  $\gamma$  and  $\mu$  determine the curve structure. If  $\mu$  is small relative to  $\gamma$ , then the resulting evolution will undergo topological changes. In practice, keeping  $\mu$  close to 1 produces appropriate results. The parameter can be weakened in order to encourage a particular genus with some flexibility (allowing small amounts of deviation of topology from the initial curve). Without tuning of the parameters, the model will encourage the topology of the curve to remain close to the initial structure.

There is an additional parameter  $k$  which is used to accelerate the evolution and avoid local minima. This is not always necessary, but may be more practical in applications. In the general level set framework, it is common to add a balloon term  $k|\nabla \phi|$ , for constant  $k$ , which helps to shrink or grow the curve (depending on the sign of  $k$ ). For our dynamics, the additional term would force equation (2.7) out of the true steady state, for non-zero  $k$ . In order to avoid this effect, the parameter can be made time-dependent  $k(t)$ , with the condition that  $k(t) = 0$  for all  $t > T$ . This is done in some numerical experiments to accelerate the curve towards the edge set.

**3. Numerical method**

We set the time step to  $dt$  and the space step  $dx = 1$  (in the equations below, we drop  $dx$ ). To solve equation (2.7) to steady state, we use an additive operator splitting scheme as in [10]. The discretized equation is below:

$$\phi^{n+1} = \frac{1}{2} \sum_p (I - 2dt A_p(\phi^n))^{-1} \left( \phi^n + dt \gamma ((f - c_2)^2 - (f - c_1)^2) \right)$$

$$+ 4 \frac{dt}{d^2} \mu W_l(\phi^n) \int_{\Omega} (x-y) \cdot \nabla \phi^n(y) e^{-\frac{\|x-y\|^2}{d^2}} W_l(\phi^n(y)) dy, \quad (3.1)$$

where  $p$  is the direction ( $x$  and  $y$ ) and a vectorial representation of  $\phi^n$  is used via concatenation of rows, for instance. The operator  $A_p := (a_{ij})$  is defined pixel-wise as follows:

$$a_{ij}(\phi) = \begin{cases} |\nabla \phi|_i \left( \frac{2}{|\nabla \phi|_i + |\nabla \phi|_j} \right), & \text{if } j \in \mathcal{N}(i), \\ -|\nabla \phi|_i \sum_{k \in \mathcal{N}(i)} \left( \frac{2}{|\nabla \phi|_i + |\nabla \phi|_k} \right), & \text{if } j = i, \\ 0, & \text{otherwise,} \end{cases} \quad (3.2)$$

where  $\mathcal{N}(i)$  is the neighborhood around  $i$  (adjacent pixels). For each  $p$ , the system can be solved via the Thomas algorithm, because it is a strictly diagonally dominant tridiagonal linear system. The resulting method has linear complexity at each time step. If one considers the method without the topological force, then it can be shown that the discretization is unconditionally stable.

The dimensional generalizations are direct, for example, the 3D discretized equation is below:

$$\begin{aligned} \phi^{n+1} = & \frac{1}{3} \sum_p (I - 3dt A_p(\phi^n))^{-1} \left( \phi^n + dt \gamma((f - c_2)^2 - (f - c_1)^2) \right. \\ & \left. + 4 \frac{dt}{d^2} \mu W_l(\phi^n) \int_{\Omega} (x-y) \cdot \nabla \phi^n(y) e^{-\frac{\|x-y\|^2}{d^2}} W_l(\phi^n(y)) dy \right). \end{aligned} \quad (3.3)$$

One example of segmentation using our algorithm in 3 dimensions is provided.

Because the topological term must have the level set function close to a signed distance function, re-initialization is required. Following the method in [14], we iterate the following systems to convergence:

$$\psi^0 := \phi^n, \quad (3.4)$$

$$\psi_{ij}^{k+1} = \begin{cases} \psi_{ij}^k - dt (\text{sign}(\psi_{ij}^0) |\psi_{ij}^k| - D_{ij}), & \text{if } (i, j) \in \Lambda, \\ \psi_{ij}^k - dt \text{sign}(\psi_{ij}^0) G(\psi)_{ij}, & \text{otherwise,} \end{cases} \quad (3.5)$$

where the set  $\Lambda$  contains all  $(i, j)$  such that

$$\phi_{ij}^n \phi_{i+1,j}^n < 0, \quad \phi_{ij}^n \phi_{i,j+1}^n < 0, \quad \phi_{ij}^n \phi_{i-1,j}^n < 0, \quad \text{or} \quad \phi_{ij}^n \phi_{i,j-1}^n < 0.$$

In equation (3.5),  $D_{ij}$  is the numerical distance to  $\mathcal{C}$  and can be calculated to be

$$D_{ij} = \frac{\psi_{ij}^0}{\sqrt{(D_x^0 \psi_{ij}^0)^2 + (D_y^0 \psi_{ij}^0)^2}}, \quad (3.6)$$

where  $D^0$  is the central difference operator. The upwind discretized re-initialization equation is given by

$$G(\psi)_{ij} := \begin{cases} \sqrt{\max((D_x^- \psi_{ij})_+^2, (D_x^+ \psi_{ij})_-^2) + \max((D_y^- \psi_{ij})_+^2, (D_y^+ \psi_{ij})_-^2)} - 1, & \text{if } \psi_{ij} > 0, \\ \sqrt{\max((D_x^- \psi_{ij})_-^2, (D_x^+ \psi_{ij})_+^2) + \max((D_y^- \psi_{ij})_-^2, (D_y^+ \psi_{ij})_+^2)} - 1, & \text{if } \psi_{ij} < 0, \end{cases}$$

where  $D^+$  and  $D^-$  are the forward and backward differences,  $f_+ := \max(f, 0)$ , and  $f_- := \min(f, 0)$ . Once this iterative process converges we assign  $\phi^n := \psi^\infty$  and continue

the evolution. The re-initialization is only done for a few iterations, for example, when  $n$  is a multiple of 50.

It should be noted that from [14], we know that this method's error is independent of the number of iterations, therefore the re-initialization process does not change the location of the curve. This is particularly important for the topology preservation, because the drifting caused by some re-initialization algorithms could change the results.

#### 4. Results

The method is tested on several synthetic and real images containing various features. We provide a three dimensional result using the current algorithm as well as a possible extension for textured images. For the noisy images presented here, the noise variance is reported as the percent of the maximum intensity value of the given image.

**4.1. Two dimensional examples.** In figure 4.1 the algorithm is tested on a synthetic image containing two black discs on a white background. Noise is added in order to test the algorithms ability to preserve topology with highly corrupted images. As the curve evolves, it first captures part of the boundary of the discs then shrinks inward along the edges. The steady state solution resembles a bent dumbbell and is homeomorphic to the initial curve.

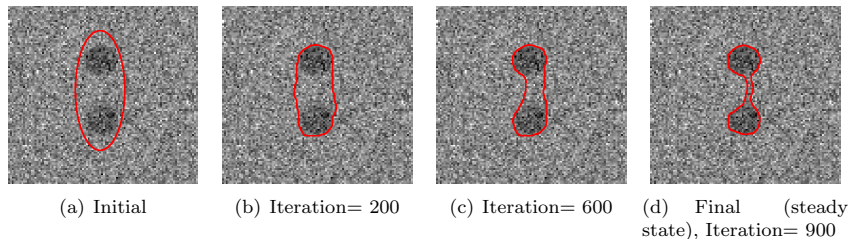


FIG. 4.1. Our algorithm applied to the two discs example with 70% noise. The model parameters are set to  $\gamma=0.195$  and  $\mu=0.4$ .

For comparison to existing methods, we test our algorithm on the Hand image in figure 4.2. As the curve grows outward along each digit, each segment evolves separately. The steady state solution contains one continuous curve. Similar results can be found in [7] and in [10] for the noise-free case only. The addition of the large amount of noise further connects the digits, making the segmentation more complicated than in the noise-free case.

In figure 4.3, the algorithm is tested on a photograph of a bear. The image is highly textured, which can cause issues with gradient-based edge detectors. The curve locates the boundary of the bear without capturing the nose or grass (whose mean is closer to the background).

For the next few examples, the algorithm is tested on MRI scans of a human brain with Gaussian noise. In the first image (figure 4.4), the curve quickly locates the boundary of the brain (within 90 iterations), and continues to grow inward to refine the detection. In the other two images (figure 4.5 and 4.6), with the choice of initialization, the curve grows along the boundary of the object as well as shrinks

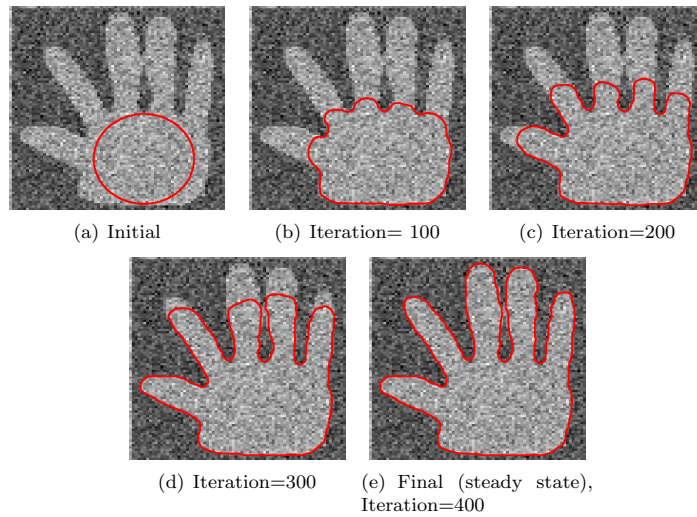


FIG. 4.2. Our algorithm applied to the Hand image with 15% noise. The model parameters are set to  $\gamma=2.2$  and  $\mu=0.5$ .

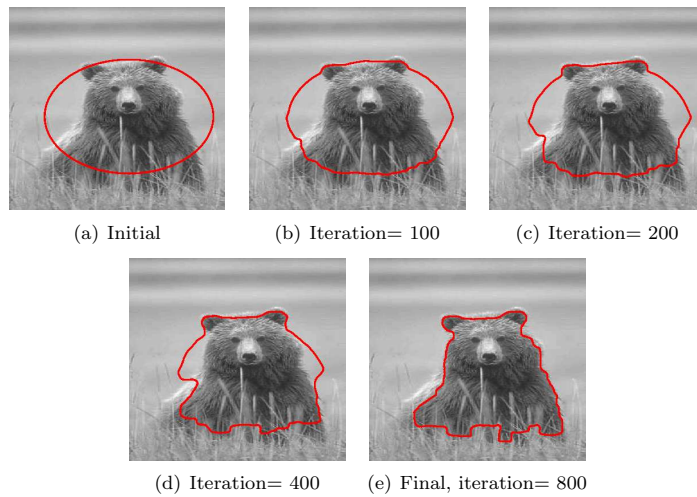


FIG. 4.3. Our algorithm applied to the highly textured Bear photograph. The model parameters are set to  $\gamma=3$  and  $\mu=0.8$ .

within the small regions. The steady state solutions are all homeomorphic to the initial condition as well as contain the fine details of the detected object.

In figure 4.7, we apply the algorithm from [10] to two noisy images to compare the results. In both cases, the curve is initialized the same way as in our corresponding examples, and the parameters are optimized manually. In figure 4.7(a), the curve is stuck in a local minimum and does not locate many of the edges. In figure 4.7(b), the

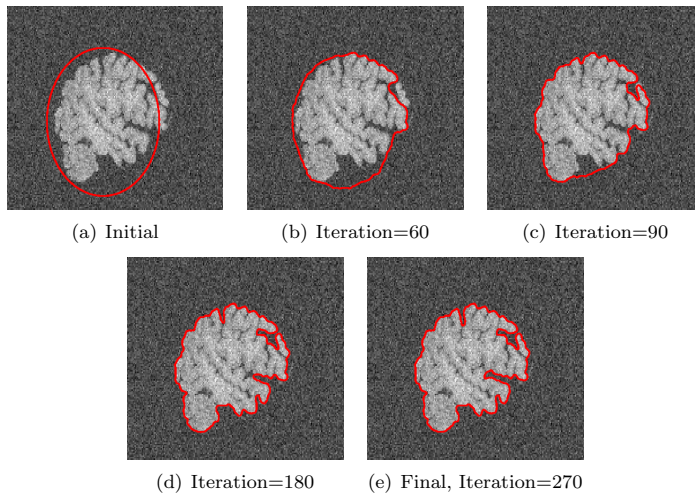


FIG. 4.4. *Our algorithm applied to an MRI scan of a brain. The model parameters are set to  $\gamma = 1.45$  and  $\mu = 0.5$ .*

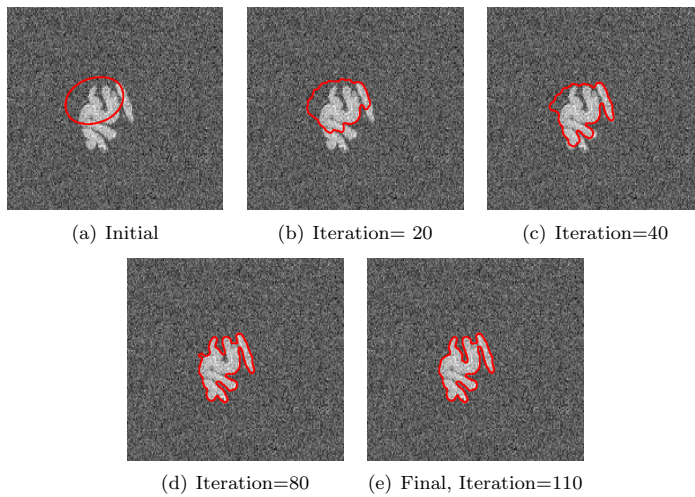


FIG. 4.5. *Our algorithm applied to an MRI scan of a brain. The model parameters are set to  $\gamma = 2$  and  $\mu = 1.2$ .*

curve finds the correct outer edge, but because of the high level of noise, is unable to locate the interior structures.

**4.2. Three dimensional examples.** As a proof of concept, we provide a 3D example using an MRI brain scan in figure 4.8. By monitoring the Euler characteristic of the zero level set function, we can numerically verify that the structure is preserved. From the two different perspectives of the steady state solution displayed in figure 4.8,

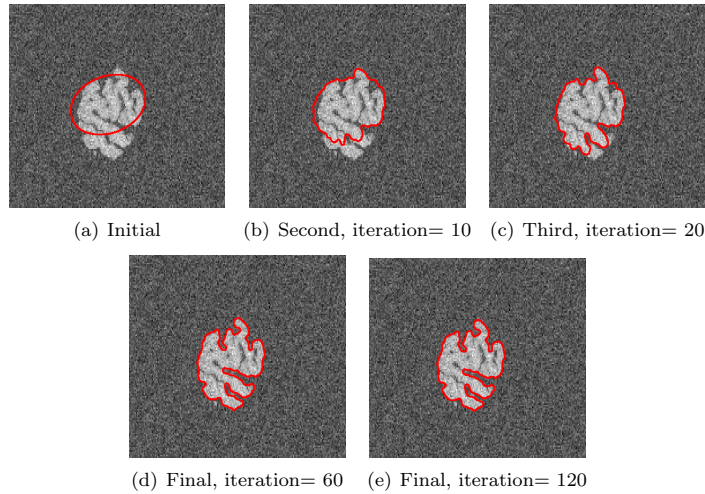


FIG. 4.6. Our algorithm applied to an MRI scan of a brain. The model parameters are set to  $\gamma=2$  and  $\mu=2$ .

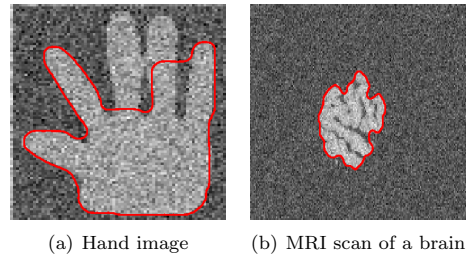


FIG. 4.7. Results of the method in [10] applied to the hand and MRI scan of a brain. The resulting curve on the hand image is stuck in a local minimum. The curve in the brain image is able to locate the outer edges, but cannot locate the interior ones.

the finer boundary structures can be seen as well as the crevasses. In the 3D case, to accelerate the convergence to steady state, we add the term  $k(t)|\nabla\phi|$  to the evolution equation and set  $k(t)=0.05$  for  $t < 400$  and  $k(t)=0$  otherwise.

**4.3. Extensions.** The regional terms used in equation (2.3) fit the data to the means in each region; however, it is possible to fit the data to any probabilistic model. For textured images, the authors of [13] proposed modeling the regional intensity values as samples from a Gaussian distribution. Using the regional term from [13], our model can be extended to the following:

$$\begin{aligned} & \min_{\phi, c_1, c_2, \sigma_1, \sigma_2} E_G(\phi, c_1, c_2, \sigma_1, \sigma_2) \\ &= \int_{\Omega} \delta(\phi) |\nabla\phi| + \mu T(\phi) + \gamma \int_{\Omega} \left( \log(\sigma_1) + \frac{(f - c_1)^2}{\sigma_1} \right) H(\phi) \end{aligned}$$

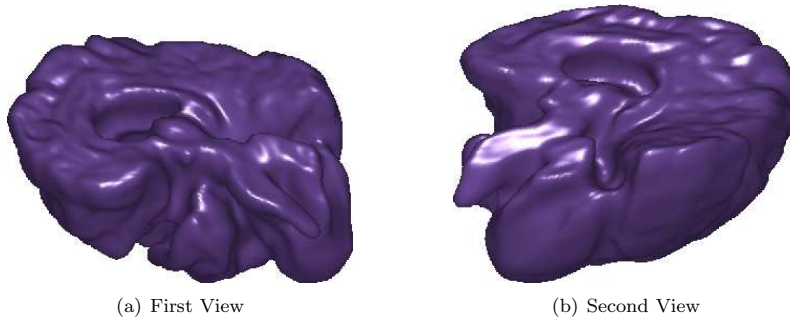


FIG. 4.8. Our algorithm applied to a 3D MRI scan of a brain. The model parameters are set to  $\gamma=1 \times 10^{-6}$  and  $\mu=0.2$ .

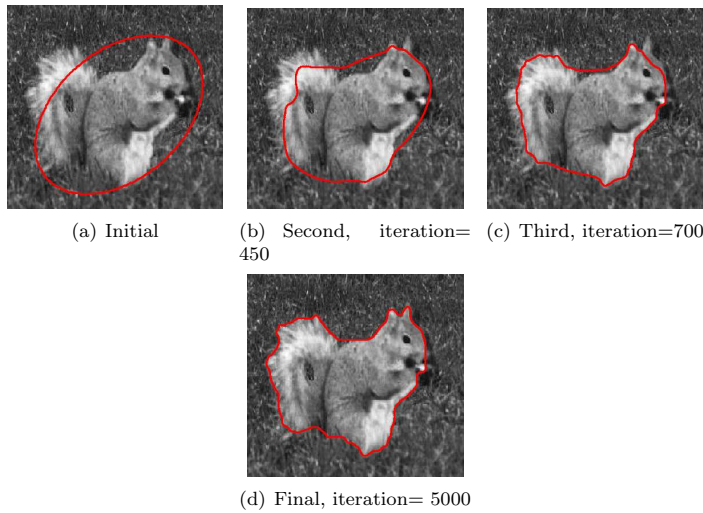


FIG. 4.9. Our algorithm applied to a 3D MRI scan of a brain. The model parameters are set to  $\gamma=2.8 \times 10^{-5}$  and  $\mu=0.3$ .

$$+ \left( \log(\sigma_2) + \frac{(f - c_2)^2}{\sigma_2} \right) H(-\phi) \, dx. \tag{4.1}$$

As a proof of concept, we test this extension on an image of a squirrel in figure 4.9. In order to avoid local minima, we include a balloon forcing term with coefficient equal to 0.12. Because the foreground and background texture are seemingly random, modeling their intensity values as Gaussian with different parameters seems to capture the correct boundary.

**5. Conclusion**

We have proposed a region based topology preserving active contours model. Unlike previous work on topology preserving segmentation, our method is not depen-

dent on an edge detector for pre-segmenting the image. Also, as demonstrated in the results, our method handles noisy and highly textured images well. For further applications, the model can easily be extended by either including a geodesic length term in place of the standard length or by changing the regional forces.

**Acknowledgement.** This research was supported by the UC Lab Fees Research Grant 12-LR-236660 and NSF DMS 1217239. H. Schaeffer was supported by the Department of Defense (DoD) through the National Defense Science and Engineering Graduate Fellowship (NDSEG). N. Duggan would like to acknowledge the support of the Irish Research Council (formerly the Irish Research Council for Science, Engineering and Technology) and the contribution of Dr. Martin Glavin and Dr. Edward Jones of Electrical and Electronic Engineering at the National University of Ireland, Galway in the completion of her research.

#### REFERENCES

- [1] O. Alexandrov and F. Santosa, *A topology-preserving level set method for shape optimization*, J. Comput. Phys., 204(1), 121–130, 2005.
- [2] R. Caselles, V. Kimmel, and G. Sapiro, *Geodesic active contours*, Inter. J. Comput. Vision, 22(1), 61–79, 1997.
- [3] T.F. Chan, B.Y. Sandberg, and L.A. Vese, *Active contours without edges for Vector-Valued images*, J. Visual Commun. Image Represent., 11(2), 130–141, 2000.
- [4] T.F. Chan and L.A. Vese, *Active contours without edges*, IEEE Trans. Image Proc., 10(2), 266–277, 2001.
- [5] G. Chung and L.A. Vese, *Image segmentation using a multilayer level-set approach*, Comput. Vis. Sci., 12(6), 267–285, 2008.
- [6] L.C. Evans and R.F. Gariepy, *Measure Theory and Fine Properties of Functions*, CRC Press, 1992.
- [7] X. Han, C. Xu, and J.L. Prince, *A topology preserving level set method for geometric deformable models*, IEEE Trans. Pattern Anal. Machine Int., 25(6), 755–768, 2003.
- [8] M. Kass, A. Witkin, and D. Terzopoulos, *Snakes: Active contour models*, Inter. J. Comput. Vision, 1(4), 321–331, 1988.
- [9] S. Kichenassamy, A. Kumar, P. Olver, A. Tannenbaum, and A. Yezzi, *Gradient flows and geometric active contour models*, in Proceedings of the Fifth International Conference on Computer Vision, 810–815, 1995.
- [10] C. Le Guyader and L.A. Vese, *Self-repelling snakes for topology-preserving segmentation models*, IEEE Trans. Image Proc., 17(5), 767–779, 2008.
- [11] D. Mumford and J. Shah, *Optimal approximations by piecewise smooth functions and associated variational problems*, Commun. Pure Appl. Math., 42(5), 577–685, 1989.
- [12] S. Osher and J.A. Sethian, *Fronts propagating with curvature-dependent speed: Algorithms based on Hamilton-Jacobi formulations*, J. Comput. Phys., 79(1), 12–49, 1988.
- [13] M. Rousson and R. Deriche, *Adaptive segmentation of vector valued images*, in Geometric Level Set Methods in Imaging, Vision, and Graphics, 195–205, 2003.
- [14] G. Russo and P. Smereka, *A remark on computing distance functions*, J. Comput. Phys., 163(1), 51–67, 2000.
- [15] H. Schaeffer, *Active arcs and contours*, UCLA CAM Report, 12–54, 2012.
- [16] H. Schaeffer and L. Vese, *Active contours with free endpoints*, J. Math. Imaging and Vision, 49(1), 20–36, 2014.
- [17] L.A. Vese and T.F. Chan, *A multiphase level set framework for image segmentation using the Mumford and Shah model*, Inter. J. Comput. Vision, 50(3), 271–293, 2002.

Hayden Schaeffer, **Nóirín Duggan**, Carole Le Guyader, Luminita Vese, Topology Preserving Active Contours, Communications in Mathematical Sciences. Volume 12, Issue 7. Pages: 1329–1342. DOI: 10.4310/CMS.2014.v12.n7.a8. Published.

## BOUNDARY DETECTION IN ECHOCARDIOGRAPHY USING A SPLIT BREGMAN EDGE DETECTOR AND A TOPOLOGY PRESERVING LEVEL SET APPROACH

*N. Duggan<sup>1,2</sup>, H. Schaeffer<sup>2</sup>, C. Le Guyader<sup>3</sup>, E. Jones<sup>1</sup>, M. Glavin<sup>1</sup>, L. Vese<sup>2</sup>*

<sup>1</sup> Electrical & Electronic Engineering, National University of Ireland, Galway, Ireland

<sup>2</sup> Dept. of Mathematics, University of California, Los Angeles, CA, USA

<sup>3</sup> INSA ROUEN, Laboratoire de Mathématiques de l'INSA, Saint-Étienne-du-Rouvray cedex, France

### ABSTRACT

In the current paper a novel approach for echocardiographic segmentation is proposed based on a combination of the Geometric Active Contour Split Bregman (GSB) method with a topology preserving level set method. The proposed method was tested against manual delineations on 20 frames across 2 datasets and achieved an average Hausdorff distance of  $4.01 \pm 1.06$ mm and Mean Absolute distance of  $1.62 \pm 0.3$ mm, which represented an enhanced performance when compared with intensity gradient and region based methods.

**Index Terms**— Segmentation, Echocardiography, Geometric Split Bregman, Topology Preserving Level Set Method

### 1. INTRODUCTION

Echocardiography remains one of the most popular medical imaging modalities, however degradations due to speckle, signal drop out, intensity inhomogeneity as well as relatively low spatial resolution make accurate visualization of cardiac structures difficult. In this context, the development of computer aided segmentation schemes aimed at improving visualization and investigation is particularly relevant. In the current work a combination of variational and convex segmentations methods is proposed for application to 2D echocardiographic sequences.

In a variational setting, segmentation is viewed as an energy minimization process, where segmentation of a given image is computed by evolving curves in the direction of the negative energy gradient. In this setting the curve can be expressed by an explicit contour following the approach of [1], or implicitly using techniques based on curve evolution theory [2, 3]. In either case the energy terms evolve the curve towards discontinuities in the image which are taken to 'abstractly' represent objects of interest. For a summary of the mathematical description of variational methods for image segmentation, we refer the reader to [4].

In [5], the authors integrated boundary and regional information in one model. The level set based evolution equations are determined by three main terms: a boundary attracting term, an intensity (region) term, and a motion-based term. The effectiveness of the region based terms are highly dependent on the quality of the images since they depend on global statistics [5]. Due to high levels of noise, intensity inhomogeneity, and the presence of false contours in our data, this approach typically is not optimal for echocardiography.

This research was supported by the Irish Research Council for Science, Engineering and Technology (IRCSET) Embark Initiative, UC Lab Fees Research grant 12-LR-23660, by a National Defense Science and Engineering Graduate (NDSEG) Fellowship, and the National Science Foundation grant NSF-DMS 0714945.

To better handle the low contrast and high noise levels in echocardiography images, the authors in [6] proposed a real-time intensity invariant method to extract edge (feature) information. The proposed filter uses a local phase based method to extract boundary information. The method provides a finer edge extraction than gradient detectors; however, due to its intensity invariance, it tends to over-segment the image.

An interesting work for the segmentation of 3D radio frequency echocardiography using a spatio-temporal predictor is proposed in [7]. The left ventricular endocardial boundaries are segmented.

In the present paper we propose to use the Split Bregman method for Geometric Applications [8] as a front end preconditioning step to the Topology Preserving Level Set (TPLS) method of [9], we then apply a diffusion based post processing method to produce the final segmentation. The remainder of this paper is organized as follows.

In section 2 we describe our proposed model. The validation process is described in section 3. In section 4 we present our conclusions.

### 2. METHODOLOGY

In the current section, we present our proposed sequential segmentation model for echocardiography which addresses some of the weaknesses of these previous methods; firstly to increase contrast between significant structures, we apply a geometric segmentation method from [4] to the dataset that combines geodesic active contours [3] with active contours without edges [10] and solved using the split Bregman method [11] (see also [12]). This is different from the standard edge detectors in the literature, since typically non-linear filters are difficult to compute, while the use of the split Bregman technique efficiently computes an appropriate edge set. To obtain a single curve which captures the inner boundary of the chamber, we apply the TPLS method [9] to the dataset, finally a diffusion based post processing method is applied to smooth the final set of curves (removing any local variations due to the data). The integration of the regional information through the edge detector provides a different combination model than in previous methods.

#### 2.1. Geometric Split Bregman Method

The first step in the method was to produce a clean edge-detector to accurately capture the structure under observation, for this the Geometric Split Bregman method was used. Let  $I$  be the given input image defined on an open and bounded set  $\Omega$  in the plane. In [4] the

authors solve the model:

$$\min_{0 \leq u \leq 1} |\nabla u|_g + \mu \langle u, r \rangle \quad (1)$$

where  $r = (c_1 - I)^2 - (c_2 - I)^2$

In this equation,  $|\nabla u|_g = \int_{\Omega} g |\nabla u| dx dy$  is the weighted Total Variation,  $g$  is an edge-function, while  $\langle u, r \rangle$  is the data fidelity term, defined as

$$\langle u, r \rangle = \int_{\Omega} ur dx dy$$

for which  $\mu$  acts as a scaling parameter. We refer the reader to [8] for specific details of the solution, here we simply provide the resulting sequence of optimization problems:

$$\begin{aligned} (u^{k+1}, \bar{d}^{k+1}) = \arg \min_{0 \leq u \leq 1, \bar{d}} & |\bar{d}|_g + \mu \langle u, r \rangle \\ & + \frac{\lambda}{2} \|\bar{d} - \nabla u - \bar{b}^k\|^2 \\ \bar{b}^{k+1} = & \bar{b}^k + \nabla u^k - \bar{d}^k. \end{aligned} \quad (2)$$

The constants  $c_1$  and  $c_2$  are updated at each step  $k$  as the averages of  $I$  inside and outside of the set  $\{(x, y) \in \Omega : u(x, y) > \mu\}$  respectively, thus the output  $\bar{I}$  is a binary image taking the final values  $c_1$  and  $c_2$  over the two regions. In the problem we are investigating, a gradient based edge detector oversegments the image by locating false edges outside the chamber region. The above Geometric Split Bregman method acts as a regularized edge detector, locating major regions of interest, while avoiding these false edges. Using the Split Bregman implementation makes the computational cost of implementing this method equivalent to those of simple edge detectors (*i.e.* Canny). However, it also locates the inner and outer chamber regions, since those locations have a sharp contrast.

## 2.2. Topology Preserving Level Set Method

Once the edge detector is obtained, the second step in our proposed solution was to produce curves representing the outline of the endocardium boundary.

For our contour finding approach we made use of the topology constraining model developed in [9]. To initialize the method for frame 1 of our dataset, we placed an initial guess inside the left ventricle chamber. Each subsequent frame was initialized by the final segmentation of the previous frame. The segmentation model proposed in [9] minimizes a functional formed of the geodesic active contour term [3] and

$$\begin{aligned} E(\phi) = & - \int_{\Omega} \int_{\Omega} \exp\left(\frac{-\|x-y\|^2}{\sigma^2}\right) \langle \nabla \phi(x), \nabla \phi(y) \rangle \\ & \cdot H(\phi(x) + l) H(l - \phi(x)) H(\phi(y) + l) H(l - \phi(y)) dx dy \end{aligned} \quad (3)$$

Here  $x$  and  $y$  are two neighboring points as determined by the windowing function  $\exp(\frac{-\|x-y\|^2}{\sigma^2})$ ;  $l$  and  $\sigma$  are parameters and the unknown  $\phi$  is a level set function whose zero-level curve will define the evolving contour, while  $H$  is the Heaviside function. If the outward normal vectors to the level lines passing through  $x$  and  $y$  have opposite directions, the inner product term  $-\langle \nabla \phi(x), \nabla \phi(y) \rangle$  causes the energy functional to increase sharply thereby avoiding breaking or merging of the curve. The associated Euler-Lagrange equation for

the complete TPLS model is given by:

$$\begin{aligned} \frac{\partial \phi}{\partial t} = & \delta_{\epsilon}(\phi) \operatorname{div} \left( g \frac{\nabla \phi}{\|\nabla \phi\|} \right) \\ & + 4 \frac{\chi}{\sigma^2} H_{\epsilon}(\phi(x) + l) H_{\epsilon}(l - \phi(x)) \\ & \cdot \int_{\Omega} \left[ ((x_1 - y_1) \frac{\partial \phi}{\partial y_1}(y) + (x_2 - y_2) \frac{\partial \phi}{\partial y_2}(y)) \right. \\ & \left. \cdot \exp\left(\frac{-\|x-y\|^2}{\sigma^2}\right) H_{\epsilon}(\phi(y) + l) H_{\epsilon}(l - \phi(y)) \right] dy \end{aligned} \quad (4)$$

where  $\chi$  is a weighting parameter for the topology constraint and  $\sigma$  and  $l$  are constants. In (4)  $g$  is a function of  $\|\nabla I\|$ , however this is limiting since in practice it leads to a noisy edge set. By using the binary output image,  $\bar{I}$  from Section 2.1 we define  $g(\bar{I}, \|\nabla \bar{I}\|)$  thus attracting the curve to the regions of major interest while avoiding false edges. In particular we choose:

$$g(\bar{I}, \|\nabla \bar{I}\|) := \gamma \bar{I} + \frac{1}{1 + \beta \|\nabla \bar{I}\|^2} \quad (5)$$

## 2.3. Edge Refinement Step

To overcome the effects of the low spatial resolution of 2D echocardiography which together with imaging acquisition effects combine to produce boundaries often defined by jagged and oscillatory edges, we evolved the output contour from the TPLS method according to a mean curvature smoothing model defined by:

$$\frac{\partial \phi}{\partial t} = b \kappa |\nabla \phi| \quad (6)$$

where  $b$  is a positive constant while  $\kappa$  represents the mean curvature [2].

The output of this model is a smooth curve which accurately captures the boundary of the chamber, it is this output which we take as our final segmentation result.

## 2.4. Complete Segmentation Model

Altogether, the proposed method combines variations of both the GSB and the TPLS methods, which are both adapted to boundary detection in 2D echocardiography. To summarize, we first create a binary form of the original image and extract the major edge set using GSB. This information is used to better initialize the TPLS, which locates the endocardial boundary. At the end, we slightly evolve the curve by mean curvature flow in order to smooth the final edge set.

In the following section we apply the proposed method to real-world echocardiographic images and analyze the results in comparison to manually delineated curves.

## 3. EXPERIMENTAL RESULTS

To validate the method we tested it on 20 frames from 2 echocardiographic datasets exhibiting low to medium image quality and compared the results to those obtained from the GAC method [3] alone and the ACWE model [10] alone using as a performance benchmark manually delineated frames performed by an expert observer.

The initial step was to apply the GSB method to the datasets, where  $\mu$ , the weighting parameter for the fidelity term was set to 0.002. Figure 1 shows a sample output of the GSB method, together with its corresponding edge map.

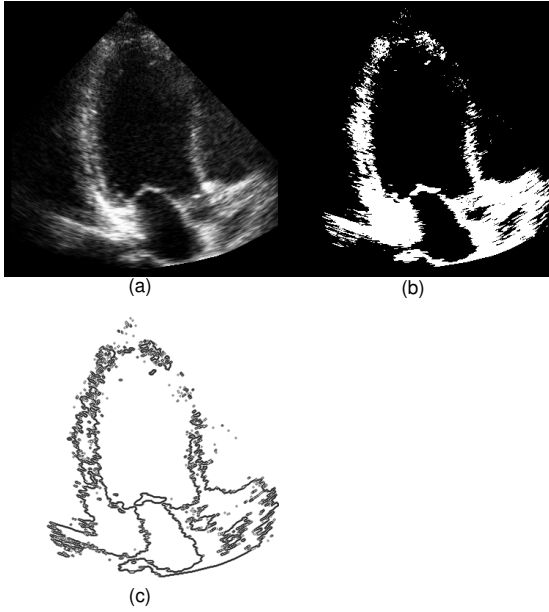


**Fig. 1.** In this figure (a) is the original frame, (b) is the output of the GSB method, (c) is the edge set extracted from the binary output of the GSB method. It is this output which is supplied to the topology preserving step.

In the topology preserving model, we set the topology constant  $\chi = -0.5$  and the balloon term  $\nu$  to 0.3. The initialization for the segmentation was done by manually placing a contour in the first frame of each dataset. The initial curve had similar curvature properties to the final boundary and identical topology. As a stopping criterion, the  $l_2$  norm between the current and previous  $\phi$  was used

$$\|\phi_n - \phi_{n-1}\|_2 \quad (7)$$

A sample of the results obtained with the proposed model, together with those obtained with the GAC and ACWE methods is shown in Figure 2. In this figure, the GAC method ‘leaks’ through the open valves (located at the bottom region of the image), while the ACWE method is disrupted due to the lack of intensity homogeneity of the echocardiographic data. The common result observed by the ACWE method applied to the dataset is that the curve partitions the image into two parts: the cleanest part of the interior chamber (dark region inside of the heart) and the rest of the image. This can be seen in both the oscillatory structure in the final curves as well as the odd final shape. It can be seen that the result produced by the GSB+TPLUS method achieves the best similarity to the manually delineated result.

### 3.1. Quantitative Evaluation

Contours drawn manually by an expert observer were used to quantitatively evaluate our results. The metrics used for comparison were the Dice Coefficient, the Hausdorff distance and the Mean Absolute

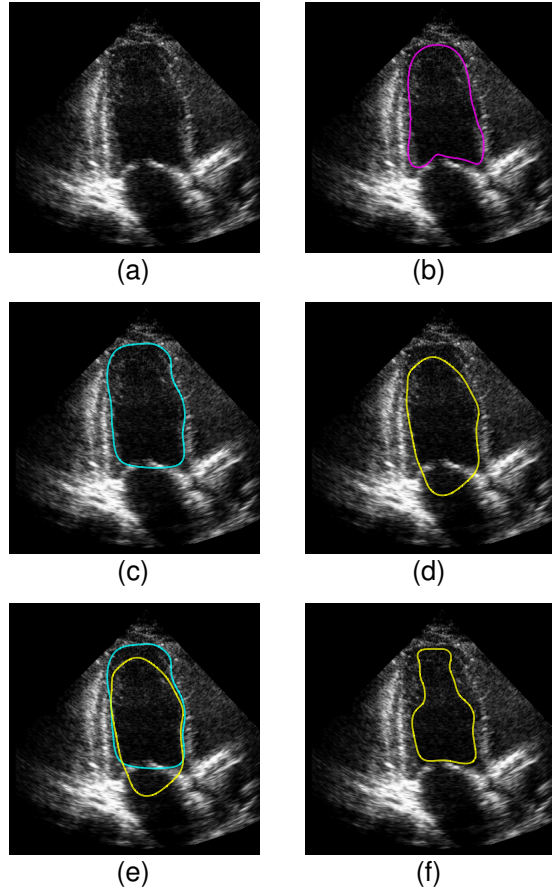


**Fig. 2.** In this figure (a) is the original frame, (b) is the manually delineated result (c) is the result of the GSB+TPLUS method, (d) is the GAC result and (e) represents both results, while (f) shows the ACWE result. It can be observed that the GAC method fails to accurately segment the top of the chamber and also the region in the area of the valve, while the ACWE method finds the region of highest intensity homogeneity, which does not correspond to the chamber boundary.

distance. The Dice coefficient measures the percentage overlap between 2 areas. It is defined to be:

$$\text{Dice}(A, B) = \frac{2\|area(A) \cap area(B)\|}{\|area(A)\| + \|area(B)\|}. \quad (8)$$

The Hausdorff metric is the maximum of the set of distances between corresponding points calculated for two curves. It is defined to be

$$\text{HD}(A, B) = \max\{\max_i\{d(\mathbf{a}_i, B)\}, \max_j\{d(\mathbf{b}_j, A)\}\}. \quad (9)$$

The mean absolute distance measures the average absolute distance between the set of corresponding points calculated for two curves. It

is defined to be

$$\text{MAD}(A, B) = \frac{1}{2} \left\{ \frac{1}{n} \sum_{i=1}^n d(\mathbf{a}_i, B) + \frac{1}{m} \sum_{j=1}^m d(\mathbf{b}_j, A) \right\} \quad (10)$$

where  $A$  and  $B$  represent two curves, consisting of pointsets  $A = \{\mathbf{a}_1, \mathbf{a}_2, \dots, \mathbf{a}_m\}$  and  $B = \{\mathbf{b}_1, \mathbf{b}_2, \dots, \mathbf{b}_m\}$  and  $d(\mathbf{a}_i, B) = \min_j \|\mathbf{b}_j - \mathbf{a}_i\|$  computes the distance between corresponding points in  $A$  and  $B$ . All of the contour points from the corresponding curves were used to compute each metric.

A summary of the results of this validation for each method is given in Table 1.

**Table 1.** Mean and standard deviation (SD) results of comparison with reference manual delineations over 20 frames. HD = Hausdorff Distance; MAD = Mean Absolute Difference; Measurement unit = millimeters.

	HD		MAD		Dice	
	Mean	SD	Mean	SD	Mean	SD
GSB+TPLS	4.01	1.06	1.62	0.3	0.89	0.04
ACWE	7.12	6.43	2.43	2.12	0.82	0.17
GAC	5.14	1.77	2.07	0.64	0.87	0.06

With respect to the Hausdorff measurement in Table 1, the GSB+TPLS method obtained an average Hausdorff distance of 4.01mm from the reference contour, which was a significant improvement on the either of the ACWE or GAC methods, which obtained averages of 7.12mm and 5.14mm respectively. The improved performance of the proposed model as measured by each of the other metrics can also be examined in Table 1.

#### 4. CONCLUSION

In the present paper we proposed a variational segmentation scheme which is comprised of a novel combination of regional and intensity based information, combining the efficiency of Geometric Split Bregman based processing [8] with the topological preserving framework proposed in [9]. The model's improved performance compared with classical segmentation approaches was demonstrated on low quality real world echocardiographic data.

#### 5. REFERENCES

- [1] M. Kass, A. Witkin, and D. Terzopoulos, "Snakes: Active contour models," *Int J Comput Vision*, pp. 321–331, 1987.
- [2] S. Osher and J. A. Sethian, "Fronts propagating with curvature-dependent speed: algorithms based on hamilton-jacobi formulations," *J Comput Phys*, vol. 79, pp. 12–49, November 1988.
- [3] V. Caselles, R. Kimmel, and G. Sapiro, "Geodesic active contours," *Int J Comput Vision*, vol. 22, no. 1, pp. 61–79, 1997.
- [4] X. Bresson, S. Esedoglu, P. Vanderghenst, J.P. Thiran, and S. Osher, "Fast global minimization of the active contour/snake model," *J Math Imaging Vis*, vol. 28, no. 2, pp. 151–167, June 2007.
- [5] N. Paragios and R. Deriche, "Unifying boundary and region-based information for geodesic active tracking," in *IEEE Conference on Computer Vision and Pattern Recognition (CVPR)*, 1999, vol. 2, pp. 300–305.
- [6] K. Rajpoot, V. Grau, and J.A. Noble, "Local-phase based 3d boundary detection using monogenic signal and its application to real-time 3-d echocardiography images," in *IEEE International Symposium on Biomedical Imaging*, July 2009, pp. 783–786.
- [7] Pearlman P.C., Tagare H.D., Lin B.A., Sinusas A.J., and Duncan J.S., "Segmentation of 3d radio frequency echocardiography using a spatio-temporal predictor," *Medical Image Analysis*, vol. 16, no. 2, pp. 351–360., 2012.
- [8] T. Goldstein, X. Bresson, and S. Osher, "Geometric applications of the split bregman method: Segmentation and surface reconstruction," *J. Sci. Comput.*, vol. 45, pp. 272–293, October 2010.
- [9] C. Le Guyader and L. A. Vese, "Self-repelling snakes for topology preserving segmentation models," *IEEE T Image Process*, vol. 17, no. 5, pp. 767–779, May 2008.
- [10] T.F. Chan and L.A. Vese, "Active contours without edges," *IEEE Transactions on Image Processing*, vol. 66, no. 5, pp. 1632–1648., 2004.
- [11] T. Goldstein and S. Osher, "The split bregman method for 11-regularized problems," *SIAM Journal on Imaging Sciences*, vol. 2, no. 2, pp. 323–343., 2009.
- [12] T.F. Chan, S. Esedoglu, and M. Nikolova, "Algorithms for finding global minimizers of image segmentation and denoising models," *SIAM J. Appl. Math.*, vol. 10, no. 2, pp. 266–277, 2001.

**Nóirín Duggan**, Hayden Schaeffer, Carole Le Guyader , Edward Jones, Martin Glavin, Luminita Vese, Boundary Detection in Echocardiography Using a Split Bregman Edge, IEEE International Symposium on Biomedical Imaging: From Macro to Nano 2013. San Francisco. DOI:10.1109/ISBI.2013.6556415. Published.

**B**

Manuscripts currently under review

# 1 A technique for lung nodule candidate detection 2 in CT using global minimization methods

3 N.Duggan, E.Bae, S.Shen, W.Shu, E.Jones, M.Glavin, L.Vese

4 No Institute Given

5 **Abstract.** The first stage in computer aided pulmonary nodule detec-  
6 tion schemes is a candidate detection step designed to provide a sim-  
7 plified representation of the lung anatomy, such that features like the  
8 lung wall, and large airways are removed leaving only data which has  
9 greater potential to be a nodule. Nodules which are connected to blood  
10 vessels tend to be characterized by irregular geometrical features which  
11 can result in their remaining undetected by rule-based classifiers relying  
12 only local image metrics. In the current paper a novel approach for lung  
13 nodule candidate detection is proposed based on the application of global  
14 segmentation methods combined with mean curvature minimization and  
15 simple rule-based filtering. Experimental results indicate that the pro-  
16 posed method can accurately detect nodules displaying a diverse range  
17 of geometrical features.

## 18 1 Introduction

19 Every year, deaths due to lung cancer outnumber those related to other types  
20 of cancers around the world [1]. The most important indicator of the disease  
21 is the presence of pulmonary lung nodules [2,3], the early detection of which is  
22 essential to increase the chances of successful treatment [4].

23 The most popular modality for imaging the thorax is Computed Tomography  
24 (CT) [2]. Currently the most common method for quantifying lesion development  
25 using CT is through manual detection and measurement of the nodule diameter.  
26 In addition to being error-prone and subjective [5], this technique is limiting  
27 because a 1-D measure is used to describe a 3-D non-symmetric, non- spherical  
28 object. At the same time, manually characterizing the tumor using all of the 3-D  
29 data available would be extremely time-consuming [6].

30 Numerous studies have shown that computer aided detection (CAD) systems  
31 can effectively assist radiologists in detecting lung nodules [7,8,9,10,11,12]. In  
32 studies by Martin et al. [13] and Lee et al. [14] it was shown that the sensitivity  
33 of CAD systems for detecting small, isolated nodules was greater than achieved  
34 by a radiologist but that this sensitivity was lower than that of a radiologist for  
35 nodules with vascular attachment.

36 In [15] a nodule detection scheme is presented in which the first step is lung  
37 segmentation. This is achieved by thresholding the lung volume on a frame-  
38 by-frame basis. Noting that the volume histogram displays 2 prominent peaks,  
39 corresponding respectively to pixels inside the lungs and to pixels representing

40 soft tissue and bone, for each frame, the authors in [15] select as a threshold  
 41 the broad minimum which existing between these peaks. The next step is a  
 42 corrective stage which has the purpose of excluding structures such as airways  
 43 and including juxta-pleura nodule (*i.e.* lung wall-connected) excluded by the  
 44 thresholding step. To re-include juxta-pleura nodules they apply morphological  
 45 opening; to exclude the airways, they apply a 2-D region growing technique. This  
 46 is followed by a region-labeling technique designed to group contiguous structures  
 47 in three dimensions. Finally, to obtain the candidacy mask the authors apply a  
 48 volume threshold to these contiguous structures.

49 In Tan *et al.* [16] lung segmentation is performed using a similar technique  
 50 as proposed in [15]. In the next step the authors compute the divergence of  
 51 normalised gradient (DNG) of the volume to estimate the center of nodules,  
 52 they then use this in combination with nodule and vessel enhancement filters  
 53 proposed in [17,18] to detect nodule candidates. To obtain the nodule candi-  
 54 dacy mask, the authors apply a different thresholding/filtering combination to  
 55 each nodule type; *i.e.* isolated, juxtavascular (or vessel-connected), and juxta-  
 56 pleural nodules. For example for isolated nodules they apply a threshold of -600  
 57 Hounsfields Units (a quantitative scale for describing radiodensity) to the output  
 58 of the lung segmentation, they then apply the nodule enhancement filter to this  
 59 result. Subsequently another (gray level) threshold of 6 is applied to this nodule  
 60 enhanced image. The output of this system is then combined with the result of  
 61 the DNG method. Finally to this result, another volume threshold of 9 voxels is  
 62 applied. The outputs of this last step are taken to be the isolated nodule candi-  
 63 dacies. The steps to extract both juxtavascular and juxtapleural nodules are  
 64 similar to those outlined above and similarly involve a specific set of threshold  
 65 parameters. The result of the procedure described above is multiple thresholded  
 66 volumes consisting of nodule clusters corresponding to isolated, juxtavascular,  
 67 and juxtapleural nodules. A logical OR-ing operation is then carried out to con-  
 68 solidate the results in one volume. In [19], the detection scheme starts with the  
 69 generation of a lung mask in a scheme similar to that proposed in [15]. The  
 70 authors then apply multi-level thresholding [15] to the remainder of the vol-  
 71 ume to produce multiple 3-D lung nodule candidate masks. To remove vessels,  
 72 they apply a morphological opening operation with specific radius to each mask,  
 73 which is followed by another rule based filter (with sphericity and area criteria)  
 74 to remove false positives. The final nodule mask is generated by logically or-ing  
 75 these intermediate masks. The thresholds as well as the radii of the structuring  
 76 elements are determined empirically. In [20] the authors apply a 2-D filter to  
 77 each axial slice image to highlight structures similar to discs or half-discs. To  
 78 reduce the false positives, 6 3-D features based on size, compactness, sphericity  
 79 and gradient-intensity, are calculated for each candidate. The authors use an  
 80 SVM to classify the data.

81 In consecutive CT slices, blood vessels often appear as circular objects closely  
 82 resembling nodules; using this fact, the authors in [21] proposed a scheme to  
 83 generate multiple 2-D images based on different spherical viewpoints of each  
 84 3-D nodule candidate. The authors show that these different viewpoints allow

85 the noncircular linear structure of components corresponding to vessels to be  
86 more easily identified. The authors then combined features generated from these  
87 images features with 3-D features such as diameter and compactness [22]. They  
88 then employ a linear classifier [22,23] to classify the results.

89 Murphy *et al.* [24] proposed a detection scheme which uses shape index and  
90 curvedness to detect nodule candidates. Using these features the authors fil-  
91 tered the datasets to produce seed points in areas of high filter response and  
92 expanded these points using hysteresis thresholding to produce region clusters.  
93 To reduce false positives, they applied two consecutive classification steps us-  
94 ing k-Nearest-Neighbour. In analysing the results according to nodule size, the  
95 authors reported that for nodules with a diameter greater than 8.6mm, the sen-  
96 sitivity rate was under 45 %. These findings highlight the difficulty in detecting  
97 nodules characterized by irregular shapes by means of local image features alone,  
98 a fact which the authors themselves acknowledged.

99 The purpose of this paper is to present an algorithm for the detection of the  
100 lung lobe interior with particular emphasis on detecting nodules with vascular  
101 attachment. The output of the algorithm is a set of regions that can be analyzed  
102 further either manually or by an advanced classifier to determine whether they  
103 represent a true nodule. As can be observed in the previous review, several of  
104 the proposed schemes make use of a combination of multi-thresholding methods  
105 and as well as spherical shape filters to isolate nodules [15,19,21,16], however  
106 as noted in [25], when nodules are connected to other high density structures,  
107 separating them with intensity thresholds alone is in most cases, impossible. In  
108 the same way, incorporating spherical constraints early into a detection scheme  
109 can be limiting especially in the case of nodules which exhibit a high degree of  
110 vascular attachment and which therefore represent quite a complex geometry. In  
111 this paper, we make use of more sophisticated variational models [26] and a re-  
112 cently developed efficient convex optimization algorithm for obtaining solutions  
113 numerically. The entire algorithm consists of several successive steps that are  
114 described in detail below.

## 115 2 Methodology

116 A challenge for obtaining a good segmentation is that many objects inside the  
117 lung have very similar intensity distributions to the nodule, in particular blood  
118 vessels and the chest wall. This makes it difficult to separate the intensity profile  
119 of the nodule from other tissue classes using a multiregion segmentation frame-  
120 work. We develop an algorithm where a two region segmentation model is first  
121 used to capture the nodules, chest wall and other objects of similar intensity in  
122 a foreground region, and the air and remaining objects in a background region.  
123 The remaining parts of the algorithm attempt to separate the potential nodules  
124 from the rest of the tissue that were captured in the foreground region. This  
125 concerns mainly the chest wall and surrounding blood vessels, which is handled  
126 in two separate steps.

## 127 2.1 Computation of a Global 2-phase Segmentation output

128 The first step of our method aims to extract the chest wall, nodules, blood  
 129 vessels and other tissue of similar intensity values into one region using the  
 130 active contour model with two regions [26]:

$$\min_{S, c_1, c_2} \int_{\Omega \setminus S} |I(x) - c_1|^2 dx + \int_S |I(x) - c_2|^2 dx + \nu |\partial S|. \quad (1)$$

131 In recent work, efficient algorithms have been proposed for computing global  
 132 minimizers to this model. In [27] it was shown that (1) can be exactly minimized  
 133 via the convex problem

$$\min_{\phi(x) \in [0,1]} \int_{\Omega} |I(x) - c_1|^2 \phi(x) + |I(x) - c_2|^2 (1 - \phi(x)) dx + \nu \int_{\Omega} |\nabla \phi(x)| dx. \quad (2)$$

134 It was shown that if  $\phi^*$  is a minimizer of (2) and  $t \in (0, 1]$  is any threshold  
 135 level, the partition  $S = \{x \in \Omega : \phi(x) \geq t\}$ ,  $\Omega \setminus S = \{x \in \Omega : \phi(x) < t\}$  is a  
 136 global minimizer to the model (1). The binary function

$$\phi^t(x) := \begin{cases} 1, & \phi(x) \geq t \\ 0, & \phi(x) < t \end{cases}, \quad (3)$$

137 is the characteristic function of the region  $S$ .

We make use of an efficient augmented Lagrangian algorithm for solving a  
 dual formulation of (1) proposed in [28,29], which could be interpreted as a  
 maximum flow problem. By introducing a Lagrange multiplier for the flow con-  
 servation constraint, the following augmented Lagrangian primal-dual problem  
 was obtained

$$\sup_{\phi} \inf_{p_s, p_t, p} \int_{\Omega} p_s dx + \int_{\Omega} \phi (\operatorname{div} p - p_s + p_t) dx - \frac{c}{2} \|\operatorname{div} p - p_s + p_t\|^2 \quad (4)$$

such that

$$|p(x)|_2 \leq \nu, \quad \forall x \in \Omega; \quad p_s(x) \leq |I(x) - c_1|^2, \quad p_t(x) \leq |I(x) - c_2|^2, \quad \forall x \in \Omega \quad (5)$$

138 where  $p_s, p_t : \Omega \mapsto \mathbb{R}$  and  $p : \Omega \mapsto \mathbb{R}^N$  and  $N$  is the dimension of  $\Omega$ .  
 139 By applying the augmented Lagrangian method, the following algorithm was  
 140 derived for solving (2)

$$141 \quad - \quad p_s^{k+1} := \arg \max_{p_s(x) \leq |I(x) - c_1|^2 \quad \forall x \in \Omega} \left( \int_{\Omega} p_s dx - \frac{c}{2} \|p_s - p_t^k - \operatorname{div} p^k + \phi^k/c\|^2 \right)$$

142 which can easily be computed pointwise in closed form.

$$143 \quad - \quad p^{k+1} := \arg \max_{\|p\|_{\infty} \leq \nu} -\frac{c}{2} \|\operatorname{div} p - p_s^{k+1} + p_t^k - \phi^k/c\|^2,$$

144 where  $\|p\|_{\infty} = \sup_{x \in \Omega} |p(x)|_2$ . This problem can either be solved iteratively  
 145 or approximately in one step via a simple linearization [29]. In our imple-  
 146 mentation we used the linearization.

$$147 \quad - \quad p_t^{k+1} := \arg \max_{p_t(x) \leq |I(x) - c_2|^2 \quad \forall x \in \Omega} - \frac{c}{2} \|p_t - p_s^{k+1} + \operatorname{div} p^{k+1} - \phi^k / c\|^2$$

148 This problem can also easily be computed in closed form pointwise.

$$149 \quad - \quad \phi^{k+1} = \phi^k - c(\operatorname{div} p^{k+1} - p_s^{k+1} + p_t^{k+1});$$

150 - Set  $k = k + 1$  and repeat.

151 The output  $\phi$  at convergence will be a solution to (2) and one can obtain a  
 152 partition which solves (1) by the thresholding procedure described above. More  
 153 details can be found in [29].

154 In simple cases, the two region segmentation algorithm may separate out the  
 155 nodule as a single connected component. In more difficult scenarios, the nodule  
 156 region may be connected to either the chest wall or surrounding blood vessels.

## 157 2.2 Lung Wall removal Process

158 The 3-D global segmentation described above essentially segments the volume  
 159 into 2 classes: tissue and air. The next step is to separate the lung wall from  
 160 the structures that are interior to the lung. This is done using a combination of  
 161 connected component labeling as well as morphological opening.

162 First a connected component labeling operation is used to identify the largest  
 163 component in the volume. This step identifies the lung wall together with addi-  
 164 tional structures which are connected via vessels to the lung wall. A correction  
 165 step which consists of a morphological opening operation [30] is used to remove  
 166 these additional structures. The result of the morphological opening operation,  
 167 which corresponds to the lung wall is then subtracted from the 3-D segmentation  
 168 result leaving just structures in the interior lung lobe.

## 169 2.3 Nodule Separation Scheme

170 We address the issue of separating the nodules from surrounding tissue by  
 171 applying mean curvature minimization using the method of Merriman-Bence-  
 172 Osher (MBO) [31] to the output of the segmentation scheme. The effect of this  
 173 scheme is to ‘simplify’ the underlying structures of the nodule candidates (or ves-  
 174 sels); essentially, through the diffusion process, a spiculated mass will become  
 175 smoother/more spherical, while structures connected to each other by (rela-  
 176 tively) thin connections will be separated.

177 Let  $\phi^0$  denote the binary function indicating the segmentation result after  
 178 removal of the lung wall. The MBO algorithm applied to  $\phi^0$  is a discrete time  
 179 approximation of mean curvature motion and can be described as follows:

For  $k = 1, 2, \dots, K$

$$\psi = G_\sigma * \phi^k \tag{6}$$

$$\phi^{k+1}(x) = \begin{cases} 1, & \text{if } \psi(x) \geq 0.5 \\ 0, & \text{if } \psi(x) < 0.5 \end{cases} \tag{7}$$

180 Step (6) above is time step of the heat equation, which is equivalent to convo-  
 181 lution with the Gaussian kernel  $G_\sigma$ , and can be solved efficiently by the fast  
 182 Fourier transform (FFT). After each MBO iteration, a rule based classifier is  
 183 applied to each connected component of the result, to check if the component  
 184 is a nodule candidate. The rule based classifier is described in the next section.  
 185 The number of iterations  $K$  is set in advance to prevent too much smoothing.

## 186 2.4 Rule Based Classifier

187 The effect of the MBO step is to make a spiculated mass smoother and more  
 188 spherical in shape, which allows structures to be identified as potential nodules  
 189 using simple geometric features. The final step in determining nodule candi-  
 190 dacy is the application of a simple rule-based classifier, in which candidacy is  
 191 determined by the following features: area, volume, circularity, elongation.

192 The following definitions are used for each feature: assuming that the nodules  
 193 are spherical, the area and volume of the nodule candidates can computed using  
 194 the standard formulae: Area =  $\pi r^2$ ; Volume =  $3/4\pi r^3$   
 Elongation is defined simply as the ratio of the largest dimension in the x,y or  
 z direction over the minimum dimension in any direction i.e.

$$\text{Elongation} = \frac{\max([x\text{Length}, y\text{Length}, z\text{Length}])}{\min([x\text{Length}, y\text{Length}, z\text{Length}])}$$

Circularity is defined as

$$\text{Circularity} = \frac{4\pi \text{Area}}{\text{Perimeter}^2}$$

195 In the above equation, ‘Area’ and ‘Perimeter’ are calculated using the me-  
 196 dian slice of the connected component. The respective maximum and minimum  
 197 thresholds for each feature are listed in section 3. This step follows closely the  
 198 method proposed by Choi et al. in [32] and further details can be found therein.

## 199 2.5 Summary of the Complete Algorithm

200 In summary, the proposed nodule candidacy detection scheme comprises the fol-  
 201 lowing steps; first a global 2 phase segmentation is performed, which segments  
 202 the volume into 2 classes: tissue and air. The next step is to further segment  
 203 the tissue into lung wall and interior lobe data; this is done using morphological  
 204 techniques. The main part of the proposed scheme is the use of mean curvature  
 205 smoothing to isolate vascular connected nodules. The detection step is carried  
 206 out by applying the rule-based classifier once before the MBO smoothing and  
 207 subsequently on each connected component after each MBO iteration. The final  
 208 lung nodule candidacy mask is obtained by logically OR-ing all of the interme-  
 209 diate detection results. The entire algorithm is outlined below.

210

211

Input: 3D CT lung image

1. Obtain two region segmentation by global minimization of (2).
2. Remove lung wall from the segmentation result as described in section 2.2 and let  $\phi^0$  denote indicator function of the remaining region.
3. Apply rule based classifier to each remaining connected component as in section 2.4
  - Store positive connected components as potential nodule candidates
4. For iterations  $k=1, \dots, K$ :
  - Apply one step of MBO scheme (6), (7) to obtain  $\phi^k$ .
  - Apply rule based classifier on each component of  $\phi^k$ . If positive: store connected component as potential nodule candidate and for all points  $x$  inside connected component and set indicator function  $\phi^k(x) = 0$ .

Output: Set of nodule candidates, represented by a binary function.

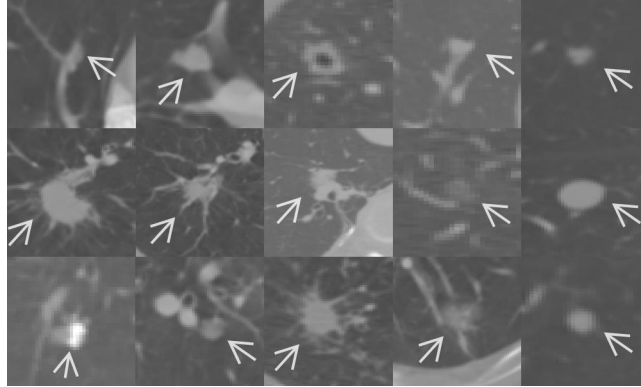


Fig. 1: Examples of nodules included in the test subset. The majority of the nodules in the test set exhibit some degree of attachment to surrounding vascular tissue; isolated nodules were also included (as can be observed in the rightmost column)

### 212 3 Experiments

213 A test set of 16 datasets were selected from the lung image consortium (LIDC)  
 214 database [33,34] which consisted of both nodules exhibiting vascular attachment  
 215 as well as isolated nodules. Our standard of reference were the expert annotations  
 216 provided with this database. The test set includes a total of 27 nodules.

217 Figure 1 shows examples of nodules in the test subset. Figure 2 highlights  
 218 the normal operation of the rule based classifier. It can be observed in figure

219 **2(b)** that the nodule in question is isolated from other structures in the lung  
 220 after application of the first segmentation step and the filter easily selects the  
 221 nodule. The results of the algorithm are demonstrated in figure **3**, which displays  
 222 6 sample slices from the test set. Compared with the data set in figure **2(a)**,  
 223 each nodule in figure **3** exhibits connectivity with surrounding tissue. The first  
 224 segmentation step is unable to sufficiently separate the nodules from surrounding  
 225 tissue in these cases due to their similar intensity profiles. Application of the  
 226 MBO scheme has the effect of either removing fine structures attached to the  
 227 nodule, such as fine blood vessels, or splitting the regions into two or more  
 228 geometrically simpler components, one of which encompasses the nodule region.

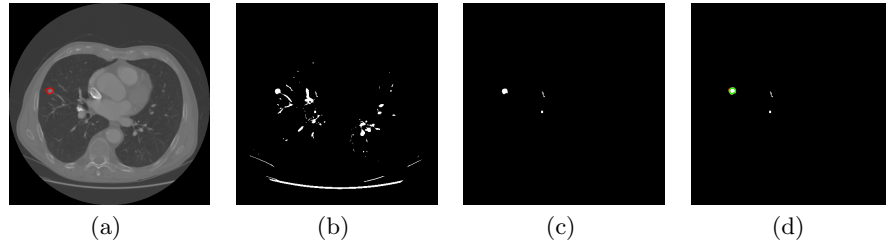


Fig. 2: Example of normal operation of rule-based classifier: (a) Annotated Data indicating nodule (b) Initial Segmentation Results + lung wall removal (c) Corresponding Detection Results (d) Corresponding Detection Results with annotation

229  
 230 In figures **4** and **5**, two examples are shown of nodules which in **4(a)** and  
 231 **5(a)** appear to be isolated. Using only steps 1-3 of the algorithm results in the  
 232 nodules remaining undetected because, as adjacent slices reveal, there is some  
 233 degree of vascular attachment. The nodules are detected (Figures **4(e)** and **5(e)**)  
 234 when the MBO scheme (step 4) is used as part of the detection scheme.

235 Figure **6** shows a case where the detection scheme fails to detect a nodule. In  
 236 this case, the degree of connectivity between the nodule and surrounding struc-  
 237 tures was too extensive for the proposed method to work. Figure **6(c)** shows the  
 238 connected structure of which the nodule forms a part. Ongoing work is focused  
 239 on a more complex algorithm for removing the lung wall taking into account prior  
 240 geometrical knowledge about the shape, such that potential nodules attached to  
 241 the lung wall gets disconnected.

242 The following empirically derived parameter values were used in the experi-  
 243 ments: the length parameter,  $\nu$  was set to  $1e-12$ , for the 3-D global segmentation.  
 244 The initial estimates for the mean value of both regions,  $c1$  and  $c2$ , were set to  
 245 0.3 and 0.6 respectively. The morphological opening operation used to remove  
 246 the lung wall was carried out using a spherical kernel of radius 13. With respect  
 247 to the MBO scheme, with the exception of 1 dataset,  $\sigma$  for the Gaussian kernel

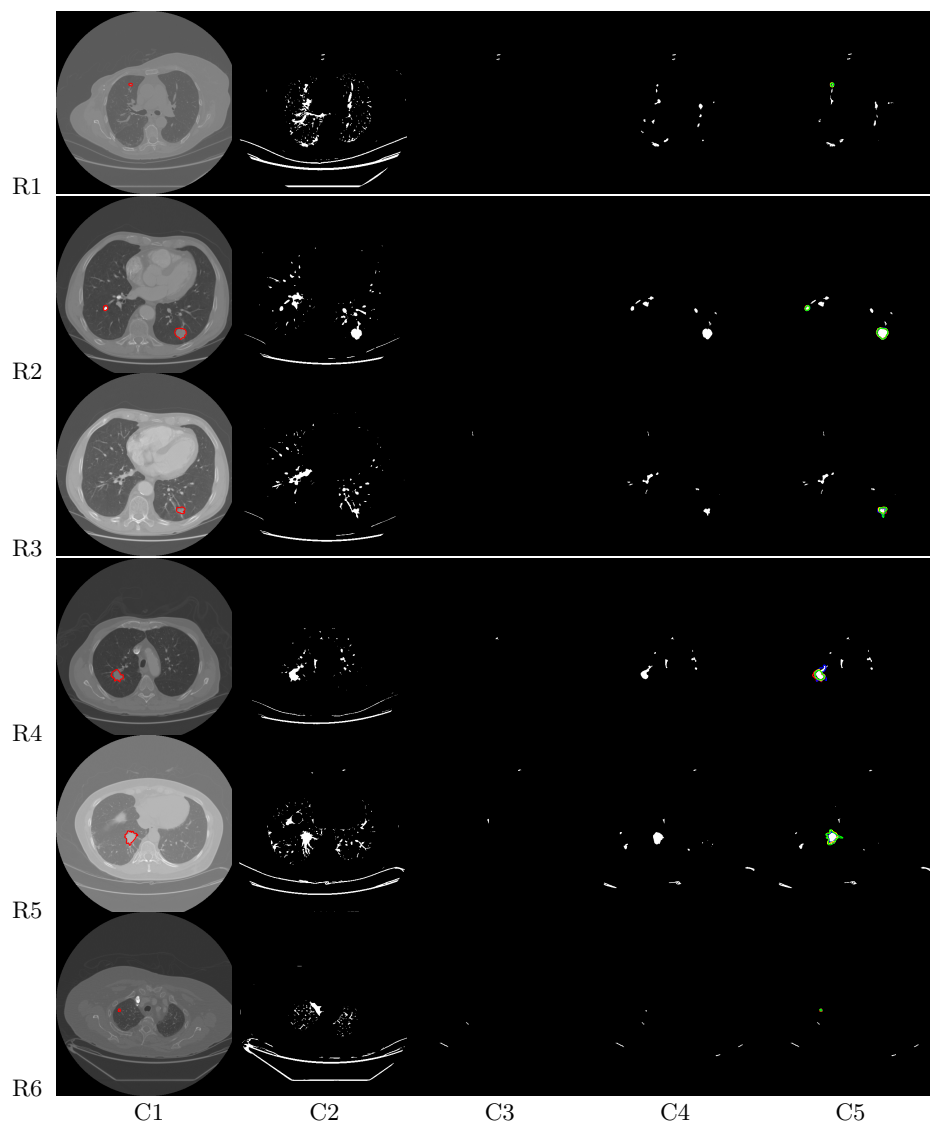


Fig. 3: Results achieved by the method on 6 sample frames (Rows R1-R6). Each row shows an example of a nodule with vascular attachment. C1: The original data with expert annotation. C2: 2 phase global segmentation result C3: Results of the rule-based detection method C4: Detection results post MBO processing C5: Detection results with superimposed expert annotation.

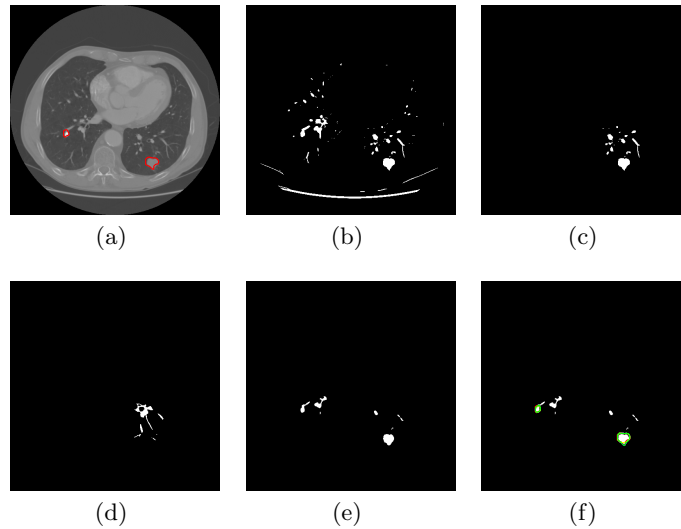


Fig. 4: Example of a nodule which is processed using only the rule-based classifier (i.e. using only steps 1-3 of the algorithm) (a) Original Annotated dataset (b) slice 71 of dataset: nodule looks well delineated from surrounding structures but is actually part of a large connected component (c) the connected component which contains the nodule (d) an adjacent slice (e) Step 4: Detection with MBO (f) Annotation overlaid on result

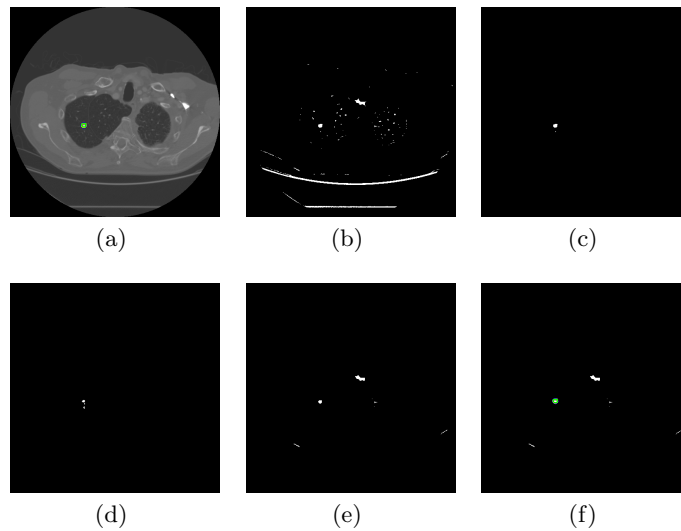


Fig. 5: Second example of a nodule which is processed using only the rule-based classifier (i.e. using only steps 1-3 of the algorithm) (a) Original Annotated dataset (b) nodule looks well isolated from surrounding structures but is actually part of a large connected component (c) connected component which includes the nodule (d) an adjacent slice (e) Step 4: Detection with MBO (f) Annotation overlaid on result

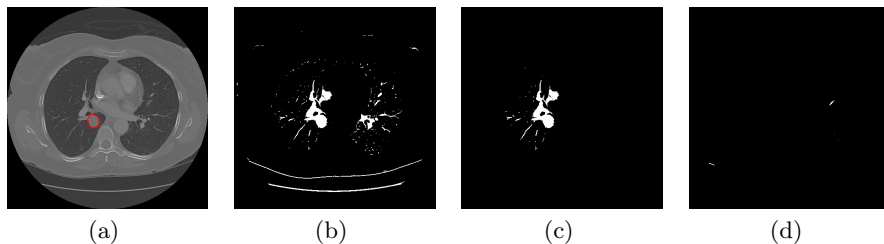


Fig. 6: Example of a case where MBO-detection scheme fails (a) Original Annotated dataset (b) 2-phase segmentation (c) Connected component (d) Detection with MBO - failure

248 was set to 1, while the maximum number of iterations used was 20. For one  
 249 dataset, sigma was reduced to 0.7, with the number iterations remaining at 20.  
 250 The thresholds used for the rule based classifier were the following: maximum  
 251 diameter,  $T_{max}^d$ , was set to 30, minimum diameter  $T_{min}^d$  was set to 3, correspond-  
 252 ingly the maximum area threshold was  $(T_{max}^d/2)^2\pi$ , minimum area threshold  
 253 was  $(T_{max}^d/2)^2\pi$ , maximum volume threshold was set to  $3(T_{max}^d/2)^3\pi/4$ , min-  
 254 imum threshold was set to  $3(T_{min}^d/2)^3\pi/4$ , maximum elongation was set to 4,  
 255 while minimum circularity was set to  $\frac{1}{6}$ .

256 Minimum and maximum diameter thresholds for the rule-based classifier were  
 257 chosen based on data in the LIDC dataset, where 97% of the nodules recorded  
 258 have a diameter in the 3-30mm range (with 86% in the 3-12mm range with  
 259 a further 11% in the 12-30mm range). With respect to the test set used in  
 260 these experiments, 80% of the nodules were in the 3-12mm diameter range, with  
 261 the remaining 20% in the 12-30mm range. The greater representation of larger  
 262 nodules in our test set was a design decision taken in response to the previously  
 263 discussed findings in [24], in which it was reported that larger nodules tended to  
 264 be characterized by irregular shapes and thus were harder to detect.

265 As described, the MBO parameters were changed for one dataset. This dataset  
 266 presented a nodule with a diameter of 6mm and which also exhibited a connection  
 267 with neighboring blood vessels. For this nodule a sigma value of 1 represented  
 268 an over-smoothing and consequent detection failure, while a sigma value of 0.7  
 269 resulted in accurate detection. To make the system more robust with respect to  
 270 parameter choice a smaller sigma value can be used and the number of iterations  
 271 increased.

272 The experiments show that the algorithm successfully detected all but one  
 273 of the nodules present (see figure 6). This resulted in an average detection rate  
 274 of 96%, while an average of 16 false positives were detected per scan. Without  
 275 the MBO smoothing step the detection rate was 44%.

276 **4 Conclusion**

277 Several studies [24,14,13] have highlighted the difficulty in detecting larger nod-  
 278 ules in lung images, which tend to be characterized by greater shape diversity.  
 279 In the current paper an algorithm was described for handling this task using  
 280 variational and PDE based methods. The algorithm was tested on 16 datasets  
 281 containing 27 nodules with various degrees of attachment to surrounding tissue.  
 282 A 96% detection rate was obtained. These initial results show that the proposed  
 283 method has the potential to be an effective module in an automated detection  
 284 pipeline.

285 Future work is focused on a more complex algorithm for separating the most  
 286 difficult nodules from the lung wall to improve the detection rate further, and a  
 287 finer segmentation step applied in the end, using the detected nodule candidates  
 288 as location prior information.

289 **References**

- 290 1. American Cancer Society: Cancer Facts and Figures 2014. (2014) **1**
- 291 2. Goo, J.M.: A computer-aided diagnosis for evaluating lung nodules on chest CT:  
 292 the current status and perspective. *Korean Journal of Radiology* **12** (2011) 145–155  
 293 **1**
- 294 3. Weir, H., Thun, M., Hankey, B., Ries, L., Howe, H., Wingo, P., Jemal, A., Ward,  
 295 E., Anderson, R., Edwards, B.: Annual report to the nation on the status of cancer,  
 296 1975-2000. *J. National Cancer Institute* **95** (2003) 12761299 **1**
- 297 4. Henschke, C., McCauley, D., Yankelevitz, D., Naidich, D., McGuinness, G., Miettinen,  
 298 O., Libby, D., Pasmantier, M., Koizumi, J., Altorki, N., Smith, J.: Early lung  
 299 cancer action project: overall design and findings from baseline screening. *Lancet*  
 300 **354** (1999) 99–105 **1**
- 301 5. Moltz, J.H., Bornemann, L., Kuhnigk, J.M., Dicken, V., Peitgen, E., Meier, S.,  
 302 Bolte, H., Fabel, M., Bauknecht, H.C., Hittinger, M., Kießling, A., Pusken, M.,  
 303 Peitgen, H.O.: Advanced segmentation techniques for lung nodules, liver metas-  
 304 tases, and enlarged lymph nodes in CT scans. *IEEE Journal of Selected Topics in*  
 305 *Signal Processing* **3** (2009) 122–134 **1**
- 306 6. Bornemann, L., Dicken, V., Kuhnigk, J.M., Wormanns, D., Shin, H.O., Bauknecht,  
 307 H.C., Diehl, V., Fabel, M., Meier, S., Kress, O., Krass, S., Peitgen, H.O.: On-  
 308 cotreat: a software assistant for cancer therapy monitoring. *International Journal*  
 309 *of Computer Assisted Radiology and Surgery* **1** (2007) 231–242 **1**
- 310 7. Sahiner, B., Chan, H.P., Hadjiiski, L.M., Cascade, P.N., Kazerooni, E.A., Chughtai,  
 311 A.R., Poopat, C., Song, T., Frank, L., Stojanovska, J., Attili, A.: Effect of CAD  
 312 on radiologists’ detection of lung nodules on thoracic CT scans: analysis of an  
 313 observer performance study by nodule size. *Acad Radiol* **16** (2009) 1518–1530 **1**
- 314 8. Park, E.A., Goo, J.M., Lee, J.W., Kang, C.H., Lee, H.J., Lee, C.H., Park, C.M.,  
 315 Lee, H.Y., Im, J.G.: Efficacy of computer-aided detection system and thin-slab  
 316 maximum intensity projection technique in the detection of pulmonary nodules in  
 317 patients with resected metastases. *Invest Radiol* **44** (2009) 105–113 **1**
- 318 9. Hirose, T., Nitta, N., Shiraishi, J., Nagatani, Y., Takahashi, M., Murata, K.: Evalu-  
 319 ation of computer-aided diagnosis (CAD) software for the detection of lung nodules

- 320 on multidetector row computed tomography (MDCT): JAFROC study for the im-  
 321 provement in radiologists' diagnostic accuracy. *Acad Radiol* **15** (2008) 1505–1512  
 322 [1](#)
- 323 10. Goo, J.M., Kim, H.Y., Lee, J.W., Lee, H.J., Lee, C.H., Lee, K.W., Kim, T.J.,  
 324 Lim, K.Y., Park, S.H., Bae, K.T.: Is the computer-aided detection scheme for  
 325 lung nodule also useful in detecting lung cancer? *Journal of Computer Assisted*  
 326 *Tomography* **32** (2008) 570–575 [1](#)
- 327 11. Beigelman-Aubry, C., Raffy, P., Yang, W., Castellino, R.A., Grenier, P.A.:  
 328 Computer-aided detection of solid lung nodules on follow-up MDCT screening:  
 329 evaluation of detection, tracking, and reading time. *AJR Am J Roentgenol* **189**  
 330 (2007) 948–955 [1](#)
- 331 12. Awai, K., Murao, K., Ozawa, A., Komi, M., Hayakawa, H., Hori, S., Nishimura, Y.:  
 332 Pulmonary nodules at chest CT: effect of computer-aided diagnosis on radiologists  
 333 detection performance 1. *Radiology* **230** (2004) 347352 [1](#)
- 334 13. Marten, K., Engelke, C., Seyfarth, T., Grillhsl, A., Obenauer, S., Rummeny, E.:  
 335 Computer-aided detection of pulmonary nodules: influence of nodule characteristics  
 336 on detection performance. *Clinical Radiology* **60** (2005) 196 – 206 [1](#), [12](#)
- 337 14. Lee, J.W., Goo, J.M., Lee, H.J., Kim, J.H., Kim, S., Kim, Y.T.: The potential  
 338 contribution of a computer-aided detection system for lung nodule detection in  
 339 multidetector row computed tomography. *Invest Radiol* **39** (2004) 649–655 PMID:  
 340 15486524. [1](#), [12](#)
- 341 15. Armato III, S.G., Giger, M.L., MacMahon, H.: Automated detection of lung nod-  
 342 ules in CT scans: preliminary results. *Medical physics* **28** (2001) 1552–1561 [1](#), [2](#),  
 343 [3](#)
- 344 16. Tan, M., Deklerck, R., Jansen, B., Bister, M., Cornelis, J.: A novel computer-aided  
 345 lung nodule detection system for CT images. *MEDICAL PHYSICS* **38** (2011)  
 346 5630–5645 [2](#), [3](#)
- 347 17. Li, Q., Sone, S., Doi, K.: Selective enhancement filters for nodules, vessels, and  
 348 airway walls in two- and three-dimensional CT scans. *Medical Physics* **30** (2003)  
 349 2040–2051 [2](#)
- 350 18. Li, Q., Arimura, H., Doi, K.: Selective enhancement filters for lung nodules, in-  
 351 tracranial aneurysms, and breast microcalcifications. *International Congress Series*  
 352 **1268** (2004) 929 – 934 [2](#)
- 353 19. Messay, T., Hardie, R., SK., R.: A new computationally efficient CAD system for  
 354 pulmonary nodule detection in CT imagery. *Medical Image Analysis* **14** (2010)  
 355 390–406 [2](#), [3](#)
- 356 20. Opfer, R., Wiemker, R.: Performance analysis for computer-aided lung nodule  
 357 detection on lidc data. In: *Society of Photo-Optical Instrumentation Engineers*  
 358 *(SPIE) Conference Series*. Volume 6515. (2007) [2](#)
- 359 21. Guo, W., Li, Q.: High performance lung nodule detection schemes in CT using  
 360 local and global information. *Medical Physics* **39** (2012) 5157–5168 [2](#), [3](#)
- 361 22. Li, Q., Li, F., Doi, K.: Computerized detection of lung nodules in thin-section  
 362 CT images by use of selective enhancement filters and an automated rule-based  
 363 classifier. *Academic Radiology* **15** (2008) 165 – 175 [3](#)
- 364 23. Li, Q., Doi, K.: Analysis and minimization of overtraining effect in rule-based  
 365 classifiers for computer-aided diagnosis. *Medical Physics* **33** (2006) 320–328 [3](#)
- 366 24. Murphy, K., van Ginneken, B., Schilham, A., de Hoop, B., Gietema, H., Prokop,  
 367 M.: A large-scale evaluation of automatic pulmonary nodule detection in chest CT  
 368 using local image features and k-nearest-neighbour classification. *Medical Image*  
 369 *Analysis* **13** (2009) 757 – 770 [3](#), [11](#), [12](#)

- 370 25. Kuhnigk, J.M., Dicken, V., Bornemann, L., Bakai, A., Wormanns, D., Krass, S.,  
371 Peitgen, H.O.: Morphological segmentation and partial volume analysis for vol-  
372 umetry of solid pulmonary lesions in thoracic CT scans. *IEEE Transactions on*  
373 *Medical Imaging* **25** (2006) 417–434 [3](#)
- 374 26. Chan, T., Vese, L.: Active contours without edges. *IEEE Transactions on Image*  
375 *Processing* **10** (2001) 266–277 [3](#), [4](#)
- 376 27. Chan, T.F., Esedoglu, S., Nikolova, M.: Algorithms for finding global minimizers of  
377 image segmentation and denoising models. *SIAM Journal on Applied Mathematics*  
378 **66** (2006) 1632–1648 [4](#)
- 379 28. Yuan, J., Bae, E., Tai, X.C.: A study on continuous max-flow and min-cut ap-  
380 proaches. In: *IEEE Conference on Computer Vision and Pattern Recognition*  
381 *(CVPR)*. (2010) 2217–2224 [4](#)
- 382 29. Yuan, J., Bae, E., Tai, X.C., Boykov, Y.: A spatially continuous max-flow and  
383 min-cut framework for binary labeling problems. *Numerische Mathematik* **126**  
384 (2014) 559–587 [4](#), [5](#)
- 385 30. Giardina, C.R., Dougherty, E.R.: *Morphological Methods in Image and Signal*  
386 *Processing*. Prentice-Hall, Inc., Upper Saddle River, NJ, USA (1988) [5](#)
- 387 31. B. Merriman, J.B., Osher, S.: Diffusion generated motion by mean curvature. In:  
388 *Crystal Grower’s Workshop. MS Selected Letters* (1993) 73–83 [5](#)
- 389 32. Choi, W.J., Choi., T.S.: Genetic programming-based feature transform and classifi-  
390 cation for the automatic detection of pulmonary nodules on computed tomography  
391 images. *Information Sciences* **212** (2012) 57–78 [6](#)
- 392 33. Armato, S., McLennan, G., McNitt-Gray, M., Meyer, C., Yankelevitz, D., Aberle,  
393 D., Henschke, C., Hoffman, E., Kazerooni, E., MacMahon, H., Reeves, A., Croft,  
394 B., Clarke, L.: L.I.D.C.R. group, lung image database consortium: developing a  
395 resource for the medical imaging research community. *Radiology* **232** (2004) 739–  
396 748 [7](#)
- 397 34. McNitt-Gray, M.F., III, S.G.A., Meyer, C.R., Reeves, A.P., McLennan, G., Pais,  
398 R.C., Freymann, J., Brown, M.S., Engelmann, R.M., Bland, P.H., Laderach, G.E.,  
399 Piker, C., Guo, J., Towfic, Z., Qing, D.P.Y., Yankelevitz, D.F., Aberle, D.R., van  
400 Beek, E.J., MacMahon, H., Kazerooni, E.A., Croft, B.Y., Clarke, L.P.: The lung  
401 image database consortium (LIDC) data collection process for nodule detection  
402 and annotation. *Academic Radiology* **14** (2007) 1464 – 1474 [7](#)

Accepted to the International Conference on Energy Minimization Methods in Computer Vision and Pattern Recognition, Hong Kong, 2015. For latter publication in the Lecture Notes in Computer Science Series. Springer.

# C

## Theorem 4.2.3 Expanded

An expanded version of Theorem (4.2.3) is presented here.

**Theorem C.0.1.** *Let  $\phi(t, x) \in C^1([0, T]; W^{1, \infty}(\Omega))$  be the solution to Equation (4.9) with homogeneous Neumann boundary conditions and  $|\nabla\phi| = 1$  a.e. in  $\Omega$ . Then for all  $t > 0$ , the evolution equation decreases an energy, i.e.  $\partial_t \bar{E}(\phi, c_1, c_2) \leq 0$ , where the energy is defined below:*

$$\bar{E}(\phi, c_1, c_2) = \int_{\Omega} |\nabla\phi| + \mu T(\phi) + \gamma \int_{\Omega} ((I - c_1)^2 - (I - c_2)^2)\phi \, dx \quad (\text{C.1})$$

*Proof.* It is possible to formally differentiate under the integral to find the energy's time derivative as follows (for simplicity, the subscript on the integrals is dropped).

$$\begin{aligned}
\partial_t \bar{E}(\phi(t, -), c_1(t), c_2(t)) &= \int \frac{\nabla \phi}{|\nabla \phi|} \cdot \nabla \phi_t \, dx \\
&- \mu \iint [\nabla \phi_t(x) \cdot \nabla \phi(y) + \nabla \phi(x) \cdot \nabla \phi_t(y)] e^{-\frac{\|x-y\|^2}{d^2}} W_l(\phi(x)) W_l(\phi(y)) \\
&+ \nabla \phi(x) \cdot \nabla \phi(y) e^{-\frac{\|x-y\|^2}{d^2}} [W_l'(\phi(x)) W_l(\phi(y)) \phi_t(x) + W_l(\phi(x)) W_l'(\phi(y)) \phi_t(y)] \, dx \, dy \\
&+ \gamma \int 2(I - c_1) c_{1t} \phi + (I - c_1)^2 \phi_t + 2(I - c_1) c_{2t} \phi - (I - c_2)^2 \phi_t \, dx \quad (C.2) \\
&= \text{Term}_1 + \text{Term}_2 + \text{Term}_3
\end{aligned}$$

Investigating this expression term by term; using integration by parts the first term yields:

$$\text{Term}_1 = \int \frac{\nabla \phi}{|\nabla \phi|} \cdot \nabla \phi_t \, dx = \int_{\Gamma} \phi_t \left( \frac{\nabla \phi}{|\nabla \phi|} \cdot \hat{\mathbf{n}} \right) \, d\Gamma - \int \text{div} \left( \frac{\nabla \phi}{|\nabla \phi|} \right) \phi_t \, dx \quad (C.3)$$

where the boundary terms vanish because of the boundary conditions, therefore:

$$\text{Term}_1 = - \int \text{div} \left( \frac{\nabla \phi}{|\nabla \phi|} \right) \phi_t \, dx \quad (C.4)$$

For the third term in the expression, it is noted that since  $c_1$  and  $c_2$  satisfies the first variation exactly (for a given  $t$ ) the expression simplifies to:

$$\text{Term}_3 = \gamma \int ((I - c_1)^2 - (I - c_2)^2) \phi_t \, dx \quad (C.5)$$

And lastly, the second term is made up of two subterms which will be handled separately:

$$\begin{aligned}
\text{Term}_2 &= -\mu \iint [\nabla \phi_t(x) \cdot \nabla \phi(y) + \nabla \phi(x) \cdot \nabla \phi_t(y)] e^{-\frac{\|x-y\|^2}{d^2}} W_l(\phi(x)) W_l(\phi(y)) \\
&+ \nabla \phi(x) \cdot \nabla \phi(y) e^{-\frac{\|x-y\|^2}{d^2}} [W_l'(\phi(x)) W_l(\phi(y)) \phi_t(x) + W_l(\phi(x)) W_l'(\phi(y)) \phi_t(y)] \, dx \, dy \quad (C.6) \\
&= -\mu(\text{Term}_{2a} + \text{Term}_{2b})
\end{aligned}$$

The main task is to separate the variables  $x$  and  $y$  as is done in [7]. This can be done via Fubini's theorem [89], by switching integration order and recombining terms to get:

$$\begin{aligned}
\text{Term}_{2a} &= \iint [\nabla\phi_t(x) \cdot \nabla\phi(y) + \nabla\phi(x) \cdot \nabla\phi_t(y)] e^{-\frac{\|x-y\|^2}{d^2}} W_l(\phi(x))W_l(\phi(y)) \, dx \, dy \\
&= \iint \nabla\phi_t(x) \cdot \nabla\phi(y) e^{-\frac{\|x-y\|^2}{d^2}} W_l(\phi(x))W_l(\phi(y)) \, dx \, dy \\
&\quad + \iint \nabla\phi(x) \cdot \nabla\phi_t(y) e^{-\frac{\|x-y\|^2}{d^2}} W_l(\phi(x))W_l(\phi(y)) \, dx \, dy
\end{aligned}$$

Letting  $x = (x_1, x_1)$ ,  $y = (y_1, y_2)$  and  $\nabla\phi(y) = \left(\frac{\partial\phi}{\partial y_1}, \frac{\partial\phi}{\partial y_2}\right)$ , applying integration by parts yields:

$$\begin{aligned}
\text{Term}_{2a} &= - \int \left( \int \frac{\partial}{\partial x_1} \left( \nabla\phi(y) e^{-\frac{\|x-y\|^2}{d^2}} W_l(\phi(x))W_l(\phi(y)) \right) + \frac{\partial}{\partial x_2} \left( \nabla\phi(y) e^{-\frac{\|x-y\|^2}{d^2}} W_l(\phi(x))W_l(\phi(y)) \right) \, dy \right) \phi_t(x) \, dx \\
&\quad - \int \left( \int \frac{\partial}{\partial y_1} \left( \nabla\phi(x) e^{-\frac{\|x-y\|^2}{d^2}} W_l(\phi(x))W_l(\phi(y)) \right) + \frac{\partial}{\partial y_2} \left( \nabla\phi(x) e^{-\frac{\|x-y\|^2}{d^2}} W_l(\phi(x))W_l(\phi(y)) \right) \, dx \right) \phi_t(y) \, dy
\end{aligned}$$

which can be written more concisely as

$$\begin{aligned}
&= - \int \left( \int \text{div}_x \left( \nabla\phi(y) e^{-\frac{\|x-y\|^2}{d^2}} W_l(\phi(x))W_l(\phi(y)) \right) \, dy \right) \phi_t(x) \, dx \\
&\quad - \int \left( \int \text{div}_y \left( \nabla\phi(x) e^{-\frac{\|x-y\|^2}{d^2}} W_l(\phi(x))W_l(\phi(y)) \right) \, dx \right) \phi_t(y) \, dy
\end{aligned} \tag{C.7}$$

where  $\text{div}_x = \left(\frac{\partial}{\partial x_1}, \frac{\partial}{\partial x_2}\right) \cdot (\cdot, \cdot)$

Switching the order of integration in (C.7) and relabelling the variables, allows the terms to be added to obtain:

$$\text{Term}_{2a} = -2 \int \left( \int \text{div}_x \left( \nabla\phi(y) e^{-\frac{\|x-y\|^2}{d^2}} W_l(\phi(x))W_l(\phi(y)) \right) \, dy \right) \phi_t(x) \, dx \tag{C.8}$$

Computing  $\text{div}_x \left( \nabla\phi(y) e^{-\frac{\|x-y\|^2}{d^2}} W_l(\phi(x))W_l(\phi(y)) \right)$

$$\begin{aligned}
&\text{div}_x \left( \nabla\phi(y) e^{-\frac{\|x-y\|^2}{d^2}} W_l(\phi(x))W_l(\phi(y)) \right) = \\
&\frac{\partial}{\partial x_1} \left( \frac{\partial\phi(y)}{\partial y_1} e^{-\frac{\|x-y\|^2}{d^2}} W_l(\phi(x))W_l(\phi(y)) \right) + \frac{\partial}{\partial x_2} \left( \frac{\partial\phi(y)}{\partial y_2} e^{-\frac{\|x-y\|^2}{d^2}} W_l(\phi(x))W_l(\phi(y)) \right)
\end{aligned}$$

Separating terms in  $x$  from terms in  $y$  and rearranging gives

$$\begin{aligned}
&= \frac{\partial \phi(y)}{\partial y_1} W_l(\phi(y)) \left[ \frac{\partial}{\partial x_1} e^{-\frac{\|x-y\|^2}{d^2}} W_l(\phi(x)) \right] + \frac{\partial \phi(y)}{\partial y_2} W_l(\phi(y)) \left[ \frac{\partial}{\partial x_2} e^{-\frac{\|x-y\|^2}{d^2}} W_l(\phi(x)) \right] \\
&= \frac{\partial \phi(y)}{\partial y_1} W_l(\phi(y)) \left[ \frac{2(x-y)}{d^2} e^{-\frac{\|x-y\|^2}{d^2}} W_l(\phi(x)) \right] + \frac{\partial \phi(y)}{\partial y_1} W_l(\phi(y)) \left[ e^{-\frac{\|x-y\|^2}{d^2}} W_l'(\phi(x)) \frac{\partial}{\partial x_1} \phi(x) \right] \\
&\quad + \frac{\partial \phi(y)}{\partial y_2} W_l(\phi(y)) \left[ \frac{2(x-y)}{d^2} e^{-\frac{\|x-y\|^2}{d^2}} W_l(\phi(x)) \right] + \frac{\partial \phi(y)}{\partial y_2} W_l(\phi(y)) \left[ e^{-\frac{\|x-y\|^2}{d^2}} W_l'(\phi(x)) \frac{\partial}{\partial x_2} \phi(x) \right]
\end{aligned}$$

Simplifying the terms yields:

$$\nabla \phi(y) W_l(\phi(y)) \left( \frac{2(x-y)}{d^2} e^{-\frac{\|x-y\|^2}{d^2}} W_l(\phi(x)) \right) + \nabla \phi(y) \cdot \nabla \phi(x) W_l'(\phi(x)) W_l(\phi(y)) e^{-\frac{\|x-y\|^2}{d^2}} \quad (\text{C.9})$$

Replacing (C.8) by (C.9) yields:

$$\begin{aligned}
\text{Term}_{2a} &= -2 \int \left( \int \left( \frac{2(x-y)}{d^2} \cdot \nabla \phi(y) e^{-\frac{\|x-y\|^2}{d^2}} W_l(\phi(x)) W_l(\phi(y)) \right) dy \right) \phi_t(x) dx \\
&\quad - 2 \int \left( \int \left( \nabla \phi(y) \cdot \nabla \phi(x) e^{-\frac{\|x-y\|^2}{d^2}} W_l'(\phi(x)) W_l(\phi(y)) \right) dy \right) \phi_t(x) dx
\end{aligned} \quad (\text{C.10})$$

For the second subterm, a similar approach yields:

$$\begin{aligned}
\text{Term}_{2b} &= \\
&\iint \nabla \phi(x) \cdot \nabla \phi(y) e^{-\frac{\|x-y\|^2}{d^2}} [W_l'(\phi(x)) W_l(\phi(y)) \phi_t(x) + W_l(\phi(x)) W_l'(\phi(y)) \phi_t(y)] dx dy \\
&= \iint \nabla \phi(x) \cdot \nabla \phi(y) e^{-\frac{\|x-y\|^2}{d^2}} W_l'(\phi(x)) W_l(\phi(y)) \phi_t(x) dx dy \\
&\quad + \iint \nabla \phi(x) \cdot \nabla \phi(y) e^{-\frac{\|x-y\|^2}{d^2}} W_l(\phi(x)) W_l'(\phi(y)) \phi_t(y) dx dy \\
&= 2 \int \left( \int \nabla \phi(x) \cdot \nabla \phi(y) e^{-\frac{\|x-y\|^2}{d^2}} W_l'(\phi(x)) W_l(\phi(y)) dy \right) \phi_t(x) dx \quad (\text{C.11})
\end{aligned}$$

In this form both of the subterms can be combined together to get (with some cancellation):

$$\text{Term}_2 = \frac{4\mu}{d^2} \int \left( \int \left( (x-y) \cdot \nabla \phi(y) e^{-\frac{\|x-y\|^2}{d^2}} W_l(\phi(x)) W_l(\phi(y)) \right) dy \right) \phi_t(x) dx \quad (\text{C.12})$$

Factoring out  $\phi_t$  and combining all the computed terms yields:

$$\begin{aligned}
& \partial_t \bar{E}(\phi(t, -), c_1(t), c_2(t)) \\
&= - \int \left[ \operatorname{div} \left( \frac{\nabla \phi}{|\nabla \phi|} \right) + \gamma ((I - c_1)^2 - (I - c_2)^2) \right. \\
&\quad \left. + \frac{4\mu}{d^2} W_l(\phi) \int (x - y) \cdot \nabla \phi(y) e^{-\frac{\|x-y\|^2}{d^2}} W_l(\phi(y)) \, dy \right] \phi_t(x) \, dx \\
&= - \int \phi_t^2 \, dx \\
&\leq 0
\end{aligned} \tag{C.13}$$

since  $\phi$  satisfies Equation (4.9) and  $|\nabla \phi| = 1$  a.e.

□

# D

## Software Implementation

Implementations of the GAC as well as CV models can be found on Matlab file-exchange. See in particular <http://www.mathworks.com/matlabcentral/fileexchange/24998-2d-3d-image-segmentation-toolbox><sup>1</sup>. A modified version of these codes were used as part of the boundary reinforcement scheme presented in chapter 3. The codes for implementing the nodule separation scheme is presented below.

```
function [noduleCandidates] = separate_nodules(phi_b, ...
    xyzspacing, sigma, iters)

%         outputs just noduleCandidates
%         inputs: phi_b, xyzspacing, sigma_MBO, iters_MBO
%         phi_b - output of background removal code
```

---

<sup>1</sup>Last accessed May 28 2015

```

%           xyzspacing -
%           sigma_MBO -
%           iters_MBO -

[Nx,Ny,Nz]=size(phi_b);
phi_t = phi_b;

% setup system variables
binaryMask=false(Nx,Ny,Nz);
noduleCandidates=false(Nx,Ny,Nz);

% Separate out connected components
roiCC=bwconncomp(phi_t,18);
NumberCCs = roiCC.NumObjects;

nodule_idx = 1; % index for 'indices_detected_nodules' cell array
indices_detected_nodules = {};
[noduleCandidates, flags] = preselection(phi_b,xyzspacing); % run ...
    classifier on pre smoothed result
if nnz(flags) ~=0
    indices_detected_nodules{nodule_idx,1} = ...
        vertcat(roiCC.PixelIdxList{flags>0});
    nodule_idx = nodule_idx + 1;
end

i = 1;

idx = find(cellfun(@(x)(length(x)>10), roiCC.PixelIdxList)); % ...
    find indices of cells containing arrays of length greater than ...
    5 voxels
numel(idx)
components_subset = zeros([numel(idx) 1]);
cmpnts_idx = 1;

```

```

while (i < iters) && (~isempty(find(phi_t)))

    % 1. apply MBO scheme in order to eliminate extraneous detail and
        % smooth objects with complex geometry.
    psi = gauss3filter(phi_t, sigma);

    phi_t = double( psi > 1/2);

    % 2. Compute intersection between MBO output and phase 1 result ...
        i.e.
        % retrieve the detail in smoothed result
    phi = logical(phi_t) & logical(phi_b);

    for j=1:length(idx)

        binaryMask=false(Nx,Ny,Nz);
        objectPosition=roiCC.PixelIdxList{idx(j)};
        binaryMask(objectPosition)=1; % a volume containing just ...
            component(j) of original unsmoothed segm. result % ...
            comment: potential memory wastage here

        binaryMask(vertcat(cell2mat(indices_detected_nodules(1:end)))) ...
            = 0;
        phi(vertcat(cell2mat(indices_detected_nodules(1:end)))) = 0;

        % 4. Compute intersection between phi and CC(j)
        indicator = phi & binaryMask;

        if nnz(indicator) == 0 % this occurs with (typically) small ...
            components existing in the presmoothed segm. result, ...
            and which have been subsequently eliminated by the MBO scheme
            components_subset(cmpnts_idx) = j;
            cmpnts_idx=cmpnts_idx+1;
            continue;

```

```

end

% Count number of components in indicator
CCindicator = bwconncomp(indicator,18);
numIndCompnts = CCindicator.NumObjects;

% apply preselector:
[noduleCandidateMask, flags] = ...
    preselection(indicator,xyzspacing); % flags = true if ...
    noduleCandidate is detected
if nnz(flags) ~=0
    % store component indices of detected (potential) nodule
    indices_detected_nodules{nodule_idx,1} = ...
        vertcat(CCindicator.PixelIdxList{flags>0});

    nodule_idx = nodule_idx + 1;
    noduleCandidates = noduleCandidates | noduleCandidateMask;

end

end

idx(components_subset(components_subset~= 0)') = []; % remove ...
    components which the MBO scheme has eliminated
components_subset = zeros([numel(idx) 1]);
cmpnts_idx=1;
i = i + 1;

end

end

```

The 3-D max-flow code used to obtain a segmentation of the lungs is presented below (note that a 2-D version of this code was used as part of the method presented chapter 3, to obtain the segmentation of the echocardiography data).

```

function [ut, iter, ulab] = CMF3D_Cutcv(ur, lp, errb, ulab)

% Performs the continuous max-flow algorithm to solve the
% continuous min-cut problem in 3-D
% The code minimizes wrt c_in and c_out, as well as lambda
% Has adaptable error bound, having the effect that
% lambda is not solved to such a high accuracy until c1 and c2 ...
% start to
% converge.

% Usage: [u, timet] = CMF3D_Cutcv(ur, lp, errb, ulab);
%
% Inputs: ur      - data term
%          lp      - length parameter. This parameters controls the ...
% level
%                  of fine detail in the result. Range: ...
% [1e-12, 1]
%          errb    - [1x2] vector. The error bound for convergence.
%                  errb(1) error bound for convergence of u
%                  errb(2) error bound for convergence of c1 and c2
%          ulab    - Initial estimates of background and foreground
%                  intensity
%
%
% Outputs:
%   - u: the final results u(x) in [0,1]. As the following paper,
%       the global binary result can be available by ...
%       thresholding u
%       by any constant alpha in (0,1):
%
%       Nikolova, M.; Esedoglu, S.; Chan, T. F.
%       Algorithms for Finding Global Minimizers of Image ...
%       Segmentation and Denoising Models
%       SIAM J. App. Math., 2006, 66, 1632-1648

```

```
%
%
%   - timet: gives the total computation time.
%   - ulab: final estimates of background and foreground
%           intensity
%
% Please email noirinduggan@gmail.com for any questions, ...
% suggestions and bug reports
%
% The Software is provided "as is", without warranty of any kind.

[rows, cols, heights]=size(ur);
szVol = rows*cols*heights;

% define the required parameters:

%   - cc: gives the step-size of the augmented Lagrangian method.
%       The optimal range of cc is [0.2, 3].

%
%   - numIter: the maximum iteration number.

%
%   - steps: the step-size for the gradient-projection step to the
%           total-variation function. The optimal range of steps is [0.07,
%           0.12].
%
%

alpha =lp*ones(rows,cols,heights); % default

cc = 0.35; % default = 0.35;
```

```
c_convergence = 3e-4;
steps = 0.11;
beta = 2;

% build up the priori L-2 data terms
Cs = abs(ur - ulab(1)).^beta;
Ct = abs(ur - ulab(2)).^beta;

% set the starting values
u = double((Cs-Ct) >= 0);
ps = min(Cs, Ct);
pt = ps;

pp1 = zeros(rows, cols+1, heights);
pp2 = zeros(rows+1, cols, heights);
pp3 = zeros(rows, cols, heights+1);
divp = - pp2(1:rows, :, :) + pp2(2:rows+1, :, :) + pp1(:, 2:cols+1, :) ...
- pp1(:, 1:cols, :) + pp3(:, :, 2:heights+1) - pp3(:, :, 1:heights);

erriter = zeros(300,1);
err_c = zeros(300,1);

tic

iter = 1;
err_c(1) = 1;

while (err_c(iter) > errb(2))

    % if cs and ct are beginning to converge, tighten the ...
    % convergence limit
    % for lambda
    if err_c(iter) < c_convergence
        errb(1) = 5e-4;
    end
end
```

```

i=1;
erriter(1) = 1;

while (erriter(i) > errb(1))

    i=i+1;

    % update the spatial flow field p = (pp1, pp2, pp3):
    % the following steps are the gradient descent step with ...
    % steps as the
    % step-size.

    pts = divp - (ps - pt + u/cc);
    pp1(:,2:cols,:) = pp1(:,2:cols,:) + steps*(pts(:,2:cols,:) ...
        - pts(:,1:cols-1,:));
    pp2(2:rows,,:) = pp2(2:rows,,:) + steps*(pts(2:rows,,:) ...
        - pts(1:rows-1,,:));
    pp3(:, :, 2:heights) = pp3(:, :, 2:heights) + ...
        steps*(pts(:, :, 2:heights) - pts(:, :, 1:heights-1));

    % the following steps give the projection to make |p(x)| <= ...
    alpha(x)

    gk = sqrt((pp1(:,1:cols,).^2 + pp1(:,2:cols+1,).^2 + ...
        pp2(1:rows,).^2 + pp2(2:rows+1,).^2 + ...
        pp3(:, :, 1:heights).^2 + pp3(:, :, 2:heights+1).^2)*0.5);

    gk = double(gk <= alpha) + double(~(gk <= alpha)).*(gk ./ ...
        alpha);
    gk = 1 ./ gk;

    pp1(:,2:cols,:) = (0.5*(gk(:,2:cols,:) + ...
        gk(:,1:cols-1,:))).*pp1(:,2:cols,:);
    pp2(2:rows,,:) = (0.5*(gk(2:rows,,:) + ...
        gk(1:rows-1,,:))).*pp2(2:rows,,:);
    pp3(:, :, 2:heights) = (0.5*(gk(:, :, 2:heights) + ...

```

```

        gk(:, :, 1:heights-1)) .* pp3(:, :, 2:heights);

divp = - pp2(1:rows, :, :) + pp2(2:rows+1, :, :) + ...
        pp1(:, 2:cols+1, :) ...
- pp1(:, 1:cols, :) + pp3(:, :, 2:heights+1) - pp3(:, :, 1:heights);

% update the source flow ps

pts = divp - u/cc + pt + 1/cc;
Cs = abs(ur - ulab(1)).^beta;
ps = min(pts, Cs);

% update the sink flow pt

pts = - divp + ps + u/cc;
Ct = abs(ur - ulab(2)).^beta;
pt = min(pts, Ct);

% update the multiplier u

erru = cc*(divp + pt - ps);
u = u - erru;

% evaluate the average error

erriter(i) = sum(sum(sum(abs(erru))))/szVol;

if (erriter(i) < errb(1))
    break;
end
end

ut = u > 0.5;

ulab_p = ulab;

```

```
ulab(1) = sum(sum(sum( ur(:, :, :) .* (1-ut(:, :, :)) ) ) ./ sum(sum( ...  
    (1-ut(:, :, :)) ) ) ) / heights;  
ulab(2) = sum(sum(sum( ur(:, :, :) .* ut(:, :, :)) ) ./ sum(sum( ...  
    ut(:, :, :)) ) ) / heights;  
iter  
iter = iter + 1;  
err_c(iter) = abs(ulab_p(1) - ulab(1)) + abs(ulab_p(2) - ulab(2));
```

```
end
```

# Bibliography

- [1] X. Bresson, Image segmentation with variational active contours. PhD thesis, STI, Lausanne, 2005. [12](#), [16](#)
- [2] H. C. Ford, X. Hui, R. Ciardullo, G. H. Jacoby, and K. C. Freeman, “The stellar halo of M104. I. A survey for planetary nebulae and the planetary nebula luminosity function distance,” Astrophysical Journal, vol. 458, pp. 455–466, 1996. [42](#), [45](#)
- [3] X. Han, C. Xu, and J. L. Prince, “A topology preserving level set method for geometric deformable models,” Pattern Analysis and Machine Intelligence, IEEE Transactions on, vol. 25, no. 6, pp. 755–768, 2003. [55](#), [67](#)
- [4] T. Chan and L. Vese, “Active contours without edges,” IEEE T Image Process, vol. 10, pp. 266–277, Feb 2001. [6](#), [13](#), [15](#), [22](#), [23](#), [25](#), [29](#), [55](#), [74](#), [75](#), [76](#), [85](#)
- [5] S. G. Armato, G. McLennan, L. Bidaut, M. F. McNitt-Gray, C. R. Meyer, A. P. Reeves, B. Zhao, D. R. Aberle, C. I. Henschke, E. A. Hoffman, E. A. Kazerooni, H. MacMahon, E. J. Van Beeke, D. Yankelevitz, A. M. Biancardi, P. H. Bland, M. S. Brown, R. M. Engelmann, G. E. Laderach, D. Max, R. C. Pais, D. P. Qing, R. Y. Roberts, A. R. Smith, A. Starkey, P. Batrah, P. Caligiuri, A. Farooqi, G. W. Gladish, C. M. Jude, R. F. Munden, I. Petkovska, L. E. Quint, L. H. Schwartz, B. Sundaram, L. E. Dodd, C. Fenimore, D. Gur, N. Petrick, J. Freymann, J. Kirby, B. Hughes, A. V. Castelee,

- S. Gupte, M. Sallamm, M. D. Heath, M. H. Kuhn, E. Dharaiya, R. Burns, D. S. Fryd, M. Salganicoff, V. Anand, U. Shreter, S. Vastagh, and B. Y. Croft, “The Lung Image Database Consortium (LIDC) and Image Database Resource Initiative (IDRI): a completed reference database of lung nodules on CT scans,” Med Phys, vol. 38, pp. 915–931, Feb 2011. [76](#), [89](#)
- [6] M. F. McNitt-Gray, S. G. A. III, C. R. Meyer, A. P. Reeves, G. McLennan, R. C. Pais, J. Freymann, M. S. Brown, R. M. Engelmann, P. H. Bland, G. E. Laderach, C. Piker, J. Guo, Z. Towfic, D. P.-Y. Qing, D. F. Yankelevitz, D. R. Aberle, E. J. van Beek, H. MacMahon, E. A. Kazerooni, B. Y. Croft, and L. P. Clarke, “The lung image database consortium (lidc) data collection process for nodule detection and annotation,” Academic Radiology, vol. 14, no. 12, pp. 1464 – 1474, 2007. [76](#), [89](#)
- [7] C. Le Guyader and L. A. Vese, “Self-repelling snakes for topology-preserving segmentation models,” Image Processing, IEEE Transactions on, vol. 17, no. 5, pp. 767–779, 2008. [23](#), [25](#), [26](#), [27](#), [53](#), [55](#), [56](#), [57](#), [59](#), [61](#), [67](#), [74](#), [75](#), [76](#), [77](#), [154](#)
- [8] J. Yuan, E. Bae, and X.-C. Tai, “A study on continuous max-flow and min-cut approaches,” in IEEE Conference on Computer Vision and Pattern Recognition (CVPR), pp. 2217–2224, 2010. [23](#), [35](#), [74](#), [77](#), [78](#), [79](#)
- [9] J. Yuan, E. Bae, X.-C. Tai, and Y. Boykov, “A spatially continuous max-flow and min-cut framework for binary labeling problems,” Numerische Mathematik, vol. 126, no. 3, pp. 559–587, 2014. [23](#), [35](#), [36](#), [74](#), [77](#), [78](#), [79](#), [99](#)
- [10] R. M. Haralick and L. G. Shapiro, Computer and Robot Vision. Boston, MA, USA: Addison-Wesley Longman Publishing Co., Inc., 1st ed., 1992. [2](#)
- [11] E. T. Rolls, High-level vision: Object recognition and visual cognition, vol. 1. Cambridge, Mass. MIT Press, 1997. [3](#)

- [12] K. Grill-Spector and N. Kanwisher, “Visual recognition: As soon as you know it is there, you know what it is,” Psychological Science, vol. 16, no. 2, pp. 152–160, 2005. 5
- [13] M. A. Peterson, Overlapping partial configurations in object memory: An alternative solution to classic problems in perception and recognition. Perception of faces, objects, and scenes: Analytic and holistic processes. Advances in visual cognition, New York: Oxford University Press, 2003. 5
- [14] M. Peterson and B. Gibson, “Shape recognition contributions to figure-ground organization in three-dimensional display,” Cognitive Psychology, vol. 25, pp. 383–429, 1993. 5
- [15] M. Peterson and B. Gibson, “Must shape recognition follow figure-ground organization? an assumption in peril,” Psychological Science, vol. 5, pp. 253–259, 1994. 5
- [16] M. Peterson and J. Kim, “On what is bound in figures and grounds,” Visual Cognition, vol. 8, p. 329348, 2001. 5
- [17] M. Peterson and D. Lampignano, “Implicit memory for novel figure-ground displays includes a history of cross-border competition,” Journal of Experimental Psychology: Human Perception and Performance, vol. 29, pp. 808–822, 2003. 5
- [18] S. Mallat, A Wavelet Tour of Signal Processing, Third Edition: The Sparse Way. Academic Press, 3rd ed., 2008. 6
- [19] A. Chambolle, R. De Vore, N.-Y. Lee, and B. Lucier, “Nonlinear wavelet image processing: variational problems, compression, and noise removal through wavelet shrinkage,” Image Processing, IEEE Transactions on, vol. 7, pp. 319–335, March 1998. 6

- [20] H. Choi and R. Baraniuk, “Image segmentation using wavelet-domain classification,” in Proceedings of SPIE technical conference on Mathematical Modeling, Bayesian Estimation, and Inverse Problems, pp. 306–320, 1999. 6
- [21] A. Rosenfeld and J. Weszka, “Picture recognition,” in Digital Pattern Recognition (K. Fu, ed.), vol. 10 of Communication and Cybernetics, pp. 135–166, Springer Berlin Heidelberg, 1980. 6
- [22] M. Zou and D. Wang, “Texture identification and image segmentation via fourier transform,” vol. 4550, pp. 34–39, 2001. 6
- [23] S. Z. Li, Markov Random Field Modeling in Image Analysis. Springer Publishing Company, Incorporated, 3rd ed., 2009. 6
- [24] S. Geman and D. Geman, “Stochastic relaxation, gibbs distributions, and the bayesian restoration of images,” IEEE Trans. Pattern Anal. Mach. Intell., vol. 6, pp. 721–741, Nov. 1984. 6, 17
- [25] M. Kass, A. Witkin, and D. Terzopoulos, “Snakes: Active contour models,” International Journal of Computer Vision, pp. 321–331, 1987. 6, 13, 14
- [26] V. Caselles, R. Kimmel, and G. Sapiro, “Geodesic active contours,” Int J Comput Vision, vol. 22, no. 1, pp. 61–79, 1997. 6, 14, 22, 23, 25, 27, 29
- [27] Y. Boykov, O. Veksler, and R. Zabih, “Fast approximate energy minimization via graph cuts,” IEEE Transactions on Pattern Analysis and Machine Intelligence, vol. 23, pp. 1222–1239, NOV 2001. 6, 18
- [28] Y. Boykov and V. Kolmogorov, “An experimental comparison of min-cut/max-flow algorithms for energy minimization in vision,” Pattern Analysis and Machine Intelligence, IEEE Transactions on, vol. 26, pp. 1124–1137, Sept 2004. 6
- [29] J. M. Morel and S. Solimini, Variational Methods in Image Segmentation. Cambridge, MA, USA: Birkhauser Boston Inc., 1995. 6

- [30] T. McInerney and D. Terzopoulos, “Deformable models in medical image analysis,” Mathematical Methods in Biomedical Image Analysis, 1996., Proceedings of the Workshop on, pp. 171–180, Jun 1996. [6](#)
- [31] D. Mumford and J. Shah, “Optimal approximations by piecewise smooth functions and associated variational problems,” Communications on Pure and Applied Mathematics, vol. 42, no. 5, pp. 577–685, 1989. [11](#), [14](#)
- [32] M. A. Peletier, “Variational modelling: Energies, gradient flows, and large deviations,” ArXiv e-prints, Feb. 2014. [11](#)
- [33] G. Sapiro, Geometric Partial Differential Equations and Image Analysis. New York, NY, USA: Cambridge University Press, 2006. [12](#)
- [34] J. B. MacQueen, “Some methods for classification and analysis of multivariate observations,” in Proc. of the fifth Berkeley Symposium on Mathematical Statistics and Probability (L. M. L. Cam and J. Neyman, eds.), vol. 1, pp. 281–297, University of California Press, 1967. [12](#)
- [35] J. A. Hartigan and M. A. Wong, “A k-means clustering algorithm,” Applied Statistics, vol. 28, pp. 100–108, 1979. [12](#)
- [36] S. Osher and J. A. Sethian, “Fronts propagating with curvature-dependent speed: algorithms based on hamilton-jacobi formulations,” J. Comput. Phys., vol. 79, pp. 12–49, Nov. 1988. [14](#), [28](#)
- [37] S. Kichenassamy, A. Kumar, P. Olver, A. Tannenbaum, and A. Yezzi, “Conformal curvature flows: from phase transitions to active vision,” Arch. Rat. Mech. Anal., vol. 134, pp. 275–301, 1996. [14](#)
- [38] L. Vese and T. Chan, “A multiphase level set framework for image segmentation using the mumford and shah model,” International Journal of Computer Vision, vol. 50, pp. 271–293, DEC 2002. [15](#), [55](#), [104](#)

- [39] L. A. Vese and T. F. Chan, “A multiphase level set framework for image segmentation using the mumford and shah model,” International Journal of Computer Vision, vol. 50, no. 3, pp. 271–293, 2002. 15
- [40] G. Chung and L. A. Vese, “Image segmentation using a multilayer level-set approach,” Computing and Visualization in Science, vol. 12, pp. 267–285, Apr. 2008. 15
- [41] B. Sandberg, T. Chan, and L. Vese, “A level-set and gabor-based active contour algorithm for segmenting textured images,” tech. rep., UCLA Department of Mathematics CAM report, 2002. 15
- [42] H. Schaeffer, “Active arcs and contours,” UCLA CAM Report, vol. 12–54, 2012. 15
- [43] H. Schaeffer and L. Vese, “Active contours with free endpoints,” Journal of Mathematical Imaging and Vision, pp. 1–17, 2013. 15
- [44] D. Greig, B. Porteous, and B. Seheult, “Exact maximum a posteriori estimation for binary images,” Journal of the Royal Statistical Society Series B, vol. 51, no. 2, pp. 271–279, 1989. 17, 18
- [45] S. Birchfield and C. Tomasi, “Multiway cut for stereo and motion with slanted surfaces,” in International Conference of Computer Vision, pp. 489–495, 1999. 18
- [46] Y. Boykov, O. Veksler, and R. Zabih, “Markov random fields with efficient approximations,” in Computer Vision and Pattern Recognition, 1998. Proceedings, pp. 648–655, Jun 1998. 18
- [47] H. Ishikawa and D. Geiger, “Occlusions, discontinuities, and epipolar lines in stereo,” in Proceedings of the 5th European Conference on Computer Vision-Volume I - Volume I, ECCV '98, (London, UK, UK), pp. 232–248, Springer-Verlag, 1998. 18

- [48] J. Kim, V. Kolmogorov, and R. Zabih, “Visual correspondence using energy minimization and mutual information,” in Computer Vision, 2003. Proceedings. Ninth IEEE International Conference on, pp. 1033–1040 vol.2, Oct 2003. 18
- [49] V. Kolmogorov and R. Zabih, “Computing visual correspondence with occlusions using graph cuts,” in Computer Vision, 2001. ICCV 2001. Proceedings. Eighth IEEE International Conference on, vol. 2, pp. 508–515 vol.2, 2001. 18
- [50] Y. Boykov and M.-P. Jolly, “Interactive organ segmentation using graph cuts,” in Medical Image Computing and Computer-Assisted Intervention MICCAI 2000 (S. Delp, A. DiGoia, and B. Jaramaz, eds.), vol. 1935 of Lecture Notes in Computer Science, pp. 276–286, Springer Berlin Heidelberg, 2000. 18
- [51] Y. Boykov and M.-P. Jolly, “Interactive graph cuts for optimal boundary and region segmentation of objects in n-d images,” in Computer Vision, 2001. ICCV 2001. Proceedings. Eighth IEEE International Conference on, vol. 1, pp. 105–112 vol.1, 2001. 18
- [52] J. Kim and R. Zabih, “A segmentation algorithm for contrast-enhanced images,” in International Conference on Computer Vision, pp. 502–509, 2003. 18
- [53] J. Kim, J. W. Fisher, III, A. Tsai, C. Wible, A. S. Willsky, and W. M. Wells, III, “Incorporating spatial priors into an information theoretic approach for fmri data analysis,” in Proceedings of the Third International Conference on Medical Image Computing and Computer-Assisted Intervention, MICCAI '00, (London, UK, UK), pp. 62–71, Springer-Verlag, 2000. 18
- [54] Y. Boykov and V. Kolmogorov, “Computing geodesics and minimal surfaces via graph cuts,” in Proceedings of International Conference on Computer Vision - Volume 2, ICCV '03, (Washington, DC, USA), pp. 26–, IEEE Computer Society, 2003. 18

- [55] V. Kolmogorov and R. Zabih, “Multi-camera scene reconstruction via graph cuts,” in Proceedings of the 7th European Conference on Computer Vision-Part III, ECCV '02, (London, UK, UK), pp. 82–96, Springer-Verlag, 2002. 18
- [56] H. Ishikawa and D. Geiger, “Segmentation by grouping junctions,” in Proceedings of the IEEE Computer Society Conference on Computer Vision and Pattern Recognition, CVPR '98, (Washington, DC, USA), pp. 125–, IEEE Computer Society, 1998. 18
- [57] L. Ford and D. Fulkerson, Flows in networks. Princeton: Princeton University Press, 1962. 18
- [58] T. Pock, A. Chambolle, D. Cremers, and H. Bischof, “A convex relaxation approach for computing minimal partitions,” in Computer Vision and Pattern Recognition, 2009. CVPR 2009. IEEE Conference on, pp. 810–817, June 2009. 18
- [59] V. Kolmogorov, “Convergent tree-reweighted message passing for energy minimization,” Pattern Analysis and Machine Intelligence, IEEE Transactions on, vol. 28, pp. 1568–1583, Oct 2006. 18
- [60] V. Kolmogorov and Y. Boykov, “What metrics can be approximated by geocuts, or global optimization of length/area and flux,” in Proceedings of the Tenth IEEE International Conference on Computer Vision (ICCV'05) Volume 1 - Volume 01, ICCV '05, (Washington, DC, USA), pp. 564–571, IEEE Computer Society, 2005. 18
- [61] P. Kohli, M. P. Kumar, and P. H. S. Torr, “P & beyond: Solving energies with higher order cliques,” in IN COMPUTER VISION AND PATTERN RECOGNITION, 2007. 18

- [62] T. Chan, S. Esedoglu, and M. Nikolova, “Algorithms for finding global minimizers of image segmentation and denoising models,” SIAM J. Appl. Math., vol. 10, no. 2, pp. 266–277, 2001. [19](#), [25](#), [34](#)
- [63] N. Paragios and R. Deriche, “Unifying boundary and region-based information for geodesic active tracking,” in IEEE Conference on Computer Vision and Pattern Recognition, vol. 2, 1999. [22](#)
- [64] X. Bresson, S. Esedoglu, P. Vandergheynst, J.-P. Thiran, and S. Osher, “Fast global minimization of the active contour/snake model,” Journal of Mathematical Imaging and Vision, vol. 28, pp. 151–167, June 2007. [22](#), [23](#), [25](#)
- [65] L. Wang, J. H. Moltz, L. Bornemann, and H. K. Hahn, “A minimally interactive method to segment enlarged lymph nodes in 3d thoracic ct images using a rotatable spiral-scanning technique,” pp. 83150D–83150D–8, 2012. [22](#), [23](#)
- [66] T. Pock, D. Cremers, H. Bischof, and A. Chambolle, “An algorithm for minimizing the mumford-shah functional,” in ICCV, pp. 1133–1140, 2009. [22](#)
- [67] T. D. Bui, S. Gao, and Q. Zhang, “A generalized mumford-shah model for roof-edge detection,” in ICIP (2), pp. 1214–1217, 2005. [22](#), [23](#)
- [68] P. Perona and J. Malik, “Scale-space and edge detection using anisotropic diffusion,” IEEE Trans. Pattern Anal. Mach. Intell., vol. 12, no. 7, pp. 629–639, 1990. [23](#)
- [69] K. Rajpoot, V. Grau, and J. Noble, “Local-phase based 3d boundary detection using monogenic signal and its application to real-time 3-d echocardiography images,” in IEEE International Symposium on Biomedical Imaging, pp. 783–786, 28 2009-july 1 2009. [23](#), [39](#)
- [70] M. Felsberg and G. Sommer, “The monogenic signal,” IEEE Transactions on Signal Processing, vol. 49, no. 12, pp. 3136–3144, 2001. [23](#)

- [71] M. Mulet-Parada and J. Noble, “2d+t acoustic boundary detection in echocardiography,” MEDICAL IMAGE ANALYSIS, vol. 4, pp. 21–30, MAR 2000. 1st International Conference on Medical Image Computing and Computer-Assisted Intervention (MICCAI 98), CAMBRIDGE, MASSACHUSETTS, OCT 11-13, 1998. 23
- [72] J. A. Noble and D. Boukerroui, “Ultrasound image segmentation: a survey,” Medical Imaging, IEEE Transactions on, vol. 25, no. 8, pp. 987–1010, 2006. 24
- [73] M. K. Feldman, S. Katyal, and M. S. Blackwood, “Us artifacts,” RadioGraphics, vol. 29, no. 4, pp. 1179–1189, 2009. PMID: 19605664. 24
- [74] A. Schuler, “Image artifacts and pitfalls,” in Chest Sonography (G. Mathis, ed.), pp. 177–186, Springer Berlin Heidelberg, 2011. 24
- [75] T. Goldstein and S. Osher, “The split bregman method for l1-regularized problems,” SIAM Journal on Imaging Sciences, vol. 2, no. 2, pp. 323–343., 2009. 25
- [76] T. Goldstein, X. Bresson, and S. Osher, “Geometric applications of the split bregman method: Segmentation and surface reconstruction,” J. Sci. Comput., vol. 45, pp. 272–293, October 2010. 25, 26
- [77] Y. Yang, C. Li, C.-Y. Kao, and S. Osher, “Split bregman method for minimization of region-scalable fitting energy for image segmentation,” in Advances in Visual Computing (G. Bebis, R. Boyle, B. Parvin, D. Koracin, R. Chung, R. Hammound, M. Hussain, T. Kar-Han, R. Crawfis, D. Thalmann, D. Kao, and L. Avila, eds.), vol. 6454 of Lecture Notes in Computer Science, pp. 117–128, Springer Berlin Heidelberg, 2010. 25
- [78] L. Dice, “Measures of the amount of ecologic association between species,” Ecology, vol. 26, pp. 297–302, 1945. 31

- [79] G. Gerig, M. Jomier, and M. Chakos, “Valmet: A new validation tool for assessing and improving 3d object segmentation,” in Medical Image Computing and Computer-Assisted Intervention MICCAI 2001 (W. Niessen and M. Viergever, eds.), vol. 2208 of Lecture Notes in Computer Science, pp. 516–523, Springer Berlin Heidelberg, 2001. 31
- [80] J. M. Hyman and M. J. Shashkov, “Natural discretizations for the divergence, gradient, and curl on logically rectangular grids,” Comput. Math. Appl., vol. 33, no. 4, pp. 81–104, 1997. 35
- [81] X. C. Tai, Parallel computing with splitting-up methods and the distributed parameter identification problems. PhD thesis, University of Jyväskylä, 1991. 37
- [82] J. Weickert, B. M. T. H. Romeny, and M. A. Viergever, “Efficient and reliable schemes for nonlinear diffusion filtering,” IEEE Transactions on Image Processing, vol. 7, pp. 398–410, 1998. 37
- [83] K. Rajpoot, J. A. Noble, V. Grau, C. Szmigielski, and H. Becher, “Image-driven cardiac left ventricle segmentation for the evaluation of multiview fused real-time 3-dimensional echocardiography images,” in MEDICAL IMAGE COMPUTING AND COMPUTER-ASSISTED INTERVENTION - MICCAI 2009, PT II, PROCEEDINGS (G. Yang, D. Hawkes, D. Rueckert, A. Nobel, and C. Taylor, eds.), vol. 5762 of Lecture Notes in Computer Science, pp. 893–900, 2009. 12th International Conference on Medical Image Computing and Computer-Assisted Intervention (MICCAI2009), London, ENGLAND, SEP 20-24, 2009. 39
- [84] O. Alexandrov and F. Santosa, “A topology-preserving level set method for shape optimization,” Journal of Computational Physics, vol. 204, no. 1, pp. 121–130, 2005. 56

- [85] S. Osher and J. A. Sethian, “Fronts propagating with curvature-dependent speed: Algorithms based on Hamilton-Jacobi formulations,” Journal of Computational Physics, vol. 79, pp. 12–49, Nov. 1988. 57
- [86] L. C. Evans and R. F. Gariepy, Measure Theory and Fine Properties of Functions. CRC Press, 1992. 57
- [87] H. Hele-Shaw, “The flow of water,” Nature, vol. 58, pp. 34–36, 1898. 60
- [88] L. Paterson, “Radial fingering in a hele shaw cell. journal of fluid mechanics,” Journal of Fluid Mechanics, vol. 113, pp. 513–529, 1981. 60
- [89] J. Thomas, G. B. and R. L. Finney, Calculus and Analytic Geometry. Addison-Wesley, 8 ed., 1996. 61, 154
- [90] L. H. Thomas, “Elliptic problems in linear differential equations over a network,” tech. rep., Columbia University, 1949. 64
- [91] G. Russo and P. Smereka, “A remark on computing distance functions,” Journal of Computational Physics, vol. 163, no. 1, pp. 51–67, 2000. 64, 65
- [92] R. Courant, E. Isaacson, and M. Rees, “On the solution of nonlinear hyperbolic differential equations by finite differences,” Communications on Pure and Applied Mathematics, vol. 5, no. 3, pp. 243–255, 1952. 65
- [93] M. Rousson and R. Deriche, “Adaptive segmentation of vector valued images,” in Geometric Level Set Methods in Imaging, Vision, and Graphics, pp. 195–205, Springer, 2003. 72
- [94] American Cancer Society, Cancer Facts and Figures 2014, 2014. 82
- [95] J. M. Goo, “A computer-aided diagnosis for evaluating lung nodules on chest ct: the current status and perspective,” Korean Journal of Radiology, vol. 12, pp. 145–155, MAR-APR 2011. 82

- [96] H. Weir, M. Thun, B. Hankey, L. Ries, H. Howe, P. Wingo, A. Jemal, E. Ward, R. Anderson, and B. Edwards, “Annual report to the nation on the status of cancer, 1975-2000,” J. National Cancer Institute, vol. 95, p. 12761299, 2003. 82
- [97] C. Henschke, D. McCauley, D. Yankelevitz, D. Naidich, G. McGuinness, O. Miettinen, D. Libby, M. Pasmantier, J. Koizumi, N. Altorki, and J. Smith, “Early lung cancer action project: overall design and findings from baseline screening,” Lancet, vol. 354, pp. 99–105, 1999. 82
- [98] J. H. Moltz, L. Bornemann, J.-M. Kuhnigk, V. Dicken, E. Peitgen, S. Meier, H. Bolte, M. Fabel, H.-C. Bauknecht, M. Hittinger, A. Kießling, M. Pusken, and H.-O. Peitgen, “Advanced segmentation techniques for lung nodules, liver metastases, and enlarged lymph nodes in ct scans,” IEEE Journal of Selected Topics in Signal Processing, vol. 3, pp. 122–134, Feb. 2009. 82
- [99] L. Bornemann, V. Dicken, J.-M. Kuhnigk, D. Wormanns, H.-O. Shin, H.-C. Bauknecht, V. Diehl, M. Fabel, S. Meier, O. Kress, S. Krass, and H.-O. Peitgen, “Oncotreat: a software assistant for cancer therapy monitoring,” International Journal of Computer Assisted Radiology and Surgery, vol. 1, no. 5, pp. 231–242, 2007. 82
- [100] B. Sahiner, H.-P. Chan, L. M. Hadjiiski, P. N. Cascade, E. A. Kazerooni, A. R. Chughtai, C. Poopat, T. Song, L. Frank, J. Stojanovska, and A. Attili, “Effect of cad on radiologists’ detection of lung nodules on thoracic ct scans: analysis of an observer performance study by nodule size,” Acad Radiol, vol. 16, pp. 1518–1530, Dec. 2009. 82
- [101] E.-A. Park, J. M. Goo, J. W. Lee, C. H. Kang, H. J. Lee, C. H. Lee, C. M. Park, H. Y. Lee, and J.-G. Im, “Efficacy of computer-aided detection system and thin-slab maximum intensity projection technique in the detection of pulmonary nodules in patients with resected metastases,” Invest Radiol, vol. 44, pp. 105–113, Feb. 2009. 82

- [102] T. Hirose, N. Nitta, J. Shiraishi, Y. Nagatani, M. Takahashi, and K. Murata, “Evaluation of computer-aided diagnosis (cad) software for the detection of lung nodules on multidetector row computed tomography (MDCT): JAFROC study for the improvement in radiologists’ diagnostic accuracy,” Acad Radiol, vol. 15, pp. 1505–1512, Dec. 2008. 82
- [103] J. M. Goo, H. Y. Kim, J. W. Lee, H. J. Lee, C. H. Lee, K. W. Lee, T. J. Kim, K. Y. Lim, S. H. Park, and K. T. Bae, “Is the computer-aided detection scheme for lung nodule also useful in detecting lung cancer?,” Journal of Computer Assisted Tomography, vol. 32, pp. 570–575, July 2008. 82
- [104] C. Beigelman-Aubry, P. Raffy, W. Yang, R. A. Castellino, and P. A. Grenier, “Computer-aided detection of solid lung nodules on follow-up MDCT screening: evaluation of detection, tracking, and reading time,” AJR Am J Roentgenol, vol. 189, pp. 948–955, Oct. 2007. 82
- [105] K. Awai, K. Murao, A. Ozawa, M. Komi, H. Hayakawa, S. Hori, and Y. Nishimura, “Pulmonary nodules at chest CT: effect of computer-aided diagnosis on radiologists detection performance 1,” Radiology, vol. 230, no. 2, p. 347352, 2004. 82
- [106] K. Marten, C. Engelke, T. Seyfarth, A. Grillhsl, S. Obenauer, and E. Rummeny, “Computer-aided detection of pulmonary nodules: influence of nodule characteristics on detection performance,” Clinical Radiology, vol. 60, no. 2, pp. 196 – 206, 2005. 82, 97
- [107] J. W. Lee, J. M. Goo, H. J. Lee, J. H. Kim, S. Kim, and Y. T. Kim, “The potential contribution of a computer-aided detection system for lung nodule detection in multidetector row computed tomography,” Invest Radiol, vol. 39, pp. 649–655, Nov. 2004. PMID: 15486524. 82, 97
- [108] S. G. Armato III, M. L. Giger, and H. MacMahon, “Automated detection of lung nodules in ct scans: preliminary results,” Medical physics, vol. 28, no. 8, pp. 1552–1561, 2001. 82, 83, 84

- [109] M. Tan, R. Deklerck, B. Jansen, M. Bister, and J. Cornelis, “A novel computer-aided lung nodule detection system for ct images,” MEDICAL PHYSICS, vol. 38, no. 10, pp. 5630–5645, 2011. 83, 84
- [110] Q. Li, S. Sone, and K. Doi, “Selective enhancement filters for nodules, vessels, and airway walls in two- and three-dimensional ct scans,” Medical Physics, vol. 30, no. 8, pp. 2040–2051, 2003. 83
- [111] Q. Li, H. Arimura, and K. Doi, “Selective enhancement filters for lung nodules, intracranial aneurysms, and breast microcalcifications,” International Congress Series, vol. 1268, no. 0, pp. 929 – 934, 2004. 83
- [112] T. Messay, R. Hardie, and R. SK., “A new computationally efficient cad system for pulmonary nodule detection in ct imagery,” Medical Image Analysis, vol. 14, no. 3, pp. 390–406, 2010. 83, 84
- [113] R. Opfer and R. Wiemker, “Performance analysis for computer-aided lung nodule detection on lide data,” in Society of Photo-Optical Instrumentation Engineers (SPIE) Conference Series, vol. 6515, Mar. 2007. 83
- [114] W. Guo and Q. Li, “High performance lung nodule detection schemes in CT using local and global information,” Medical Physics, vol. 39, pp. 5157–5168, July 2012. 84
- [115] Q. Li, F. Li, and K. Doi, “Computerized detection of lung nodules in thin-section {CT} images by use of selective enhancement filters and an automated rule-based classifier,” Academic Radiology, vol. 15, no. 2, pp. 165 – 175, 2008. 84
- [116] Q. Li and K. Doi, “Analysis and minimization of overtraining effect in rule-based classifiers for computer-aided diagnosis,” Medical Physics, vol. 33, no. 2, pp. 320–328, 2006. 84
- [117] K. Murphy, B. van Ginneken, A. Schilham, B. de Hoop, H. Gietema, and M. Prokop, “A large-scale evaluation of automatic pulmonary nodule detection

- in chest ct using local image features and k-nearest-neighbour classification,” Medical Image Analysis, vol. 13, no. 5, pp. 757 – 770, 2009. 84, 96, 97
- [118] J.-M. Kuhnigk, V. Dicken, L. Bornemann, A. Bakai, D. Wormanns, S. Krass, and H. O. Peitgen, “Morphological segmentation and partial volume analysis for volumetry of solid pulmonary lesions in thoracic ct scans,” IEEE Transactions on Medical Imaging, vol. 25, pp. 417–434, April 2006. 84
- [119] C. R. Giardina and E. R. Dougherty, Morphological Methods in Image and Signal Processing. Upper Saddle River, NJ, USA: Prentice-Hall, Inc., 1988. 86
- [120] B. Merriman, J. Bence, , and S. Osher, “Diffusion generated motion by mean curvature,” in Computational Crystal Grower’s Workshop, MS Selected Letters, pp. 73–83, 1993. 86
- [121] W.-J. Choi and T.-S. Choi., “Genetic programming-based feature transform and classification for the automatic detection of pulmonary nodules on computed tomography images,” Information Sciences, vol. 212, pp. 57–78, 2012. 88, 96
- [122] E. Bae, J. Yuan, and X.-C. Tai, “Global minimization for continuous multi-phase partitioning problems using a dual approach,” International journal of computer vision, vol. 92, no. 1, pp. 112–129, 2011. 104
- [123] R. Yildizoglu, J.-F. Aujol, and N. Papadakis, “A convex formulation for global histogram based binary segmentation,” in Energy Minimization Methods in Computer Vision and Pattern Recognition (A. Heyden, F. Kahl, C. Olsson, M. Oskarsson, and X.-C. Tai, eds.), vol. 8081 of Lecture Notes in Computer Science, pp. 335–349, Springer Berlin Heidelberg, 2013. 104
- [124] X. Bresson, P. Vandergheynst, and J. Thiran, “A variational model for object segmentation using boundary information and statistical shape prior driven

by the mumford-shah functional,” International Journal of Computer Vision,  
vol. 68(2), pp. 145–162, 2006. 104